Regional and Local Hydrologic Responses to Climate Fluctuations and Land Use Change, Columbia River Basin, Washington

By

Leslie Lyons Duncan

Dissertation

Submitted to the Faculty of the
Graduate School of Vanderbilt University
in partial fulfillment of the requirements
for the degree of

DOCTOR OF PHILOSOPHY
in
Environmental Engineering

May, 2017
Nashville, Tennessee

Approved:

George M. Hornberger, Ph.D.

David J. Furbish, Ph.D.

Jonathan M. Gilligan, Ph.D.

David S. Kosson, Ph.D.

Eugene J. LeBoeuf, Ph.D.

To Cooper.

ACKNOWLEDGEMENTS

This work would not have been possible without the support and guidance of two people: my advisor, George Hornberger, and dissertation committee member, David Furbish. Their wisdom and altruism helped me through many moments of bewilderment. They are individuals that I will always respect as advisors, mentors, scientists, and friends. I would also like to thank Charles Powers and David Kosson for their tireless attempts in arranging the field work that, ultimately, did not happen. I would also like to thank my other dissertation committee members for their guidance, and especially Jonathan Gilligan for his support and enthusiasm during this process.

I cannot proceed without acknowledging the financial support provided by Vanderbilt University and the United States Department of Energy. I am grateful for the opportunity to work on such an interesting project and for the freedom my financial support has allowed me.

Finally, I have to thank my colleagues, friends, and family for being so generous with their time and support. Thanks to my research group for all the constructive criticism, Elizabeth Stone and Chelsea Peters for the perfectly-timed coffee breaks, Scott Worland for the job, Yi Mei for the endless hours of help, and Debra Perrone and John Jacobi for the numerous, wonderful hours that we spent working together. Thank you to Dad, Mom, Laura, Bro, Bobby, Tammy, Dennis, Samantha, and the rest of my family for all the love, inspiration, and encouragement. And, finally, thank you to my loving husband, Ben, and my adoring son, Cooper. I couldn't have done this without Ben, and I wouldn't have wanted to do this for anyone else but Cooper.

This dissertation thesis was completed with the financial support by U.S. Department of Energy, under Cooperative Agreement Number DE-FC01-06EW07053 entitled “The Consortium for Ris Evaluation with Stakeholder Participation III” awarded to Vanderbilt University. This research was carried out as part of the Hanford Cultural Resources project supported by the U.S. Department of Energy. The opinions, findings, conclusions, or recommendations expressed herein are those of the author and do not necessarily represent the views of the U.S. Department of Energy or Vanderbilt Univeristy.

TABLE OF CONTENTS

Page

LIST OF TABLES

Table Page

LIST OF FIGURES

Figure Page

CHAPTER 1

INTRODUCTION

1.1. Background to the Problem

Anthropogenic alteration of the global environment is a principal interest confronting the world today, and this issue will maintain its significance in the future, as decisions made within this century will affect future generations to come. Human adaptation of natural resources to meet our needs impacts hydrology on both an atmospheric and terrestrial level. Humans have historically altered the global environment primarily through the conversion of native land to agricultural and urban land and through the atmospheric release of greenhouse gases from burning fossil fuels. Throughout the coming decades, agricultural expansion and intensification, urban growth, and natural resource extraction will likely accelerate in response to a growing and increasingly wealthy world population. There are multiple consequences for Earth systems, at all scales, from anthropogenic alteration of the Earth's land surface and atmosphere [*Kalnay and Cai*, 2003; *Pimm and Raven*, 2000; *Rose and Peters*, 2001; *Storck et al.*, 1998; *Werth and Avissar*, 2002]. Furthermore, scientific concern has been expressed regarding climate change impacts on future temperature and precipitation, with emphasis on drought frequency, duration, and severity over various regions of the globe [*Intergovernmental Panel on Climate Change*, 2001]. Therefore, land use and climate changes are chief concerns facing the world this century, and the consequences of land use change may outweigh those from climate change [*Sala et al.*, 2000; *Vörösmarty et al.*, 2000].

Thus far, much of the research on land-use change consequences has focused on two issues: (1) the effects of land-use change on climate [*Bonan*, 1997; *DeFries and Eshleman*, 2004; *Houghton*, 1995], and (2) the effects of habitat loss on biodiversity [*Sala et al.*, 2000]. Despite the many studies examining the relationships between vegetation, hydrological processes, and water quality, the effects of anthropogenic land-use change on hydrology have received little attention in land-use change research [*Lambin et al.*, 1999]. Understanding the consequences of land-use change on hydrological processes represents an opportunity for academic inquiry [*DeFries and Eshleman*, 2004]. One such consequence is the changes in water supply from altered infiltration, runoff, and groundwater recharge.

Identification and quantification of the hydrological consequences of land-use change are large undertakings and are complicated by: 1) the length and continuity of hydrological records; 2) the relatively high natural variability of most hydrological systems; 3) the inability to fully, "experimentally control" land-use changes in catchments; 4) the relatively small number of controlled small-scale experimental studies that have been performed; and 5) the difficulties involved in extrapolating results from such controlled small-scale experimental studies to other larger, natural systems [*DeFries and Eshleman*, 2004]. The present understanding of land-use change on hydrology is predominately derived from controlled, experimental manipulations of the land surface, paired with pre- and post-manipulation observations of hydrological processes such as precipitation inputs and streamflow outputs [*Bosch and Hewlett*, 1982; *Harr*, 1981, 1986; *Harr et al.*, 1975; *Hornbeck et al.*, 1970; *Likens et al.*, 1977; *Swank and Crossley*, 1988]. While an extensive literature on urbanization and agricultural management practices exists, most studies are based on analysis of observational data from comparative or case studies [*Hollis*,

1975; *Potter*, 1991; *Rose and Peters*, 2001]. The science of the hydrological impacts of land use change can benefit from more than this traditional macro-level discernment.

In order to explore land use changes on hydrology, the effects of natural climate variability on hydrology must first be understood. Climate change has the potential to increase water scarcity in dry regions. This vulnerability to water scarcity has highlighted the need to better understand the causes of hydrological variability [*Intergovernmental Panel on Climate Change*, 2007]. Climate and hydrology create an intricately coupled system, as large-scale atmospheric and oceanic oscillations produce shifts in precipitation, air temperature, soil moisture, and runoff. Drastic and persistent changes in these variables may alter the likelihood of extreme events or cause changes in the form of seasonal precipitation. Understanding the natural climate drivers of variability in hydrology, particularly at decadal timescales, is of critical importance. At these time scales, inter-decadal to multi-decadal oceanic-atmospheric climate oscillations are important forcing mechanisms of hydroclimatic variability. The effects of anthropogenic climate change will be superimposed upon this natural variability. Detection of consistent phases of these natural oscillations and attribution of hydrologic anomalies to these phases are fundamental to understanding future climate change, both natural and anthropogenic, and managing water resources.

The effects accompanying land use change and climate change, both natural and anthropogenic, span all scales. General understandings of some of these effects exist, but regional to local effects may vary. The effects on hydrology are not often visible, or they are difficult to distinguish. Through examination of drought indices, some of which are designed to capture the

hydrological effects of drought (e.g., groundwater recharge, reservoir levels, etc.), a description of the effects of natural climate change on groundwater and streamflow in regulated river basins may exist. Furthermore, understanding the effects of land use change on hydrology involves more than just precipitation inputs and streamflow outputs – effects on groundwater-surface water (GW-SW) interactions are very important in such an endeavor as well.

The White Bluffs along the Columbia River, near Locke Island, in south central Washington State provide a case study for exploring the effects of climate and land use change on local hydrology and, more specifically, GW-SW interactions. The prehistoric and modern landsliding activity along the bluffs and the relatively recent land use changes within the Columbia River Basin only serve to increase the relevance of this case study to such an area of research. In as much as the general subsurface conditions and the GW-SW interactions bear upon understanding the stability and mechanics of the landslide, land use changes and dam-induced river stage fluctuations directly impact these conditions and interactions. Natural climate change in turn influences GW-SW interaction and the broader, regional hydroclimatology. Therefore, in order to explore the timing, frequency, and proximal cause of landslide occurrence along the White Bluffs, first natural climate variability and then the impacts of land use change on GW-SW interaction must be understood.

The research presented herein incorporates three objectives, narrowing from the broad, basin-scale, temporal and spatial hydroclimatology to the regional landsliding activity and finally to the local GW-SW interaction between the bluffs and the river, in order to explore the effects of climate and land use change across the multiple scales of impact. Water and its effects are often

implicated as causes of slope failure; therefore, the overall research goal of this work is to develop a quantitative description of the hydrological conditions of the Locke Island landslide and the White Bluffs. Natural climate variability and land use change can increase recharge to the groundwater system, which, in turn, can increase storage within the system and discharge from the system. The two main research goals of this work are: (1) to understand the impacts of climate variability on the regional subsurface conditions, and (2) to understand the impacts of land use change on the regional and local subsurface conditions. The Palmer Drought Severity Index (PDSI) is used as a measure of subsurface moisture. Since this particular metric can be calculated at any spatial scale for which input data exists, two corollary research objectives of this work are: (1) to determine how representative regional PDSI values are of finer-scale PDSI values, and (2) to determine the conditions that control the differences in PDSI values between the two spatial scales. In assessing the impacts of climate variability on regional subsurface conditions, two seconday research objectives of this work are: (1) to determine the existence of low frequency periods of wetness and dryness over the Pacific Northwest of the United States, and (2) to assess solar insolation as a forcing mechanism for any low frequency periods of wetness and dryness. In examining the impacts of land use change on regional and local subsurface conditions, a secondary research objective of this work is to determine the groundwater flow response to changes in subsurface recharge from dam-induced river fluctuations, local irrigation wastewater ponds, and increased regional precipitation.

There is evidence that landslides occurred along the White Bluffs in prehistoric times, within the last 11,000 years or so [*Triangle Associates, Inc.*, 2003]. There is also evidence of younger landslides that were probably active in the last several hundred years [*Triangle Associates, Inc.*,

2003]. Modern, active landslide activity along the Bluffs, however, began in the late 1960s, and toe erosion by the Columbia River was most likely the major cause of landsliding prior to irrigation on the land adjacent to the bluffs [*Schuster et al.*, 1987]. Between 1953 and 1964, when irrigation water began to be supplied to the Pasco Basin, the Columbia River Project delivered the equivalent of an eight-fold annual increase in water to the area [*Schuster et al.*, 1987]. Irrigation water is provided to the area approximately six months of the year via an extensive network of canals and laterals that deliver water to fields for crop irrigation. Wasteways take water from the system and return it to the Columbia River; storage ponds are also a part of the irrigation wastewater system [*Neff*, 1989]. Because most of the canals, laterals, wasteways, and wasteway ponds behind the White Bluffs are unlined, seeps from these various channels percolate through the soil and recharge the groundwater [*Neff*, 1989]. Recharge from canal seepage and applied irrigation accounted for almost ninety percent of the increase in inflow to the groundwater system and the resulting rise in groundwater levels [*Drost et al.*, 1993]. Between approximately 1946 and the mid-1980s, groundwater levels rose by an average of 60 m (200 ft); this resulted in a seven-fold increase in the annual flow through the groundwater system [*Drost et al.*, 1993].

According to several reports within the last 25 years, modern landsliding of the White Bluffs at Locke Island began as a result of irrigation water delivered to unlined wastewater ponds and canals behind the bluffs [*Bjornstad*, 2006; *Hays and Schuster*, 1987; *Nickens et al.*, 1998; *Schuster et al.*, 1987; *Triangle Associates, Inc.*, 2003]. *Bjornstad* [2006] maintains that the wastewater ponds were located over a glaciofluvial sediment-filled paleochannel eroded into the Ringold Formation and perpendicular to the bluff face opposite Locke Island. The percolating

irrigation water moves downward through the relatively permeable sands of the Hanford Formation until it reaches the fine-grained, fluvial-lacustrine Ringold Formation. *Bjornstad* [2006] and *Bennett et al.* [2002] suggest that the percolating water perches on top of the Ringold clays and silts and moves laterally along the old channel. Landslides occur where excess perched water seeps out from the paleochannel along the bluff face [*Bjornstad,* 2006].

Slumping of the White Bluffs adjacent to Locke Island began in the late 1970s, with the majority of the landslide movement occurring between 1982 and 1996. Even though the ponds were completely drained in the mid-1990s in an attempt to stop the sliding, slumping of the Bluffs continued into the mid-2000s [*Bjornstad,* 2006]. Although the slide has moved up to 24 m (80 ft) between 1998 and 2002 [*Bennett et al.*, 2002], the rate of movement at the toe of the landslide gradually slowed to the point where there was little movement in the years leading up to 2006 [*Bjornstad,* 2006]. *Bennett et al.* [2002] suggest that the continued presence of the landslide debris in its present position is essential for maintaining the stability of the hillside, and the erosional loss of the debris to the Columbia River should be taken seriously.

1.2. Structure of Dissertation

The work presented in this dissertation represents a multi-level approach to investigate the regional and local hydrological responses to climate fluctuations and land use change in the Columbia River Basin, with specific attention given to the role of groundwater and surface water in the landslide activity along the White Bluffs adjacent to Locke Island in Washington State. So

that the relative importance of land use change on local hydrological responses can be understood, the hydrological response to climate fluctuations must first be identified.

Drought indices provide information on the hydrological response to both precipitation and temperature on multiple timescales. There are several different drought indices that are routinely used in research, water resource management, and drought adaptation and mitigation, and the Palmer drought indices are used in this dissertation. Chapter 2 examines the effects of spatial resolution on the Palmer drought indices. This suite of drought indices can be calculated at any spatial resolution provided the climate and soil information data that serve as inputs to the model are available. Regional drought indices are typically used by researchers and policy makers, with the assumption that little information is lost in the aggregation. Chapter 2 examines the degree of variability between drought indices calculated at different spatial scales and explores the advantages gained in using fine-scale data for calculating the Palmer drought indices. This information provides insight into the appropriateness of the drought index data used to examine the effect of historical climate fluctuations on hydrology in the Columbia River Basin.

Evidence of past landslide activity – within both the last several hundred years and the last several thousand years – indicates that climate may have a profound impact on the hydrology along the White Bluffs. Chapter 3 uses wavelet analysis to infer longer period climate cycles and changes in event periodicity from an existing 2000 year drought dataset. The drought metric within this dataset is the Palmer Drought Severity Index (PDSI), which has been reconstructed from annually dated tree-ring records. The climate cycles identified within the wavelet analysis are indicative of wet and dry periods within the Columbia River Basin; extensive wet and dry

periods can produce intense hydrological responses, especially with regard to soil moisture and recharge. Results from this regional analysis provide a background against which to assess the relationship between local groundwater fluxes and relatively recent landslide activity along the White Bluffs.

Agriculture – specifically irrigated agriculture – has grown tremendously within the Columbia River Basin in the last half-century. Networks of canals and wasteways transport irrigation water behind the bluffs. Recent landslide activity at Locke Island has been attributed to the creation of ponds behind the bluff. Chapter 4 uses a two-dimensional finite element model to simulate the head changes and hence changes in groundwater fluxes at the toe of the landslide in response to stream stage variation, pond recharge, and increased precipitation recharge. Results from this chapter provide information on the relative importance of stream stage, irrigation wastewater ponds, and precipitation regimes in landslide activity.

Finally, this dissertation concludes with a synthesis of the work. Chapter 5 draws inferences from the results contained in Chapters 2-4 and attempts to identify the roles of climate fluctuations and land use change in landslide activity. There is some speculation on how the whole system functions.

CHAPTER 2

DROUGHT PLANNING AND MANAGEMENT: USING HIGH SPATIAL RESOLUTION AS PART OF THE SOLUTION[1]

2.1. Introduction

Water scarcity is a frequent problem in many parts of the world [*Intergovernmental Panel on Climate Change*, 2008]. As population grows, and agriculture, industry, and energy use expand, competition for water between demand-side sectors will continue to increase. Projected effects of climate change may combine with these stresses to reduce water availability in some parts of the world and simultaneously offset large increases in water demands in other parts of the world [*Fung et al.*, 2011]. Moreover, given projected climate warming and precipitation changes for the twenty-first century, drought is likely to worsen in the future [*Dai*, 2011; *Meehl et al.*, 2007; *Sheffield and Wood*, 2008]. Drought exacerbates water scarcity [*Riebsame et al.*, 1991]. Drought affects virtually all climate zones, and drought is an aggravating phenomenon in that it impacts many sectors of society, often reaching beyond the area that is physically experiencing drought. It is therefore imperative that scientists and policy makers to quantify drought for analysis, monitoring, agricultural planning, and emergency planning and preparedness.

Drought indices are routinely used to quantify drought. These indices assimilate large quantities of data on rainfall, snowpack, streamflow, and other water supply indicators into a

[1] This chapter of the dissertation has been previously published as Duncan, L. L., D. Perrone, J. H. Jacobi, and G. M. Hornberger (2015). Drought planning and management: Using high spatial resolution as part of the solution. *Environmental Science & Technology*, 49(5), 2639-2647.

comprehensible big picture of moisture availability. The Palmer Index [*Palmer*, 1965] is a popular group of drought indices. The term "Palmer Index" collectively refers to three indices: Z Index, Palmer Drought Severity Index (PDSI), and Palmer Hydrological Drought Index (PHDI). The index numbers signify, in terms of moisture, the departure of the weather for a particular month and year from the average climate of that month. The Z Index reflects the monthly, short-term soil moisture anomaly. The PDSI is a meteorological measure of drought, whereas the PHDI is a hydrological measure of drought. The primary distinction between the PDSI and PHDI is their beginning and ending times of a dry spell. With the PDSI, a spell is considered to have ended when the drought-inducing meteorological conditions end [*Palmer*, 1965]. With the PHDI, however, a spell does not end until the environment recovers from the drought [*Palmer*, 1965].

Drought indices can be calculated and analyzed at a range of spatial scales. For example, regional values of the Palmer Index are one of the key parameters that make up the current US Drought Monitor scheme [*Svoboda et al.*, 2002]. Studies have used regional values of the Palmer Index within probability models, such as Markov chain models [*Lohani and Loganathan*, 1997; *Lohani et al*., 1998; *Steinemann*, 2003] and dyadic wavelet transforms and neural networks [*Kim and Valdés*, 2002], to characterize and forecast drought. Regional drought values have also been used to examine drought frequency and duration [*Kim et al.*, 2002; *Soulé*, 1992], probe the spatial and temporal characteristics of drought [*Diaz*, 1983; *Eder et al.*, 1987; *Jones et al*, 1996; *Karl and Koscielny*, 1982; *Klugman*, 1978; *Skaggs*, 1975], and investigate teleconnection patterns to drought [*Özger et al*., 2009; *Piechota and Dracup*, 1996; *Rajagopalan et al.*, 2000; *Stahl and Demuth*, 1999]. The PDSI has been used extensively to study dry and pluvial periods at multiple spatial scales and to place recent and historical events within the context of the

historical drought record [*Briffa et al.*., 1994; *Dai*, 2011; *Dai et al.*, 1998; *Dai et al.*, 2004; *Heim*, 2002; *Karl and Quayle*, 1981; *Palmer*, 1965; *van der Schrier et al.*, 2006a; *van der Schrier et al.*, 2006b; *van der Schrier et al.*, 2007]. Studies have also calculated PDSI using global climate models to assess future drought scenarios [*Burke et al.*, 2006; *Dubrovsky et al.*, 2009; *Kothavala*, 1999; *Mavromatis*, 2007].

Heterogeneity and variability in variables required for drought quantification manifest themselves at a range of scales. Precipitation is frequently intermittent and discontinuous, with rainfall events forming discrete zones of cumulation across often small areas. Likewise, soil types and properties exhibit a stunning degree of heterogeneity at the catchment and regional scales. Despite this variability and the fact that drought indices can be calculated at a range of spatial scales, regional index values are most commonly used for research and real-time drought assessments. Such aggregation leads to a loss of detail. Variation is subsumed in the aggregate, and the high-frequency characteristics of the fine-scale components are damped. The spatial resolution of national drought monitors and forecasts is a particular challenge for water resource managers. One respondent to a 2005 survey of water managers protested the use of general climate forecasts for regional areas specifically because of the lack of local information: "…it can rain in one [watershed], but not in the next…Unless I know what's going to happen in exact places I can't use the forecasts" [*Rayner et al.*, 2005]. The degree to which spatial variability matters in quantifying drought is not clear. Just how different are drought indices calculated at different spatial scales; and are they different enough that it matters to planners?

This paper serves two purposes: (1) to determine how representative regional drought indices are of finer-resolution drought indices, and (2) to determine the conditions that control the differences in spatial patterns between the two scales. To accomplish these objectives, drought is quantified at both regional and finer-resolutions. Spatial and temporal patterns of differences in drought between the two scales are then statistically examined, and the relationships that determine these differences are parsed. The Pacific Northwest US, including most of the Columbia River Basin, serves as the study area, due to the sharp contrast in climate across the region. This analysis is confined to the Palmer Index, as it is used by a diverse group of people, including scientists and policy makers, to monitor and assess wet and dry conditions in both the US and other parts of the world [*Briffa et al.*, 1994; *Burke et al.*, 2006; *Dai*, 2011; *Dai et al.*, 1998; *Dubrovsky et al.*, 2009; *Hu and Willson*, 2000; *Jones et al.*, 1996; *Kim and Valdés*, 2003; *Kim et al.*, 2002; *Kogan*, 1995; *Kothavala*, 1999; *Mavromatis*, 2007; *Sakamoto*, 1978; *Szinell et al.*, 1998]. Finer-resolution drought is quantified with a high resolution grid. To measure regional drought, the climate division classification system is employed. Divisional boundaries cover the entire area of the state and they often, but not always, coincide with county boundaries. Although the climate division classification system is based only partially on climate considerations [*Guttman and Quayle*, 1996], numerous studies have employed the divisional spatial scale in using the Palmer drought indices to analyze drought [*Davis and Rappaport*, 1974; *Karl*, 1986a; *Karl*, 1986b; *Karl and Heim*, 1990; *Karl et al.*, 1987; *Karl et al.*, 2012; *Keyantash and Dracup*, 2002; *Klugman*, 1978; *Lohani and Loganathan*, 1997; *Özger et al.*, 2009; *Skaggs*, 1975; *Soulé*, 1992; *Whittemore et al.*, 1989]. While this particular regional classification system is unique to the US, regional classification systems in general are common throughout the world.

2.2. Data and Methods

2.2.1. Overview of the Palmer Drought Model

The Palmer drought model incorporates antecedent precipitation and moisture supply and demand into a hydrologic accounting system [*Palmer*, 1965]. The model requires only temperature, precipitation, and a soil water holding capacity (available water capacity, AWC, in the Palmer notation). Palmer's method begins with a water balance, which uses a two-layered model for soil moisture computations; the division of AWC between the two soil layers and the transfer of moisture between the layers are part of the model specifications [*Alley*, 1984]. Air temperature is used to calculate potential evapotranspiration (PET), generally using Thornthwaite's method [*Thornthwaite*, 1948; *Willmott and Rowe*, 1985; *Wilm et al.*, 1944], which then becomes part of the water balance computations. Palmer used what he called a Climatologically Appropriate for Existing Conditions (CAFEC) precipitation quantity to calculate the “normal” moisture for a particular month. The moisture departure from “normal” for a particular month can subsequently be computed. A weighting factor is used to adjust these departures from normal precipitation with the intent that values would be comparable across space and time. The weighted departure is the Z Index. The calculation proceeds by computing three intermediate indices and a probability term. The intermediate indices quantify an incipient wet spell, an incipient dry spell, and the existing wet or dry spell, which is also called the PHDI; a probability term quantifies the beginning and ending of dry or wet periods. The drought severity for a particular month depends on the moisture anomaly (Z Index) for that month and on the drought severity for both preceding and succeeding months. Palmer used a backtracking

procedure, dependent upon the probability term, to assign one of the three intermediate indices as the PDSI. This procedure and the rules employed are not trivial [*Alley*, 1984]. When information on future drought severity is not available, an operational version of the PDSI, the Palmer Modified Drought Index (PMDI), is available for real-time drought monitoring [*Heddinghaus and Sabol*, 1991], and this variation is used in the US Drought Monitor scheme.

2.2.2. Study Area

Our study area includes all or part of five northwestern US states - Idaho, Montana, Oregon, Washington, and Wyoming (Figure 2.1). Since the US climate division classification system is used to quantify regional drought, climate divisions within these states that also contained a large proportion of the Columbia River basin were selected as the areal extent of this study. The area is bounded by the Rocky Mountains to the east, and the Cascade Mountains and low-lying valleys to the west.

The region's mountains create sharp spatial contrasts in climate. The Cascade Mountains create a barrier between the maritime climate influences to the west and the continental climate influences to the east. Climate west of the Cascades is characterized by mild temperatures throughout the year, with abundant winter rains and dry summers. Sunshine and dry conditions become more common east of the Cascades, and annual and daily temperature ranges are considerably greater. While most of the entire region's precipitation occurs in just half of the year (October through March), a greater fraction of precipitation east of the Cascades falls in the warm half of the year, particularly in May and June [*Mote et al.*, 2003]. Although precipitation

exhibits the greatest seasonality west of the Cascades, summer precipitation to the west is only slightly greater than that to the east [*Mote et al.*, 2003].

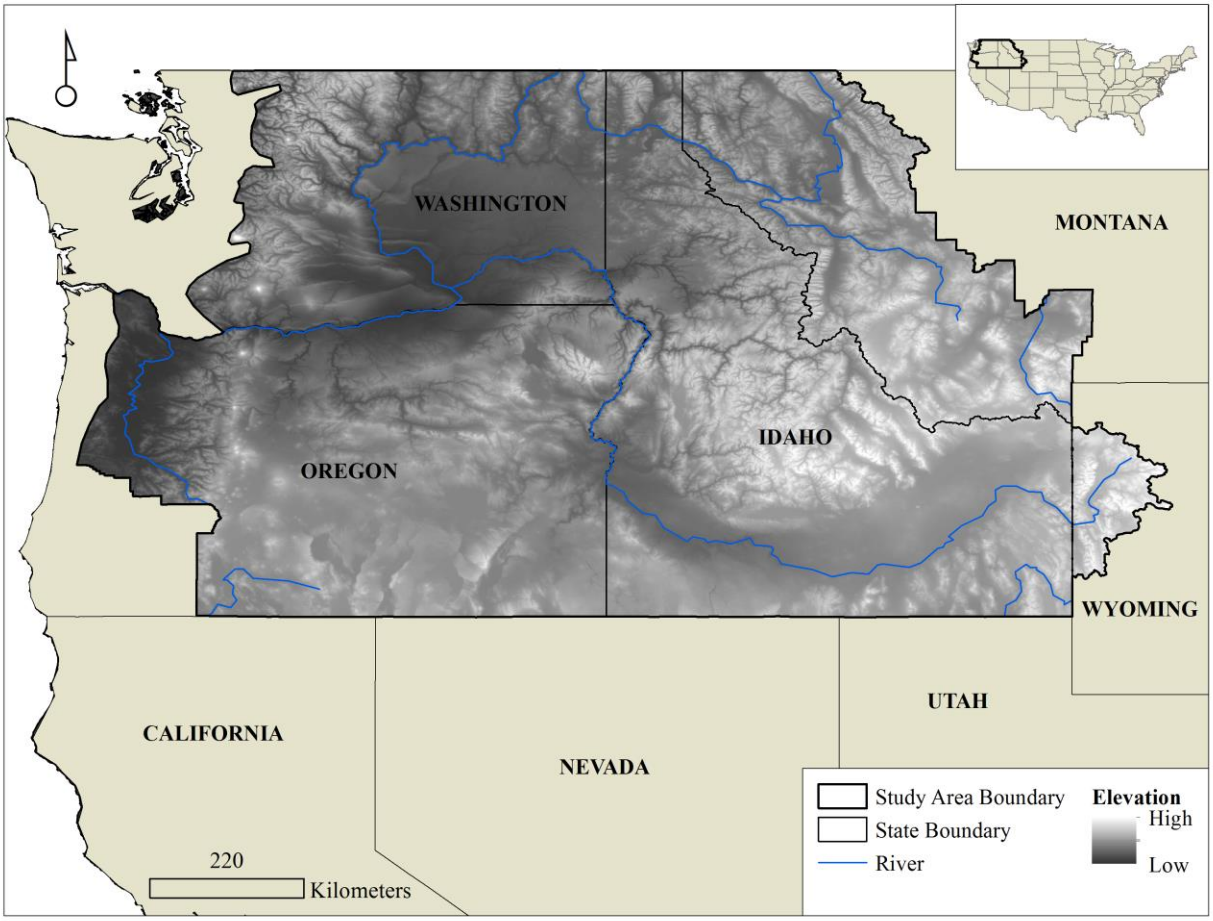

Figure 2.1 | Study area map

2.2.3. Data

University of Delaware (UDEL) 1900-2010 gridded monthly air temperature [*Matsuura and Willmott*, 2012a] and precipitation [*Matsuura and Willmott*, 2012b] data were obtained from the Physical Sciences Division of the Earth Science Research Laboratory at the National Oceanic

and Atmospheric Administration (http://www.esrl.noaa.gov/psd/, accessed April 11, 2013). The gridded monthly air temperature data were created by interpolating monthly averages of station air temperature to a 0.5° by 0.5° latitude/longitude grid, where the grid nodes are centered on the 0.25°. The gridded fields were estimated from monthly weather-station averages using a combination of spatial interpolation methods [*Matsuura and Willmott*, 2012a]. The gridded monthly precipitation data were created by interpolating station values of monthly total raingage-measured precipitation to a 0.5° by 0.5° latitude/longitude grid, where the grid nodes are centered on the 0.25° [*Matsuura and Willmott*, 2012b]. Climatologically aided interpolation [*Willmott and Robeson*, 1995] was used to estimate the monthly total precipitation fields [*Matsuura and Willmott*, 2012b].

Although monthly temperature and precipitation data for climate divisions can be obtained from the National Climatic Data Center (NCDC), in order to be consistent, these divisional values were determined using the gridded, high resolution UDEL dataset. Gridded temperature and precipitation data (1900-2010) were aggregated, using area-weighted averages, to the climate division scale. Latitudes at climate division centroids were obtained from the NCDC.

AWC data from the National Resources Conservation Service (NRCS) state soil geographic (STATSGO) database were obtained from the Earth System Science Center at The Pennsylvania State University (http://www.soilinfo.psu.edu/, accessed August 23, 2013) [*Miller and White*, 1998]. The AWC data were then aggregated, using area-weighted averages, to both the climate division scale and the 0.5° by 0.5° grid.

The monthly Z Index, PDSI, and PHDI for the 26 climate divisions and 344 grid boxes were calculated using a tool [*Jacobi et al.*, 2013] that requires only average monthly temperature and precipitation, latitude, and AWC. The tool allows the user to choose between the Hamon [*Hamon*, 1963] and Thornthwaite [*Thornthwaite*, 1948; *Willmott and Rowe*, 1985; *Wilm et al.*, 1944] methods of calculating PET and the period used in calibrating certain variables derived from the water balance. For this analysis, the Thornthwaite method was used to calculate PET. This PET calculation method is not without caveats; for example, the Thornthwaite method has been shown to have a tendency to overestimate PET in the summer and at high latitudes [*Amatya et al.*, 1995]. *Sheffield and Wood* [2012] argue that PDSI based on Thornthwaite PET is too temperature sensitive and a Penman-style PET model should be used instead. Still, the Thornthwaite method of calculating PET may be reasonably accurate for temperate climates [*Rosenberry et al.*, 2004], and this method is used in practice throughout the United States and globally. The Thornthwaite method is also simple, requiring only measurements of air temperature, which is advantageous when long historical records of radiation data are not available. The entire period of record was chosen to calibrate water balance variables.

2.2.4. Quantifying Differences

The two sample Kolmogorov-Smirnov (K-S) test is used to determine how much the regional drought indices differ from the finer-resolution drought indices. This statistical test is advantageous, as it makes no assumption about the distribution of the data – i.e., it is non-parametric and distribution free. The K-S test compares the equality of the two empirical cumulative distribution functions (EDFs), and it is sensitive to differences in both location and

shape of the EDFs. Of interest is not only how much the regional and finer-resolution drought indices differ from each other but whether the two are different enough that it matters (e.g., to water managers and planners). Therefore, grid and climate division PDSI are mapped for a specific month and year, which helps to visualize the differences in spatial variability that can arise, specifically during a dry period.

Cumulative distribution functions for grid and climate division Z Index, PDSI, and PHDI were developed from the historical data. The two-sample K-S test was applied to the two EDFs, which were estimated from the calculated climate division drought index series $(x_{11}, x_{12}, \cdots, x_{1m})$ and the calculated grid drought index series $(x_{21}, x_{22}, \cdots, x_{2n})$. The maximum difference, D_{mn}, between the two EDFs is the K-S statistic,

$$D_{mn} = \max_{x} |F_m(x_1) - F_n(x_2)|. \tag{2.1}$$

If the K-S statistic D_{mn} is larger than the critical value,

$$D_{mn} > \left[\frac{1}{2}\left(\frac{1}{m} + \frac{1}{n}\right) ln\left(\frac{\alpha}{2}\right)\right]^{\frac{1}{2}}, \tag{2.2}$$

the null hypothesis is rejected at the $\alpha \times 100\%$ significance level. For this analysis, α was set to 0.05.

The K-S test, however, is predicated on the assumption of independent sampling. Plots of autocorrelation functions for the 78 climate division drought indices showed significant

autocorrelation. Ljung-Box Q-tests for autocorrelation at lags of one, five, and nine were conducted on residual time series calculated from the same data. Results from these tests suggest that there is significant autocorrelation at all lags in the residuals at the 5% significance level.

The assumption of independent sampling is important, since it is essential for determining the critical values at the $\alpha \times 100\%$ significance level [*Semenov and Welham*, 2004]. Serial correlation in the data, such as that in the drought indices, causes the effective sample size or effective number of degrees of freedom to be smaller than the data sample size used in the test. When the data sample sizes m and n are used to determine the critical value for the test at a given significance level, the critical value is then smaller than the one anticipated under the independent sampling assumption. This causes the K-S test to reject the null hypothesis more often than expected at a given significance level. Therefore, instead of using the values of the K-S statistic D_{mn} estimated from the assumed probability distributions, determining valid critical values of the K-S statistic with resampling tests or Monte Carlo tests [*Wilks*, 1995] may offer a potential solution [*Qian et al.*, 2004].

The critical values of the K-S statistic D_{mn} were estimated through resampling tests for each of the 584 grid box-climate division pairs. Three resampling tests were performed for every grid box-climate division pair - one each for the Z Index, PDSI, and PHDI. Following the methodology of *Qian et al.* [2004], the resampling procedure involved: (1) pooling the 111-year grid box observations for each drought index and the corresponding 111-year climate division observations for each drought index to form a 222-year data pool; (2) randomly selecting a year from the 222-year data pool without replacement 111 times to form a 111-year mixed sample;

(3) pooling the remaining 111-year data to form the second mixed sample; (4) computing the K-S statistic D_{mn} from the EDFs estimated from the two 111-year mixed samples; (5) repeating steps two through four 1000 times to obtain 1000 values of D_{mn}; (6) taking the 95th percentile of the 1000 values of D_{mn} as the K-S statistic at the 5% significance level. This significance level is the probability of a Type I error. The critical values of D_{mn} determined through resampling were used to either reject or fail to reject the null hypothesis of the K-S tests.

2.2.5. Understanding Spatial Differences

Multiple linear regression is used to examine the conditions that control the spatial patterns of differences between the grid and climate division drought. Average positive and negative differences between the grid and climate division drought indices serve as predictors, since differences between drought indices can be either positive or negative and the numbers of positive and negative differences are similar in magnitude. Histograms are used to determine the fraction of grid and climate division pairs that experience large positive and negative PDSI and PHDI differences with varying frequency.

Three drought index time series are associated with each grid box and each climate division: Z Index, PDSI, and PHDI; and there are 584 different grid box-climate division pairs. Differences between the grid box Z Index time series and climate division Z Index time series were calculated for each pair, by subtracting the climate division value from the grid box value. These differences were either positive or negative. Positive differences in Z Index were averaged for each pair, and negative differences in Z Index were averaged for each pair. This process was

repeated for the PDSI and PHDI. This resulted in 584 average positive differences and 584 average negative differences for each of the three drought indices. Average positive and negative precipitation and temperature differences for each grid box-climate division pair were calculated in the same way. AWC differences for each pair were calculated by subtracting the climate division value from the grid box value. Note that AWC differences are not averages, since there is only one AWC value for each grid box and only one AWC value for each climate division.

Multiple linear regression was used to model the relationship between the average positive and negative drought index differences $(y_{i1}, y_{i2}, \cdots, y_{in})$ and temperature, precipitation, and AWC differences $(x_{i1}, x_{i2}, \cdots, x_{ip})$. Formally, the model given n observations is

$$y_{in} = \beta_0 + \beta_1 x_{i1} + \beta_2 x_{i2} + \cdots + \beta_p x_{ip} + \varepsilon_i, \tag{2.3}$$

for $i = 1, 2, \cdots, n$, where $\beta_0,\ \beta_1,\ \beta_2, \cdots,\ \beta_p$ are unknown coefficients to be estimated by $b_0, b_1, b_2, \cdots, b_p$ and $\varepsilon_1, \varepsilon_2, \cdots, \varepsilon_n$ are independent random variables each with zero mean and unknown variance. Six response variables $(m = 6)$ were used in this analysis: average positive Z Index, average negative Z Index, average positive PDSI, average negative PDSI, average positive PHDI, and average negative PHDI. Four predictors $(p = 4)$ were used in this analysis: average temperature difference, average precipitation difference, AWC difference, and one constant. Response variables and predictors each contained 584 observations $(n = 584)$.

The relationships between drought indices and temperature, precipitation, and AWC can be looked at in a slightly different way, in order to supplement the multiple linear regression. The

PDSI, temperature, and precipitation time series, as well as the difference in AWC, are analyzed for two grid box-climate division pairs: (1) one that experiences small average positive (and negative differences (i.e., between -1 and 1), and (2) one that experiences large average positive differences (i.e., ≥ 2) and large average negative differences (i.e., ≤ -2).

The differences between the grid box drought time series and climate division drought time series were also used to create histograms. For each grid box-climate division pair, the number of differences in the grid box and climate division PDSI where the absolute value was greater than or equal to two was counted; the same was done for differences in the grid box and climate division PHDI. This resulted in 584 numbers, one for each grid box-climate division pair. These raw numbers were then converted to percentages of total historical time (111 years). The percentages of total time were binned to create two histograms – one for differences in PDSI, and one for differences in PHDI.

Average difference between grid and climate division PDSI values for historically dry, wet, and near normal periods were also calculated. These periods are defined by, first, calculating a weighted average PDSI value for the entire study area using climate division PDSI values and climate division areas as weights. Dry periods are classified as PDSI values less than or equal to -2; wet periods are classified as PDSI values greater than or equal to 2; and near normal periods are classified as PDSI values between -2 and 2. Differences are calculated by subtracting the climate division PDSI value from the grid box PDSI value and taking the absolute value.

2.3. Results

The resampled K-S test rejects the null hypothesis that both the grid box and climate division Z Index data are generated from the same distribution for 81 of the 584 pairs at the 95% significance level (Table 2-1). Similarly, the test rejects the null hypothesis that the PDSI and PHDI values come from the same distribution for 412 and 416 pairs, respectively (Table 2-1). As expected, resampling decreases the number of times that the K-S test rejects the null hypothesis for all three indices; the reductions in number of rejections, while considerable at the 99% significance level, are small at the 95% significance level (Table A-1 in Appendix A).

Table 2.1 | Resampled Two-Sample K-S Test Results

Drought Index	p-value	Number (%) of Grid Box-Climate Division Pairs for which the Null Hypothesis is Rejected
Z	$p<0.01$	53 (9%)
	$p<0.05$	81 (14%)
PDSI	$p<0.01$	187 (32%)
	$p<0.05$	412 (71%)
PHDI	$p<0.01$	180 (31%)
	$p<0.05$	416 (71%)

Notes: The K-S test returns a test decision for the null hypothesis that the two data samples are from the same continuous distribution; the test either rejects or fails to reject the null hypothesis. Numbers and percentages of grid box-climate division pairs where $p<0.05$ also include those where $p<0.01$.

The resampled K-S tests yield three common groups of test decisions among the grid box-climate division pairs. In one group, the test fails to reject the null hypothesis for all three drought indices. The medians of the pair distributions in this group are very close to the same,

and the tails of the distributions are similar in density (Figure 2.2a – 2.2c). In another group, the test rejects the null hypothesis for the PDSI and PHDI only. Z Index distributions for pairs in this group are similar (Figure 2.2d), while PDSI and PHDI distributions may reflect shifts in the median (Figure 2.2e) or changes in densities near the tails (Figure 2.2e and 2.2f). In the last group, the test rejects the null hypothesis for all three drought indices. EDFs in this group may be remarkably different, showing large shifts in the medians (Figure 2.2g – 2.2i). In addition to tangible differences in probability distributions, drought at the coarser, climate division scale and drought at the finer, grid box scale are spatially different (Figure 2.3a and 2.3b).

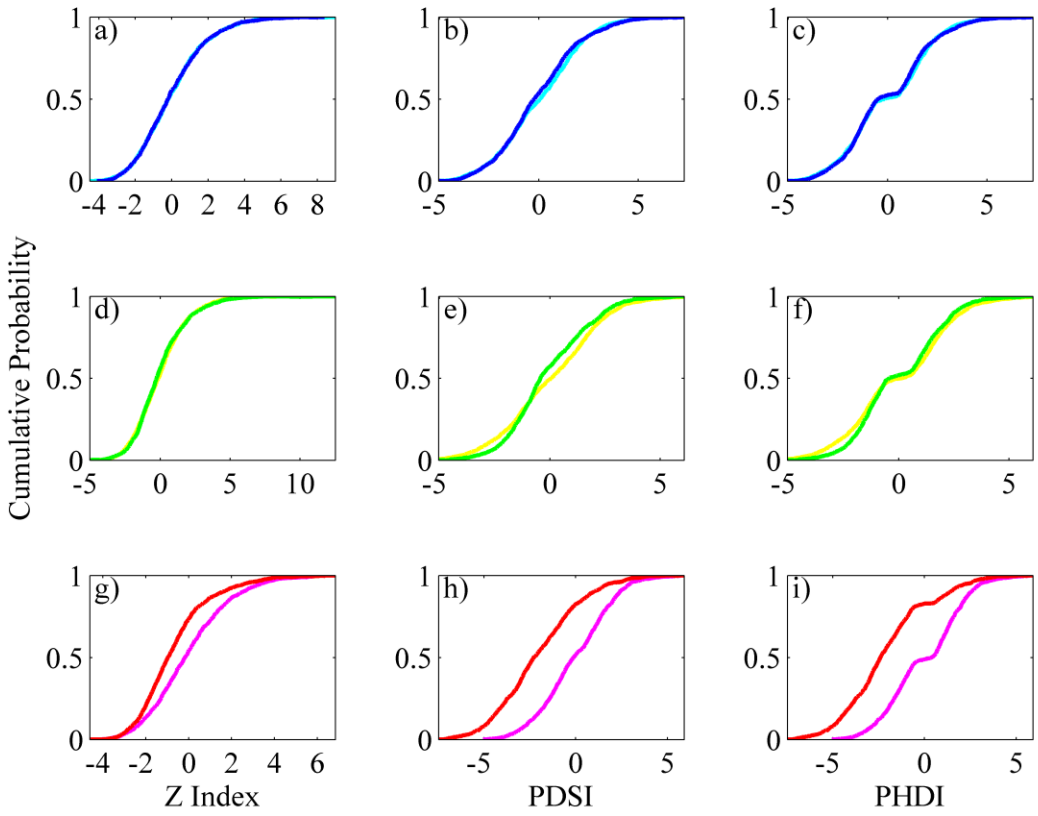

Figure 2.2 | EDFs of historical monthly Z, PDSI, and PHDI for the grid box-climate division pairs highlighted in Figure 4. The K-S test rejects the null hypothesis for (e-i).

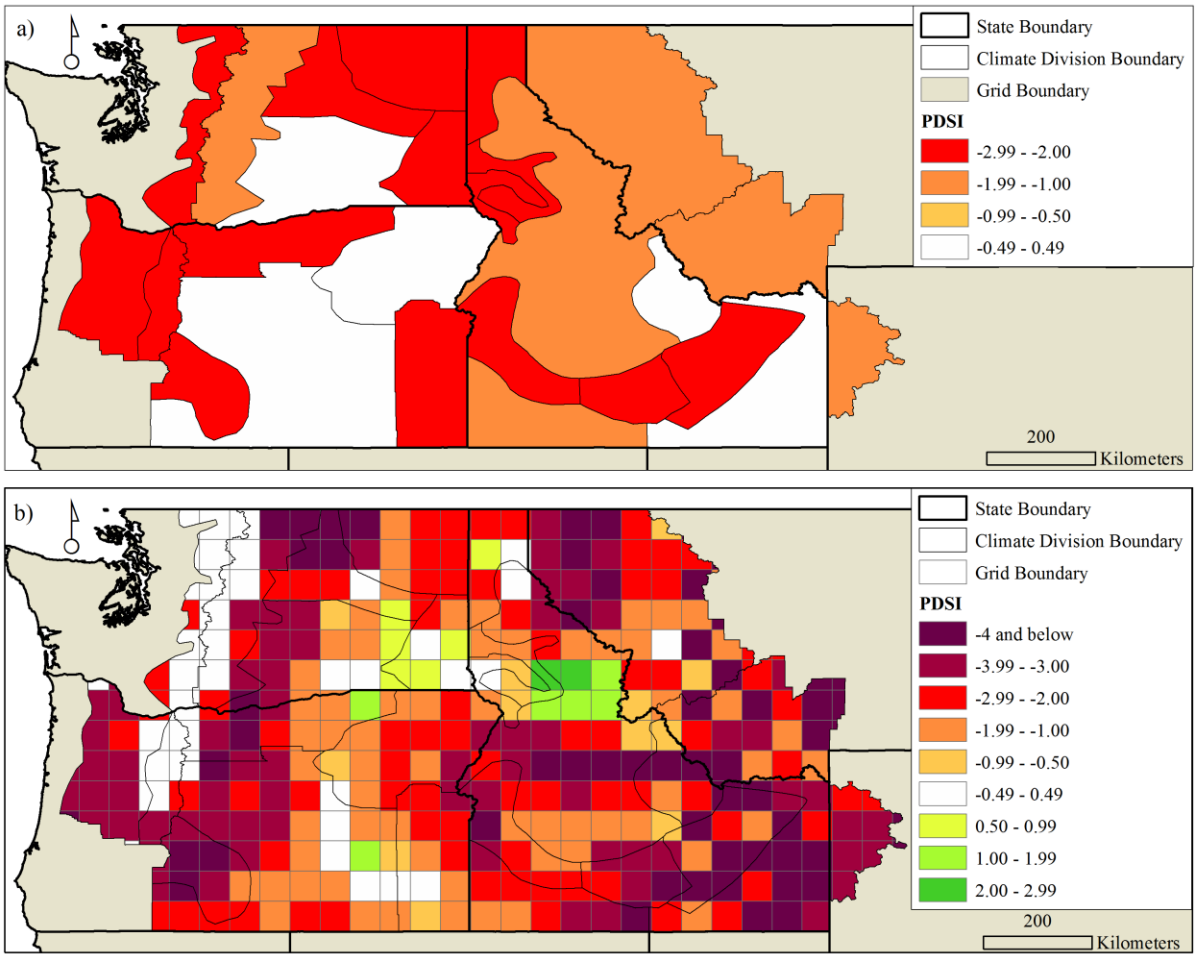

Figure 2.3 | Map of a) May 2001 PDSI calculated at the climate division spatial resolution and b) May 2001 PDSI calculated at the 0.5° by 0.5° latitude/longitude spatial resolution.

There are no obvious spatial patterns in the resampled K-S test results for PDSI and PHDI (Figure 2.4a and 2.4b). A map of the resampled K-S test results for the Z Index is not shown due to the small number of grid box-climate division pairs where the null hypothesis is rejected (Table 2.1). The resampled K-S test results for PDSI and PHDI, however, are spatially congruent with average positive and negative differences in grid box and climate division PDSI and PHDI (Figure 2.5a – 2.5d). The null hypothesis is rejected for much of the far eastern portion of the study area, particularly grid box-climate division pairs along the Rocky Mountains, and along the

southern periphery. Similarly, average positive and negative drought index differences tend to be larger in magnitude and can exceed ±2. The resampled K-S test fails to reject the null hypothesis for much of the interior of the study area, where average positive and negative index differences tend to be smaller in magnitude.

For monthly PDSI and PHDI, the difference between the grid box value and the climate division value is greater than or equal to two between zero and sixty percent of the time. Forty-nine percent of grid box-climate division pairs experience PDSI differences greater than or equal to two at least thirty percent of the time (Figure 2.6a). Similarly, fifty-six percent of grid box-climate division pairs experience PHDI differences greater than or equal to two at least thirty percent of the time (Figure 2.6b).

There are no direct correlations between average drought index differences and average temperature and precipitation differences or AWC differences, as evidenced by low coefficient of determination values (Table A.1 in Appendix A). While these are not predictive relationships, some are significant. Average temperature and precipitation differences are significant ($p<0.01$) for both average positive and negative differences in all three drought indices. AWC is significant ($p<0.05$) for average negative PDSI and PHDI differences only. For one of the grid box-climate division pairs where average positive and negative differences are large, the difference in AWC is small, while both temperature and precipitation values vary – at times drastically – between the grid and climate division (Figure A.1 in Appendix A). For one of the grid box-climate division pairs where average positive and negative differences are small, the difference in AWC is quite large; and, while temperature and precipitation values vary between

the grid and climate division, precipitation values are much closer for this pair (Figure A.2 in Appendix A), where average positive and negative differences are small, than the previous pair (Figure A.1 in Appendix A), where average positive and negative differences are large.

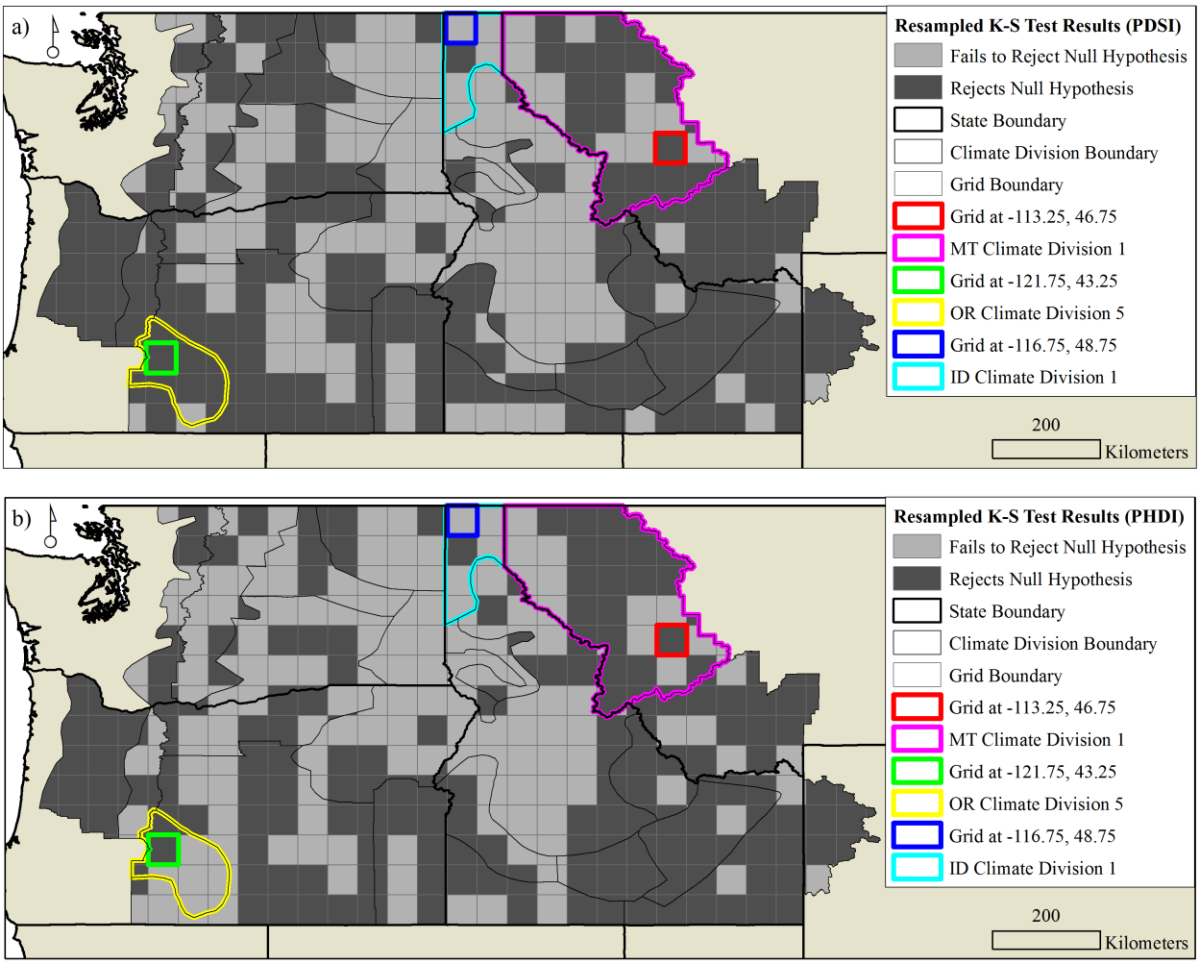

Figure 2.4 | Maps of resampled two-sample K-S test results for (a) PDSI and (b) PHDI. Grid boxes and climate division outlined in color correspond to those identified in Figure 2.

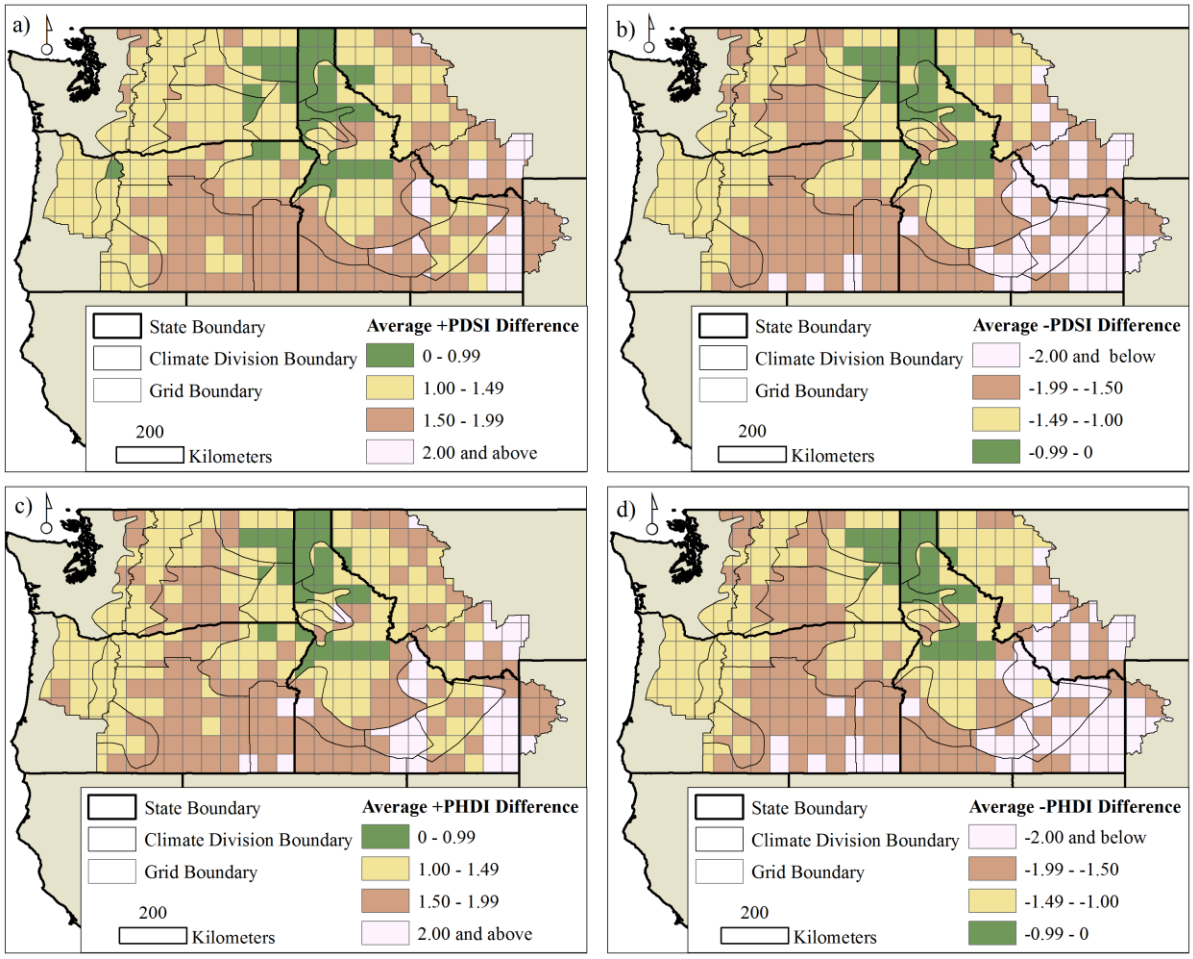

Figure 2.5 | Maps of (a) average positive PDSI difference, (b) average negative PDSI difference, (c) average positive PHDI difference, and (d) average negative PHDI difference.

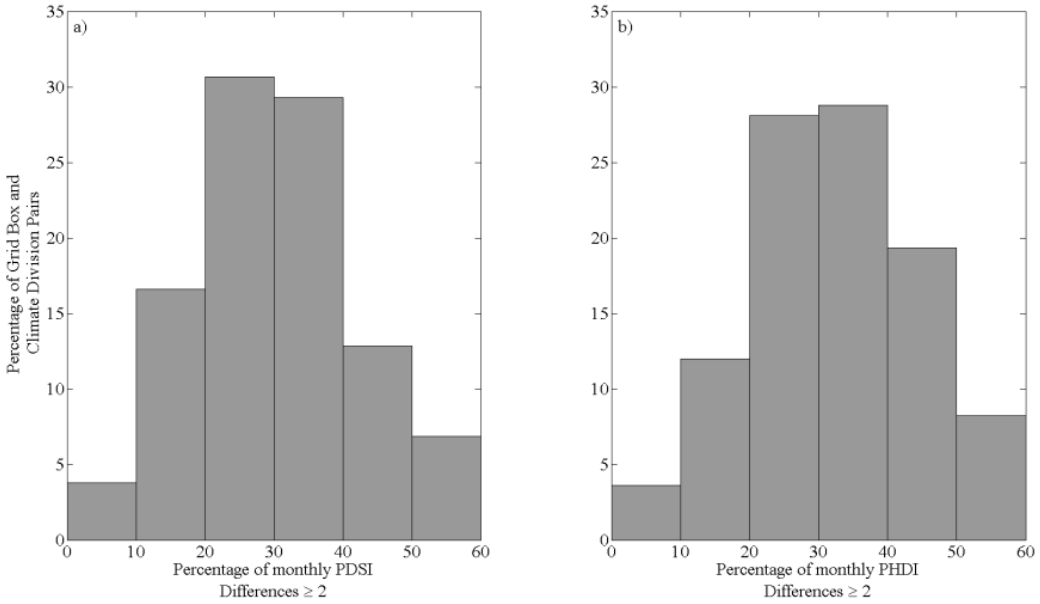

Figure 2.6 | Histograms of (a) percentages of monthly PDSI differences where the absolute value is ≥ 2 and (b) percentages of monthly PHDI differences where the absolute value is ≥ 2.

2.4. Discussion

Drought is most commonly quantified by calculating drought indices at regional spatial scales. These regional index values are largely used for both research and real-time drought assessments, with the assumption that little important information is lost in regionalizing drought indices. The results from this study provide an indication of how representative regional drought indices are of finer-resolution drought indices, spatially, temporally, and in terms of statistical probability. Our analysis goes a step further by examining the relationships that determine the spatial patterns in differences between regional and finer-resolution drought indices.

In general, the regional values of the cumulative Palmer drought indices (i.e., PDSI and PHDI) do not represent the finer-resolution values very well. The disparities between regional and finer-

resolution drought indices are reflected in the EDFs (Figure 2.2a – 2.2i), where the K-S test rejects the null hypothesis that the two data samples are from the same distribution for most PDSI and PHDI pairs (Table 2.1). The Z Index, unlike both the PDSI and PHDI, is not a cumulative index; it depends on the moisture departure from "normal" precipitation and a weighting factor [*Alley*, 1984]. Therefore, periodic large differences between the regional and finer-resolution Z Index do not accumulate; systematic large differences, however, are possible and indicate systematic large differences are present between the regional and finer-resolution data that are used to calculate drought. Conversely, PDSI and PHDI depend on current moisture anomalies and preceding and succeeding drought severities [*Alley*, 1984]. These indices, therefore, respond more slowly to changing conditions and allow differences between local and regional values to propagate over extended periods of time. Resampling only slightly decreases the number of times the null hypothesis is rejected for all three indices at the 95% significance level (Table 2.1), which suggests that most of the differences in grid and climate division drought index distributions are not due to autocorrelation within the data itself. This indicates that the shifts in medians and differences in tail densities between the grid and climate division EDFs (Figure 2.2e – 2.2i) are due to real differences in grid and climate division drought index values.

The resampled K-S test tends to reject the null hypothesis where average positive and negative differences between grid and climate division drought indices are the largest (Figures 2.4 and 2.5). The Palmer drought model uses only temperature, precipitation, and AWC in assigning a drought severity class. Therefore, differences between grid and climate division drought indices must be due to differences in one or some combination of these input variables. The multiple

linear regression results indicated no direct correlation between average drought index differences and average temperature and precipitation differences or AWC difference (Table A-2 in Appendix A). The PDSI and PHDI are cumulative indices, while temperature and precipitation reflect conditions at specific points in time. Therefore, differences in grid box and climate division drought indices at specific points in time do not precisely correlate to differences in temperature or precipitation at the same points in time. For whatever reason, there are localities within climate divisions that systematically or periodically deviate from the average climate division drought index. While the relationships between drought indices and temperature, precipitation, and AWC are not predictive, some relationships are significant. Other studies have also shown PDSI and PHDI to be sensitive to precipitation [*Guttman*, 1991; *Hu and Willson*, 2000], temperature [*Guttman*, 1991; *Hu and Willson*, 2000], and AWC [*Karl*, 1983].

Although regional limitations may prevent a direct generalization of some of these results to other regions in the world, this study sheds light on the effects of regionalizing drought indices. Calculating drought indices at finer resolutions has appeal from both a statistical perspective and a spatial resolution perspective. Median index values, modes, and extreme index value probabilities may significantly vary from regional to finer resolutions. These distributional shifts give rise to average differences in drought index values, which are related to average differences in precipitation and temperature, and, to a lesser extent, differences in AWC. Finer resolution drought index surfaces provide a much more detailed view of meteorological conditions, which is of greater importance in planning and mitigation. For example, variability in land use and water demand-side sectors necessitates localized climate information so that drought and pluvial risks can be better understood and managed by stakeholders. Subsequently, the availability of

gridded data, often at finer-resolutions, and easy-to-use drought calculators [e.g., *Jacobi et al.*, 2013], make such analyses straightforward.

Drought is a particularly vexing phenomenon - one that is common to virtually all regions of the world. Not only do the effects of drought ripple through many different sectors of society, but, in our globalized society, they often reach beyond the area that is physically experiencing drought. Realistically quantifying drought, then, is prudent to both scientists and policy makers. Results presented in this paper suggest that it may be useful to calculate drought at finer resolutions in order to better capture a more detailed picture of moisture availability, since a significant amount of information tends to be lost between regional and finer-resolution drought indices.

CHAPTER 3

EVIDENCE OF SOLAR FORCING OF HYDROCLIMATE CYCLES IN THE COLUMBIA RIVER BASIN FOR THE PAST 2000 YEARS

3.1. Introduction

Recent droughts in western North America are among the most severe on record [*Cook et al.*, 2004; *Seager*, 2007; *Luebehusen*, 2014]. Drought increases the competition for limited water resources, as population grows, and agriculture, industry, and energy use expand. The competition for water resources provides the motivation to improve our understanding of the long-term moisture balance, so that we can better plan for future drought and pluvial periods. Similarly, the vulnerability of regions to the adverse effects of water scarcity due to climate change precipitates the urgent need to better understand causes of variability in the hydrological cycle [*Intergovernmental Panel on Climate Change*, 2007], particularly drought.

It has become apparent that drought over North America is not random, but is heavily influenced by cyclical climate patterns. The ocean forcing phenomenon that has attracted most attention has been the El Niño Southern Oscillation (ENSO). El Niño conditions typically occur every three to seven years [*Cane*, 1986], and, while ENSO effects on local to regional climate can be severe, the impacts are typically transient, varying from several months to slightly more than a year. Low-frequency climate variability, however, has shown remarkable persistence relative to that attributed to ENSO events. Recent studies suggest that ENSO teleconnections with North American climate are strongly dependent on the phase of the Pacific Decadal Oscillation (PDO)

[*Mantua et al.*, 1997], such that the conventional ENSO patterns are only valid during years in which ENSO and PDO extremes are in phase with each other [*Dettinger et al*., 1998; *Gershunov and Barnett*, 1999; *Gershunov et al*., 1999; *McCabe and Dettinger*, 1999; *Wise*, 2010; *Brown*, 2011]. During moderate to strong positive (warm) phases of the PDO and ENSO (El Niño), the Pacific Northwest region is relatively dry. During moderate to strong negative (cool) phases of the PDO and ENSO (La Niña), more storms track across the Pacific Northwest, bringing above average amounts of precipitation to the region. Changes between these two phases of the PDO have occurred at bi-decadal (23-28 year) and pentadecadal (50-70 year) timescales over the past century [*MacDonald and Case*, 2005; *Shen et al.*, 2006]. *Hidalgo* [2004], *McCabe et al.* [2010], and *Huang et al.* [2005] have contended that both Pacific and Atlantic decadal variability contribute substantially to the low-frequency modulation of wetness and dryness over North America.

While ENSO and, to a lesser degree, Pacific and Atlantic multi-decadal oscillations are well represented in observational records, longer period centennial scale climate cycles are not. Since the early Holocene, summer insolation has gradually decreased from values greater than present, while winter insolation has gradually increased from values less than present [*Anderson*, 2012]. Climate model studies suggest that these changes may have influenced the variability and intensity of ENSO [*Bartlein et al*., 1998; *Kutzbach et al*., 1998; *Harrison et al*., 2003; *Cane*, 2005; *Diffenbaugh et al*., 2006]. Several well-known late Holocene climate transitions are also known to have occurred prior to the transition from the Little Ice Age during the late 19th and early 20th centuries: the transition into the Medieval Climate Anomaly (~AD 800) during the late

Holocene glaciation that followed peak summer solar insolation, and the transition into the Little Ice Age from the Medieval Climate Anomaly (~AD 1300).

The mechanisms responsible for these cycles and transitions and their impacts on climate and hydrological systems need to be determined in order to improve our understanding of longer-term climate change. Variability in radiation emitted from the Sun has been suggested as a possible driver of lower frequency climate cycles [*Horiuchi et al*., 2008; *Knudsen et al*., 2009]. Peaks in ^{10}Be and ^{14}C cosmogenic isotope records at ≈88 and 208-212 years correspond to the Gleissberg and Suess solar cycles [*Knudsen et al*., 2009]. The change in solar irradiance of ~0.1%, however, is often regarded as too small to affect climate [*Rind et al.*, 2008]. Yet amplification mechanisms by which slight changes in solar irradiance can affect climate have been proposed [*Haigh*, 2009].

Most knowledge of pre-instrumental-period drought comes from annually dated tree-ring records that allow precise regional comparison and data synthesis [*Cook et al*., 1999; *Cook et al*., 2004; *Knapp et al*., 2004; *Gedalof et al*., 2005]. Here, an approximately 2000 year drought dataset, reconstructed from paleoclimate records, is examined for longer period climate cycles and changes in event periodicity. The drought record is further analyzed in conjunction with a reconstructed total solar irradiance dataset that covers much of the Holocene. The aim here is to assess solar insolation as a forcing mechanism for longer periods of wetness and dryness over the northwestern United States. Documenting decadal- to century-scale aridity patterns over several millennia will improve knowledge of drought frequency and duration, and improve our

understanding of how these characteristics respond to long-term changes in oceanic- and solar-forcing.

3.2. Data

3.2.1. Study Area

This study includes 25 of the 286 grid points contained in the summer drought reconstruction dataset of *Cook et al.* [2008] (Figure 2.1). This area encompasses all of the U. S. states Idaho, Oregon, and Washington, and parts of California, Montana, Nevada, Utah, and Wyoming. Each grid box is 2.5° latitude by 2.5° longitude. The U.S. grid points are based on inverse distance weighted single-station Palmer Drought Severity Index (PDSI) records estimated from the U.S. historical climatology network of homogeneous monthly temperature and precipitation data [*Cook et al.*, 1999]. The PDSI data cover the period 1900-1990 at all locations.

3.2.2. Drought Data

The time period of coverage varies over the area. For grid boxes 25, 32, 33, 43, 44, and 55, the summer drought reconstructions date from AD 530 to AD 2006. For grid boxes 68, 83, and 99, the summer drought reconstructions date from AD 359 to AD 2006. For grid boxes 34, 35, 45, 46, 56, 57, 58, 69, 70, 71, 84, 85, 86, 100, 101, and 102, the summer drought reconstructions date from AD 0 to AD 2006. The drought metric used is the summer average (June-July-August) PDSI – the PDSI is a widely used tool for assessing water balance [*Cook et al*., 2004].

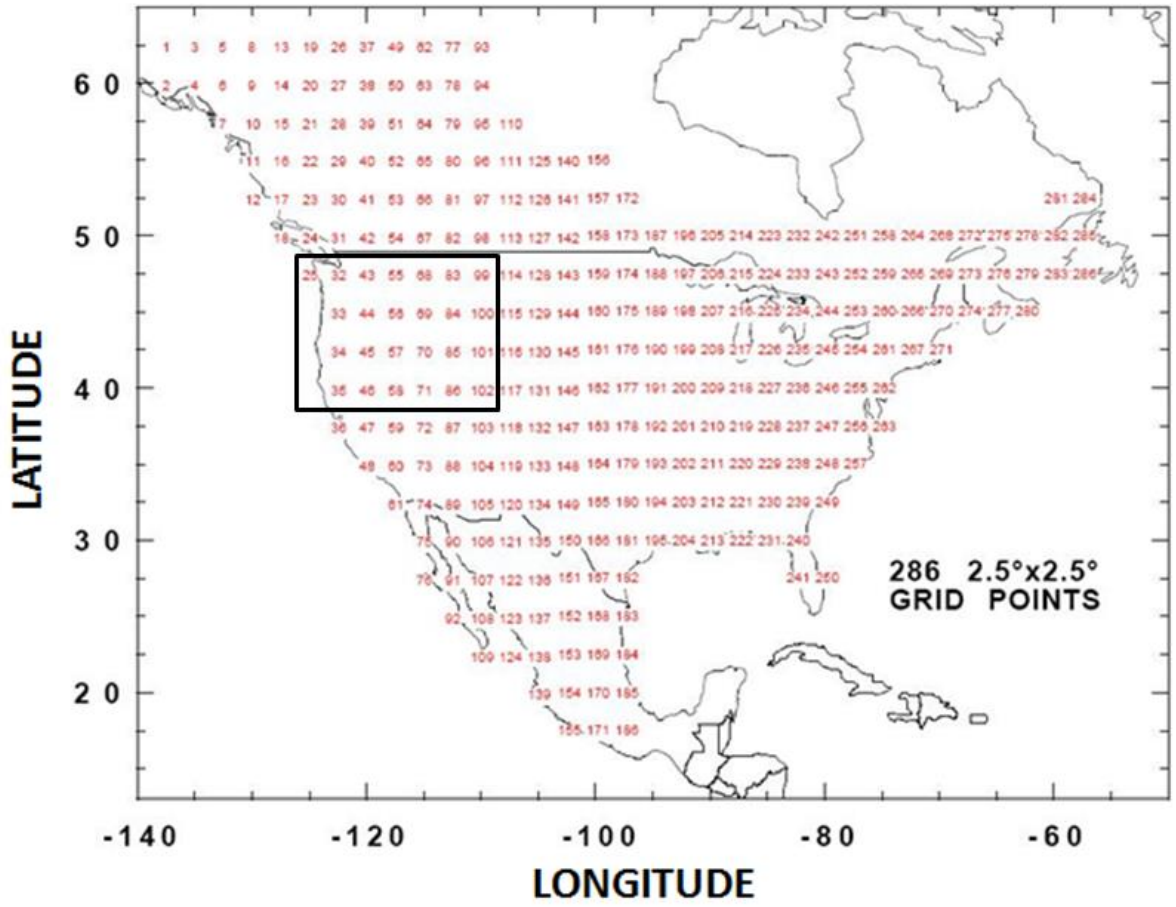

Notes: The black outline encloses the grid points used in this analysis. This figure has been adapted from http://www.ncdc.noaa.gov/paleo/image/pdsi2004-gridpoint-map.jpg, accessed February 7, 2014.

Figure 3.1 | PDSI Grid for *Cook et al.* [2008] Drought Reconstructions in Canada, United States, and Mexico.

The method used to reconstruct the PDSI grid from tree rings is the point-by-point regression (PPR) method [*Cook et al.*, 1999], which has been proven to be a robust method for reconstructing past drought [*Zhang et al.*, 2004]. The tree-ring chronology network used for PDSI reconstruction over North America is composed of 835 annually-resolved records. These chronologies cover the past 245 to 2,000 years, and all end on or after AD 1979. It should be noted that the large range of ages results in a declining number of tree-ring chronologies being available as candidate predictors for PDSI reconstruction as one goes back in time. For

information regarding the impact of this decline on the fidelity of the resulting grid point reconstructions, the reader is referred to the supporting online material of *Cook et al.* [2004]. For a detailed explanation of how the PDSI reconstructions were updated to AD 2006, the reader is again referred to the supporting online material of *Cook et al.* [2004] and *Cook et al.* [2008].

3.2.3. Solar Data

A reconstructed record of total solar irradiance [*Steinhilber et al.*, 2009a] was also used in this study. Total solar irradiance is based on a composite described in *Steinhilber et al.* [2008] using cosmogenic radionuclide ^{10}Be data from the Greenland Ice core Project (GRIP) [*Vonmoos et al.*, 2006] and South Pole [*McCracken et al.*, 2004] ice cores, and neutron monitor count rates [*Usoskin et al.*, 2005] from the worldwide neutron monitor network. The data, then, represent both hemispheres and are measured in different archives. Atmospheric mixing, transport, and deposition affect the ^{10}Be concentration of an ice sample; to some extent these "system effects" can be corrected. The reader is referred to *Steinhilber et al.* [2012] for further details. The reconstructed total solar irradiance data are 40-year running means and are re-sampled to a 5-yr time resolution. While the dataset dates back approximately 9300 years, only the record coincident with the reconstructed PDSI data is used in this analysis.

3.3. Methods

3.3.1. Determining Periodic Oscillations

Following the method outlined in *Torrence and Compo* [1998], wavelet power spectra of the detrended reconstructed PDSI data were derived for the 25 grid boxes under investigation. The wavelet transform can be used to analyze time series that contain non-stationary power at many different frequencies [*Daubechies*, 1990]. The wavelet power spectra were computed by convolving each of the 25 PDSI time series with a scaled and translated version of a mother wavelet. Given equal time spacing δt in a time series X_n ($n = 0,1, \dots, N-1$), a wavelet function, $\psi_0(\eta)$ (η is a non-dimensional time parameter), must have zero mean and be localized in both time and frequency space [*Farge*, 1992]. A Morlet wavelet was chosen as the mother wavelet, due to its extensive applications in studies involving hydroclimatic time series analysis. Also, Morlet wavelets provide adequate time and superior frequency resolution compared to other wavelet types [*Labat*, 2005; *Soniat et al.*, 2006].

Following *Torrence and Compo* [1998], the Morlet wavelet is characterized by a Gaussian modulated plane wave:

$$\psi_0(\eta) = \pi^{-1/4} e^{i\omega_0 \eta} e^{-\eta^2/2}, \tag{3.1}$$

where $\omega_0$is the non-dimensional angular frequency, here taken to be six to satisfy the admissibility condition [*Farge*, 1992].

Torrence and Compo [1998] define the continuous wavelet transform of a discrete sequence X_n as the convolution of X_n with a scaled and translated version of $\psi_0(n)$:

$$W_n(s) = \sum_{n'=0}^{N-1} X_{n'}\, \psi * \left[\frac{(n'-n)\delta t}{s}\right], \tag{3.2}$$

where $W_n(s)$ are the wavelet transform coefficients, ψ is the normalized wavelet, s is the wavelet scale, n is the localized time index, n' is the translated time index, and $(*)$ indicates the complex conjugate. Although it is possible to compute the wavelet transform using (2), it is considerably faster to do the calculations in Fourier space. The reader is referred to *Torrence and Compo* [1998] for the mathematical representations of the Fourier space calculations.

Because time series are finite in length, errors will occur at the beginning and end of the wavelet power spectrum. The time series in this study are padded with sufficient zeroes to bring the total length, N, of the time series up to the next-higher power of two, which both limits the edge effects and speeds up the Fourier transform [*Torrence and* Compo, 1998]. Padding with zeroes, however, introduces discontinuities at the endpoints and, at larger scales, decreases the amplitude near the edges [*Torrence and* Compo, 1998]. In order to delineate the region of the wavelet spectrum in which edge effects become important, the cone of influence (COI) is also calculated for the 25 PDSI time series.

Significance levels are determined for each of the 25 wavelet spectra using Monte Carlo methods, in order to isolate significant periods. It is assumed that different realizations of the

geophysical process – in this study, drought – will be randomly distributed about some expected background, and the actual spectrum can be compared against this random distribution. For this analysis, red noise (increasing power with decreasing frequency) is chosen as the appropriate background spectrum, and 95% is chosen as the confidence level.

Following *Torrence and Compo* [1998], the time-average wavelet spectrum over all the local wavelet spectra gives the global wavelet spectrum

$$\bar{W}^2(s) = \frac{1}{N}\sum_{n=0}^{N-1}|W_n(s)|^2. \tag{3.3}$$

It has been shown that the global wavelet spectrum provides an unbiased and consistent estimation of the true power spectrum of a time series [*Percival*, 1995]. It also has been suggested that the global wavelet spectrum can provide a useful measure of the background spectrum, against which peaks in the local wavelet spectra could be tested [*Kestin et al.*, 1998]. Once the 25 wavelet power spectra were calculated, the global wavelet spectra were computed. Scales with large global wavelet spectrum values were considered to contribute more spectral energy. While scales with small global wavelet spectrum values may contribute less spectral energy globally, these scales may still contribute large spectral energy locally [*Torrence and* Compo, 1998]. The global wavelet spectrum values, therefore, were used in concert with the continuous wavelet spectra to identify scales within the reconstructed PDSI time series with high potential of periodic signals. All wavelet spectra and associated cones of influence, confidence

levels, and global wavelet spectra were computed using the software provided by *Torrence and Compo* [1998][2].

3.3.2. Linking Periodic Oscillations

It is often desirable to examine together two time series that may be expected to be linked in some way. It is of specific interest to consider whether regions in time-frequency space with large common power have a consistent phase relationship, which may suggest a causal relationship between the two time series [*Grinsted et al.*, 2004]. The two time series used in this analysis are the reconstructed PDSI and total solar irradiance data. Because the total solar irradiance record is a re-sampled time series from 40-year running means, 40-year running means were calculated for each of the 25 reconstructed PDSI time series, and the PDSI running means were then re-sampled at the same 5-yr time resolution.

The cross wavelet transform was constructed from the two continuous wavelet transforms using the software provided by *Grinsted et al.* [2004][3], which exposes their common power and relative phase in time-frequency space. The cross wavelet transform of two time series x_n and y_n is defined as $W^{XY} = W^X W^{Y*}$, where $*$ denotes complex conjugation; the cross wavelet power can be further defined as $|W^{XY}|$, where the complex argument $\arg(W^{xy})$ can be interpreted as the local relative phase between x_n and y_n in time-frequency space [*Grinsted et al.*, 2004]. The

[2] A MATLAB software package by *Torrence and Compo* [1998] for performing the wavelet transform can be found at URL: http://www.paos.colorado.edu/research/wavelets/ (accessed February 7, 2014).
[3] A MATLAB software package by *Grinsted et al.* [2004] for performing the cross wavelet transform and wavelet coherence can be found at URL: http://www.pol.ac.uk/home/research/waveletcoherence/ (accessed February 7, 2014).

theoretical distribution of the cross wavelet power of two time series with background power spectra P_k^X and P_k^Y is given in *Torrence and Compo* [1998] and *Grinsted et al.* [2004] as

$$D\left(\frac{|W_n^X(s)W_n^{Y*}(s)|}{\sigma_X\sigma_Y} < p\right) = \frac{Z_v(p)}{v}\sqrt{P_k^X P_k^Y}\,, \tag{3.4}$$

where $Z_v(p)$ is the confidence level associated with the probability p for a probability density function defined by the square root of the product of two χ^2 distributions. In this study the 95% confidence level is used.

While the cross wavelet transform exposes areas with high common power, it is also valuable to measure the coherence of the cross wavelet transform in time frequency space. The wavelet coherence acts as a localized correlation coefficient between the two time series in time frequency space. *Grinsted et al.* [2004], following *Torrence and Webster* [1999], define the wavelet coherence of two time series, x_n and y_n, as

$$R_n^2(s) = \frac{\left|S\left(s^{-1}W_n^{XY}(s)\right)\right|^2}{S(s^{-1}|W_n^X(s)|^2)\cdot S(s^{-1}|W_n^Y(s)|^2)}, \tag{3.5}$$

where S is a smoothing operator with a footprint similar to that of the mother wavelet used. *Grinsted et al*. [2004] define the smoothing operator S as

$$S(W) = S_{scale}\left(S_{time}(W_n(s))\right), \tag{3.6}$$

where S_{scale} denotes smoothing along the wavelet scale axis and S_{time} denotes smoothing along the wavelet time axis. For the Morlet wavelet *Grinsted et al*. [2004], following *Torrence and Webster* [1999], give the smoothing operator as

$$S_{time}(W)|_s = \left(W_n(s) * c_1^{-t^2/2s^2}\right)\Big|_s, \tag{3.7}$$

$$S_{time}(W)|_s = \left(W_n(s) * c_2 \prod(0.6\, s)\right)\Big|_n, \tag{3.8}$$

where c_1 and c_2 are normalized constants and $\prod$ is the rectangle function. The factor 0.6 is the empirically derived scale decorrelation length for the Morlet wavelet [*Torrence and Compo*, 1998]. The statistical significance level of the wavelet coherence is estimated using Monte Carlo methods [*Grinsted et al.*, 2004]. The wavelet coherence was calculated using the software provided by *Grinsted et al.* [2004][4].

3.4. Results

Several peaks are evident in the reconstructed PDSI records. A broad peak at 6-8 years emerges in the continuous wavelet transform plots and global wavelet spectra (Figure 3.2) for much of the western half of the study area. This period range corresponds to ENSO. This frequency band is particularly noticeable around AD 600 (Figures 3.2 and 3.3) and again between the late 16th and 17th centuries (Figures 3.2-3.4). The continuous wavelet transform plots and global wavelet

[4] A MATLAB software package by *Grinsted et al.* [2004] for performing the cross wavelet transform and wavelet coherence can be found at URL: http://www.pol.ac.uk/home/research/waveletcoherence/ (accessed February 7, 2014).

spectra for a small number of the extreme northern and northeastern grid boxes indicate a peak at 40-48 years (Figure 3.3). This period range is somewhat similar to shorter periods of low-frequency Pacific and Atlantic Ocean variation. A peak at 96-128 years appears in the continuous wavelet transform plots and global wavelet spectra (Figures 3.2-3.4) for most all of the study area grid boxes. This period range partially characterizes North Pacific variability, and it also corresponds to that of the Gleissburg solar cycle. A peak at 224-256 years emerges (Figure 3.4) for several of the grid boxes with a 2006-year record; however, locally, these periods emerge both inside and outside the COI. This period range is similar to that of the Suess solar cycle.

From the cross wavelet transforms of the re-sampled PDSI and reconstructed total solar irradiance, large sections of common power exist on wavelengths varying from ~64-256 years (Figures 3.5 and 3.6). There is significant common power in the ~192-256 year band from AD 300 to AD 800 and from AD 1150 to AD 1650 (Figures 3.5 and 3.6). There is also significant common power in the ~96-160 year band from AD 900 to AD 1400 (Figures 3.5 and 3.6). For there to be a simple cause and effect relationship between the two phenomena, it is expected that oscillations are phase locked. The cross wavelet transforms show that PDSI and total solar irradiance are in-phase across much of the low-frequency sectors with significant common power. At low-frequency scales outside the areas with significant power the phase relationship is also predominately in-phase.

Compared with the cross wavelet transforms, a smaller section of the squared wavelet coherence stands out as being significant, and most of these areas show an in-phase relationship between

the re-sampled PDSI and reconstructed total solar irradiance (Figures 3.7 and 3.8). Oscillations in total solar irradiance are manifested in the PDSI on wavelengths varying from ~64-256 years. Since both time series are re-sampled from 40-year running means, the low-frequency scales from ~96-256 are of more interest here. There is significant coherence in the ~128-256 year band from AD 750 to AD 1500 (Figures 3.7 and 3.8).

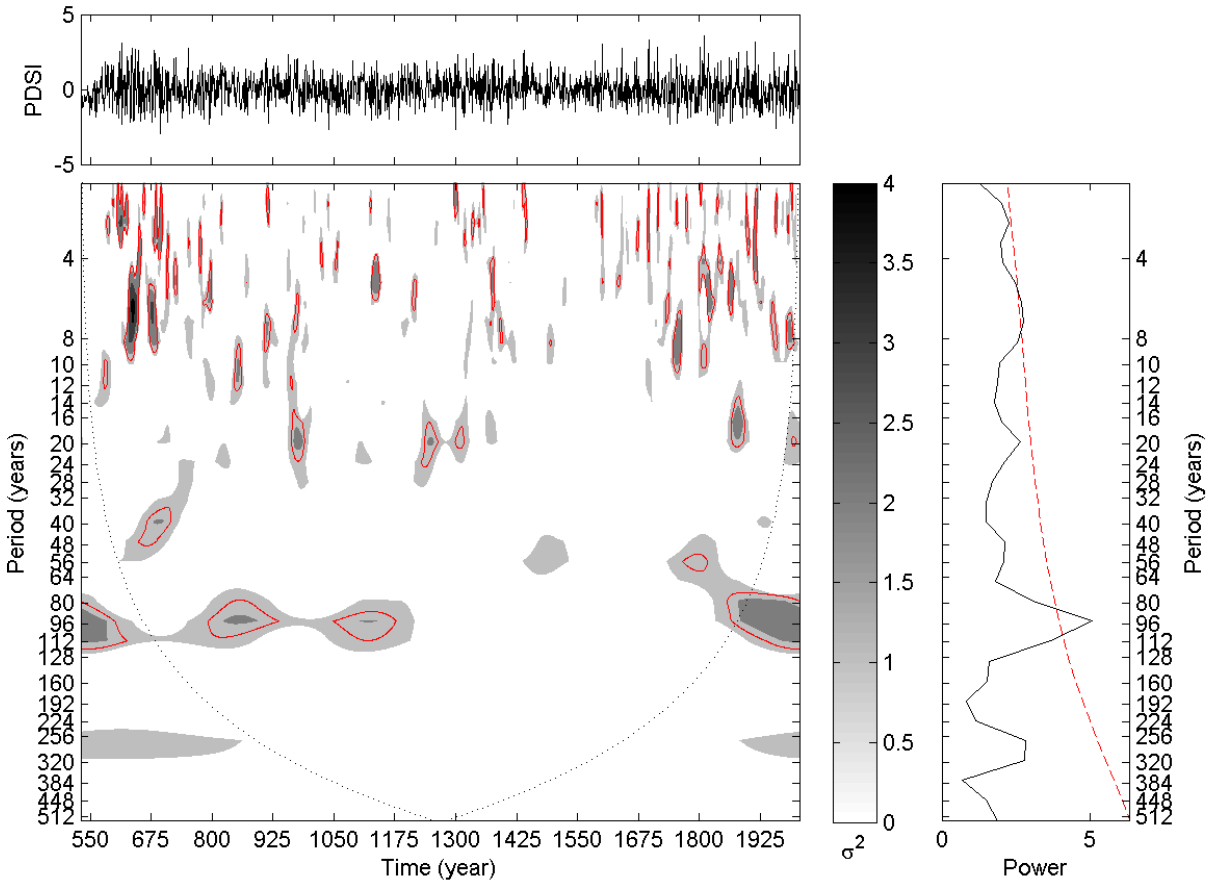

Notes: The black dotted outline on the continuous wavelet spectrum represents the COI. The 5% significance level against red noise is shown as a thin red contour on the continuous wavelet spectrum. The dashed red line on the global wavelet spectrum denotes the 95% confidence level.

Figure 3.2 | Detrended reconstructed PDSI time series (top), continuous wavelet spectrum (bottom), and global wavelet spectrum (right) for grid number 32 of the *Cook et al.* [2008] dataset.

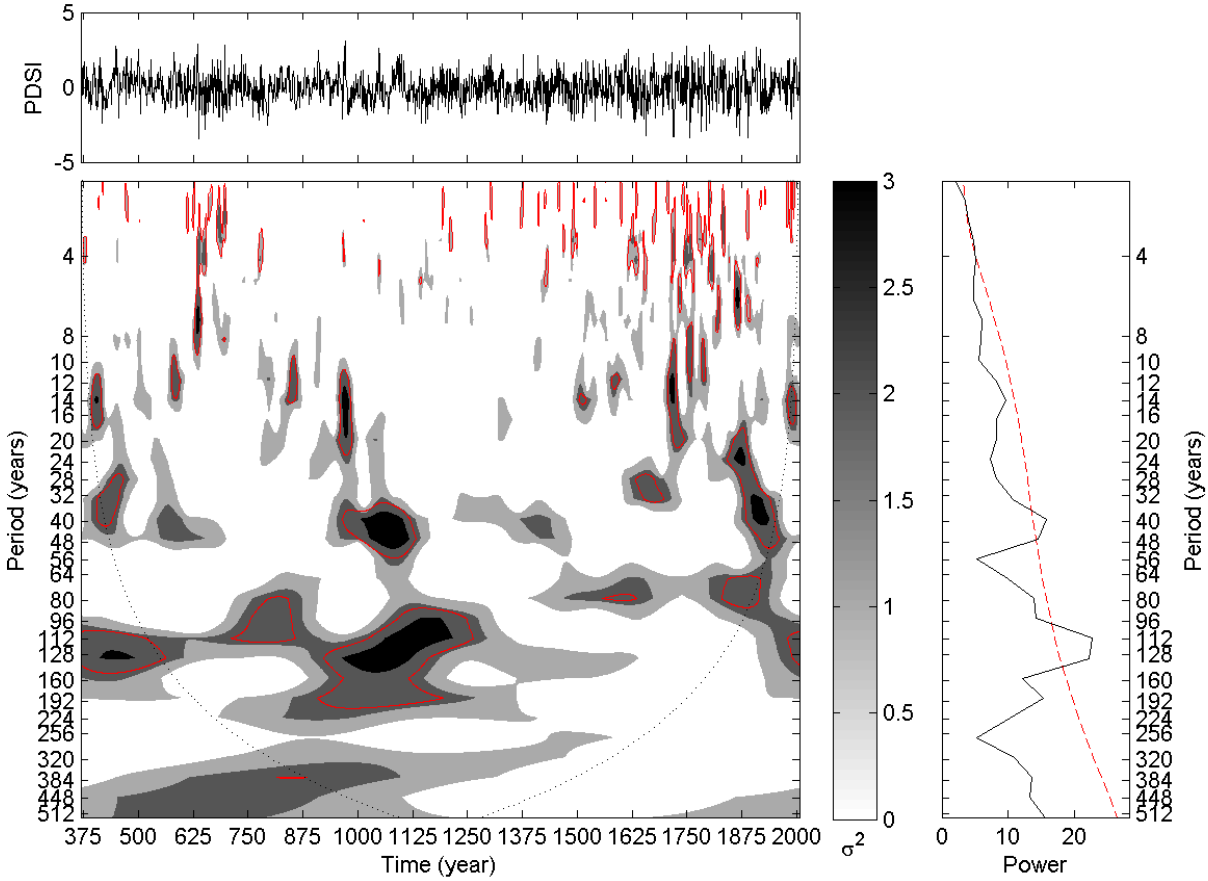

Notes: The black dotted outline on the continuous wavelet spectrum represents the COI. The 5% significance level against red noise is shown as a thin red contour on the continuous wavelet spectrum. The dashed red line on the global wavelet spectrum denotes the 95% confidence level.

Figure 3.3 | Detrended reconstructed PDSI time series (top), continuous wavelet spectrum (bottom), and global wavelet spectrum (right) for grid number 68 of the *Cook et al.* [2008] dataset.

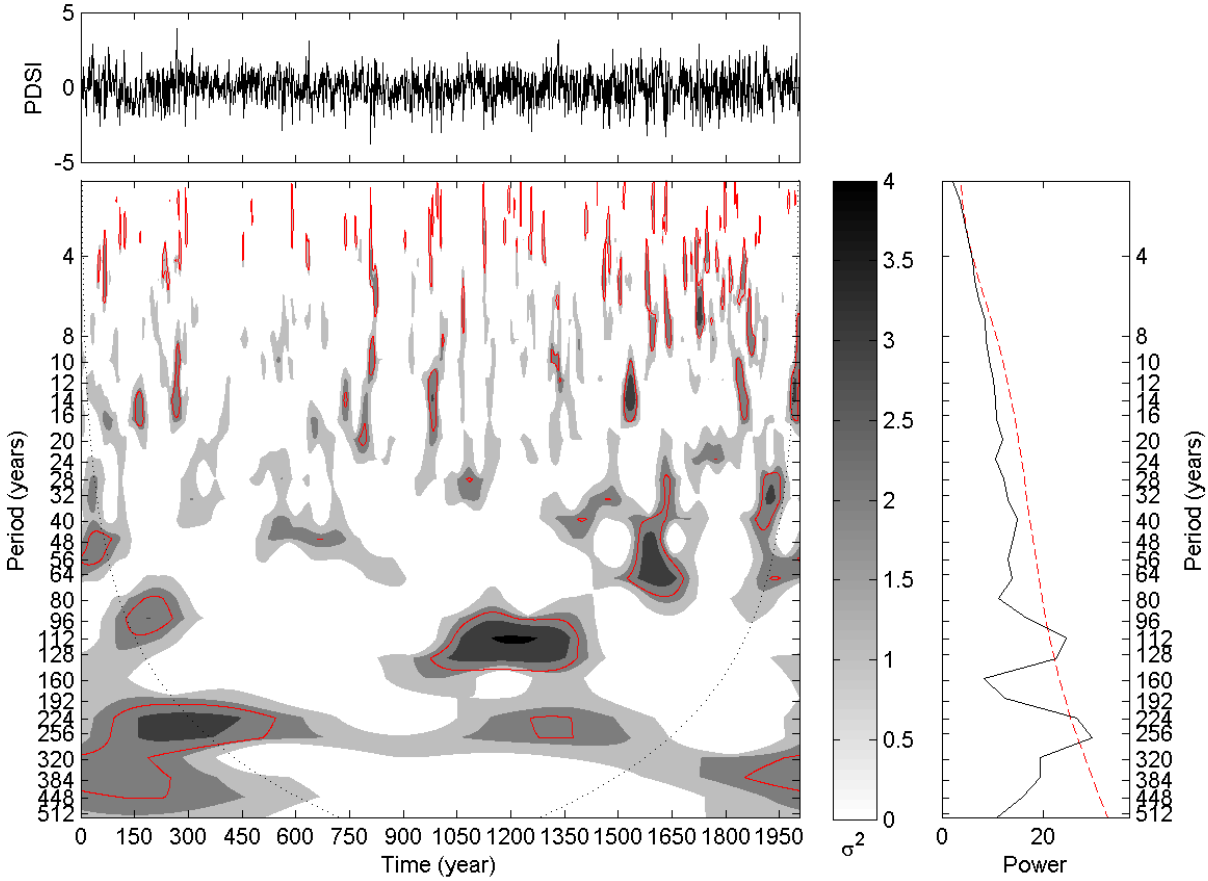

Notes: The black dotted outline on the continuous wavelet spectrum represents the COI. The 5% significance level against red noise is shown as a thin red contour on the continuous wavelet spectrum. The dashed red line on the global wavelet spectrum denotes the 95% confidence level.

Figure 3.4 | Detrended reconstructed PDSI time series (top), continuous wavelet spectrum (bottom), and global wavelet spectrum (right) for grid number 85 of the *Cook et al.* [2008] dataset.

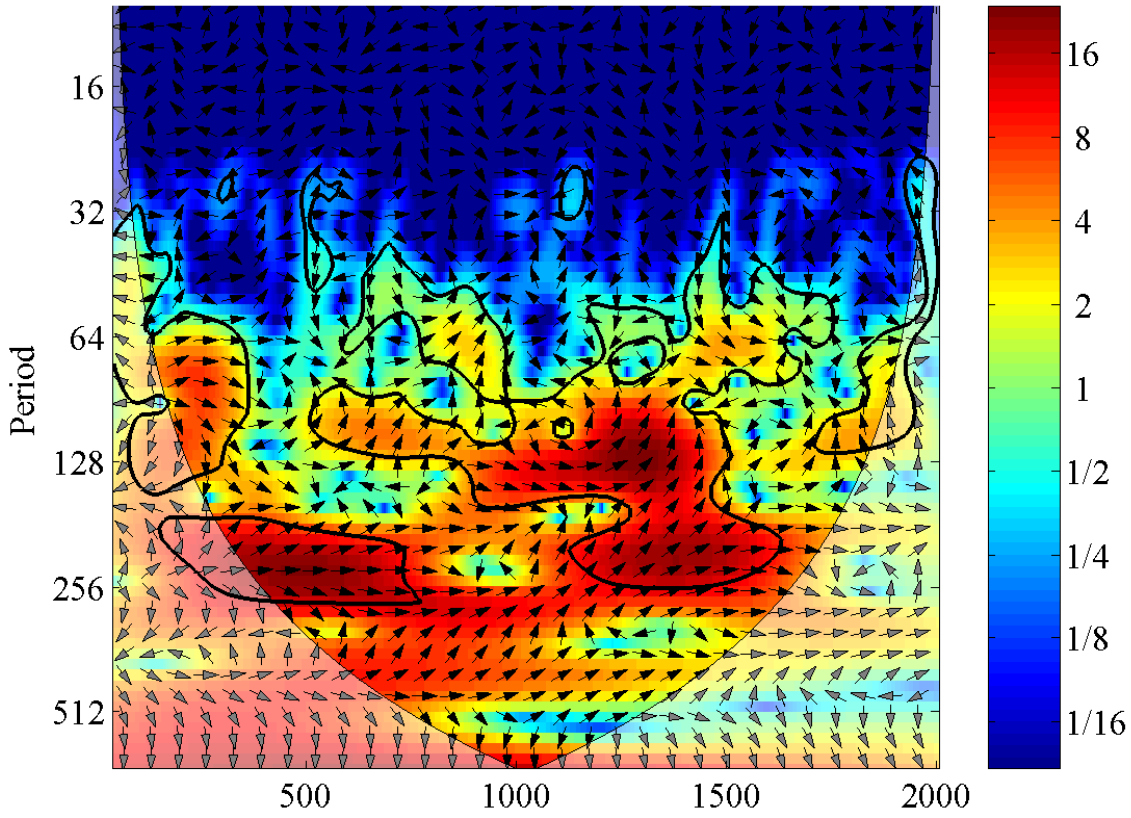

Notes: The thin black represents the COI. The 5% significance level against red noise is shown as a thick contour. The relative phase relationship is shown as arrows (with in-phase pointing right and anti-phase pointing left).

Figure 3.5 | Cross wavelet transform of the re-sampled PDSI time series for grid number 85 of the *Cook et al.* [2008] dataset and the reconstructed total solar irradiance record of *Steinhilber et al.* [2009].

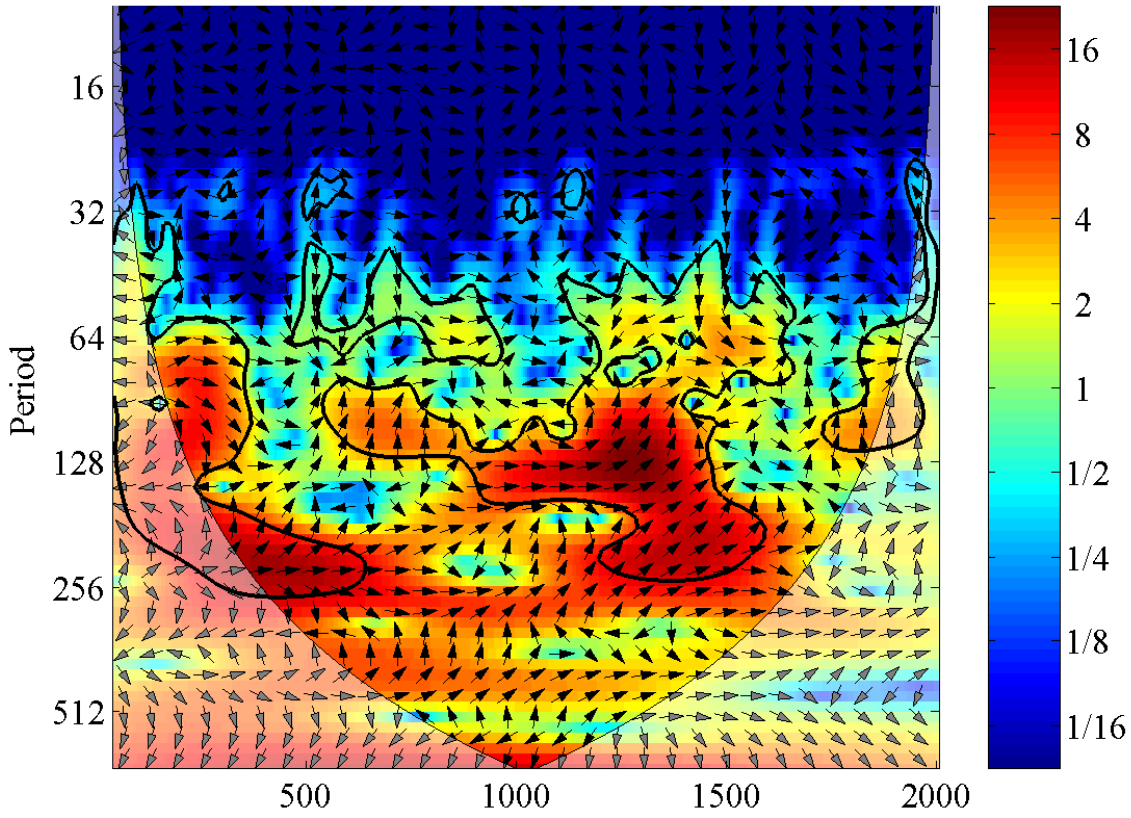

Notes: The thin black represents the COI. The 5% significance level against red noise is shown as a thick contour. The relative phase relationship is shown as arrows (with in-phase pointing right and anti-phase pointing left).

Figure 3.6 | Cross wavelet transform of the re-sampled PDSI time series for grid number 101 of the *Cook et al.* [2008] dataset and the reconstructed total solar irradiance record of *Steinhilber et al.* [2009].

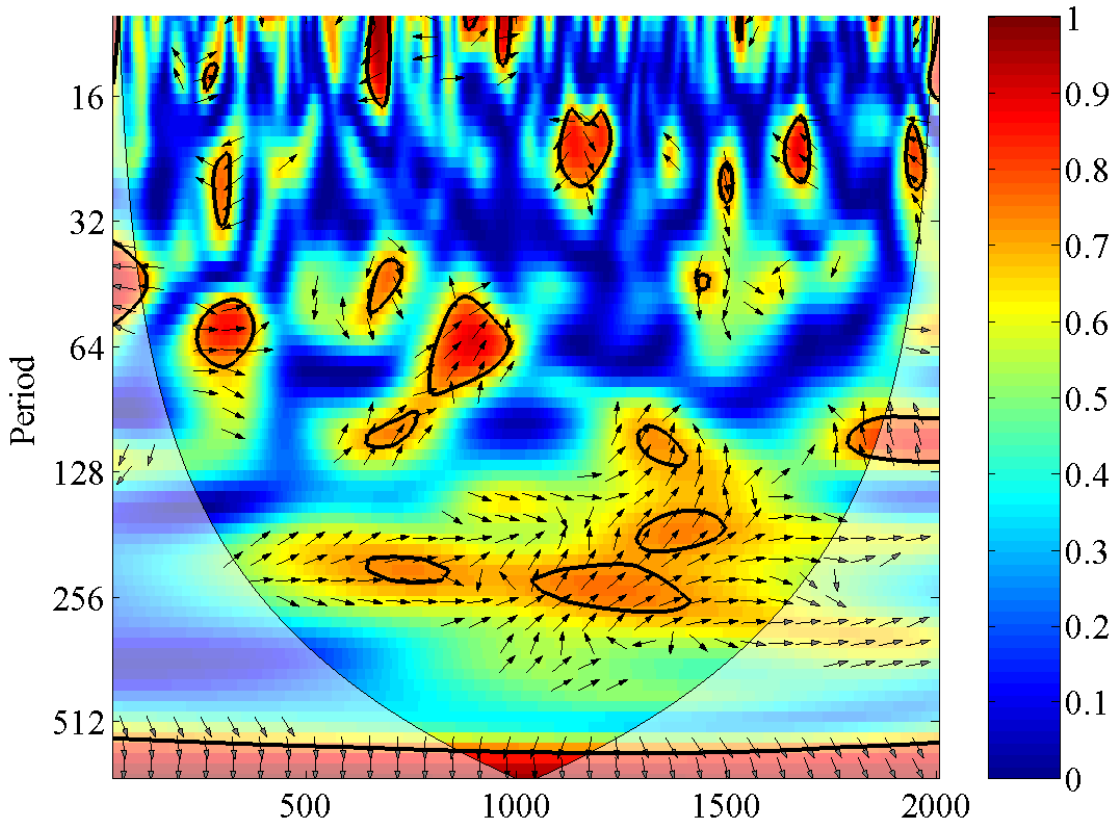

Notes: The thin black represents the COI. The 5% significance level against red noise is shown as a thick contour.

Figure 3.7 | Squared wavelet coherence between the re-sampled PDSI time series for grid number 85 of the *Cook et al.* [2008] dataset and the reconstructed total solar irradiance record of *Steinhilber et al.* [2009].

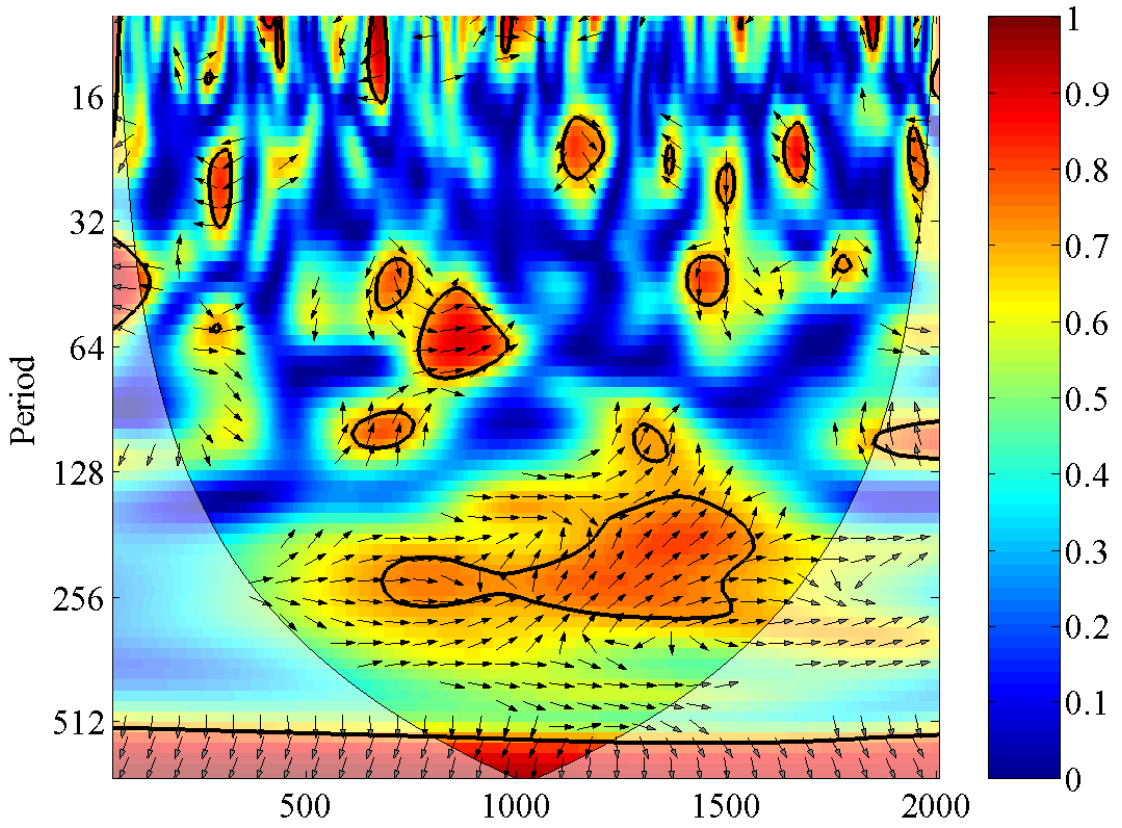

Notes: The thin black represents the COI. The 5% significance level against red noise is shown as a thick contour.
Figure 3.8 | Squared wavelet coherence between the re-sampled PDSI time series for grid number 101 of the *Cook et al.* [2008] dataset and the reconstructed total solar irradiance record of *Steinhilber et al.* [2009].

3.5. Discussion

Results demonstrate that low-frequency drought and pluvial cycles, both at multidecadal and centennial timescales, are persistent features of regional climate in the Pacific Northwest. *Nelson et al*. [2011], using a 6000-year lake sediment record from the Pacific Northwest, identify a strong periodicity in the 16-64 year band during the middle Holocene that gradually weakened around BC 2050. Results here also confirm a weakened periodicity in the 16-64 year band in the

last 2000 years. While the centennial (72-128 year) band appears insignificant throughout much of the 6000-year lake sediment record of *Nelson et al*., [2011], this component also exhibits the greatest average power in the last millennium. This same centennial band, however, appears globally significant in the PDSI reconstructions throughout the last 2000 years for much of the Pacific Northwest. A ~220-year period is also evident for many of the longer (i.e., 2000-year) Pacific Northwest drought records. Similarly, a 2100-year salinity and aridity proxy record from a lake in the northern Great Plains, shows statistically significant periodicities of ~400, 200, 130, and 100 years [*Yu and Ito*, 1999].

Nelson et al. [2011] have shown that the average duration of multi-decadal wet and dry cycles in the Pacific Northwest has increased in the last millennium. This transition to lower frequency and longer duration wet and dry cycles is coincident with increasing summer drought magnitudes between AD 900 and AD 1300 [*Cook et al*., 2004]; although, evidence from lake sediments in both the Pacific Northwest [*Steinman et al*., 2012] and the northern Colorado Rocky Mountains [*Anderson et al*., 2011] indicate wetter winters during this period. While it is possible that the lake sediment oxygen isotope data and the tree-ring based PDSI data demonstrate individual seasonal responses to climate, the relatively limited number of older tree-ring chronologies, combined with the uncertainty in low frequency variance derived from tree ring data analysis [*Jones et al*., 2009] could also contribute to the differences between the two records [*Steinman et al*., 2012].

Research suggests the transitions to lower frequency drought and pluvial cycles were driven by changes in the tropical and extratropical Pacific [*Nelson et al*., 2011] and, consequently, Atlantic

oceans [*Trouet et al*., 2009]. Other analyses and modeling by *Mann et al*. [2005] suggest that both solar and volcanic forcing may have precipitated these transitions – e.g., increased solar output and a reduction in volcanic activity could have both initiated and maintained the medieval warming. Results here support the idea that low frequency multidecadal wet and dry cycles are strongly linked to solar insolation. The predominately phase-locked oscillations in reconstructed total solar irradiance and tree-ring reconstructed PDSI suggest a causal relationship between the two phenomena at centennial timescales. The in-phase relationship between solar insolation and PDSI found in this study may appear counterintuitive at first glance – increased insolation would seem to produce drier conditions and, consequently, negative PDSI values, rather than positive PDSI values. This in-phase relationship, however, may be explained through connections between solar insolation, tropical ocean response, and the Pacific Northwest hydroclimate. There is a tendency toward La Niña conditions in response to increased solar forcing on longer timescales; similarly, there is a tendency toward El Niño conditions in response to decreased solar forcing [*Mann et al*., 2005]. La Niña conditions (and increased solar radiative forcing) generally coincide with wetter conditions (positive PDSI values) in the Pacific Northwest, while El Niño conditions (and decreased solar radiative forcing) generally coincide with drier conditions (negative PDSI values) in the Pacific Northwest. *Yu and Ito* [1999] also found solar minima to be in phase with drought periods in the northern Great Plains. It should be noted that reconstructed summer PDSI values are used in this study, and climate responds to solar variability with distinct seasonality – due to the increased latitudinal gradient of solar energy input during the winter, dynamical processes are larger in winter than in summer [*Lean,* 2010]. Therefore, wavelet correlation values may be expected to be higher between winter PDSI and total solar irradiance.

Drought is an established facet of regional climate for most parts of the world; in western North America, drought has become a familiar issue. It is clear that drought is cyclical in nature, and dry and wet periods have been linked to both oceanic and solar forcing. ENSO is the dominant control on interannual climate variability worldwide, and it has a well-understood impact on western North American climate. Lower-frequency modes of variability and their connections to ENSO are less well-understood, but their impacts – due to the long periods associated with these events – are potentially much more disruptive. Improved understanding of the long-term behavior of drought and pluvial cycles and how the hydroclimate responds to large and gradual forcing mechanisms, such as solar insolation, are among the most important issues in reducing uncertainty in climate change projections. The drought data from the Pacific Northwest document changing drought cycles in the region over the last 2000 years that were likely driven by solar insolation and the associated evolution of ENSO, thus confirming the long-term sensitivity of the region to solar activity. Therefore, long-term changes in solar insolation and its associated effects on the ENSO system are likely to have a large impact on drought, water availability, people and economies in the region.

CHAPTER 4

THE RELATIVE INFLUENCE OF LAND USE CHANGE AND CLIMATE FLUCTUATIONS ON LANDSLIDE ACTIVITY AT LOCKE ISLAND

4.1. Introduction

Landslides are among the most common and powerful natural hazards, reshaping large swaths of landscapes across the world. Almost 4 million km^2 of land and 300 million people across the globe are exposed to landslides [*Dilley et al.*, 2005] (Figure 4.1). Each year landslides cause thousands of deaths and injuries (Figure 4.2) and billions of dollars in economic losses, and the occurrence of landslide disasters certainly has the potential to increase. This is predominately a result of the growing exposure of people and infrastructure to landslides, spurred by land use change and urbanization. Recent studies directed toward understanding the effect of human-induced land use changes on slope stability have shown that, in populated areas, human impacts on the environment contribute significantly to the initiation and reactivation of landslides [e.g., *Bruschi et al.*, 2013; *Meusburger and Alewell*, 2008; *Vanacker et al.*, 2003]. Moreover, climate change – both natural and anthropogenic – may alter the intensity, frequency, and location of landslide hazard areas through altering precipitation patterns. It is well established that intense or prolonged rainfall can trigger slope movements [*Caine*, 1980; *Cannon and Ellen*, 1985; *Crozier*, 1986], and more frequent high-intensity rainfall events and higher winter precipitations may increase the risk for landslides [*Parriaux*, 2011]. Increased recharge – whether from intense or prolonged rainfall or land use change – and subsequent groundwater flow are some of the most important landslide triggering factors [*Johnson and Sitar*, 1990; *van Asch et al.*, 1999].

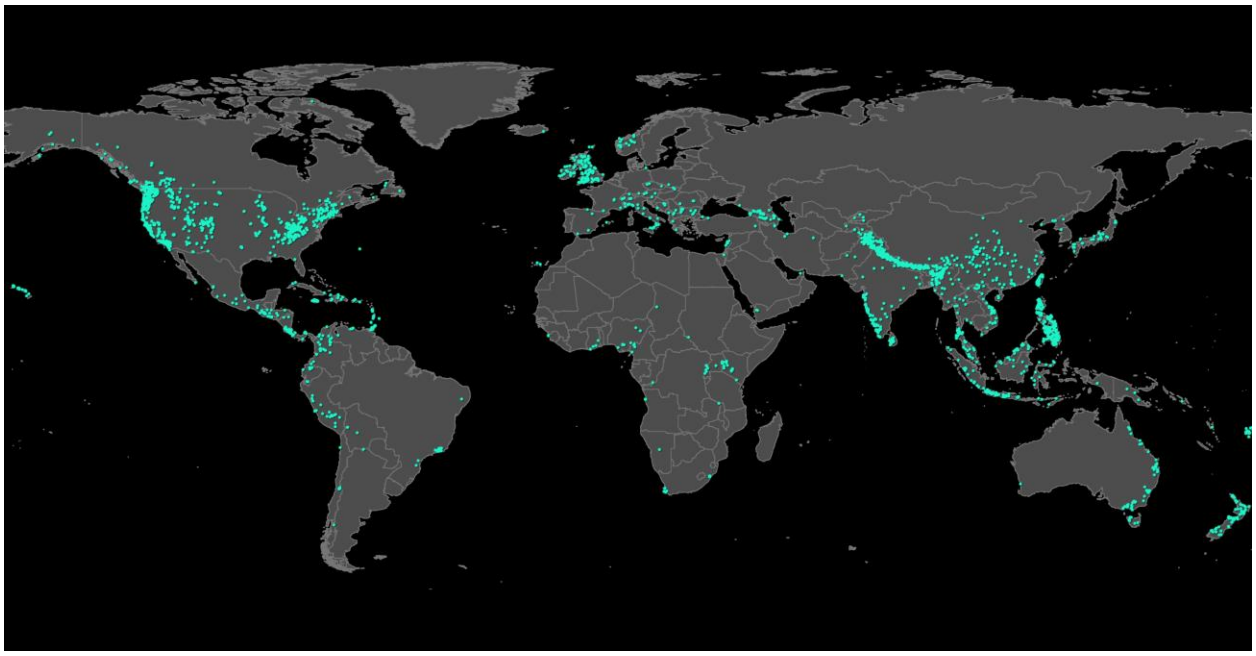

Notes: The data used to create this map comes from the Global Landslide Catalog, which is currently available at: http://ojo-streamer.herokuapp.com/ (accessed July 8, 2015). This image was created by NASA's Goddard Space Flight Center and is available for download at: http://svs.gsfc.nasa.gov/goto?11854 (accessed July 8, 2015).
Figure 4.1 | A map of the locations of 5,741 rainfall-triggered landslides from 2007-2013.

Increasing pore water pressures decreases the soil cohesion in the subsurface and shear strength of the soil, which may cause the driving forces to overcome the resisting forces on a hillslope and activate a landslide [*Iverson*, 2000; *Wieczorek*, 1996].

Landslides are often secondary natural hazards, and the difference between landslide trigger and primary causes or pre-dispositions is important here. A landslide trigger is a sudden event [*Wieczorek*, 1996] that changes the force equilibrium in a slope and leads to failure, and it can be natural or anthropogenic. Landslides, however, do not always occur instantaneously; large deep-seated landslides can also develop slowly over a long period of time. Pre-dispositions are geological, hydrogeological, hydrological, chemical, mechanical, biological, geomorphological characteristics of a slope that are crucial for stability. Most pre-disposing factors do not suddenly

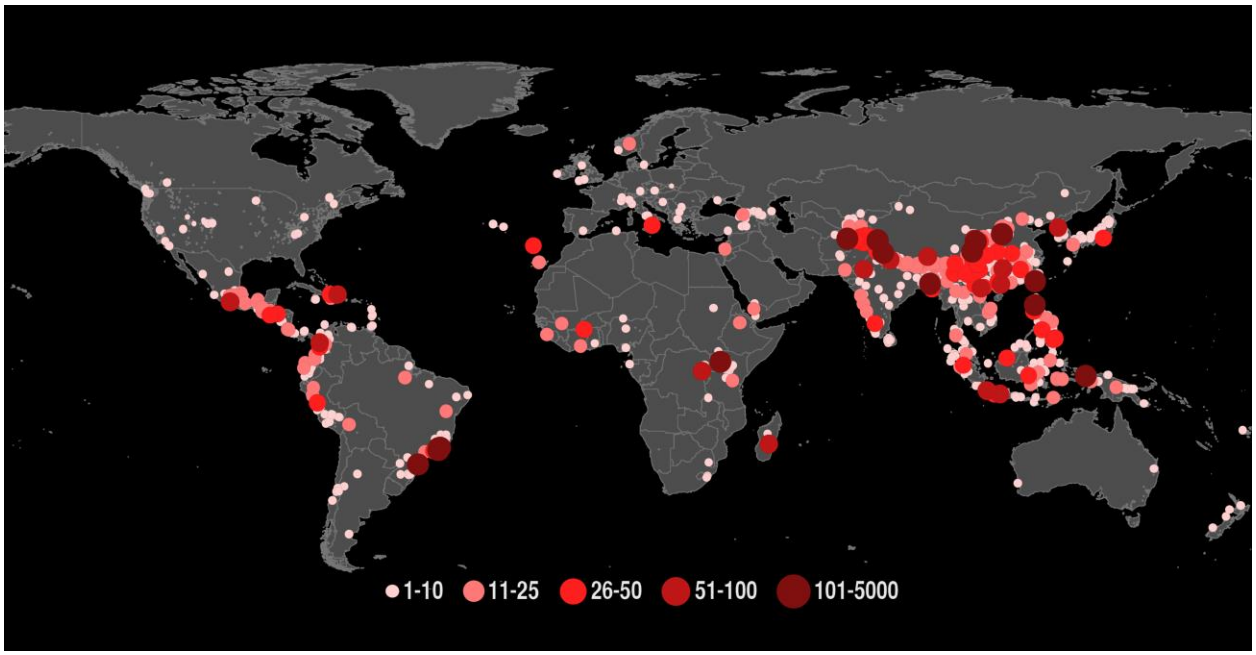

Notes: The data used to create this map comes from the Global Landslide Catalog, which is currently available at http://ojo-streamer.herokuapp.com/ (accessed July 8, 2015). This image was created by NASA's Goddard Space Flight Center and is available for download at http://svs.gsfc.nasa.gov/goto?11854 (accessed July 8, 2015).
Figure 4.2 | A map of the distribution and number of fatalities associated with 5,741 rainfall-triggered landslides from 2007-2013.

change, but they may change over a longer period of time. Long-term predispositions include slope angle, slope aspect, slope shape (i.e., convex or concave topography), altitude, vegetation, climate, and rock and soil type (i.e., lithology, tectonic activity, and structure). Other pre-dispositions, especially those related to hydrology, can change more rapidly; examples include permeability and soil saturation (as related to snowmelt, long-term precipitation, and evapotranspiration). The term "landslide cause" is often used for long-term processes leading to slope instabilities [*Sowers*, 1979], and *Cruden and Varnes* [1996] distinguish between geological, morphological, physical, and human causes. It is often impossible, however, to isolate a single cause of slope failure [*Duncan and Wright*, 2005]. Various processes operate simultaneously, and it is the interaction between several factors that leads to slope failure.

Nevertheless, it is important to evaluate the relative importance of potential causes and to consider the potential for changes with time [*Duncan and Wright,* 2005].

Changes in climate and land use pose a risk to stability of slopes along the White Bluffs of the Columbia River in south-central Washington State, but the direction and relative magnitude of these impacts are still a point of debate for local Native American tribes and government agencies. The Locke Island landslide complex along the eastern channel of the Columbia River and opposite the Hanford Nuclear Reservation is of particular interest to all parties. The erosion of Locke Island, which is under the United Sates Department of Energy stewardship, has been attributed to the landslide encroachment into the river channel and subsequent flow stricture [*Bjornstad,* 2006]. This erosion has removed substantial volumes of sediment from the island, which contains cultural resources. The material is re-distributed downstream and interferes with salmon spawning habitat along the Columbia River [*Mueller and Geist,* 1999].

Modern landsliding in the vicinity of Locke Island began in the late 1970s and continued into the early 1980s [*Chugh and Schuster,* 2003]. Additionally, there is evidence of younger landslides along the White Bluffs that occurred both in the last several hundred years and in the last 11,000 years [*Triangle Associates, Inc.,* 2003]. Much of this modern landsliding activity has been attributed to irrigation water delivered to unlined wastewater ponds and canals behind the bluffs [*Nickens et al.,* 1998; *Schuster et al.,* 1987; *Triangle Associates, Inc.,* 2003]. Longer-term climate changes, however, can have a significant impact on slope stability, as may be indicated by the younger and prehistoric landslides along the bluffs [*Triangle Associates, Inc.,* 2003].

Even though there is no doubt that land use has a significant effect on the likelihood of landslides [*Glade*, 2003; *Petley et al.*, 2007; *Tasser et al.*, 2003], the influence of irrigation from the conversion to farmland has received little attention in the literature. Overall, it is not clear if this particular change in land use has a significant influence on the occurrence of landslides, or its relative importance compared to natural factors. For land managers and policymakers the assessment of the impact of human-induced changes is necessary in order to take preventative measures. Unfortunately, the effect of anthropogenic changes on landslide activity is difficult to quantify, and few studies exist that relate actual impacts of human-induced changes with trends in landsliding [*Meusurger and Alewell*, 2008].

The primary method of studying trends in landslide occurrence involves application of physically-based slope stability models, where parameters are adjusted to simulate former climate and land use conditions [*Claessens et al.*, 2006; *Collison et al.*, 2000; *Schmidt and Dikau*, 2004, *Vanacker et al.*, 2003]. This study uses a variation on this approach due to the lack of most of the physical parameters related to the modeling of slope stability. Water influences slope stability in many ways (e.g., decreasing suction, positive pore water pressure, and seepage forces all reduce the shear strength of soil), and its effects are often implicated as causes of failure. Therefore, we use a numerical modeling framework to examine key features of hydrological conditions. The goals here are to evaluate the relative importance of land use change and climate change on landslide activity along the White Bluffs at Locke Island and to determine possible causes for the temporal variation. Of particular relevance to understanding the hydrological context for the initial failure and the longer-term stability of the Locke Island landslide are the subsurface recharge and flow conditions and the groundwater-river exchanges before and during the period of landslide movement to its current configuration. Given the

compelling connections between the initial failure of the landslide and irrigation water delivered to unlined wastewater ponds and canals behind the bluffs and the continued seepage from the bluffs, subsurface recharge is of particular interest in this modeling effort. Therefore, the groundwater response to recharge from the wastewater ponds and precipitation is examined, both separately and in conjunction with changes in river stage. Interpretations of modeling results are aimed at providing a physically-based understanding of the processes contributing to the initial failure and the longer-term stability of the landslide.

4.2. Methods

4.2.1. Elements of the Work

The size of the Columbia River and the need to understand conditions over large distances require the use of a numerical modeling framework to describe key features of the hydrological conditions. A two-dimensional variably-saturated flow finite element model (FEM) is used to describe the subsurface recharge, flow conditions, and the groundwater-river exchanges along the White Bluffs and landslide. Geologic cross-sections [*Bennett et al.*, 2002] of the recent (circa 2002) bluff-landslide configuration aided in the development of the conceptual model. Existing discharge records, groundwater level records, groundwater recharge studies, and geologic logs from drill holes [*Bennett et al.*, 2002] on the landslide and White Bluffs served as the basis for the selection of model parameters.

4.2.2. Site Description

Locke Island is located in the Hanford Reach of the Columbia River, in south-central Washington State, approximately 40 km (25 mi) upstream of Richland, Washington. The Hanford Reach of the River, an approximately 50 km section situated between Priest Rapids Dam and the backwater influence of Lake Wallula near the City of Richland, is considered the only "free-flowing" portion of the river (outside of the estuary) where water-surface slopes are not influenced by a downstream control structure. The Columbia River at Locke Island is bordered on its western bank by a low relief area of the Hanford Nuclear Reservation, and it is bordered on its eastern bank by the steep White Bluffs. Locke Island is roughly located in the center of the Columbia River; it is approximately 3.5 km in length and is generally about 375 m wide. While the western channel of the River is relatively uniform over the length of Locke Island, the eastern channel varies significantly, due to the large Locke Island landslide complex, which originated from the White Bluffs.

4.2.2.1. Dimensionality of Landslide Activity

There is evidence that landslides occurred along the White Bluffs in prehistoric times, within the last 11,000 years or so [*Triangle Associates, Inc.*, 2003]. There is also evidence of younger landslides that were probably active in the last several hundred years [*Triangle Associates, Inc.*, 2003]. Modern, active landslide activity along the Bluffs, however, began in the late 1960s. The total area of landsliding in the vicinity of Locke Island is about 68 ha; 59 ha of this area consist of landslides less than forty years old [*Schuster et al.*, 1989]. The Locke Island landslide can be

described as a series of landslides with fused boundaries [*Schuster et al.*, 1987, 1989], where the individual landslides occurred from the late 1970s to early 1980s [*Chugh and Schuster*, 2003]. The total volume of these modern landslides is estimated at 12 million m^3 [*Schuster et al.*, 1989]. In the Locke Island area, irrigation wastewater ponds were established in large local depressions behind the bluffs, within 2 km of the river, to enhance habitat for wildlife. The water supply to these ponds was terminated when landslide activity on the bluff face became obvious in the early 1980s. In an attempt to stop slumping, the ponds were completely drained in the middle of the following decade.

4.2.2.2. Climate and Land Use Characteristics

The climate of south-central Washington is arid; average annual precipitation along the White Bluffs area is about 180 mm (7 in) [*Schuster et al.*, 1989]. Irrigation in the area began during the period 1953-1964. Irrigation water is provided to the area approximately six months of the year via an extensive network of canals and laterals that deliver water to fields for crop irrigation. Water flows through wasteways that take water from the system and return it to the Columbia River; storage ponds are also a part of the wastewater system [*Neff*, 1989]. Because most of the canals, laterals, wasteways, and ponds behind the White Bluffs are unlined, seeps from these various channels percolate through the soil and recharge the groundwater [*Neff*, 1989]. Almost ninety percent of the increase in inflow to the groundwater system and the resulting rise in groundwater levels has been attributed to recharge from canal seepage and applied irrigation [*Drost et al*., 1993]. Between about 1950 and the mid-1980s, groundwater levels rose by an

average of 60 m (200 ft); this resulted in a seven-fold increase in the annual flow through the groundwater system during this time period [*Drost et al.,* 1993].

4.2.2.3. Site Geology

Located along the western boundaries of Franklin and Grant Counties, the Bluffs begin in the south at Ringold, Washington and extend to the north where they end at the northward bend of the Columbia River. The tops of the bluffs range from approximately 45 m (150 ft) to more than 150 m (500 ft) above the Columbia River [*Triangle Associates, Inc.*, 2003]. Above Locke Island, the steep faces of the Bluffs drop straight down to the river; further to the south, the bluffs step down to terrace remnants and eventually onto a floodplain of moderate relief. The White Bluffs are composed of approximately three geologic layers. The base layer consists of the Columbia River Basalt Group and slopes generally toward the river [*Triangle Associates, Inc.*, 2003]. The middle Ringold Formation consists of a mixture of loosely consolidated claystones, siltstones, and sandstones that lie horizontally, sloping about one degree toward the river [*Triangle Associates, Inc.*, 2003]. This middle layer, up to 180 m (600 ft) deep in some places, can form steep natural slopes, such as those overlooking Locke Island, as a result of vertical and lateral erosion caused by the river [*Triangle Associates, Inc.*, 2003]. The topmost layer consists of additional deposits of fine-grained sediments and gravel beds; these sediments are unconsolidated, uncemented, and highly transmissive for the flow of water [*Triangle Associates, Inc.*, 2003].

Site-specific data for the Locke Island landslide include drill logs with interpretation of the site geology and regional and local groundwater conditions. The F-F' transect, one of the five geologic cross-sections detailed by *Bennett et al.* [2002], was chosen to approximate the current landslide configuration (Figure 4.3). This transect intersects the approximate location where the irrigation wastewater ponds were known to exist and two wells, each with water-level data. The base layer (Tb) at this transect, as interpreted from drill logs, consists of black to gray, fine-grained, olivine basalt and belongs to the Columbia River Basalt Group [*Bennett et al.*, 2002]. The middle Ringold Formation consists of two subunits here. The bottom- most Ringold subunit (Trl_c) consists of differentially cemented sands and is composed primarily of fine to medium sand with silt and some clay [*Bennett et al.*, 2002]. The top-most Ringold subunit (Trl_b) consists of blue/gray fat clay [*Bennett et al.*, 2002]. Quaternary glaciofluvial sediments (Qgf) composed primarily of silt and sand with some lean clay intervals overlay the Ringold Formation; an exposure of this Qgf layer can be observed directly on top of the Trl_b subunit of the Ringold Formation in the Locke Island landslide scarp area [*Bennett et al.*, 2002]. The top-most eolian sand geologic layer (Qe) consists of wind-blown deposits composed of silt and sand; in general, this layer ranges from 3-6 m (10-20 ft) in thickness [*Bennett et al.*, 2002]. The landslide material (Qls) is composed of Ringold, glaciofluvial, and eolian deposits in a mixture of gravel, sand, silt, and clay [*Bennett et al.*, 2002].

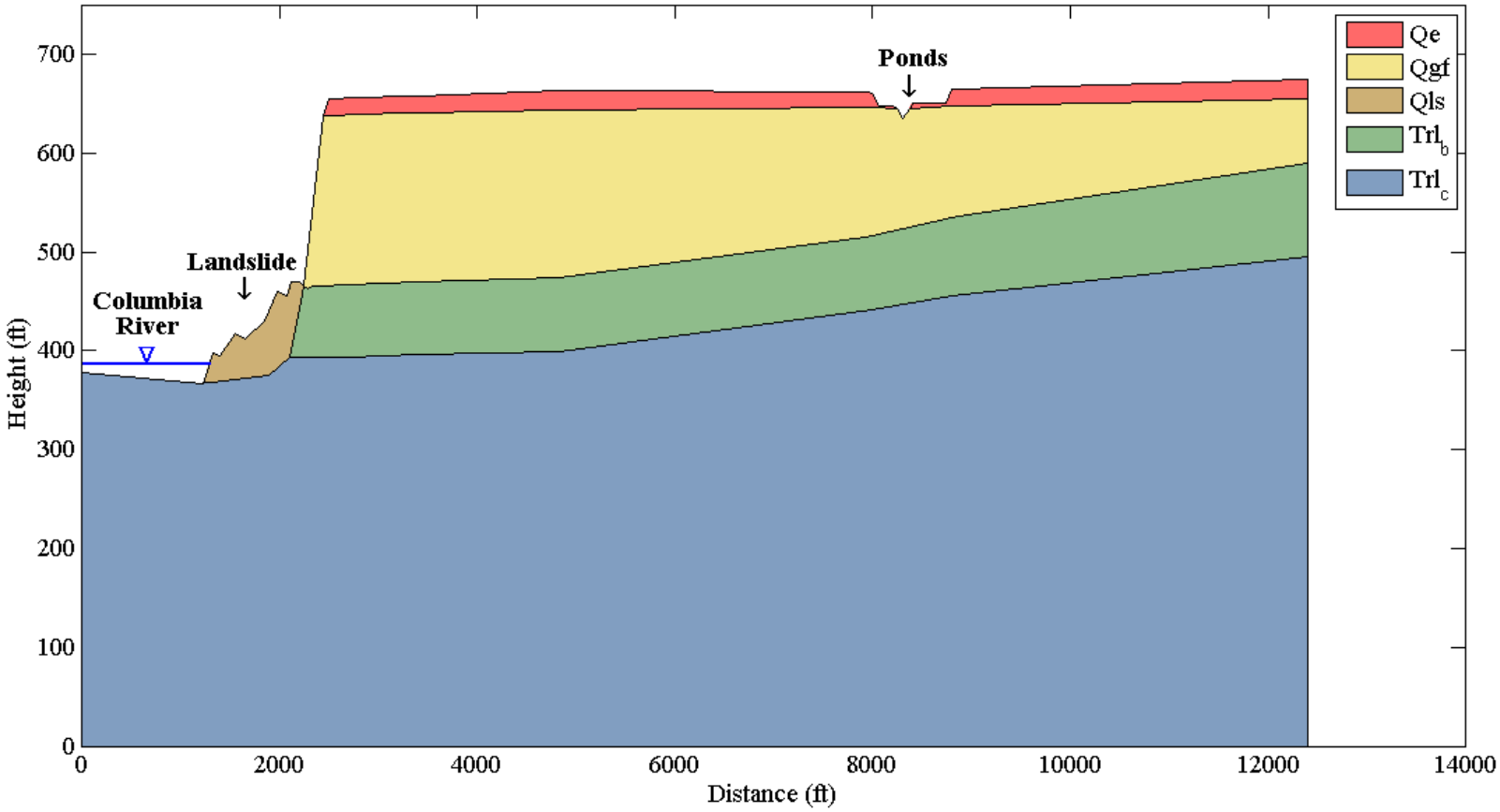

Figure 4.3 | Generalized F-F' transect, as adapted from *Bennett et al*. [2002].

4.2.3. Model Development

Problems that involve transient groundwater flow with a free surface in the saturated zone are difficult to solve analytically. The treatment of such problems is often simplified through a set of assumptions proposed by Dupuit; these assumptions, however, ignore the presence of surface of seepage. The Dupuit assumptions led to the general flow equation for two-dimensional unconfined flow, the Boussinesq equation, which has been extensively treated in the literature [e.g., *Bear et al.*, 1968].

Consequently, an exact traditional model describing time-dependent unconfined saturated-unsaturated groundwater flow [*Bear*, 1972] was used in this modeling effort. The equation used to describe this model is from *Neuman and Witherspoon* [1971]:

$$\frac{\partial}{\partial x_i}\left(K_r K_i \frac{\partial h}{\partial x_i}\right) = (S_w S_s + C(\psi))\frac{\partial h}{\partial t}, \tag{4.1}$$

where

x_i horizontal and vertical directions, respectively [L];

K_i principal components of the hydraulic conductivity tensor, aligned collinear with the x and z direction [LT^{-1}];

K_r relative permeability, assumed to be a scalar function of water saturation [LT^{-1}];

S_w water saturation, which varies between zero for dry conditions and one for saturated conditions [dimensionless];

S_s specific storage [L^{-1}];

ψ pressure head, defined as $\psi = h - z$ [L];

ϕ porosity [dimensionless];

C specific moisture capacity, defined as $C(\psi) = \phi \frac{dS_w}{d\psi}$ [L^{-1}];

h hydraulic head [L];

t time [T].

4.2.3.1. Groundwater Flow Model

The equation (4.1) used to describe subsurface water flow for this problem can be re-written using the notation of Cooley and Westphal [1974]:

$$\frac{\partial}{\partial x}\left(K_r K_{xx} \frac{\partial h}{\partial x}\right) + \frac{\partial}{\partial z}\left(K_r K_{zz} \frac{\partial h}{\partial z}\right) = \left(S_w S_s + \phi \frac{dS_w}{d\psi}\right)\frac{\partial h}{\partial t}, \quad (4.2)$$

where

x, z horizontal and vertical directions, respectively [L];

K_{xx}, K_{zz} principal components of the hydraulic conductivity tensor, aligned collinear with the x and z directions, respectively [LT^{-1}];

K_r relative permeability, assumed to be a scalar function of water saturation [LT^{-1}];

S_w water saturation, which varies between zero for dry conditions and one for saturated conditions [dimensionless];

S_s specific storage [L^{-1}];

ϕ porosity [dimensionless];

h hydraulic head [L];

ψ pressure head, defined as $\psi = h - z$ [L];

t time [T].

Additional functional relationships are needed to interrelate values of pressure head, relative permeability, and water saturation. Relationships between pressure head and water saturation and between water saturation and relative permeability are nonlinear and vary substantially for different soil and rock types [*Gu*, 2007]. The relationship used to relate values of pressure head and relative permeability can be specified as [*Brooks and Corey*, 1966; *Brutsaert*, 1966; *Cooley and Westphal*, 1974]

$$S_{wD} = \frac{A}{(-\psi^c + A)}, \tag{4.3}$$

and

$$K_r = (S_{wD})^d, \tag{4.4}$$

where S_{wD} is the normalized water saturation, defined by

$$S_{wD} = \frac{S_w - S_r}{1 - S_r}, \tag{4.5}$$

A, c, and d are empirical parameters, and S_r is the residual, non-moving, water saturation.

By incorporating Equation (4.5), Equation (4.2) can be written in a form more convenient for computations:

$$\frac{\partial}{\partial x}\left(K_r K_{xx}\frac{\partial h}{\partial x}\right)+\frac{\partial}{\partial z}\left(K_r K_{zz}\frac{\partial h}{\partial z}\right)=\left[(S_{wD}+F)S_f+S_y\frac{dS_{wD}}{d\psi}\right]\frac{\partial h}{\partial t}, \tag{4.6}$$

where

$$F=\frac{S_r}{1-S_r}, \tag{4.7}$$

$$S_f=(1-S_r)S_s, \tag{4.8}$$

$$S_y=(1-S_r)\phi, \tag{4.9}$$

and S_y is the specific yield.

To develop an appreciation of the physical meaning of the empirical parameters A, c, and d, *Winter* [1983] examined the functions in Equations (4.2), (4.3), and (4.4) for a number of different values of these parameters. The pore size distribution of the media affects the relationship between pressure head and water saturation [*Brooks and Corey*, 1966]. For example, if $A=1$, the water retention curve has a shape characteristic of a relatively uniform sand [*Winter*, 1983]. As progressively larger values of A are considered (at the same value of c), the

curve is vertically stretched [*Winter*, 1983]. Variation in the parameter c, however, has a large effect on the sharpness of water retention curve. The smaller the value of c (at the same value of A), the less sharp is the water retention curve [*Winter*, 1983]. Smaller values of c are characteristic of curves for increasingly finer-grained and more poorly sorted porous media [*Winter*, 1983]. For example, if $c = 2$, the curve has an "S" shape characteristic of silty loams and silty clay loams [*Brooks and Corey*, 1966]. The exponent in the approximation of the relationship between water saturation and relative permeability (d in Equation (4.4)) is directly related to the pore size distribution of the porous media [*Winter*, 1983]. *Brooks and Corey* [1966] show that based on laboratory analysis of many different types of rock samples, the exponent almost always is between three and four. The smaller the value of d, the closer to linear is the relationship; the curve for $d = 1$ is a straight line [*Winter*, 1983].

For simplicity, hysteresis is neglected in Equations (4.3) and (4.5). The origin and assumptions underlying Equations (4.4) and (4.5) are given by *Brooks and Corey* [1966]. Equation (4.2) also contains several simplifications, as discussed by *Cooley* [1971]: air movement is assumed to be without resistance; the effects of total stress changes at a point caused by changing saturation are neglected; and the effects of variable formation compressibility caused by deformation and changing saturating are neglected.

4.2.3.2. Selection of Water Retention Parameters and Hydraulic Properties

Soil parameters were prescribed on the basis of soil texture information gathered from existing geologic logs [*Bennett et al.*, 2002] of nine drill holes on the White Bluffs and two drill holes on

the Locke Island landslide. Holes were drilled between January 14, 1998 and April 11, 1998 on the bluffs and between April 15, 1999 and April 20, 1999 on the landslide [*Bennett et al.*, 2002]. The soil texture information contained in the existing geologic logs was derived from lab tests on samples from varying intervals. Average soil texture parameters (i.e., percent sand, percent silt, and percent clay) for each geologic layer were calculated using a weighted average of soil texture parameters from all drill logs; the interval length of each sample was used as the weighting factor. The computer program ROSETTA[5] [*Schaap et al.*, 2001] was used to estimate van Genuchten water retention parameters [*van Genuchten*, 1980] and saturated hydraulic conductivities, as well as unsaturated hydraulic conductivity parameters based on the pore-size model of *Mualem* [1976] (Table 4-1). Initial finite element model results, however, indicated that the ROSETTA-estimated saturated hydraulic conductivity values were too small to accommodate the increased flow from a doubling of recharge from precipitation. Therefore, saturated hydraulic conductivity values were multiplied by a factor of 1.4273. This multiplier and the associated upslope, fixed head boundary condition were arrived at through several trial-and-error simulations, such that a doubling of recharge from precipitation resulted in an approximate doubling of the groundwater flux at the toe of the landslide. Accurate measurements of specific storage are obtained from multiple well interference tests in the field; however, no field data were found in the literature on specific storage or porosity for any of the media considered in this study. Under such circumstances, specific storage and porosity values for each geologic unit were estimated from representative values in the literature of these parameters for various geologic materials. All geologic units were assigned the same value for specific storage based on the representative values of specific storage for various geologic materials [*Domenico and*

[5] The ROSETTA program comes with a graphical user interface, and can be downloaded from the United States Salinity Laboratory website: http://www.ussl.ars.usda.gov/, accessed May 15, 2013.

Mifflin, 1965] as reported in *Batu* [1998] (Table 4-1). Soil texture information from the geologic logs was used to obtain ranges of representative porosity values for the various materials found within each geologic unit [*Das*, 2008; *Hough*, 1969; *VSS*, 1999]; the porosity ranges were averaged for each of the different materials found within each unit, and an average porosity value was calculated for each geologic unit (Table 4-1).

Table 4.1 | ROSETTA estimated van Genuchten water retention parameters and saturated hydraulic conductivity for each geologic unit

Geologic Unit	Qe	Qgf	Qls	Trl_b	Trl_c
α	0.5773	0.6055	0.5359	0.5048	0.5733
n	1.8754	1.5736	1.2595	1.1593	1.6588
θ_s	0.4366	0.4713	0.4861	0.4934	0.4396
θ_r	0.0422	0.0421	0.1026	0.1051	0.0371
K_{xx}	0.1786	0.1004	0.0341	0.0248	0.1389
K_{zz}	0.0179	0.0100	0.0034	0.0025	0.0139
S_s	0.0001	0.0001	0.0001	0.0001	0.0001
ϕ	0.3617	0.3850	0.3908	0.4900	0.3500

Notes: ROSETTA was not used to estimate the values for specific storage (S_s) and porosity (ϕ). In absence of field data in the literature on specific storage for any of the media considered in this study, all geologic units were assigned the same value for specific storage based on the representative values of specific storage for various geologic materials [*Domenico and Mifflin*, 1965] as reported in *Batu* [1998]. Average porosity values for each geologic unit were calculated using representative values of porosity [*Das*, 2008; *Hough*, 1969; *VSS*, 1999] for the different geologic materials within each geologic unit as determined from drill logs.

The ROSETTA program implements five hierarchical pedotransfer functions (PTFs) for the estimation of water retention, and the saturated and unsaturated hydraulic conductivity. As a

result of the hierarchy in PTFs, the program can estimate van Genuchten water retention parameters and the saturated hydraulic conductivity using textural classes only and in combination with more extended input data (e.g., bulk density and one or two water retention points) [*Schaap et al.*, 2001]. The *Brooks and Corey* [1966] soil water retention model was used within the groundwater model, as fewer stability problems than with the van Genuchten model have been noted by others (e.g., *Gu*, 2007). Therefore, soil moisture characteristic curves were created for each of the five geologic units using the van Genuchten water retention parameters for each unit prescribed by ROSETTA. The retention function is given by [*van Genuchten*, 1980]

$$\theta(h) = \theta_r + \frac{\theta_s - \theta_r}{[1 + (\alpha h)^n]^{1-\frac{1}{n}}}, \tag{4.10}$$

where

$\theta(h)$ measured volumetric water content ($cm^3\,cm^{-3}$) at the suction h (cm, taken positive for increasing suctions) [L^3L^{-3}];

θ_r residual water content ($cm^3\,cm^{-3}$) [L^3L^{-3}];

θ_s saturated water content ($cm^3\,cm^{-3}$) [L^3L^{-3}];

α parameter related to the inverse of the air entry suction (>0, in cm^{-1}) [L^{-1}];

n parameter that is a measure of the pore-size distribution (> 1) [dimensionless].

Combination of Equation (4.10) with the pore-size model of *Mualem* [1976] produces the following closed-form equation for unsaturated hydraulic conductivity [*van Genuchten*, 1980]

$$K(S_{wD}) = K_0 S_{wD}^{L} \left\{ 1 - \left[1 - S_{wD}^{\frac{n}{n-1}} \right]^{1-\frac{1}{n}} \right\}^{2}, \tag{4.11}$$

where

K_0 a fitted matching point at saturation (cm day^{-1}) [LT^{-1}];

L an empirical parameter that is normally assumed to be 0.5 [dimensionless];

and the normalized water content or effective saturation, S_{wD}, is computed as

$$S_{wD} = \frac{\theta(h) - \theta_r}{\theta_s - \theta_r}. \tag{4.12}$$

Through direct substitution of the expression for the normalized water content given in Equation (4.3) in place of S_{wD} in Equation (4.12), the volumetric water content, $\theta(h)$, can be computed as

$$\theta(h) = \left(\frac{A}{-\psi^c + A} \right) (\theta_s - \theta_r) + \theta_r \tag{4.13}$$

using the *Brooks and Corey* [1966] soil water retention model. For each of the five geologic units, the parameters A and c were adjusted such that the soil moisture characteristic curve based on the *Brooks and Corey* [1966] soil water retention model best fit the soil moisture characteristic curve based on the *van Genuchten* [1980] soil water retention model (Table 4-2). Saturated and residual water contents (θ_s and θ_r, respectively) for each unit were set to those values prescribed by ROSETTA (Table 4-2).

Table 4.2 | Estimated *Brooks and Corey* [1980] water retention parameters

Geologic Unit	A	c	θ_r	θ_s
Qe	3.6	1.2	0.0422	0.4366
Qgf	5.0	0.9	0.0421	0.4713
Qls	7.5	0.5	0.1026	0.4861
Trl_b	8.0	0.4	0.1051	0.4934
Trl_c	3.7	0.9	0.0371	0.4396

Notes: The values for the residual water content (θ_r) and the saturated water content (θ_s) are those prescribed by ROSETTA.

4.2.3.3. Finite Element Discretization

The cross-sectional flow region is divided into a network of subregions when using the finite element discretization scheme, and it is convenient to adopt a network composed of triangular elements. In general, the purpose of this discretization scheme is to divide the system into an appropriate number and arrangement of elements such that the exact solution can be adequately approximated.

The shape or basis functions for linear triangular elements are specified by the dimensionless triangular coordinates, each having the value of unity at one node, the value of zero at all other nodes, and linearly varying values within the element. *Hornberger and Wiberg* [2005] give a full explanation of the relationship between the local triangular coordinate system and the global

coordinate system of the cross-section. The global and triangular coordinates can be related by the equation:

$$\begin{bmatrix} 1 \\ x \\ z \end{bmatrix} = \begin{bmatrix} 1 & 1 & 1 \\ x_i & x_j & x_k \\ z_i & z_j & z_k \end{bmatrix} \begin{bmatrix} \xi_i \\ \xi_j \\ \xi_k \end{bmatrix}. \tag{4.14}$$

where the subscripted x's and y's refer to nodal coordinate values and the subscripted ξ's refer to nodal basis functions. The basis functions can be expressed mathematically as:

$$\xi_i = \frac{(x_j z_k + x_k z_j) + (z_j - z_k)x + (x_k - x_j)z}{2\Delta_e}, \tag{4.15}$$

$$\xi_j = \frac{(x_k z_i + x_i z_k) + (z_k - z_i)x + (x_i - x_k)z}{2\Delta_e}, \tag{4.16}$$

$$\xi_k = \frac{(x_i z_j + x_j z_i) + (z_i - z_j)x + (x_j - x_i)z}{2\Delta_e},$$

where Δ_e is the area of the element.

4.2.3.4. Numerical Solution

The corners of the triangular elements are specified as nodal points; x_i, x_j, and x_k are the space coordinates for each node. Each node is associated with a unique subregion of the entire flow region, containing all elements in its vicinity. Also, for general subscript n, each node is

associated with a global coordinate function or linear basis function, $\xi_n(x_i)$. Galerkin's finite element method was used to determine approximate solutions to Equation (4.1) under the appropriate initial and boundary conditions. The time derivative $\partial h/\partial t$ in Equation (4.1) is routinely replaced by $\partial h^N/\partial t$. In the case of unsaturated flow, however, *Neuman* [1973] experienced difficulty in obtaining numerical convergence with this replacement; he obtained a much more stable solution by defining the nodal values of the time derivatives, $\partial h_n/\partial t$, as weighted averages of $\partial h/\partial t$ over the entire flow region (i.e., all elements, e) according to:

$$\frac{\partial h_n}{\partial t} = \frac{\sum_e \int_{\Omega^e} (S_w S_s + C)\frac{\partial h}{\partial t}\xi_n \, dx \, dz}{\sum_e \int_{\Omega^e} (S_w S_s + C)\xi_n \, dx \, dz} \quad , \tag{4.14}$$

where Ω^e is the functional over the entire flow region (or simply the sum of the functional over all elements e). It is also assumed that K_i, ϕ, and S_s are constant in each element, while K_r, C, and S_w vary linearly according to

$$K_r = K_{r_l}(\psi)\xi_l^e \, , \tag{4.15}$$

$$C = C_l(\psi)\xi_l^e \, , \tag{4.16}$$

$$S_w = S_{w_l}(\psi)\xi_l^e \, , \tag{4.17}$$

where l represents the corners of the triangle [*Neuman*, 1973]. This technique of using functional representations of system properties has also been used by *Pinder et al.* [1973].

The resulting set of finite element equations for groundwater flow can be written in matrix form as

$$A\{h\} + B\left\{\frac{\partial h}{\partial t}\right\} + E = 0, \tag{4.18}$$

where A and B are $n \times n$ matrices and E is a vector of length n. The matrices are expressed as:

$$\begin{aligned} A_{ij} &= \sum_e \int_{\Omega^e} \left[K_{xx_l} \xi_l \frac{\partial \xi_i}{\partial x} \frac{\partial \xi_j}{\partial x} + K_{zz_l} \xi_l \frac{\partial \xi_i}{\partial z} \frac{\partial \xi_j}{\partial z} \right] dx\, dz \\ &= \sum_e \frac{1}{12\Delta} \left[\left(\sum_{l=1}^{3} K_{xx_l} \right) b_i b_j + \left(\sum_{l=1}^{3} K_{zz_l} \right) c_i c_j \right], \end{aligned} \tag{4.19}$$

$$\begin{aligned} B_{ij} &= \sum_e \int_{\Omega^e} \left(S_{w_l} S_s + C_l \right) \xi_l \xi_i \, dx\, dz \\ &= \sum_e \frac{\Delta}{12} \left\{ \left[\left(\sum_{l=1}^{3} S_{w_l} \right) S_{w_l} \right] S_s + \left(\sum_{l=1}^{3} C_l \right) + C_i \right\}, \end{aligned} \tag{4.20}$$

for $i = j$;

$$B_{ij} = 0, \tag{4.21}$$

for $i \neq j$; and

$$E_i = \sum_e \left[\int_{\Gamma^e} q\xi_i \, d\Gamma + \int_{\Omega^e} K_{zz_l} \xi_l \frac{\partial \xi_i}{\partial z} \, dx \, dz - \int_{\Omega^e} Q_i \xi_i \, dx \, dz \right]$$
$$= \sum_e \left[\frac{(q_n L_e)_i}{2} + \left(\sum_{l=1}^{3} K_{zz_l} \right) \frac{c_i}{6} - \int_{\Omega^e} Q_i \xi_i \, dx \, dz \right], \tag{4.22}$$

where b_i and c_i are element dimensions, Δ are element areas, and q_n is the normal flux across the side of length L_e of any element, including nodal point i. A given flux, Q_i, can be specified at any internal source or sink node and is zero at all other nodes. The matrix B_{ij} is a diagonal matrix as a result of the averaging process given by Equation (4.20). The Darcy fluxes can be expressed as:

$$q_x = -\sum_e \left(K_{xx_l} \xi_l \frac{\partial N_j}{\partial x} h_j \right)$$
$$= -\sum_e \frac{1}{6\Delta} \left[\left(\sum_{l=1}^{3} K_{xx_l} \right) b_j h_j \right]. \tag{4.23}$$

The time-derivative in Equation (4.1) can be approximated using a finite difference scheme. *Neuman* [1973] recommends using a backward difference scheme rather than a time-centered scheme in the analysis of variably saturated flow systems. Implementing a fully implicit backward difference scheme in terms of h in Equation (4.18) produces

$$\left(A_{ij}^k + \frac{1}{\Delta t^k} B_{ij}^k \right) h_i^{k+1} = \frac{1}{\Delta t^k} B_{ij}^k h_i^k - E_i^k, \tag{4.24}$$

where k indicates the time t^k and $\Delta t^k = t^{k+1} - t^k$. The Douglas-Jones predictor-corrector method [*Douglas and Jones*, 1963] for solving Equation (4.19) is described by the predictor equation

$$\left(A_{ij}^k + \frac{1}{\Delta t^k/2} B_{ij}^k\right) h_i^{k+1/2} = \frac{1}{\Delta t^k/2} B_{ij}^k h_i^k - E_i^k, \tag{4.25}$$

and the corrector equation

$$\left(A_{ij}^{k+1/2} + \frac{1}{\Delta t^k} B_{ij}^{k+1/2}\right) h_i^{k+1} = \frac{1}{\Delta t^k} B_{ij}^{k+1/2} h_i^k - E_i^{k+1/2}. \tag{4.26}$$

4.2.3.5. Finite Element Mesh and Initial and Boundary Conditions

A triangular finite element mesh with 8,495 nodes and 16,057 elements was generated for use in the numerical simulations. The initial pressure heads at each computational node for each simulation were established using a steady state solution with time-constant boundary conditions. Boundary and initial conditions used for Equation (4.2) are given as

$$h = h_c \text{ on } B_c, \quad t > 0 \tag{4.21}$$

$$q_{nt} = q_t \text{ on } B_t, \quad t > 0 \tag{4.22}$$

$$q_{np} = q_p \text{ on } B_p, \quad t > 0$$

$$h = h_r \text{ on } B_r, \quad t > 0 \tag{4.23}$$

$$h = h_0 \text{ in } D, \quad t = 0 \tag{4.24}$$

where h_c is the hydraulic head specified on exterior boundary segment B_c and depends upon the river stage, q_{nt} is the precipitation recharge normal to the exterior boundary segment B_t, q_t is the specified normal precipitation recharge, q_{np} is the pond recharge normal to the exterior boundary segment B_p, q_p is the specified normal pond recharge,h_r is the hydraulic head specified on exterior boundary segment B_r, and h_0 is the initial head distribution of the solution domain D (Figure 4.4). For simulations where pond recharge was not considered $q_{np} = q_t$. Segments of the exterior boundary B_b and B_l are no-flow boundaries (Figure 4.4). A special type of specified head boundary condition is the seepage face. The pressure head is atmospheric ($\psi = 0$) along a seepage face so that

$$h = z \text{ on } B_s, \quad t \geq 0 \tag{4.25}$$

where B_s is the segment of the exterior boundary along which a seepage face can develop (Figure 4.4). The location of the seepage face is generally not know a priori and is established during the course of solution of the problem. A seepage face was allowed to develop along the part of exterior boundary segment B_s above the river stage that was saturated at the previous time step; these nodes were assigned a hydraulic head equal to the elevation head. The possible effects of evapotranspiration were ignored here to simplify the model formula. Nodes on exterior boundary segment B_s above the river stage and seepage face were assigned no-flow boundary conditions.

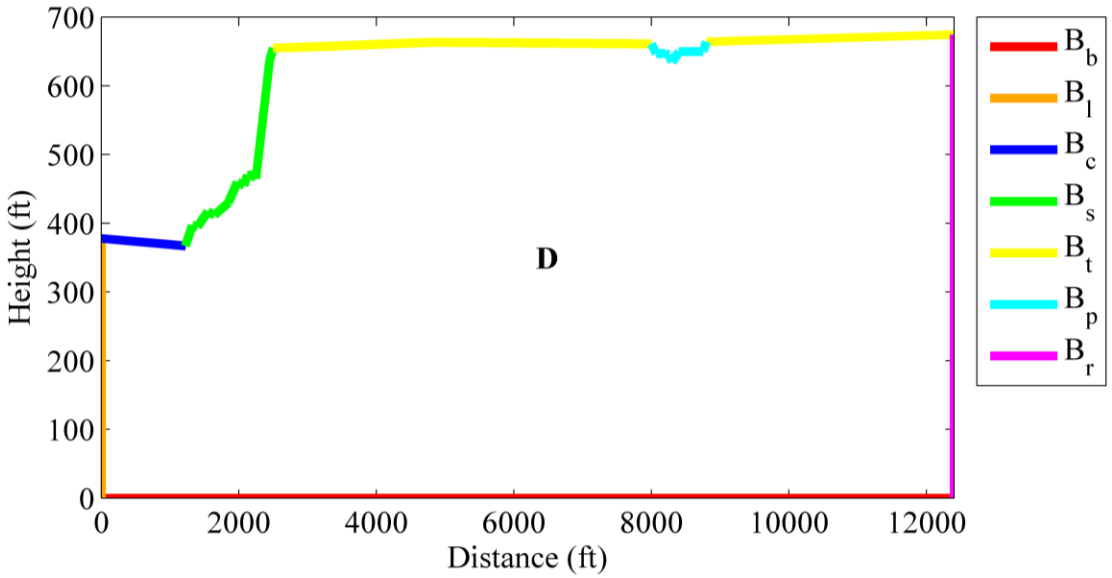

Notes: Legend entries correspond to boundary delineations used in Equations (4.21-4.25). The letter **D** in the interior of the figure refers to the solution domain.

Figure 4.4 | Boundary assignments for the domain of numerical solution.

4.2.3.6. Simulation Descriptions

Five different flow simulations, including a base simulation, were used in this study. All river stage data used in the simulations was obtained from the United States Geological Survey's (USGS) National Water Information System (NWIS) for USGS site number 12472800, the Columbia River below Priest Rapids Dam, Washington. Recharge rates used in the simulations were estimated from Hanford Site recharge rates. On the Hanford Site opposite the Locke Island landslide complex, recharge ranges from a general low of 1.5 mm/yr for areas with a natural shrub-steppe vegetation cover to a high of 52 cm/yr for unvegetated areas [*Last et al.*, 2006], with the natural recharge rate estimated at 17.2 mm/yr [*Rockhold et al.*, 2009].

The base simulation was used to compare the effects of changes in river stage and recharge on groundwater flow within the study area. For this simulation, the precipitation recharge was held constant at 7.4905×10^{-6} ft/hr or 20 mm/yr, which is on the high end of the estimated natural recharge rate across the river on the Hanford Site [*Rockhold et al.*, 2009]. Pond recharge was not considered for this simulation, and the hydraulic head above the river channel was held constant at 386.34 ft above sea level (ASL), as this number incorporates the long-term average in river stage. The hydraulic head at the upslope boundary was held constant at 527.65 ft ASL. This is a reasonable estimate, considering recent water level data from wells in the area and estimates of pre-development water level altitudes nearby. The water level altitude in one of the wells along cross section F-F' of Bennett et al. [2002] was 638.0 ft in October of 2007 [USBR, personal communication]. Similarly, in March 1986, water table altitudes along the White Bluffs in areas directly to the south of the study area, were 600-700 ft [Drost et al., 1993]. Pre-development (i.e., prior to 1950) water table altitudes in the same area were estimated at below 400 ft [Drost et al., 1997].

The second simulation examined the effect of transient (short-term) changes in river stage on groundwater flow. The precipitation recharge was held constant at 7.4905×10^{-6} ft/hr or 20 mm/yr. The hydraulic head at the upslope boundary was held constant at 527.65 ft ASL. Pond recharge was not considered for this simulation, and river stage was allowed to fluctuate hourly for a period of one week (October 1-8, 2007).

The third simulation examined the effect of the seasonal hydrograph on groundwater flow. The precipitation recharge was held constant at 7.4905×10^{-6} ft/hr or 20 mm/yr. The hydraulic

head at the upslope boundary was held constant at 527.65 ft ASL. Pond recharge was not considered for this simulation. River stage was allowed to fluctuate daily for a period of one year (October 1, 2007-October 1, 2008).

The fourth simulation examined the effect of pond recharge on groundwater flow. The precipitation recharge was held constant at 7.4905×10^{-6} ft/hr or 20 mm/yr. The hydraulic head above the river channel was held constant at 386.34 ft above sea level (ASL). The hydraulic head at the upslope boundary was held constant at 527.65 ft ASL. The simulation was run for a period of twenty years, as this provides a fair estimate of the length of time that the wastewater ponds behind the White Bluffs were in operation and allows for a return to steady state conditions. Pond recharge was held constant at 7.4905×10^{-5} ft/hr or 20 cm/yr for the first 10 years of the simulation period; this recharge value is close to the high end of the recharge range for unvegetated areas on the Hanford S40 site [*Last et al.*, 2006]. Pond recharge was limited to precipitation recharge for the last 10 years of the simulation period.

The fifth simulation examined the effect of climate fluctuations – specifically increases in precipitation and subsequent recharge – on groundwater flow. The hydraulic head above the river channel was held constant at 386.34 ft ASL. The precipitation recharge was held constant at 1.4981×10^{-5} ft/hr or 40 mm/yr, which represents an approximate two-fold increase in the estimated natural recharge rate across the river on the Hanford Site [*Rockhold et al.*, 2009]. If precipitation is assumed to scale proportionally with recharge, then this increased recharge rate and associated annual precipitation would be approximately equivalent to the annual precipitation of Spokane, Washington. The increased recharge rate used in this simulation is an

intentional overestimate, used primarily to elicit a change in groundwater flow. In fact, global climate models predict only small changes in annual precipitation (relative to variability) and show increases and decreases depending on the models, which project a change of -4% to +14% for the 2050s (relative to 1950-1999) [*Snover et al.*, 2013]. To more realistically simulate a change in climate, both precipitation recharge and the fixed head boundary condition were altered from the base simulation. The hydraulic head at the upslope boundary was held constant at 658.65 ft ASL. Since the precipitation recharge was doubled for this simulation, the upslope boundary value was fixed such that the groundwater flux into the system was approximately double that of the base simulation. The simulation was run until a steady state was reached.

4.3. Results

Groundwater tends to move horizontally across the study area. The general direction of groundwater flow is toward the Columbia River, the major area of discharge for the study area (Figure 4.5). In addition to horizontal flow, there is also vertical flow in the groundwater system. Vertical flow is upward under the river, along the major discharge area, and flow is upward along the toe of the landslide (Figure 4.5). Groundwater flow does not greatly deviate from this general pattern for any of the five simulations considered herein (Figures 4.5, 4.8-4.10).

Changes in river stage are most evident close to the river along the landslide (Table 4-3). Specific discharge normal to the seepage face increases with falling river stage and decreases with rising river stage (Figures 4.6 and 4.7). The largest changes in hourly river stage are between three and four feet, while the largest changes in daily river stage are near six feet. The

largest increases in specific discharge normal to the bank occur in response to changes in hourly and daily river stage (Table 4-3). While specific discharge normal to the seepage face at the toe of the landslide can increase more than 700 percent from the base condition, these transient fluctuations most likely do not propagate any considerable length into the bank.

Increased recharge at the irrigation wastewater ponds does not change the general groundwater flow field (Figure 4.8). In fact, specific discharge normal to the seepage face at the toe of the landslide actually decreases about one percent (Table 4-3). This additional recharge does raise the water table approximately half a foot beneath the ponds.

The majority of the water flux into the system enters through the upslope boundary. A two-fold increase in precipitation recharge and the subsequent rise in fixed head at this upslope boundary cause the specific discharge at the toe of the landslide to approximately double (Table 4-3). Unlike the dramatic, albeit short-term, increases in specific discharge induced by river stage fluctuations, this change in specific discharge represents a more permanent increase.

4.4. Discussion

Water influences slope stability in many ways (e.g., decreasing suction, positive pore water pressure, and seepage forces all reduce the shear strength of soil), and its effects are often implicated as causes of failure. Increased recharge – whether from climate fluctuations or land use change – and subsequent groundwater flow not only trigger landslides, but can pre-dispose slopes to failure. *Sowers* [1979] characterized the precarious matter of assigning causes of slope

failure: “Often the final factor [that produces failure] is nothing more than a trigger that sets a body of earth in motion that was already on the verge of failure.”

Consistent with this notion, the relative importance of potential causes of landsliding at Locke Island has been evaluated here. The majority of the groundwater flux into the study area comes from upslope; therefore, the specific discharge at the toe of the landslide is governed by regional changes to the groundwater system. Localized recharge at the irrigation wastewater ponds does not have much of an effect on groundwater fluxes at the toe of the landslide. In fact, specific discharge normal to the bank slightly decreases with increased recharge at the ponds. This result is counterintuitive, and it may be an artifact of the numerical model. The associated increase in water table altitude, however, may slow the flux by decreasing the hydraulic gradient.

Both land use change and climate fluctuations can bring about regional changes to the groundwater system. The two-fold increase in precipitation simulated in this study resulted in a doubling of the specific discharge normal to the seepage face at the landslide toe. *Drost et al.* [1997] report a seven-fold increase in annual flow through the groundwater system from pre-development time to 1986, with recharge from canal seepage and applied irrigation accounting for about 85 percent of this increase. The groundwater system adjusted to this increased flow by increasing storage of water in the ground (which equated to higher water levels) and increasing the discharge rate from the system [*Drost et al.*, 1997]. While results from the finite element simulation with increased recharge from irrigation wastewater ponds behind the bluffs at Locke Island indicate only a modest increase in groundwater levels, irrigation application and the network of water conveyance structures behind the White Bluffs are spatially extensive.

Therefore, the significant increase in flow throught the groundwater system reported by *Drost et al.* [1997] is more like the scenario presented in this study where recharge from precipitation is doubled.

Groundwater discharge from the White Bluffs, in the form of springflows and seepage faces, has been identified as the major cause of the many landslides that started around 1970 [*Schuster and Hays*, 1984] . The irrigation wastewater ponds behind the White Bluffs at Locke Island have been implicated as the source of this groundwater and subsequent cause of the Locke Island landslide activity [*Nickens et al.*, 1998; *Schuster et al.*, 1987; *Triangle Associates, Inc.*, 2003]. Results from this study indicate that the regional groundwater system has a much larger influence on groundwater fluxes along the river bank. The White Bluffs is the only significant non-irrrigated area in the vicinity where the water table is shallow (i.e., within 20 ft of land surface for at least part of the year) [*Drost et al.*, 1997]. Seepage from irrigation water conveyances and direct water application behind the bluffs is the most likely cause for increased regional groundwater flow. This increase in groundwater flow is most probably the largest single pre-disposing factor for slope failure at Locke Island.

This study is not without limitations. The stratigraphy, soil parameters, aquifer properties, recharge rates, and boundary conditions are all estimates derived from existing data and reports. Every attempt was made to characterize the system with both accuracy and parsimony. Still, as with most groundwater models, exactness is rarely achieved. Heterogeneity in the Ringold Formation in the study area, in conjunction with irrigation, has been implicated as a cause of landsliding at Locke Island in other studies. Heterogeneity in the White Bluffs at Locke Island

was upheld to the extent that the drill logs contained in *Bennett et al*. [2002] allowed. The finite element model developed herein did not allow for the development of multiple seepage faces; a single seepage face was allowed to develop along that part of the river bank above the stream stage, if it was saturated at the previous time step. While this study does not show that local recharge from the irrigation wastewater ponds significantly affects discharge at the toe of the landslide, local variations in framework and model parameters may produce different results.

In keeping with *Sowers* [1979] philosophy, attempting to decide the ultimate cause of the landsliding activity at Locke Island is technically incorrect. Factors that influence the regional groundwater system are most likely to predispose the White Bluffs at Locke Island to failure. Others have documented the drastic increase in groundwater flow through the regional system from irrigation [e.g., *Drost et al.*, 1993; *Drost et al.*, 1997]. Fluctuations in climate, such as intense or prolonged rainfall, also have the ability to alter regional groundwater flow. These sustained increases in specific discharge along the river bank can position the bluffs for landsliding activity. Large changes in river stage, such as from hydroelectric generation, can increase specific discharge at the toe of the landslide more than regional increases in groundwater flow; however, these increases tend to be short-lived. The irrigation wastewater ponds behind the bluffs at Locke Island or the large fluctuations in river stage as a result of dam regulation may have provided the final factor or trigger that set the predisposed bluff in motion, but all potential causes are influential.

The potential for changes in contributing factors with time is also important [*Duncan and Wright*, 2005]. Global climate models predict only small changes in annual precipitation (relative

to variability) and show increases and decreases depending on the models, which project a change of -4% to +14% for the 2050s (relative to 1950-1999) [*Snover et al.*, 2013]. The total recharge from applied irrigation will undoubtedly increase if irrigated acreage is increased, but the recharge rate will probably decrease as irrigators become more efficient. If existing irrigation water conveyances are improved for efficiency (e.g., lined), the recharge rate will decrease as well. Changes in river stage here are most dependent on power generation, which depends on many speculative trends. Hydrographs of wells in the White Bluffs area indicate a mixture of equilibrium conditions and rising and falling water levels [*Drost et al.*, 1997; *Triangle and Associates, Inc.*, 2003]. Regional recharge to the groundwater system from irrigation and precipitation is likely the largest influence on achieving and maintaining a state of equilibrium for the slopes along the eastern boundary of the Columbia River, below the Big Bend of the Columbia River and the city of Richland, Washington.

Table 4.3 | Specific Discharge Maxima from Finite Element Model

Precipitation Recharge (mm/yr)	**Pond Recharge** (mm/yr)	**River Stage** (ft ASL)	**Upslope Fixed Total Head Boundary Condition** (ft)	**Maximum Normal Component of Specific Discharge (q_{nmax})** (ft/hr)	**Percent Change in q_{nmax}**
20	---	386.34	527.65	0.0137	---
20	---	Fluctuates Hourly	527.65	0.1183	764%
20	---	Fluctuates Daily	527.65	0.1183	764%
20	200	386.34	527.65	0.0136	-1%
40	---	386.34	658.65	0.0279	104%

Notes: The maximum normal component (i.e., normal to the element face) of the specific discharge, q_{nmax}, is given for each of the five different simulations. The percent change between q_{nmax} for the base case (highlighted in red text) and q_{nmax} for each simulation are reported.

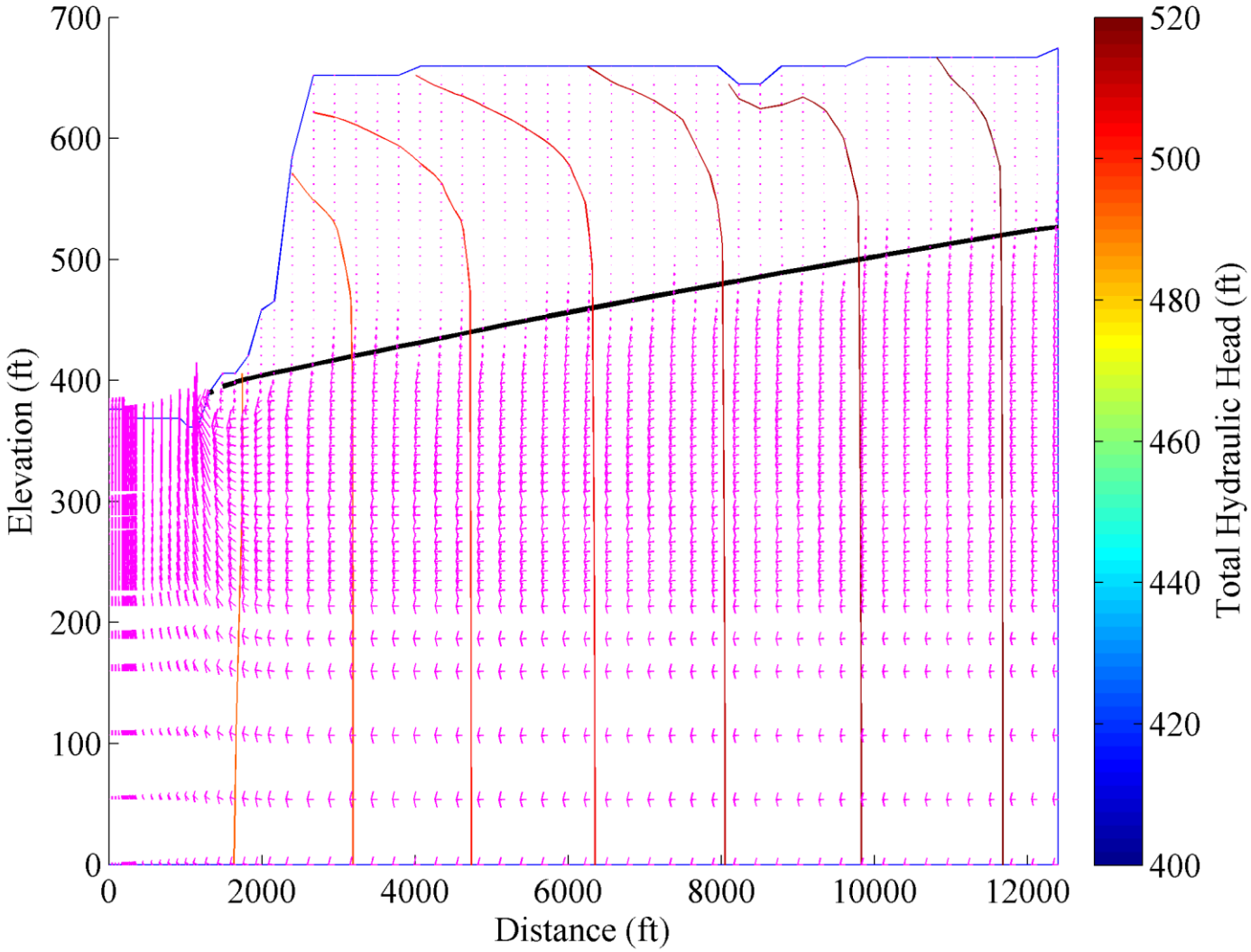

Figure 4.5 | Groundwater flow field for base simulation; thick black line represents the water table, and contours represent lines of constant total hydraulic head.

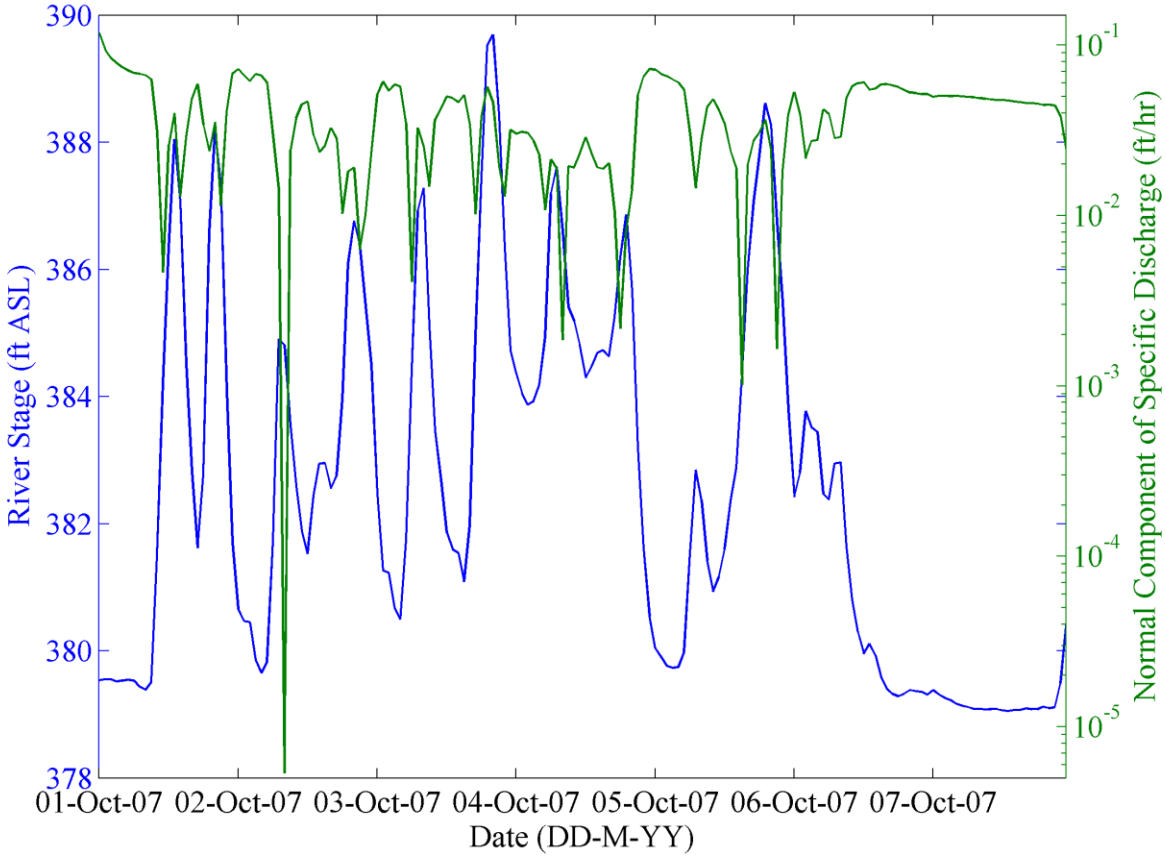

Figure 4.6 | Hourly normal component of specific discharge at seepage face element along the river channel at the toe of the landslide and hourly river stage for October 1, 2007 through October 7, 2007.

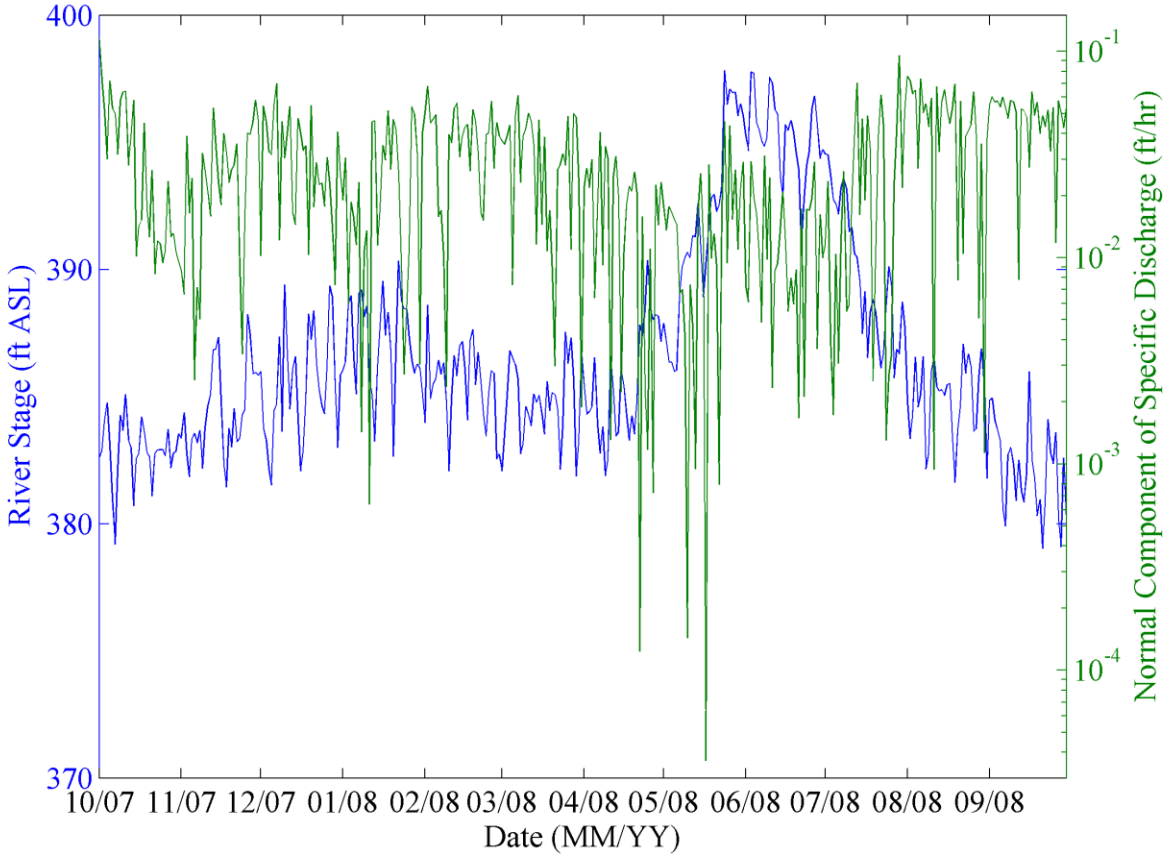

Figure 4.7 | Daily normal component of specific discharge at seepage face element along the river channel at the toe of the landslide and daily river stage for October 1, 2007 through September 30, 2008.

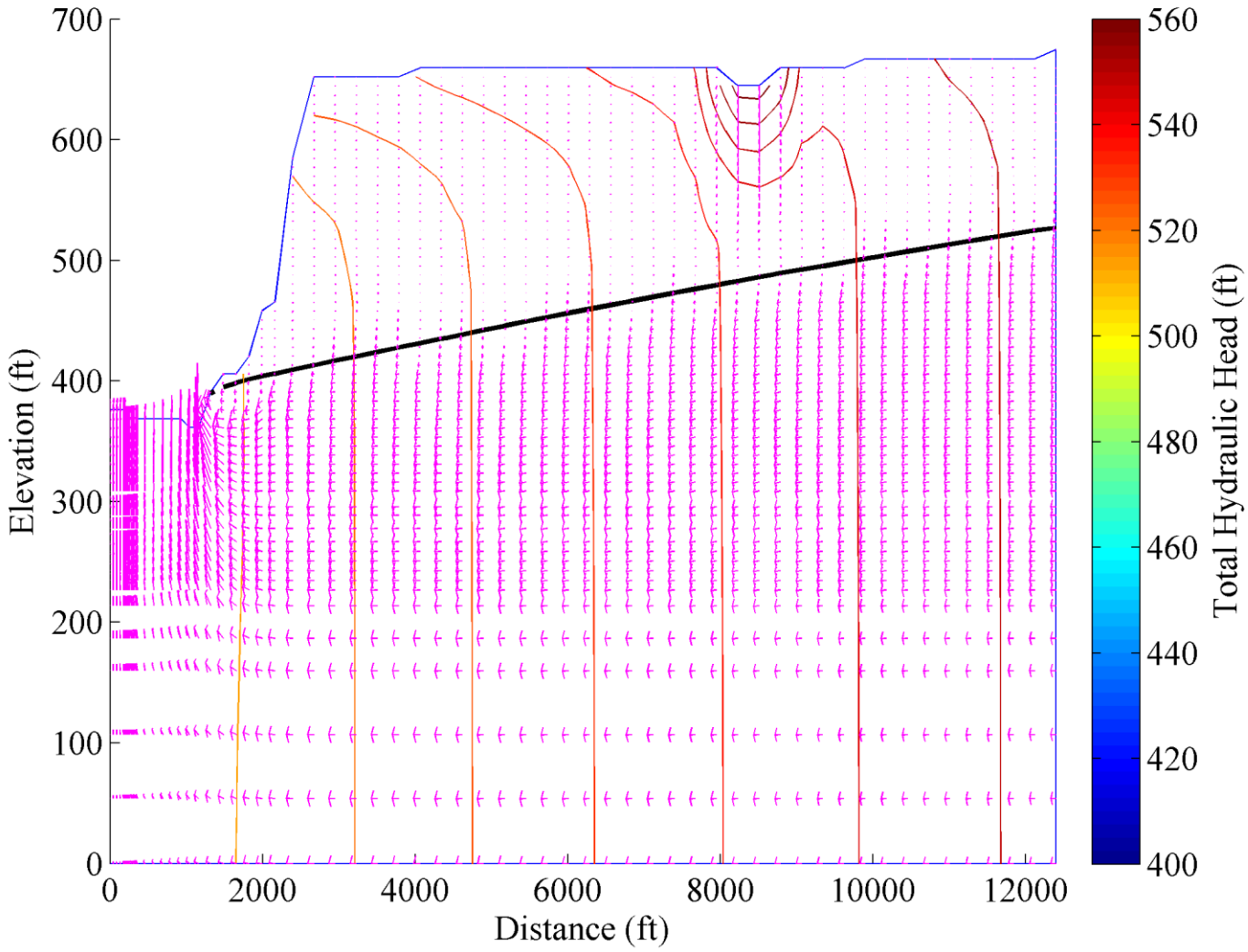

Figure 4.8 | Groundwater flow field for pond recharge simulation, at the end of the 10-year recharge application period; thick black line represents the water table, and contours represent lines of constant head.

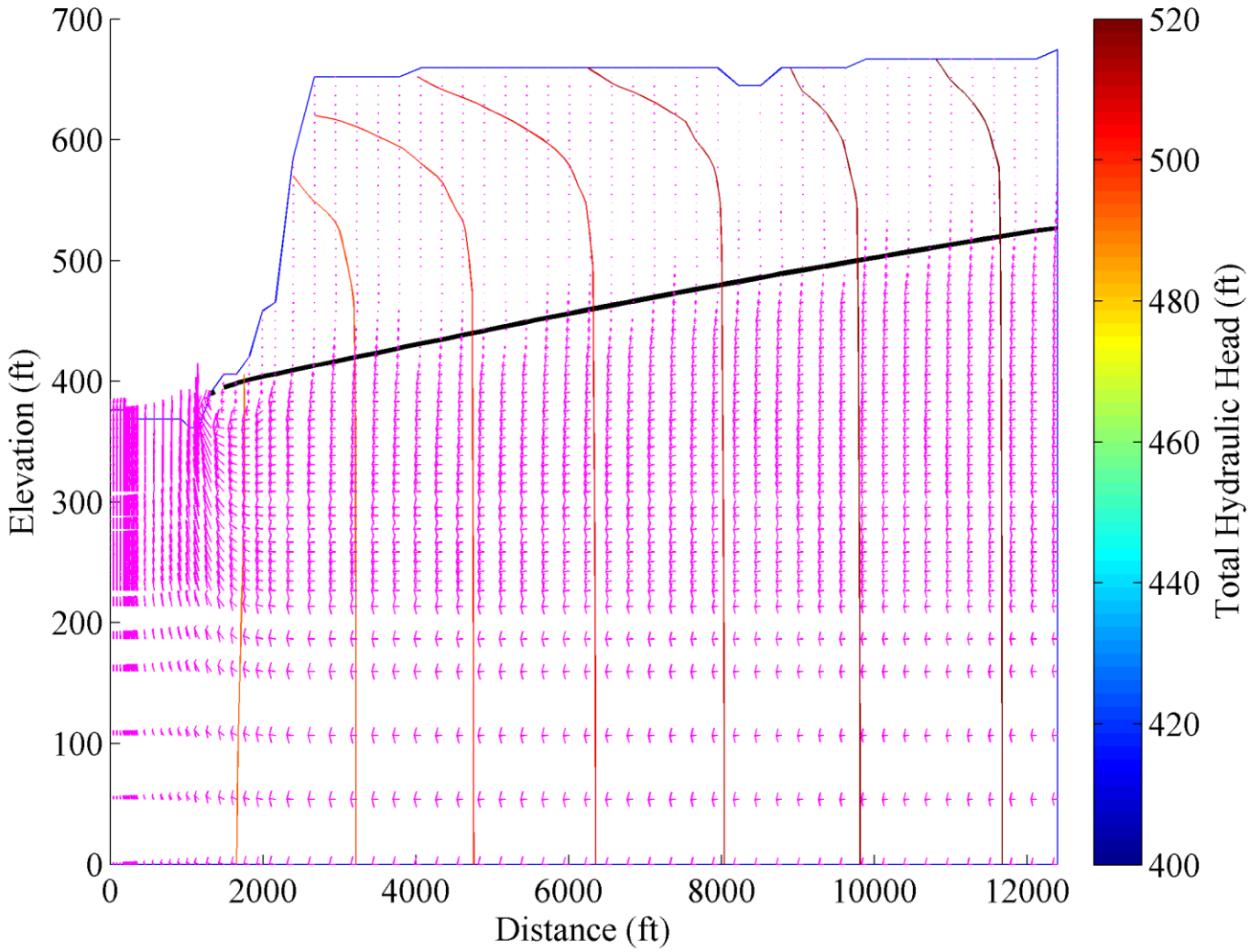

Figure 4.9 | Groundwater flow field for the pond recharge simulation, at the end of the 20 year simulation (10 years after the cessation of pond recharge); thick black line represents the water table, and contours represent lines of constant head.

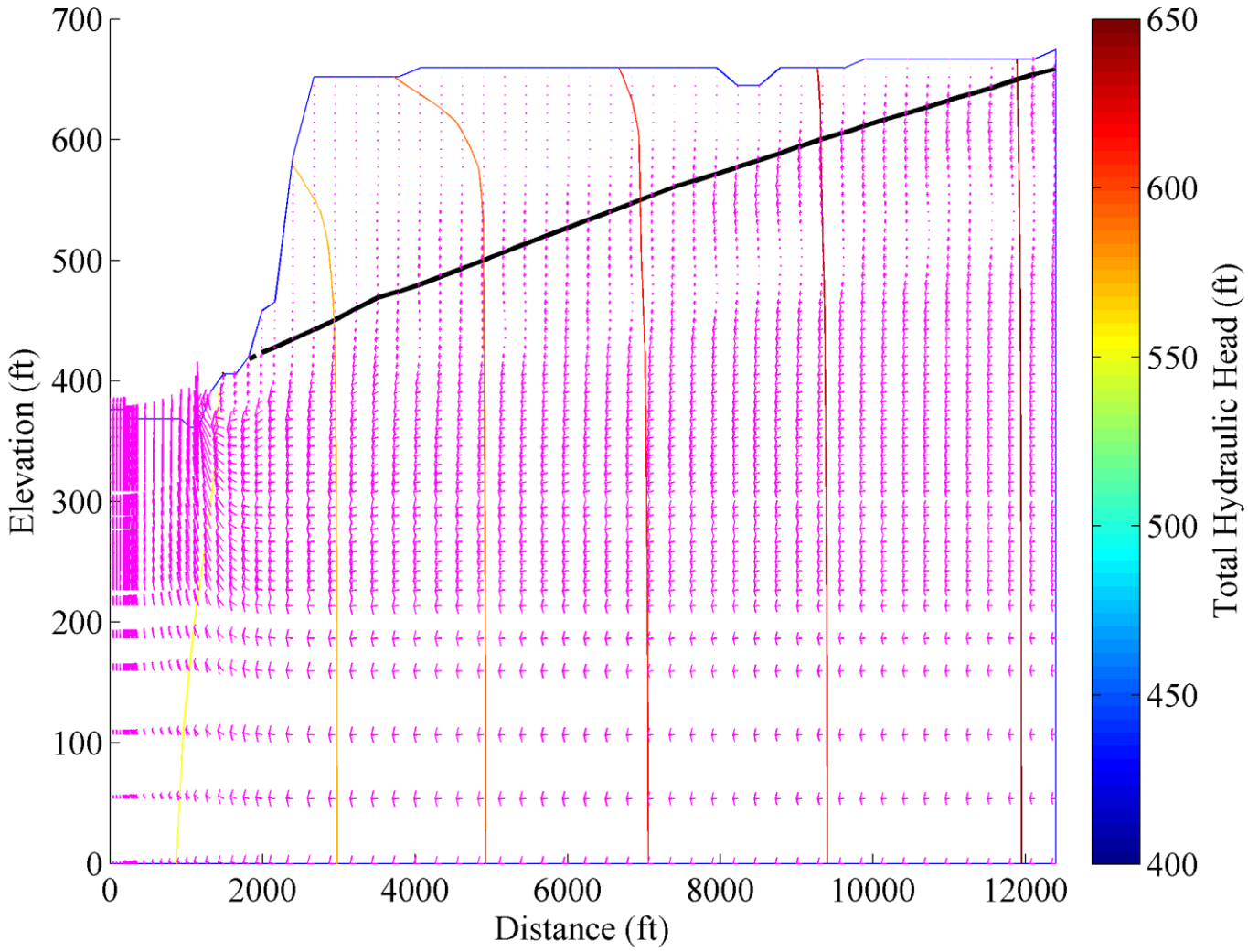

Figure 4.10 | Groundwater flow field for the climate fluctuation simulation (i.e., two-fold increase in recharge from precipitation); thick black line represents the water table, and contours represent lines of constant head.

CHAPTER 5

SYNTHESIS

The White Bluffs along the Columbia River, near Locke Island, in south central Washington State are a microcosm of the hydrological consequences of land-use change and climate fluctuations; the hydrological consequences here have even initiated natural hazards. Over the last 125 years, much of the area in south-central Washington has been converted from rangeland and dryland farming to one of the major agricultural areas of the United States. Landsliding along the bluffs, however, is not limited to modern activity; there is evidence that landslides occurred here within the last 11,000 years, with some activity in the last several hundred years [*Triangle Associates Inc.*, 2003]. Therefore, climate fluctuations and river mechanics are also important pre-disposing factors to slope failure. Prior to irrigation of the land adjacent to the bluffs, toe erosion by the Columbia River has been implicated as the major cause of landsliding [*Schuster et al.*, 1987]; and a wetter climate has been suggested as the likely cause of landsliding here in prehistoric times [*Triangle Associates, Inc*., 2003].

It is often impossible to isolate a single cause of slope failure [*Duncan and Wright*, 2005]. Various processes operate simultaneously, and it is the interaction between several factors that lead to slope failure. Attempting to assign an ultimate cause to the landsliding activity at Locke Island may be not only incorrect but uninformative. Increased recharge and subsequent groundwater flow are some of the most important landslide triggering factors [*Johnson and Sitar*, 1990; *van Asch et al.*, 1999]; these factors are thought to be two of the key hydrological

consequences of land use change and climate fluctuations. Therefore, it is important to evaluate the relative importance of climate and land use change in increasing recharge and groundwater flow, and to consider the potential for changes with time. Only then can the hydrological processes operating along the White Bluffs be integrated into a framework for understanding both the initiation and continuation of slope failure here.

Factors that influence the regional groundwater system are most likely to predispose the White Bluffs at Locke Island to failure. Others [e.g., *Drost et al.*, 1993; *Drost et al.*, 1997] have established the dramatic increase in the annual flow through the groundwater system since pre-development time (circa 1950), with groundwater levels rising by an average of 60 m (200 ft). Groundwater modeling results here indicate that an increase in regional recharge from sustained increases in precipitation can have a similar effect. This study uses a Palmer drought index reconstructed from paleoclimate data to examine the presence of such persistent climate features. While this gridded dataset is fairly coarse in resolution, results from chapter two of this study indicate that spatial resolution of the Palmer drought index has a small effect on the overall magnitude of the index in the Hanford Reach of the Columbia River. Results from wavelet analyses of the Palemr drought index derived from paleoclimate data demonstrate that low-frequency drought and pluvial cycles, both at multidecadal and centennial timescales, are persistent features of regional climate in the Pacific Northwest. Moreover, *Nelson et al*. [2011] has shown that the average duration of multidecadal wet and dry cycles in the Pacific Northwest has increased in the last millennium. The groundwater system responds to these cyclical wet (dry) cycles by increasing (decreasing) the storage of water in the ground, which equate to higher (lower) water levels, and increasing (decreasing) the discharge rate from the system. Similar

responses to changes in recharge from irrigation application and seepage from irrigation water conveyances [*Drost et al.*, 1997]. These fluctuations in climate and changes in land use certainly pre-dispose the White Bluffs to failure and, therefore, may be considered an important cause of landsliding activity.

Seepage from the numerous unlined canals and ponds in the irrigation district is cumulative, and this increased recharge to the groundwater system is superimposed upon changes to recharge produced by climate fluctuations. It has been suggested that the modern landsliding along the Bluffs at Locke Island is a result of irrigation water delivered to unlined wastewater ponds behind the bluffs [*Bjornstad*, 2006; *Hays and Schuster*, 1987; *Nickens et al.*, 1998; *Schuster et al.*, 1987; *Triangle Associates, Inc.*, 2003]. Results from groundwater modeling here indicate that this single set of unlined ponds do not significantly affect groundwater discharge at the landslide. While, alone, these ponds do not seem to be an important cause of slope failure, given the coincident timing of formation of these ponds and landslide initiation, these ponds may have been the trigger that set the pre-disposed bluffs in motion.

The wastewater ponds behind the bluffs at Locke Island were completely drained in the mid-1990s in an attempt to stop the landsliding, but slumping of the Bluffs continues [*Bjornstad*, 2006]. The rate of movement at the toe of the landslide has gradually slowed from as much as 6 m (20 ft) per year in 1998 to the point where there has been little movement in the years leading up to 2006 [*Bjornstad*, 2006]. *Bennett et al.* [2002] suggest that the continued presence of the landslide debris in its present position is essential for maintaining the stability of the hillside. Results from groundwater modeling here indicate that large daily and hourly fluctuations in river

stage (as produced by upstream dam operations) can induce very large changes in discharge at the toe of the landslide. Increasing pore water pressures and subsequent decreases in soil cohesion and shear strength facilitate erosion and can initiate failure. Therefore, changes in the position of landslide debris due to erosional loss to the Columbia River or local, small-scale slumping should be taken seriously.

The effects accompanying land use change and climate change, both natural and anthropogenic, span all scales. The effects on hydrology are not often visible or are difficult to distinguish. Hydrological records are relatively short (especially when analyzing records for climate signals) and discontinuous. Most hydrological systems are naturally highly variable, and real land use changes cannot be fully, experimentally controlled within catchments. Land use change and climate fluctuations work simultaneously to alter hydrological processes. The hydrological consequences are in some instances cumulative, as observed in the groundwater system in south-central Washington. Furthermore, the hydrological consequences of land use change and climate fluctuations can produce secondary natural hazards, such as the massive landslides along the White Bluffs in south-central Washington. Therefore, land use and climate changes are chief concerns facing the world this century. Given the impressive changes in land use over such a relatively short geologic period, the consequences of land use change may very well outweigh those from climate change [*Sala et al.*, 2000; *Vörösmarty et al.*, 2000].

REFERENCES

[*Alley*, 1984] Alley, W. M. (1984). The Palmer Drought Severity Index: Limitations and assumptions. *Journal of Climate and Applied Meteorology*, *23*(7), 1100-1109.

[*Amatya et al.*, 1995] Amatya, D., R. Skaggs, R., and J. Gregory (1995). Comparison of methods for estimating REF-ET. *Journal of Irrigation and Drainage Engineering*, *121*(6), 427-435.

[*Anderson*, 2010] Anderson, L. (2012). Rocky Mountain hydroclimate: Holocene variability and the role of insolation, ENSO, and the North American Monsoon. *Global and Planetary Change*, *92-93*, 198-208.

[*Bartlein et al*., 1998] Bartlein, P. J., K. H. Anderson, M. E. Edwards, C. J. Mock, R. S. Thompson, R. S. Webb, T. Webb III, and C. Whitlock (1998). Paleoclimate simulations for North America over the past 21,000 years: Features of the simulated climate and comparisons with paleoenvironmental data. *Quaternary Science Reviews*, *17*(6-7), 549-585.

[*Batu*, 1998] Batu, V. (1998). *Aquifer Hydraulics: A Comprehensive Guide to Hydrogeologic Data Analysis*, John Wiley and Sons: New York, NY, 727 p.

[*Bear et al.*, 1968] Bear, J., D. Zaslavsky, and S. Irmay (1968). *Physical Principles of Water Percolation and Seepage*, UNESCO: Paris, FRA, 465 p.

[*Bennett et al.*, 2002] Bennett, D. J., D. Hubbs, and A. Chugh (2002). *Locke Island Landslide Study, White Bluffs Area, Columbia Basin Project, Washington*, U.S. Department of the Interior, Bureau of Reclamation, Pacific Northwest Region, Boise, ID.

[*Bjornstad*, 2006] Bjornstad, B. N. (2006). Past, Present, Future Erosion at Locke Island. PNNL-15941. Pacific Northwest National Laboratory: Richland, WA.

[*Bonan*, 1997] Bonan, G. (1997). Effects of land-use on the climate of the United States. *Climatic Change*, *37*(3), 449-486.

[*Bosch and Hewlett*, 1982] Bosch, J. M., and J. A. Hewlett (1982). A review of catchment experiments to determine the effect of vegetation changes on wateryield and evapotranspiration. *Journal of Hydrology*, *55*(1-4), 3-23.

[*Brien and Reid*, 2008] Brien, D. L., and M. E. Reid (2008). Assessing deep-seated landslide susceptibility using 3-D groundwater and slope-stability analyses, southwestern Seattle, Washington. In Baum, R. L., Godt, J. W., and Highland, L. M., Eds., *Landslides and Engineering Geology of the Seattle, Washington Area*, 83-101. Boulder, CO: Geological Society of America.

[*Briffa et al.*, 1994] Briffa, K. R., P. D. Jones, and M. Hulme (1994). Summer moisture variability across Europe, 1892-1991: An analysis based on the Palmer Drought Severity Index. *International Journal of Climatology*, *14*(5), 575-504.

[*Brooks and Corey*, 1966] Brooks, R. H., and A. T. Corey (1966). Properties of porous media affecting fluid flow. *Journal of the Irrigation and Drainage Division Proceedings of the American Society of Civil Engineers*, *92*(IR2), 61-88.

[*Brown*, 2011] Brown, D. P. (2011). Winter circulation anomalies in the western United States associated with antecedent and decadal ENSO variability. *Earth Interactions*, *15*(3), 1-12.

[*Bruschi et al.*, 2013] Bruschi, V. M., J. Bonachea, J. Remondo, J. Gómez-Arozmena, V. Rivas, M. Barbieri, S. Capocchi, M. Soldati, and A. Cendrero (2013). Land management versus natural factors in land stability: Some examples in northern Spain. *Environmental Management*, *52*(2), 398-416.

[*Brutsaert*, 1966] Brutsaert, W. (1966). Probability laws for pore-size distribution. *Soil Science*, *101*, 85-92.

[*Burke et al.*, 2006] Burke, E. J., S. J. Brown, and N. Christidis (2006). Modeling the recent evolution of global drought and projections for the twenty-first century with the Hadley Centre climate model. *Journal of Hydrometeorology*, *7*(5), 1113-1125.

[*Caine*, 1980] Caine, N. (1980). The rainfall intensity: Duration control of shallow landslides and debris flows. *Geografiska Annaler, Series A, Physical Geography*, *62*(1/2), 23-27, doi:10.2307/520449.

[*Cane*, 2005] Cane, M. A. (2005). The evolution of El Niño, past and future. *Earth and Planetary Science Letters*, *230*(3-4), 227-240.

[*Cannon and Ellen*, 1985] Cannon, S. H., and S. D. Ellen (1985). Rainfall conditions for abundant debris avalanches, San Francisco Bay region, California. *California Geology*, *38*(12), 267-272.

[*Claessens et al.*, 2006] Claessens, L., D. J. Lowe, B. W. Hayward, B. F. Schaap, J. M. Schoorl, and A. Veldkamp (2006). Reconstructing high-magnitude/low-frequency landslide events based on soil redistribution modeling and a Late-Holocene sediment record from New Zealand. *Geomorphology*, *74*(1-4), 29-49.

[*Collison et al.*, 2000] Collison, A., S. Wade, J. Griffiths, and M. Dehn (2000). Modelling the impact of predicted climate change on landslide frequency and magnitude in SE England. *Engineering Geology*, *55*(3), 205-218.

[*Crozier*, 1986] Crozier, M. J. (1986). *Landslides: Causes, Consequences and Environment*. Croom Helm: London, GBR, 252 p.

[*Chugh and Schuster*, 2003] Chugh, A. K., and R. L. Schuster (2003). Numerical assessment of Locke Island Landslide, Columbia River Valley, Washington State, USA. In Culligan, P. J., Einstein, H. H., and Whittle, A. J., Eds., *Soil and Rock America 2003, Proc. 12th Panamerican Conf. on Soil Mechanics and Geotechnical Engineering*, 2489-2496.

[*Cooley*, 1971] Cooley, R. L. (1971). A finite difference method for unsteady flow in variably saturated porous media: Application to a single pumping well. *Water Resources Research*, *7*(6), 1607-1625.

[*Cooley and Westphal*, 1974] Cooley, R. L., and J. A. Westphal (1974). An evaluation of the theory of ground-water and river-water interchange, Winnemucca Reach of the Humboldt River, Nevada. *Hydrological Water Resources Publication 19*, Nevada Center for Water Resources Research, Desert Research Institute: Reno, NV, 74 p.

[*Cook et al.*, 1999] Cook, E. R., D. M. Meko, D. W. Stahle, and M. K. Cleaveland (1999). Drought reconstructions for the continental United States. *Journal of Climate, 12*(4), 1145-1162.

[*Cook et al.*, 2004] Cook, E. R., C. A. Woodhouse, C. M. Eakin, D. M. Meko, and D. W. Stahle (1999). Long-term aridity changes in the western United States. *Science, 306*(5698), 1015-1018.

[*Cook et al.*, 2008] Cook, E. R., et al. (2008). North American Summer PDSI Reconstructions, Version 2a. IGBP PAGES/World Data Center for Paleoclimatology Data Contribution Series #2008-046. NOAA/NCDC Paleoclimatology Program, Boulder, CO, USA (available at http://www.ncdc.noaa.gov/paleo/pdsi.html, accessed February 7, 2014).

[*Cruden and Varnes*, 1996] Cruden, D., and D. Varnes (1996). Landslide Types and Processes. In *Landslides Investigation and Mitigation*, K. A. Turner and R. L. Schuster, Eds., Transportation Research Board Special Report 247. National Academy Press: Washington, DC, pp. 36-75.

[*Dai*, 2010] Dai, A. (2010). Drought under global warming: A review. *Wiley Interdisciplinary Reviews Climate Change*, *2*(1), 45-65.

[*Dai et al.*, 1998] Dai, A., K. E. Trenberth, and T. R. Karl (1998). Global variations in droughts and wet spells: 1900-1995. *Geophysical Research Letters, 25*(17), 3367-3370.

[*Dai et al.*, 2004] Dai, A., K. E. Trenberth, and T. Qian (2004). A global dataset of Palmer Drought Severity Index for 1870-2002: Relationship with soil moisture and effects of surface warming. *Journal of Hydrometeorology*, *5*(6), 1117-1130.

[*Das*, 2008] Das, B. *Advanced Soil Mechanics*. Taylor and Francis: New York, NY.

[*Daubechies*, 1990] Daubechies, I. (1990). The wavelet transform time-frequency localization and signal analysis. *IEEE Transactions Information Theory*, *36*(5), 961-1004.

[*Davis and Rappaport*, 1974] Davis, J. M., and P. N. Rappaport (1974). The use of time series analysis techniques in forecasting meteorological drought. *Monthly Weather Review*, *102*(2), 176-180.

[*DeFries and Eshleman*, 2004] DeFries, R., and K. N. Eshleman (2004). Land-use change and hydrologic processes: A major focus for the future. *Hydrological Processes*, *18*(11), 2183-2186.

[*Dettinger et al*., 1998] Dettinger, M. D., D. R. Cayan, H. F. Diaz, and D. M. Meko (1998). North-south precipitation patterns in western North American on interannual to decadal timescales. *Journal of Climate*, *11*(12), 3095-3111.

[*Diaz*, 1983] Diaz, H. F. (1983). Some aspects of major dry and wet periods in the contiguous United States, 1895-1981. *Journal of Climate and Applied Meteorology*, *22*(1), 3-16.

[*Diffenbaugh et al*., 2006] Diffenbaugh, N. S. M. Ashfaq, B. Shuman, and J. W. Williams (2006). Summer aridity in the United States: Response to mid-Holocene changes in insolation and sea surface temperature. *Geophysical Research Letters*, *33*, L22712, doi:10.1029/2006GL028012.

[*Dilley et al.*, 2005] Dilley, M., R. S. Chen, U. Deichmann, A. L. Lerner-Lam, M. Arnold, J. Agwe, P. Buys, O. Kjekstad, B. Lyon, and G. Yetman (2005). *Natural Disaster Hotspots: A Global Risk Analysis*. Disaster Risk Management Series, Issue No. 5. The World Bank: Washington, DC.

[*Domenico and Mifflin*, 1965] Domenico, P. A., and M. D. Mifflin (1965). Water from low-permeability sediments and land subsidence. *Water Resources Research*, *1*(4), 563-576.

[*Douglas and Jones*, 1963] Douglas, J. J., and B. F. Jones (1963). On predictor-corrector method for non linear parabolic differential equations. *Journal of the Society for Industrial and Applied Mathematics*, *11*(1), 195-204.

[*Drost et al.*, 1993] Drost, B. W., J. C. Ebert, and S. E. Cox (1993). *Long-term Effects of Irrigation with Imported Water on Water Levels and Water Quality*. Water Resources Investigation Report 93-4060, United States Geological Survey, Tacoma, WA.

[*Dubrovsky et al.*, 2009] Dubrovsky, M., M. D. Svoboda, M. Trnka, M. J. Hayes, D. A. Wilhite, Z. Zalud, and P. Hlavinka (2009). Application of relative drought indices in assessing climate change impacts on drought conditions in Czechia. *Theoretical and Applied Climatology*, *96*(1-2), 155-171.

[*Duncan and Wright*, 2005]. Duncan, J. M., and S. G. Wright (2005). *Soil Strength and Slope Stability*. John Wiley & Sons, Inc.: Hoboken, NJ, 312 p.

[*Eder et al.*, 1987] Eder, B. K., J. M. Davis, and J. F. Monahan (1987). Spatial and temporal analysis of the Palmer Drought Severity Index over the southeastern United States. *Journal of Climatology*, *7*(1), 31-56.

[*Farge*, 1992] Farge, M. (1992). Wavelet transforms and their application to turbulence. *Annual Review of Fluid Mechanics, 24*, 395-457.

[*Fung et al.*, 2011] Fung, F., A. Lopez, and M. New (2011). Water availability in +2°C and +4°C worlds. *Philosophical Transactions of the Royal Society A, 369*(1934), 99-116.

[*Gedalof et al*., 2005] Gedalof, Z., D. L. Peterson, and N. J. Mantua (2005). Atmospheric, climatic, and ecological controls on extreme wildfire years in the northwestern United States. *Ecological Applications, 15*(1), 154-174.

[*Gershunov and Barnett*, 1998] Gershunov, A., and T. P. Barnett (1998). Interdecadal modulation of ENSO teleconnections. *Bulletin of the American Meteorological Society, 79*(12), 2715-2726.

[*Gernshunov et al*., 1999] Gershunov, A., T. P. Barnett, and D. R. Cayan (1999). North Pacific interdecadal oscillation seen as factor in ENSO-related North American climate anomalies. *EOS, 80*(3), 25-30.

[*Glade*, 2003] Glade, T. (2003). Landslide occurrence as a response to land use change: A review of evidence from New Zealand, *CATENA, 51*(3-4), 297-314.

[*Grinsted et al.*, 2004] Grinsted, A., J. C. Moore, and S. Jevrejeva (2004). Application of the cross wavelet transform and wavelet coherence to geophysical time series. *Nonlinear Processes in Geophysics, 11*(5/6), 561-566.

[*Gu*, 2007] Gu, C. (2007). *Hydrological Control on Nitrate Delivery through the Groundwater-Surface Water Interface* (Doctoral dissertation). Retrieved from Proquest Dissertations and Theses. (Publication number UMI 3305890)

[*Guttman*, 1991] Guttman, N. B. (1991). A sensitivity analysis of the Palmer Hydrologic Drought Index. *Water Resources Bulletin, 27*(5), 797-807.

[*Guttman and Quayle*, 1996] Guttman, N. B., and R. G. Quayle (1996). A historical perspective of U.S. climate divisions. *Bulletin of the American Meteorological Society, 77*(2), 293-303.

[*Haigh*, 2009] Haigh, J. D. (2009). Mechanisms for solar influence on the Earth's climate. In T. Tsuda, R. Fujii, K. Shibata, and M. A. Gellar, Eds., *Climate and Weather of the Sun-Earth System (CAWSES): Selected Papers from the 2007 Kyoto Symposium*, 231-256. Tokyo, JPN: TERRAPUB.

[*Hamon*, 1963] Hamon, W. R. (1963). Computation of direct runoff amounts from storm rainfall. *International Association of Scientific Hydrology Publication, 63*, 52-62.

[*Harr*, 1981] Harr, R. D. (1981). Some characteristics and consequences of snowmelt during rainfall in western Oregon. *Journal of Hydrology, 53*(3-4), 277-304.

[*Harr*, 1986] Harr, R. D. (1986). Effects of clear-cut logging on rain-on-snow runoff in western Oregon: A new look at old studies. *Water Resources Research*, *22*(7), 1095-1100.

[*Harr et al.*, 1975] Harr, R. D., W. C. Harper, J. T. Krygier, and F. S. Hsieh (1975). Changes in storm hydrographs after road building and clear-cutting in the Oregon Coast Range. *Water Resources Research, 11*(3), 431-444.

[*Harrison et al*., 2003] Harrison, S. P., J. E. Kutzbach, Z. Liu, P. J. Bartlein, B. Otto-Bliesner, D. Muhs, I. C. Prentice, and R. S. Thompson (2003). Mid-Holocene climates of the Americas: A dynamical response to change seasonality. *Climate Dynamics*, *20*(7-8), 663-688.

[*Heddinghaus and Sabol*, 1991] Heddinghaus, T. R., and P. Sabol (1991). A review of the Palmer Drought Severity Index and where do we go from here? In *Proceedings of the 7th Conference on Applied Climatology*, Salt Lake City, UT, Sep. 10-13, 1991. American Meteorological Society: Boston, MA; pp 232-246.

[*Heim*, 2002] Heim, R. R. (2002). A review of twentieth-century drought indices used in the United States. *Bulletin of the American Meteorological Society*, *83*(8), 1149-1165.

[*Hidalgo*, 2004] Hidalgo, H. G. (2004). Climate precursors of multidecadal drought variability in the western United States. *Water Resources Research*, *40*, W12504, doi:10.1029/2004WR003350.

[*Hollis*, 1975] Hollis, G. E. (1975). The effect of urbanization on floods of different recurrence interval. *Water Resources Research, 11*(3), 431-435.

[*Horiuchi et al.*, 2008] Horiuchi, K., T. Uchida, Y. Sakamoto, A. Ohta, H. Matsuzki, Y. Shibata, and H. Motoyama (2008). Ice core records of Be-10 over the past millennium from Dome Fuji, Antarctica: A new proxy record of past solar activity and a powerful tool for stratigraphic dating. *Quaternary Geochronology*, *3*(3), 253-261.

[*Hornbeck et al.*, 1970] Hornbeck, J. W., R. S. Pierce, and C. A. Federer (1970). Streamflow changes after forest clearing in New England. *Water Resources Research*, *6*(4), 1124-1132.

[*Hornberger and Wiberg*, 2005] Hornberger, G. M., and P. L. Wiberg (2005). *Numerical Methods in the Hydrologcial Sciences*. American Geophysical Union, doi:10.1002/9781118709528.

[*Hough*, 1969] Hough, B. (1969). *Basic Soil Engineering*. Ronald Press Company: New York, NY.

[*Houghton*, 1995] Houghton, R. A. (1995). Land-use change and the carbon cycle. *Global Change Biology, 1*(4), 275-287.

[*Hu and Willson*, 2000] Hu, Q., and G. D. Willson (2000). Effects of temperature anomalies on the Palmer Drought Severity Index in the central United States. *International Journal of Climatology*, *20*(15), 1899-1911.

[*Huang et al.*, 2005] Huang, H. P., R. Seager, and Y. Kushnir (2005). The 1976/77 transition in precipitation over the Americas and the influence of tropical sea surface temperatures. *Climate Dynamics*, *24*(7-8), 721-740.

[*Intergovernmental Panel on Climate Change*, 2001] Intergovernmental Panel on Climate Change (2001). *Climate Change 2001: The Scientific Basis. Contribution of Working Group I to the Third Assessment Report of the Intergovernmental Panel on Climate Change*. Houghton, J. T., Ding, Y., Griggs, D. J., Noguer, M., van der Linden, P. J., Da, X., Maskell, K., Johnson, C. A., Eds. Cambridge University Press: Cambridge, GBR, 881 pp.

[*Intergovernmental Panel on Climate Change*, 2007] Intergovernmental Panel on Climate Change (2007). *Climate Change 2007: Impacts, Adaptation and Vulnerability. Contribution of Working Group II to the Fourth Assessment Report of the Intergovernmental Panel on Climate Change*. Parry, M. L., O. F. Canziani, J. P. Palutikof, P. J. van der Linden, and C. E. Hanson, Eds. Cambridge University Press: Cambridge, GBR, 976 pp.

[*Iverson*, 2000] Iverson, R. M. (2000). Landslide triggering by rain infiltration. *Water Resources Research*, *36*(7), 1897-1910.

[*Jacobi et al.*, 2013] Jacobi, J. H., D. Perrone, L. L. Duncan, and G. M. Hornberger (2013). A tool for calculating the Palmer drought indices. *Water Resources Research*, *49*(9), 6086-6089.

[*Johnson and Sitar*, 1990] Johnson, K., and N. Sitar (1990). Hydrologic conditions leading to debris-flow initiation. *Canadian Geotechnical Journal*, *27*(6), 789-801.

[*Jones et al.*, 1996] Jones, P. D., M. Hulme, K. R. Briffa, and C. G. Jones (1996). Summer moisture availability over Europe in the Hadley Centre general circulation model based on the Palmer Drought Severity Index. *International Journal of Climatology*, *16*(2), 155-172.

[*Jones et al.*, 2009] Jones, P. D., K. R. Briffa, T. J. Osborn, J. M. Lough, T. D. van Ommen, B. M. Vinther, J. Luterbacher, E. R. Wahl, F. W. Zwiers, M. E. Mann, G. A. Schmidt, C. M. Ammann, B. M. Buckley, K. M. Cobb, J. Esper, H. Goossee, N. Graham, E. Jansen, T. Kiefer, C. Kull, M. Küttel, E. Mosley-Thompson, J. T. Overpeck, N. Riedwyl, M. Schulz, A. W. Tudhope, R. Villalba, H. Wanner, E. Wolff, and E. Xoplaki (2009). High-resolution palaeoclimatology of the last millennium: A review of current status and future prospects. *Holocene*, *19*(1), 3-49.

[*Kalnay and Cai*, 2003] Kalnay, E., and M. Cai (2003). Impact of urbanization and land-use change on climate. *Nature*, *423*(6939), 528-531.

[*Karl*, 1983] Karl, T. R. (1983). Some spatial characteristics of drought duration in the United States. *J. Climate and Applied Meteorology*, *22*(8), 1356-1366.

[*Karl*, 1986a] Karl, T. R. (1986a). The sensitivity of the Palmer Drought Severity Index and Palmer's Z-index to their calibration coefficients including potential evapotranspiration. *Journal of Climate and Applied Meteorology*, *25*(1), 78-86.

[*Karl*, 1986b] Karl, T. R. (1986b). The relationship of soil moisture parameterizations to subsequent seasonal and monthly mean temperatures in the United States. *Monthly Weather Review*, *114*(4), 675-686.

[*Karl and Heim*, 1990] Karl, T. R., and R. R. Heim (1990). Are droughts becoming more frequent or severe in the United States? *Geophysical Research Letters*, *17*(11), 1921-1924.

[*Karl and Koscielny*, 1982] Karl, T. R., and A. J. Koscielny (1982). Drought in the United States, 1895-1981. *Journal of Climatology*, *2*(4), 313-321.

[*Karl and Quayle*, 1981] Karl, T. R., and R. G. Quayle (1981). The 1980 summer heat wave and drought in historical perspective. *Monthly Weather Review*, *109*(10), 2055-2073.

[*Karl et al.*, 1987] Karl, T. R., F. Quinlan, and D. S. Ezell (1987). Drought termination and amelioration – Its climatological probability. *Journal of Climate and Applied Meteorology*, *26*(9), 1198-1209.

[*Karl et al.*, 2012] Karl, T. R. , B. E. Gleason, M. J. Menne, J. R. McMahon, R. R. Heim, M. J. Brewer, K. E. Kunkel, D. S. Arndt, J. L. Privette, J. J. Bates, P. Y. Groisman, and D. R. Easterling (2012). U.S. temperature and drought: Recent anomalies and trends. *EOS*, *93*(47), 473-496.

[*Kestin et al.*, 1998] Kestin, T. S., D. J. Karoly, J.-I. Yano, and N. A. Rayner (1998). Time frequency variability of ENSO and stochastic simulations. *Journal of Climate*, *11*(9), 2258-2272.

[*Keyantash and Dracup*, 2002] Keyantash, J., and J. A. Dracup (2002). The quantification of drought: An evaluation of drought indices. *Bulleting of the American Meteorological Society*, *83*(8), 1167-1180.

[*Kim and Valdés*, 2003] Kim, T. W., and J. B. Valdés (2003). Nonlinear model for drought forecasting based on a conjugation of wavelet transforms and neural networks. *Journal of Hydrologic Engineering*, *8*(6), 319-328.

[*Kim et al.*, 2002] Kim, T. W., J. B. Valdés, and J. Aparicio (2002). Frequency and spatial characteristics of droughts in the Conchos River basin, Mexico. *Water International*, *27*(3), 420-430.

[*Klugman*, 1978] Klugman, M. R. (1978). Drought in the upper Midwest, 1931-1969. *Journal of Applied Meteorology*, *17*(10), 1425-1431.

[*Knapp et al*., 2004] Knapp, P. A., P. T. Soulé, and H. D. Grissino-Mayer (2004). Occurrence of sustained droughts in the interior Pacific Northwest (A.D. 1733-1980) inferred from tree-ring data. *Journal of Climate, 17*(1), 140-150.

[*Knudsen et al.*, 2009] Knudsen, M. F., P. Riisager, B. H. Jacobsen, R. Muscheler, I. Snowball, and M.-S. Seidenkrantz (2009). Taking the pulse of the Sun during the Holocene by joint analysis of ^{14}C and ^{10}Be. *Geophysical Research Letters, 36*, L166701, doi:10.1029/2009GL039439.

[*Kogan*, 1995] Kogan, F. N. (1995). Droughts of the late 1980s in the United States as derived from NOAA polar-orbiting satellite data. *Bulletin of the American Meteorological Society, 76*(5), 655-668.

[*Kothavala*, 1999] Kothavala, Z. (1999). The duration and severity of drought over eastern Australia simulated by a coupled ocean-atmosphere GCM with a transient increase in CO_2. *Environmental Modelling and Software, 14*(4), 243-252.

[*Kutzbach et al*., 1998] Kutzbach, R. G., S. Harrison, P. Behling, R. Selin, and F. Laarif (1998). Climae and biome simulations for the past 21,000 years. *Quaternary Science Reviews, 17*(6-7), 473-506.

[*Labat*, 2005] Labat, D. (2005). Recent advances in wavelet analysis: Part I. A review of concepts. *Journal of Hydrology, 314*(1-4), 275-288.

[*Lambin et al.*, 1999] Lambin, E. F., X. Baulies, N. Bockstael, G. Fischer, T. Krug, R. Leemans, E. F. Moran, R. R. Rindfuss, D. Skole, B. L. Turner II, and C. Vogel (1999). *Land-Use and Land-Cover Change: Implementation Strategy*. IGBP Report No. 48/IHDP Report No. 10. IGBP: Stockholm, SE, 125 pp.

[*Last et al.*, 2006] Last, G. V., E. J. Freeman, K. J. Cantrell, M. J. Fayer, G. W. Gee, W. E. Nichols, B. N. Bjornstad, and D. G. Horton (2006). Vadose Zone Hydrogeology Data Package for Hanford Assessments, PNNL-14702, Rev. 1. Pacific Northwest National Laboratory: Richland, WA.

[*Lean*, 2010] Lean, J. L. (2010). Cycles and trends in solar irradiance and climate. *Wiley Interdisciplinary Reviews Climate Change, 1*(1), 111-122.

[*Likens et al.*, 1977] Likens, G. E., F. H. Bormann, R. S. Pierce, J. S. Eaton, and N. M. Johnson (1977). *Biogeochemistry of a Forested Ecosystem*. Springer-Verlag: New York, NY.

[*Lohani and Loganathan*, 1997] Lohani, V. K., and G. V. Loganathan (1997). An early warning system for drought management using the Palmer Drought Index. *Journal of the American Water Resources Association, 33*(6), 1375-1386.

[*Lohani et al.*, 1998] Lohani, V. K., G. V. Loganathan, and S. Mostaghimi (1998). Long-term analysis and short-term forecasting of dry spells by the Palmer Drought Severity Index. *Nordic Hydrology*, *29*(1), 21-40.

[*Luebehusen*, 2014] Luebehusen, E. (2014). United States Drought Monitor. The National Drought Mitigation Center at the University of Nebraska-Lincoln/United States Department of Agriculture/National Oceanic and Atmospheric Administration (available at http://droughtmonitor.unl.edu, accessed April 11, 2013).

[*MacDonald and Case*, 2005] MacDonald, G. M., and R. A. Case (2005). Variations in the Pacific Decadal Oscillation over the past millennium. *Geophysical Research Letters*, *32*, L08703, doi:10.1029/2005GL022478.

[*Mann et al*., 2005] Mann, M. E., M. A. Cane, S. E. Zebiak, and A. Clement (2005). Volcanic and solar forcing of the tropical Pacific over the past 1000 years. *Journal of Climate*, *18*(3), 447-456.

[*Mantua et al*., 1997] Mantua, N. J., S. R. Hare, Y. Zhang, J. M. Wallace, and R. C. Francis (1997). A Pacific interdecadal oscillation with impacts on salmon production. *Bulletin of the American Meteorological Society*, *78*(6), 1069-1079.

[*Matsuura and Willmott*, 2012a] Matsuura, K., and C. J. Willmott (2012a). Terrestrial air temperature: 1900-2010 gridded monthly time series (Version 3.01); http://climate.geog.udel.edu/~climate/html_pages/Global2011/README.GlobalTsT2011.html, accessed April 11, 2013.

[*Matsuura and Willmott*, 2012b] Matsuura, K., and C. J. Willmott (2012a). Terrestrial precipitation: 1900-2010 gridded monthly time series (Version 3.02); http://climate.geog.udel.edu/~climate/html_pages/Global2011/Precip_revised_3.02/README.GlobalTsP2011.html, Accessed April 11, 2013.

[*Mavromatis*, 2007] Mavromatis, T. (2007). Drought index evaluation for assessing future wheat production in Greece. *International Journal of Climatology*, *27*(7), 911-924.

[*McCabe and Dettinger*, 1999] McCabe, G. J., and M. D. Dettinger (1999). Decadal variations in the strength of ENSO teleconnections with precipitation in the western United States. *International Journal of Climatology*, *19*(13), 1399-1410.

[*McCabe et al*., 2010] McCabe, G. J., M. A. Palecki, J. L. Betancourt, and I. Y. Fung (2010). Pacific and Atlantic Ocean influences on multidecadal drought frequency in the United States. *Proceedings of the National Academy of Sciences of the Untied States of America*, *101*(12), 4136-4141.

[*McCracken et al.*, 2004] McCracken, K. G., F. B. McDonald, J. Beer, G. Raisbeck, and F. Yiou (2004). A phenomenological study of the long term cosmic ray modulation, 850-1985AD. *Journal of Geophysical Research*, *109*, A12103, doi:10.10129/2004JA010685.

[*Meehl et al.*, 2007] Meehl, G. A., T. F. Stocker, W. D. Collins, P. Friedlingstein, A. T. Gaye, J. M. Gregory, A. Kitch, R. Knutti, J. M. Murphy, A. Noda, S. C. B. Raper, L. G. Watterson, A. J. Weaver, and Z.-C. Zhao (2007). Global Climate Projections. In *Climate Change 2007: The Physical Science Basis, Contribution of Working Group I to the Fourth Assessment Report of the Intergovernmental Panel on Climate Change*; Solomon, S., Qin, D., Manning, M., Chen, Z., Marquis, M., Averyt, K. B, Tignor, M., Miller, H. L., Eds.; Cambridge University Press, New York, NY; pp 747-846.

[*Meusburger and Alewell*, 2003] Meusburger, K., and C. Alewell (2008). Impacts of anthropogenic and environmental factors on the occurrence of shallow landslides in an alpine catchment (Urseren Valley, Switzerland). *Natural Hazards and Earth System Sciences*, *8*(3), 509-520.

[*Miller and White*, 1998] Miller, D. A., and R. A. White (1998). A coterminous United States multi-layer soil characteristics data set for regional climate and hydrology modeling. *Earth Interactions*, *2*(2), 1-26.

[*Mote et al.*, 2003] Mote, P. W., E. A. Parson, A. F. Hamlet, W. S. Keeton, D. Lettenmaier, N. Mantua, E. L. Miles, D. W. Peterson, D. L. Peterson, R. Slaughter, and A. K. Snover (2003). Preparing for climate change: The water, salmon, and forests of the Pacific Northwest. *Climatic Change*, *61*(1-2), 45-88.

[*Mualem*, 1976] Mualem, Y. (1976). A new model predicting they hydraulic conductivity of unsaturated porous media. *Water Resources Research*, *12*(3), 513-522.

[*Mueller and Geist*, 1999] Mueller, R. P., and D. R. Geist (1999). Steelhead spawning surveys near Locke Island, Hanford Reach of the Columbia River, PNNL-13055. Pacific Northwest National Laboratory: Richland, WA.

[*Neff*, 1989] Neff, G. E. (1989). Columbia Basin Project. *Washington Division of Geology and Earth Resources Bulletin*, *78*, 535-563.

[*Nelson et al*., 2011] Nelson, D. B., M. B. Abbott, B. Steinman, P. J. Polissar, N. D. Stansell, J. D. Ortiz, M. F. Rosenmeier, B. P. Finney, and J. Riedel (2011). Drought variability in the Pacific Northwest from a 6,000-yr lake sediment record. *Proceedings of the National Academy of Sciences*, *108*(10), 3870-3875.

[*Neuman*, 1973] Neuman, S. P. (1973). Saturated-unsaturated seepage by finite elements. *Journal of the Hydraulic Division of the American Society of Civil Engineers*, *99*(12), 2233-2250.

[*Nickens et al.*, 1998] Nickens, P. R., B. N. Bjornstad, N. A. Cadoret, and M. K. Wright (1998). Monitoring bank erosion at the Locke Island Archaeological National Register District: Summary of 1996/1997 field activities, PNNL-11970. Pacific Northwest National Laboratory: Richland, WA.

[*Özger et al.*, 2009] Ozger, M., A. K. Mishra, and V. P. Singh (2009). Low frequency drought variability associated with climate indices. *Journal of Hydrologyi, 364*(1-2), 152-162.

[*Palmer*, 1965] Palmer, W. C. (1965). *Meteorological Drought*. Weather Bureau Research Paper 45, U.S. Department of Commerce: Washington, DC.

[*Parriaux*, 2011] Parriaux, A. (2011). Vulnérabilité des infrastructures géotechniques au changement climatique et measures d'adaptation selon le context géographique. World Road Association: Paris, FRA.

[*Percival*, 1995] Percival, D. P. (1995). On estimation of the wavelet variance. *Biometrika, 82*(3), 619-631.

[*Petley et al.*, 2007] Petley, D., G. Hearn, A. Hart, N. Rosser, S. Dunning, K. Oven, and W. Mitchell (2007). Trends in landslide occurrence in Nepal. *Natural Hazards, 43*(1), 23-44.

[*Piechota and Dracup*, 1996] Piechota, T. C., and J. A. Dracup (1996). Drought and regional hydrologic variation in the US: Associations with the El Niño-southern oscillation. *Water Resources Research, 32*(5), 1359-1373.

[*Pimm and Raven*, 2000] Pimm, S. L., and P. Raven (2000). Extinction by numbers. *Nature, 403*(6772), 843-845.

[*Pinder et al.*, 1973] Pinder, G. F., E. O. Frind, and S. S. Papadopolous (1973). Functional coefficients in analysis of groundwater flow. *Water Resources Research, 9*(1), 222-226.

[*Potter*, 1991] Potter, K. W. (1991). Hydrological impacts of changing land management practices in a moderate-sized agricultural catchment. *Water Resources Research, 27*(5), 845-855.

[*Qian et al.*, 2004] Qian, B., S. Gameda, H. Hayhoe, R. De Jong, and A. Bootsma (2004). Resampling tests - a possible alternative to the standard statistical tests with caution: Reply to Semenov & Wellen (2004). *Climate Research, 28*(1), 85-87.

[*Rajagopalan et al.*, 2000] Rajagopalan, B., E. Cook, U. Lall, and B. Ray (2000). Spatio-temporal variability of ENSO and SST teleconnections to summer drought over the USA during the twentieth century. *Journal of Climate, 13*(24), 4244-4255.

[*Rayner et al.*, 2005] Rayner, S., D. Leach, and H. Ingram (2005). Weather forecasts are for wimps: Why water resource managers do not use climate forecasts. *Climatic Change, 69*(2-3), 197-227.

[*Riebsame et al.*, 1991] Riebsame, W. E., S. A. Changnon, and T. R. Karl, (1991). *Drought and Natural Resource Managment in the United States: Impacts and Implication of the 1987-89 Drought*. Westview Press: Boulder, CO.

[*Rockhold et al.*, 2009] Rockhold, M. L., D. L. Saunders, C. E. Strickland, S. R. Waichler, and R. E. Clayton (2009). Soil Water Balance and Recharge Monitoring at the Hanford Site – FY09 Status Report, PNNL-18807. Pacific Northwest National Laboratory: Richland, WA.

[*Rose and Peters*, 2001] Rose, S., and N. E. Peters (2001). Effects of urbanization on streamflow in the Atlanta area (Georgia USA): A comparative hydrological approach. *Hydrological Processes*, *15*(8), 1441-1457.
[*Rosenberry et al.*, 2004] Rosenberry, D. O., D. I. Stannard, T. C. Winter, and M. L. Martinez (2004). Comparison of 13 equations for determining evapotranspiration from a prairie wetland, Cottonwood Lake area, North Dakota, USA. *Wetlands*, *24*(3), 483-497.

[*Sakamoto*, 1978] Sakamoto, C. M. (1978). The Z-Index as a variable for crop yield estimation. *Agricultural Meteorology*, *19*(4), 305-313.
[*Sala et al.*, 2000] Sala, O. E., F. S. Chapin III, J. J. Armesto, E. Berlow, J. Bloomfield, R. Dirzo, E. Huber-Sanwald, L. F. Huenneke, R. B. Jackson, A. Kinzig, R. Leemans, D. M. Lodge, H. A. Mooney, M. Oesterheld, N. L. Poff, M. T. Sykes, B. H. Walker, M. Walker, and D. H. Wall (2000). Global biodiversity scenarios for the year 2100. *Science*, *287*(5459), 1770-1774.

[*Schaap et al.*, 2001] Schaap, M. G., F. J. Leij, and M. Th. van Genuchten (2001). ROSETTA: A computer program for estimating soil hydraulic parameters with hierarchical pedotransfer functions. *Journal of Hydrology*, *251*(3-4), 163-176.

[*Schmidt and Dikau*, 2004] Schmidt, J., and R. Dikau (2004). Modeling historical climate variability and slope stability. *Geomorphology*, *60*(3-4), 433-447.

[*Schuster and Hays*, 1984] Schuster, R. L., and W. H. Hays (1984). Irrigation-induced landslides in soft rocks and sediments along the Columbia River, south-central Washington State, U.S.A.: Toronto, Canada, IV International Symposium on Landslides, 1984 Proceedings, Vol. 1, 431-436.

[*Schuster et al.*, 1987] Schuster, R. L., A. F. Chleborad, and W. H. Hays (1987). Irrigation-induced landslides in fluvial-lacustrine sediments, South Central Washington State. *5th Int. Conf. and Field Workshop on Landslides*, Christchurch, New Zealand, 147-156.

[*Schuster et al.*, 1989] Schuster, R. L., A. F. Chleborad, and W. H. Hays (1989). The White Bluffs Landslides, South-Central Washington. Galster, R. W. (ed.), *Engineering Geology in Washington*, Washington Division of Geology and Earth Resources, Olympia, Bull. 78, Vol. II, 911-920.

[*Seager*, 2007] Seager, R. (2007). The turn of the century North American drought: Global context, dynamics, and past analogs. *Journal of Climate*, *20*(22), 5527-5552.

[*Semenov and Welham*, 2004] Semenov, M. A., and S. Welham (2004). Comments on the use of statistical tests in the comparison of stochastic weather generators by Qian et al. (2004). *Climate Research*, *28*(1), 83-84.

[*Sheffield and Wood*, 2008] Sheffield, J., and E. F. Wood (2008). Projected changes in drought occurrence under future global warming from multi-model, mult-scenario, IPCC AR4 simulations. *Climate Dynamics*, *31*(1), 79-105.

[*Sheffield et al.*, 2012] Sheffield, J., E. F. Wood, E. F., and M. L. Roderick (2012). Little change in global drought over the past 60 years. *Nature*, *491*(7424), 435-438.

[*Shen et al*., 2006] Shen, C., W.-C. Wang, W. Gong, and Z. Hao (2006). A Pacific Decadal Oscillation record since 1470 AD reconstructed from proxy data of summer rainfall over eastern China. *Geophysical Research Letters*, *33*, L03702, doi:10.1029/2005GL024804.

[*Skaggs*, 1975] Skaggs, R. H. (1975). Drought in the United States, 1931-40. *Annals of the Association of American Geographers*, *65*(3), 391-402.

[*Snover et al.*, 2013] Snover, A. K., G. S. Mauger, L. C. Whitely Binder, M. Krosby, and I. Tohver (2013). *Climate Change Impacts and Adaptation in Washington State: Technical Summary for Decision Makers*. State of Knowledge Report prepared for the Washington State Department of Ecology, Climate Impacts Group, University of Washington: Seattle, WA. http://cses.washington.edu/db/pdf/snoveretalsok816.pdf, accessed July 8, 2015.

[*Soniat et al.*, 2006] Soniat, T. M., J. M. Klinck, E. N. Powell, and E. E. Hofmann (2006). Understanding the success and failure of oyster populations: Climatic cycles and Perkinsus marinus. *Journal of Shellfish Research*, *25*(1), 83-93.

[*Sophocleous*, 2002] Sophocleous, M. (2002). Interactions between groundwater and surface water: The state of the science. *Hydrogeology Journal*, *10*(1): 52-67.

[*Soulé*, 1992] Soulé, P. T. (1992). Spatial patterns of drought frequency and duration in the contiguous USA based on multiple drought event definitions. *International Journal of Climatology*, *12*(1), 11-24.

[*Sowers*, 1979] Sowers, G. (1979). *Introductory Soil Mechanics and Foundations: Geotechnical Engineering*, 4th Edition. Prentice Hall: Upper Saddle River, NJ, 640 p.

[*Stahl and Demuth*, 1999] Stahl, K, and S. Demuth (1999). Investigating the influence of atmospheric circulation patterns on regional stream-flow drought in southern Germany, In *Hydrological Extremes: Understanding, Predicting, Mitigating*; Gottschalk, L., Olivoy, J.-C., Reed, D., Rosbjerg, D., Eds., IAHS Publication No. 255, IAHS Press: Wallingford, GBR; pp 19-27.

[*Steinemann*, 2003] Steinemann, A. (2003). Drought indicators and triggers: A stochastic approach to evaluation. *Journal of the American Water Resources Association*, *39*(5), 1217-1233.

[*Steinhilber et al.*, 2008] Steinhilber, F., J. A. Abreu, and J. Beer (2008). Solar modulation during the Holocene. *Astrophysics and Space Sciences Transactions*, *4*, 1-6.

[*Steinhilber et al.*, 2009a] Steinhilber, F., et al. (2009). Holocene total Solar Irradiance Reconstruction. IGBP PAGES/World Data Center for Paleoclimatology Data Contribution Series #2009-133. NOAA/NCDC Paleoclimatology Program, Boulder, CO, USA (available at ftp://ftp.ncdc.noaa.gov/pub/data/paleo/climate_forcing/solar_variability/steinhilber2009tsi.txt, accessed February 7, 2014).

[*Steinhilber et al.*, 2009b] Steinhilber, F., J. Beer, and C. Fröhlich (2009). Total solar irradiance during the Holocene. *Geophysical Research Letters*, *36*, L19704, doi:10.1029/2009GL040142.

[*Steinhilber et al.*, 2012] Steinhilber, F., J. A. Abreu, J. Beer, M. Christl, H. Fischer, U. Heikkla, P. Kubik, M. Mann, K. G. McCracken, H. Miller, H. Miyahara, H. Oerter, and F. Wilhelms (2012). 9,400 years of cosmic radiation and solar activity from ice cores and tree rings. *Proceedings of the National Academy of Sciences*, *109*(16), 5967-5971.

[*Steinman et al*., 2012] Steinman, B. A., M. B. Abbott, M. E. Mann, N. D. Stansell, and B. P. Finney (2009). 1,500 year quantitative reconstruction of winter precipitation in the Pacific Northwest. *Proceedings of the National Academy of Sciences*, *109*(29), 11619-11623.

[*Storck et al.*, 1998] Storck, P., L. Bowling, P. Wetherbee, and D. Lettenmaier (1998). Application of a GIS-based distributed hydrology model for prediction of forest harvest effects on peak streamflow in the Pacific Northwest. *Hydrological Processes*, *12*(6), 889-904.

[*Svoboda et al.*, 2002] Svoboda, M., D. LeComte, M. Hayes, R. R. Heim, K. Gleason, J. Angel, B. Rippey, R. Tinker, M. Palecki, D. Stooksbury, D. Miskus, and S. Stephens (2002). The drought monitor. *Bulletin of the American Meteorological Society*, *83*(8), 1181-1190.

[*Swank and Crossley*, 1988] Swank, W. T., and D. A. Crossley (1988). Forest Hydrology and Ecology at Coweeta. *Ecological Studies, 66*. Springer-Verlag: New York, NY.

[*Szinell et al.*, 1998] Szinell, C. S., A. Bussay, and T. Szentimrey (1998). Drought tendencies in Hungary. *International Journal of Climatology*, *18*(13), 1479-1491.

[*Tasser et al.*, 2003] Tasser, E., M. Mader, and U. Tappeiner (2003). Effects of land use on alpine grasslands on the probability of landslides. *Basic and Applied Ecology*, *4*(3), 271-280.

[*Thornthwaite*, 1948] Thornthwaite, C. W. (1948). An approach toward a rational classification of climate. *Geographical Review*, *38*(1), 55-94.

[*Torrence and Compo*, 1998] Torrence, C., and G. P. Compo (1998). A practical guide to wavelet analysis. *Bulletin of the American Meteorological Society*, 79(1), 61-78.

[*Torrence and Webster*, 1999] Torrence, C., and P. Webster (1999). Interdecadal changes in the ENSO-Monson system. *Journal of Climate*, *12*(9), 2679-2690.

[*Triangle Associates Inc.*, 2003] Triangle Associates, Inc. (2003). *White Bluffs Landslides:*

Assessment Report. Prepared under contract to the U.S. Institute for Environmental Conflict Resolution and the U.S. Fish and Wildlife Service for the Hanford Reach National Monument, Seattle, Washington.

[*Trouet et al.*, 2009] Trouet, V., J. Esper, N. E. Graham, A. Baker, J. D. Scourse, and D. C. Frank (2009). Persistent positive North Atlantic Oscillation mode dominated the Medieval Climate Anomaly. *Science*, *324*(5923), 78-80.

[*Usoskin, et al.*, 2005] Usoskin, I. G., K. Alanko-Huotari, G. A. Kovaltsov, and K. Mursula (2005). Heliospheric modulation of cosmic rays: Monthly reconstruction for 1951-2004. *Journal of Geophysical Research, 110,* A12108, doi:10.101209/2005JA011250.

[*van Asch et al.*, 1999] van Asch, T., J. Buma, and L. P. H. van Beek (1999). A view on some hydrological triggering systems in landslides. *Geomorphology*, *30*(1-2), 25-32.

[*van der Schrier et al.*, 2006a] van der Schrier, G., K. R. Briffa, P. D. Jones, and T. J. Osborn (2006a). Summer moisture variability across Europe. *Journal of Climate*, *19*(12), 2828-2834.

[*van der Schrier et al.*, 2006b] van der Schrier, G., K. R. Briffa, T. J. Osborn, and E. R. Cook (2006b). Summer moisture availability across North America. *Journal of Geophysical Research: Atmospheres*, *111*, D11102, doi:10.1029/2005JD006745.

[*van der Schrier et al.*, 2007] van der Schrier, G., D. Efthymiadis, K. R. Briffa, and P. D. Jones (2007). European Alpine moisture variability for 1800-2003. *International Journal of Climatology*, *27*(4), 415-427.

[*van Genuchten*, 1980] van Genuchten, M. Th. (1980). A closed-form equation for predicting the hydraulic conductivity of unsaturated soils. *Soil Science Society of America Journal*, *44*(5), 892-898.

[*Vanacker et al.*, 2003] Vanacker, V. M. Vanderschaeghe, G. Govers, E. Willems, J. Poesen, J. Deckers, and B. De Bievre (2003). Linking hydrological, infinite slope stability and land-use change moels through GIS for assessing the impact of deforestation on slope stability in high Andean watersheds. *Geomorphology*, *52*(3-4), 299-315.

[*Vonmoos et al.*, 2006] Vonmoos, M., J. Beer, and R. Muscheler (2006). Large variations in Holocene solar activity: Constraints from ^{10}Be in the Greenland Ice Core Project ice core. *Journal of Geophysical Research, 111*, A10105, doi:10.1029/2005JA011500.

[*VSS*, 1999] VSS (1999). *Swiss Standard SN 670 010b. Characteristic Coefficients of Soils*. Association of Swiss Road and Traffic Engineers: Zurich, CH.

[*Vörösmarty et al.*, 2000] Vorosmarty, C. J., P. Green, J. Salisbury, and R. Lammers (2000). Global water resources: Vulnerability from climate change and population growth. *Science*, *289*(5477), 284-288.

[*Werth and Avissar*, 2002] Werth, D., and R. Avissar (2002). The local and global effects of Amazon deforestation. *Journal of Geophysical Research: Atmospheres*, *107*, D20808, doi:10-1029/2002J8000717.

[*Whittemore et al.*, 1989] Whitemore, D. O., K. M. McGregor, and G. A. Marotz (1989). Effects of variations in recharge on groundwater quality. *Journal of Hydrology*, *106*(1-2), 131-145.

[*Wieczorek*, 1996] Wieczorek, G. F. (1996). Landslide triggering mechanisms. In *Landslides Investigation and Mitigation*, K. A. Turner and R. L. Schuster, Eds., Transportation Research Board Special Report 247. National Academy Press: Washington, DC, pp. 76-88.

[*Wilks*, 1995] Wilks, D. S. (1995). *Statistical methods in the atmospheric sciences*. Academic Press: San Diego, CA.

[*Willmott and Robeson*, 1995] Willmott, C. J., and S. M. Robeson (1995). Climatologically aided interpolation (CAI) of terrestrial air temperature. *International Journal of Climatology*, *15*(2), 221-229

[*Willmott and Rowe*, 1985] Willmott, C. J., and C. M. Rowe (1985). Climatology of the terrestrial seasonal water cycle. *Journal of Climatology*, *5*(6), 589-606.

[*Wilm et al.*, 1944] Wilm, H. G., C. W. Thornthwaite, E. A. Colman, N. W. Cummings, A. R. Croft, H. T. Gisborne, S. T. Harding, A. H. Hendrickson, M. D. Hoover, I. E. Houk, J. Kittredge, C. H. Lee, C.-G. Rossby, T. Saville, and C. A. Taylor (1944). Report of the Committee on Transpiration and Evaoptranspiration, 1943-44. *EOS*, *25*, 683-693.

[*Winter*, 1983] Winter, T. C. (1983). The interaction of lakes with variably saturate porous media. *Water Resources Research*, *19*(5), 1203-1218.

[*Wise*, 2010] Wise, E. K. (2010). Spatiotemporal variability of the precipitation dipole transition zone in the western United States. *Geophysical Research Letters*, *37*, L07706, doi:10.1029/2009GL042193.

[*Yu and Ito*, 1999] Yu, Z, and E. Ito (1999). Possible solar forcing of century-scale drought frequency in the northern Great Plains. *Geology*, *27*(3), 263-266.

[*Zhang et al.*, 2004] Zhang, Z., M. E. Mann, and E. R. Cook (2004). Alternative methods of proxy-based climate field reconstruction: Application to summer drought over the coterminous United States back to AD 1700 from tree-ring data. *The Holocene*, *14*(4), 502-516.

APPENDIX A

KOLMOGORV-SMIRNOV TEST AND MULTIPLE LINEAR REGRESSION RESULTS

This Appendix contains the initial two-sample Kolmogorov-Smirnov (K-S) test results; multiple linear regression coefficient estimates; and PDSI, temperature, and precipitation time series for two grid box-climate division pairs (described in Chapter 2, Section 2.3).

A.1. Initial Two-Sample K-S Test

Table A.1 | Initial Two-Sample K-S Test Results

Drought Index	p-value	Number (%) of Grid Box-Climate Division Pairs for which the Null Hypothesis is Rejected
Z	$p<0.01$	79 (14%)
	$p<0.05$	96 (16%)
PDSI	$p<0.01$	394 (67%)
	$p<0.05$	445 (76%)
PHDI	$p<0.01$	402 (69%)
	$p<0.05$	447 (77%)

Notes: The K-S test returns a test decision for the null hypothesis that the two data samples are from the same continuous distribution; the test either rejects or fails to reject the null hypothesis. Numbers and percentages of grid box-climate division pairs where $p<0.05$ also include those where $p<0.01$.

A.2. Multiple Linear Regression

Table A.2 | Multiple Linear Regression Coefficient Estimates

Response Variables	Coefficient Estimates, b, for Predictors			R^2
	$b_{Temperature\ Difference}$	$b_{Precipitation\ Difference}$	$b_{AWC\ Difference}$	
+Z Difference	-0.0100‡	-0.0631‡	0.0165	0.1381
-Z Difference	0.0117‡	0.0841‡	-0.0227	0.1836
+PDSI Difference	-0.0131‡	-0.0949‡	0.0256	0.1674
-PDSI Difference	0.0176‡	0.1491‡	-0.0446†	0.2013
+PHDI Difference	-0.0112‡	-0.0969‡	0.0286	0.1534
-PHDI Difference	0.0189‡	0.1466‡	-0.0447†	0.2070

Notes: Drought index differences, temperature differences, and precipitation differences are all average differences. Average differences are calculated by, first, subtracting the climate division value from the grid box value, and, second, averaging the differences. In the case of drought index differences, positive and negative differences are averaged separately to create two response variables per index. ‡$p<0.01$. †$p<0.05$.

A.3. PDSI, Temperature, and Precipitation Time Series

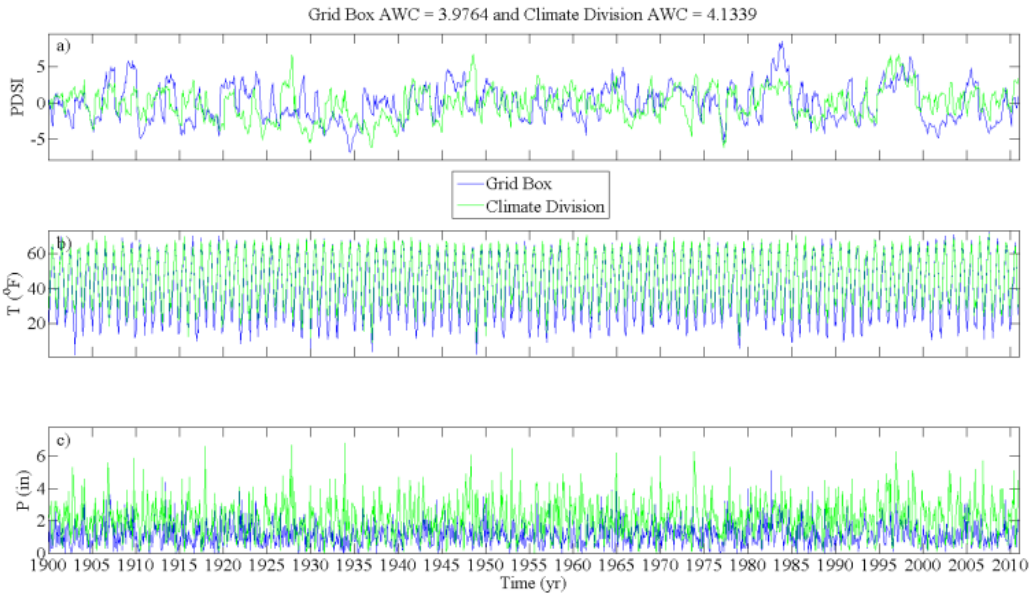

Notes: For this grid box-climate division pair, the average positive difference was ≥ 2, and the average negative difference was ≤ -2.

Figure A.1 | For the grid box located at +45.25, -115.75 and Idaho climate division 4: a) PDSI time series; b) temperature time series, and c) precipitation time series.

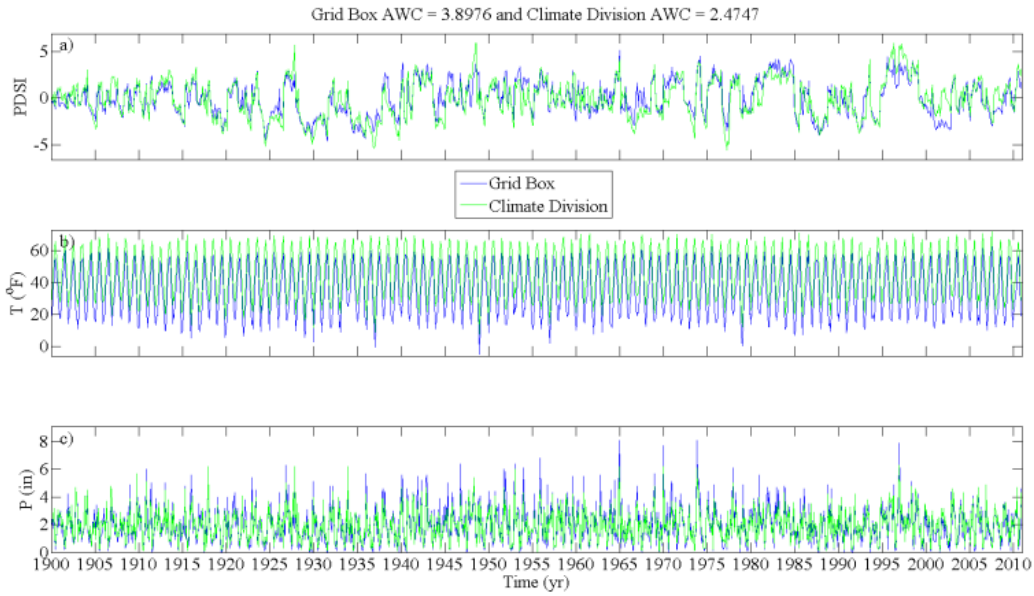

Notes: For this grid box-climate division pair, the average positive and negative differences were between -1 and 1.

Figure A.2 | For the grid box located at +42.25, -11.25 and Idaho climate division 10: a) PDSI time series; b) temperature time series, and c) precipitation time series.

APPENDIX B

CONTINUOUS WAVELET, CROSS WAVELET, AND WAVELET COHERENCE PLOTS

This Appendix contains the additional continuous wavelet transform, cross wavelet transform, and wavelet coherence plots for the grid boxes within the study area (described in Chapter 2, Sections 2.2.1-2.2.2).

B.1. Additional Continuous Wavelet Transform Plots

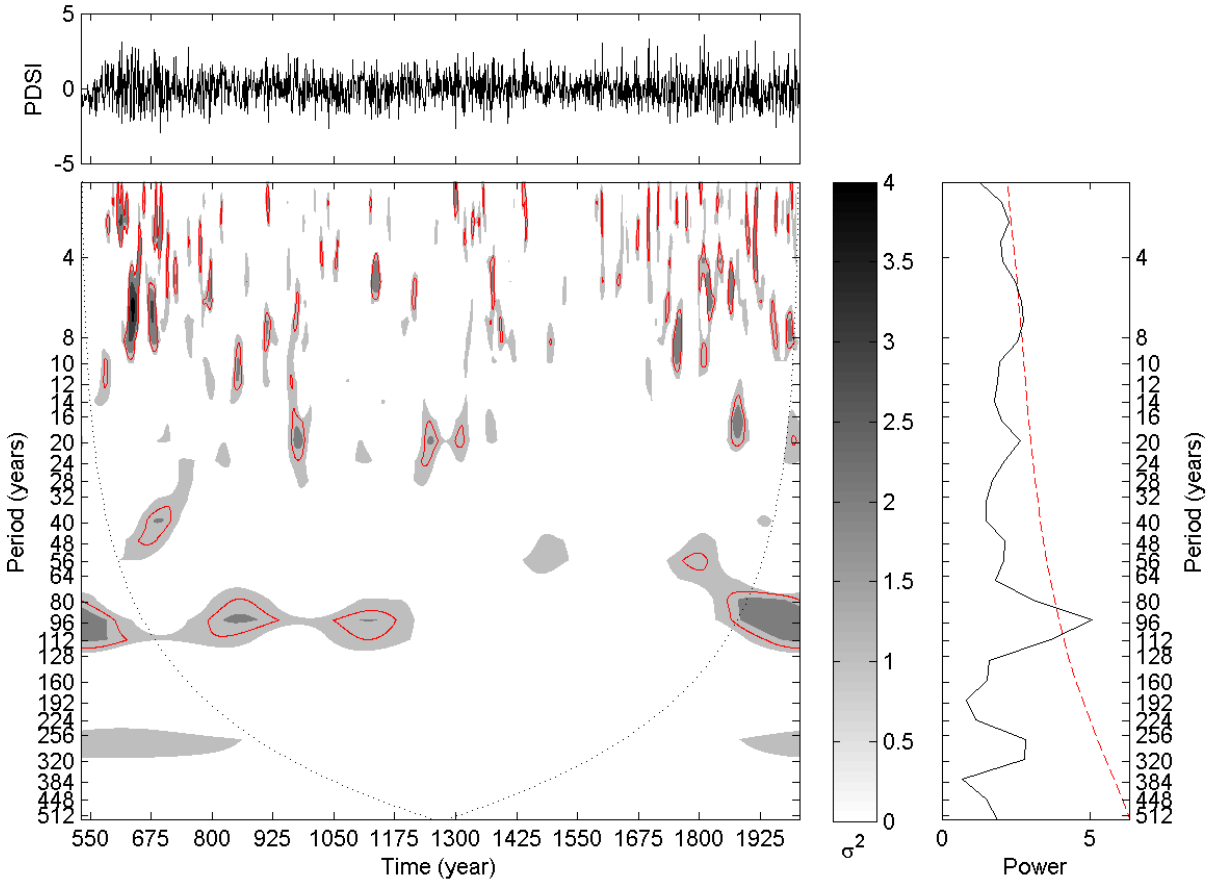

Notes: The black dotted outline on the continuous wavelet spectrum represents the COI. The 5% significance level against red noise is shown as a thin red contour on the continuous wavelet spectrum. The dashed red line on the global wavelet spectrum denotes the 95% confidence level.

Figure B.1 | Detrended reconstructed PDSI time series (top), continuous wavelet spectrum (bottom), and global wavelet spectrum (right) for grid number 25 of the *Cook et al.* [2008] dataset.

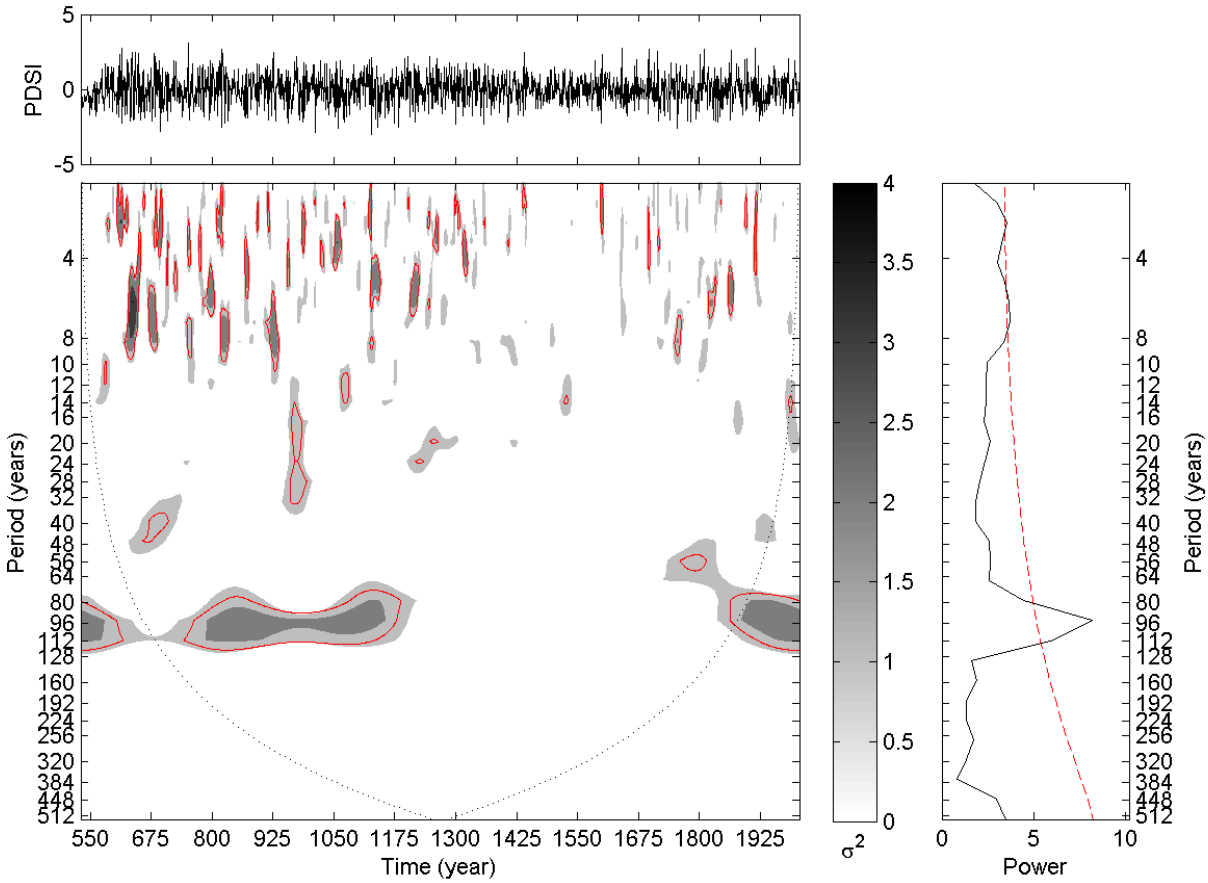

Notes: The black dotted outline on the continuous wavelet spectrum represents the COI. The 5% significance level against red noise is shown as a thin red contour on the continuous wavelet spectrum. The dashed red line on the global wavelet spectrum denotes the 95% confidence level.

Figure B.2 | Detrended reconstructed PDSI time series (top), continuous wavelet spectrum (bottom), and global wavelet spectrum (right) for grid number 33 of the *Cook et al.* [2008] dataset.

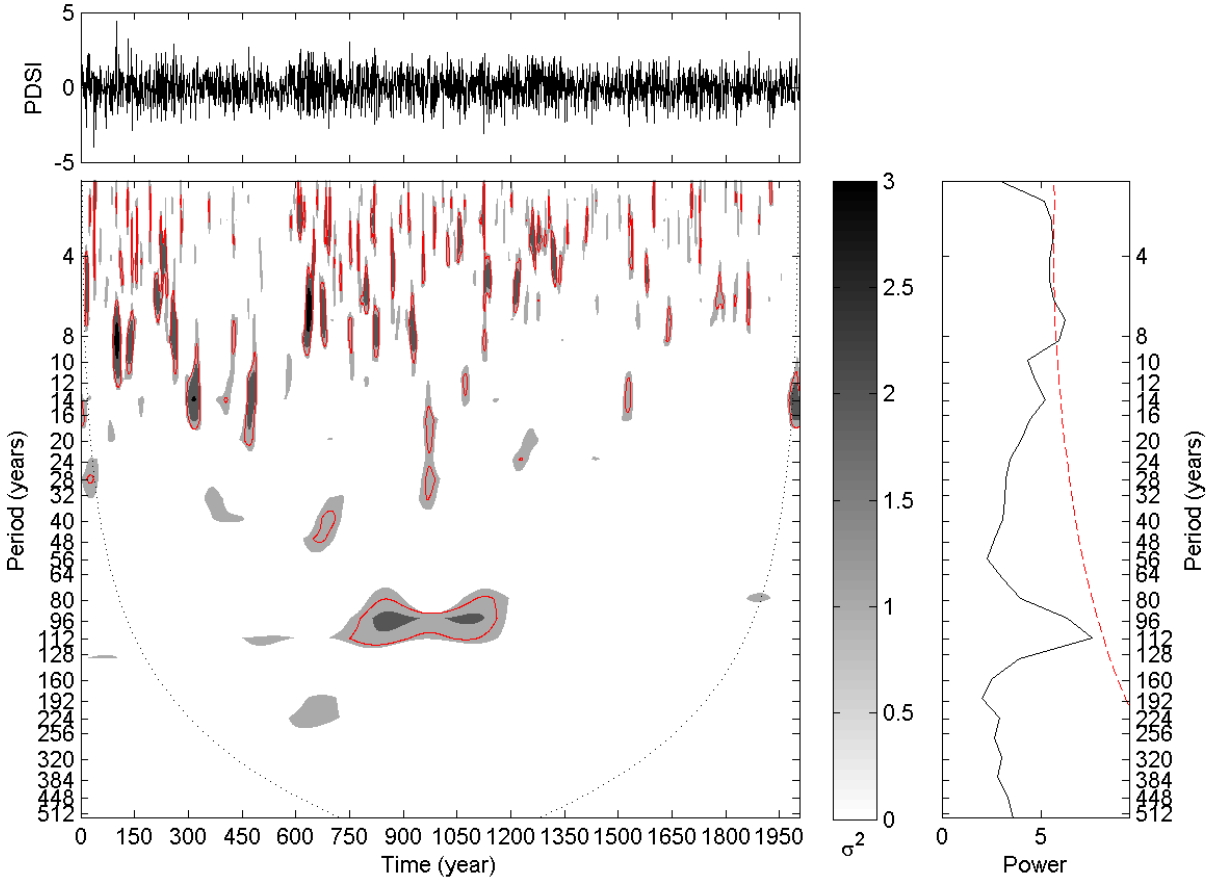

Notes: The black dotted outline on the continuous wavelet spectrum represents the COI. The 5% significance level against red noise is shown as a thin red contour on the continuous wavelet spectrum. The dashed red line on the global wavelet spectrum denotes the 95% confidence level.

Figure B.3 | Detrended reconstructed PDSI time series (top), continuous wavelet spectrum (bottom), and global wavelet spectrum (right) for grid number 34 of the *Cook et al.* [2008] dataset.

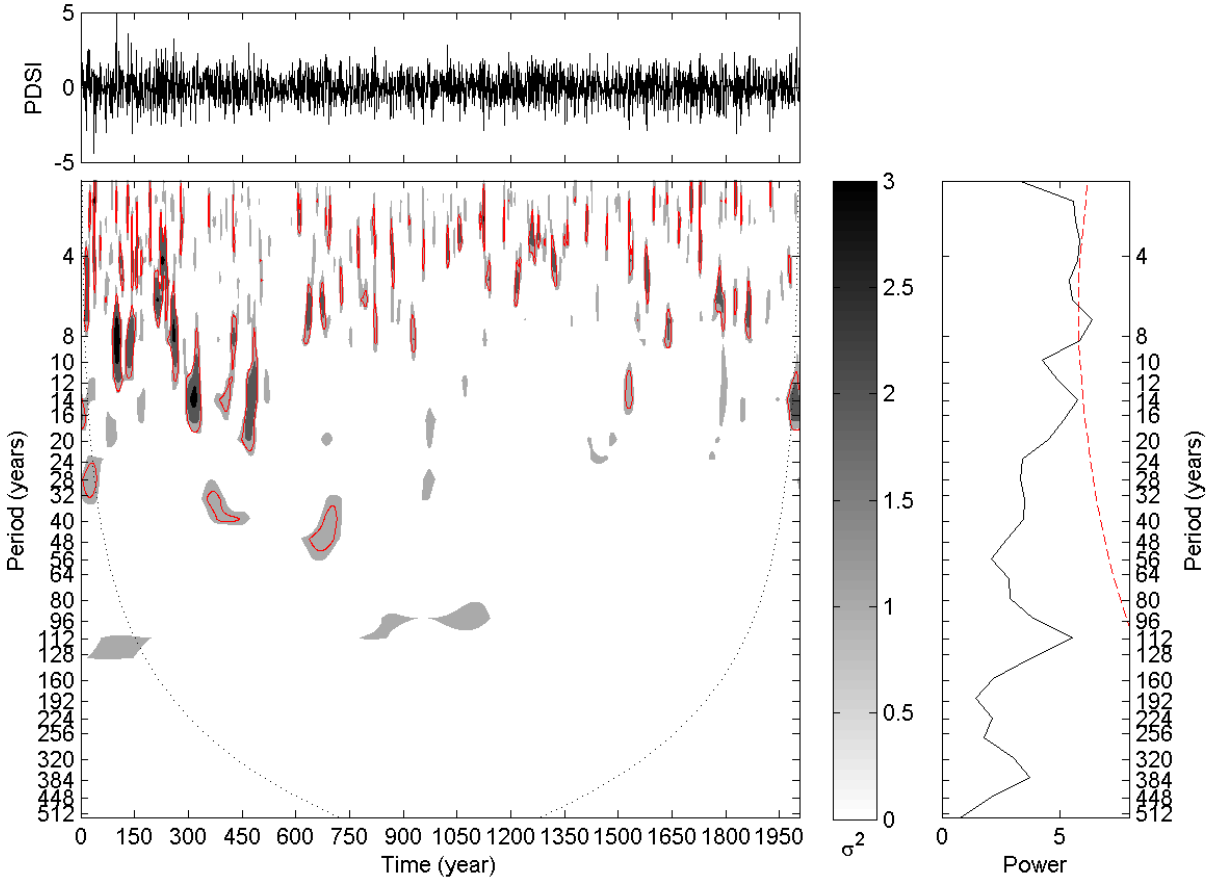

Notes: The black dotted outline on the continuous wavelet spectrum represents the COI. The 5% significance level against red noise is shown as a thin red contour on the continuous wavelet spectrum. The dashed red line on the global wavelet spectrum denotes the 95% confidence level.

Figure B.4 | Detrended reconstructed PDSI time series (top), continuous wavelet spectrum (bottom), and global wavelet spectrum (right) for grid number 35 of the *Cook et al.* [2008] dataset.

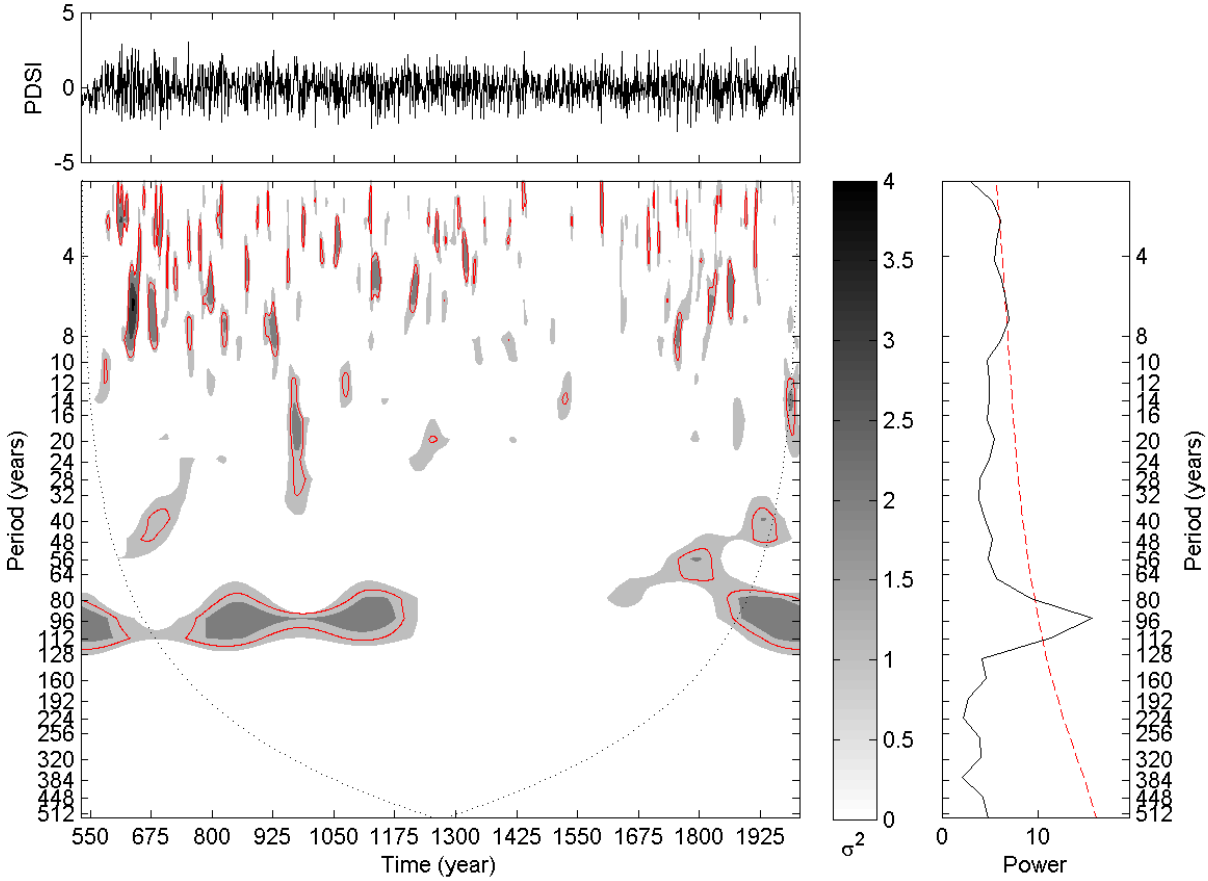

Notes: The black dotted outline on the continuous wavelet spectrum represents the COI. The 5% significance level against red noise is shown as a thin red contour on the continuous wavelet spectrum. The dashed red line on the global wavelet spectrum denotes the 95% confidence level.

Figure B.5 | Detrended reconstructed PDSI time series (top), continuous wavelet spectrum (bottom), and global wavelet spectrum (right) for grid number 43 of the *Cook et al.* [2008] dataset.

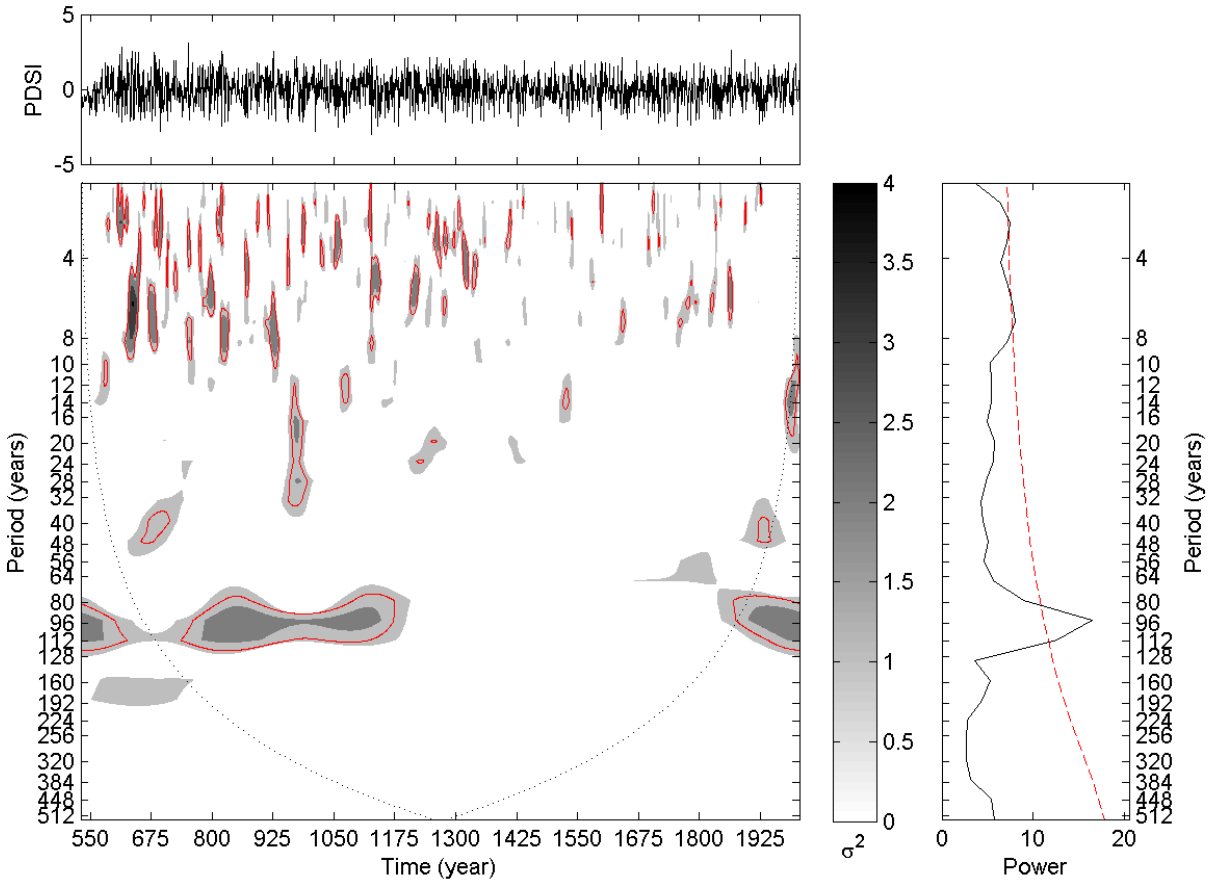

Notes: The black dotted outline on the continuous wavelet spectrum represents the COI. The 5% significance level against red noise is shown as a thin red contour on the continuous wavelet spectrum. The dashed red line on the global wavelet spectrum denotes the 95% confidence level.

Figure B.6 | Detrended reconstructed PDSI time series (top), continuous wavelet spectrum (bottom), and global wavelet spectrum (right) for grid number 44 of the *Cook et al.* [2008] dataset.

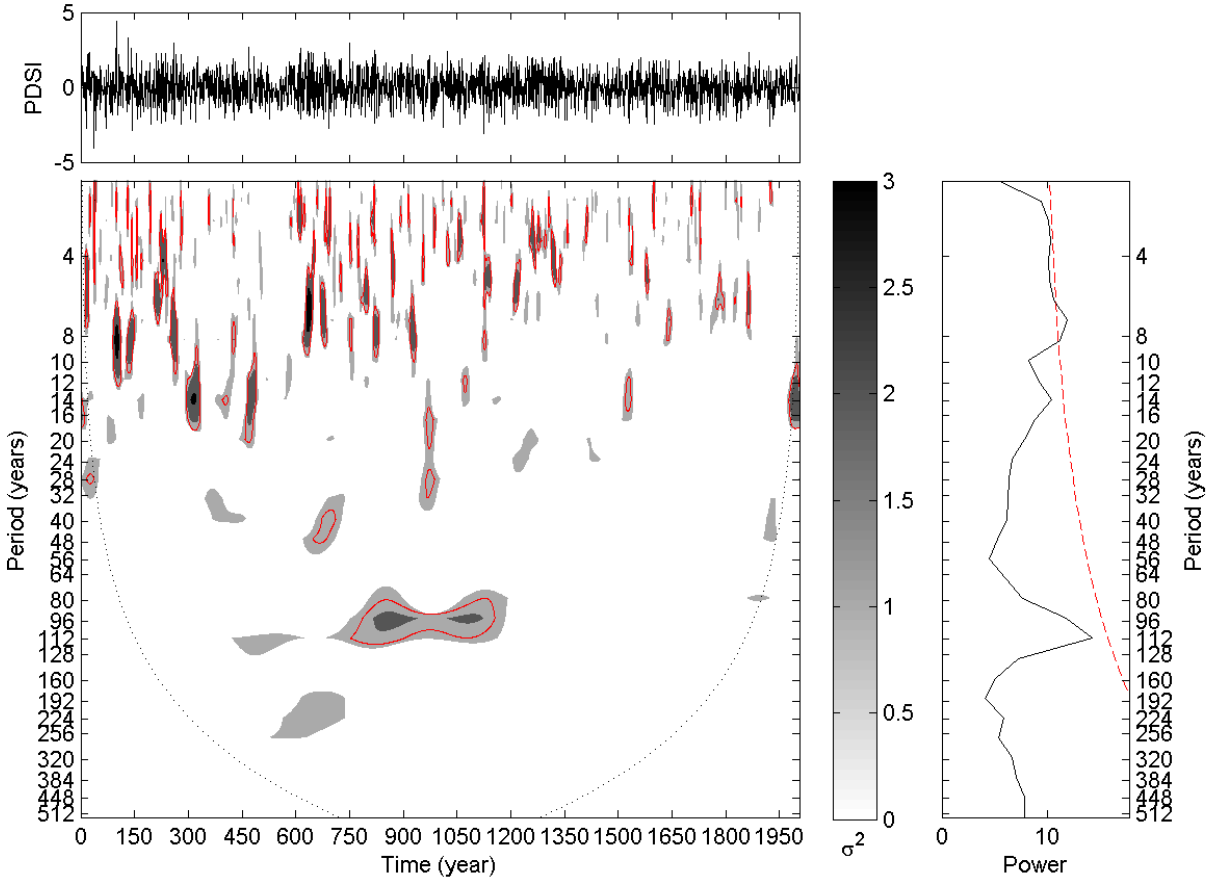

Notes: The black dotted outline on the continuous wavelet spectrum represents the COI. The 5% significance level against red noise is shown as a thin red contour on the continuous wavelet spectrum. The dashed red line on the global wavelet spectrum denotes the 95% confidence level.

Figure B.7 | Detrended reconstructed PDSI time series (top), continuous wavelet spectrum (bottom), and global wavelet spectrum (right) for grid number 45 of the *Cook et al.* [2008] dataset.

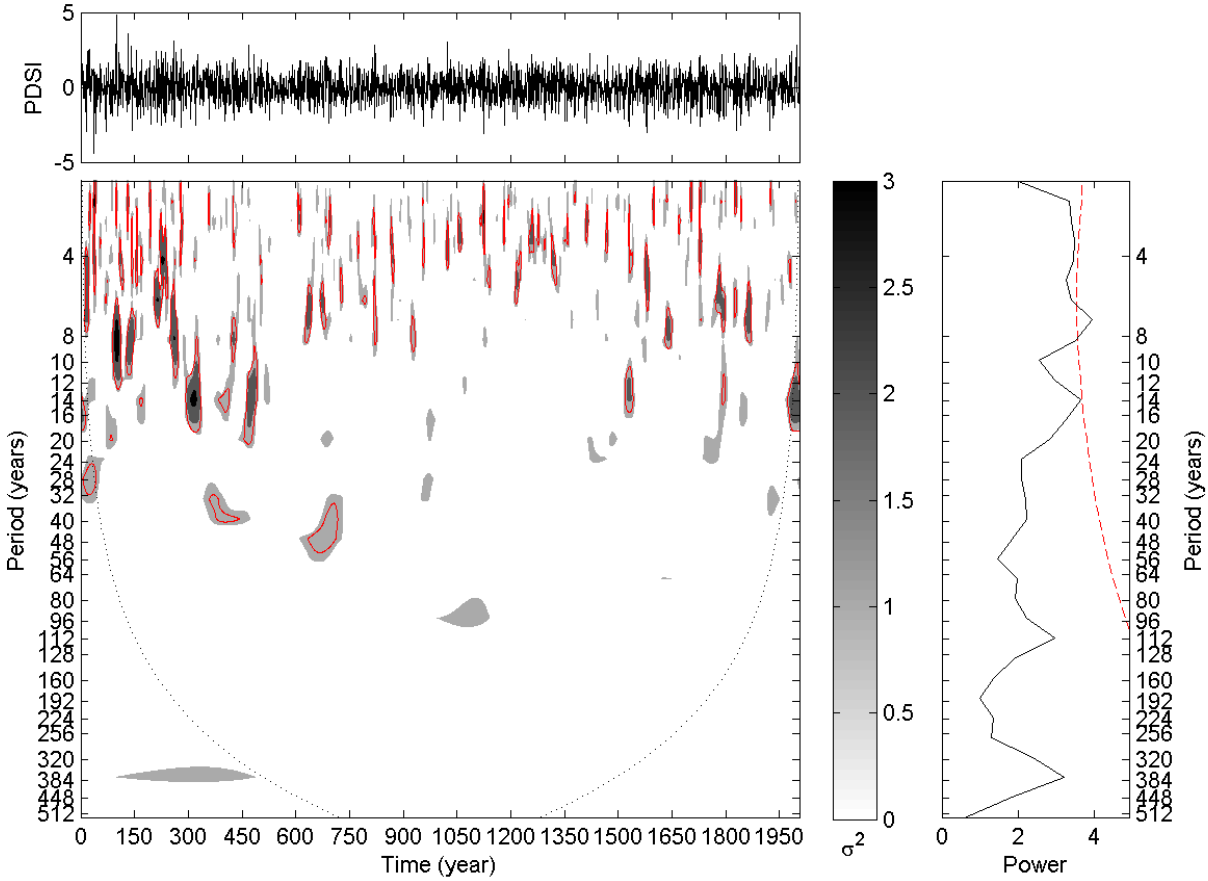

Notes: The black dotted outline on the continuous wavelet spectrum represents the COI. The 5% significance level against red noise is shown as a thin red contour on the continuous wavelet spectrum. The dashed red line on the global wavelet spectrum denotes the 95% confidence level.

Figure B.8 | Detrended reconstructed PDSI time series (top), continuous wavelet spectrum (bottom), and global wavelet spectrum (right) for grid number 46 of the *Cook et al.* [2008] dataset.

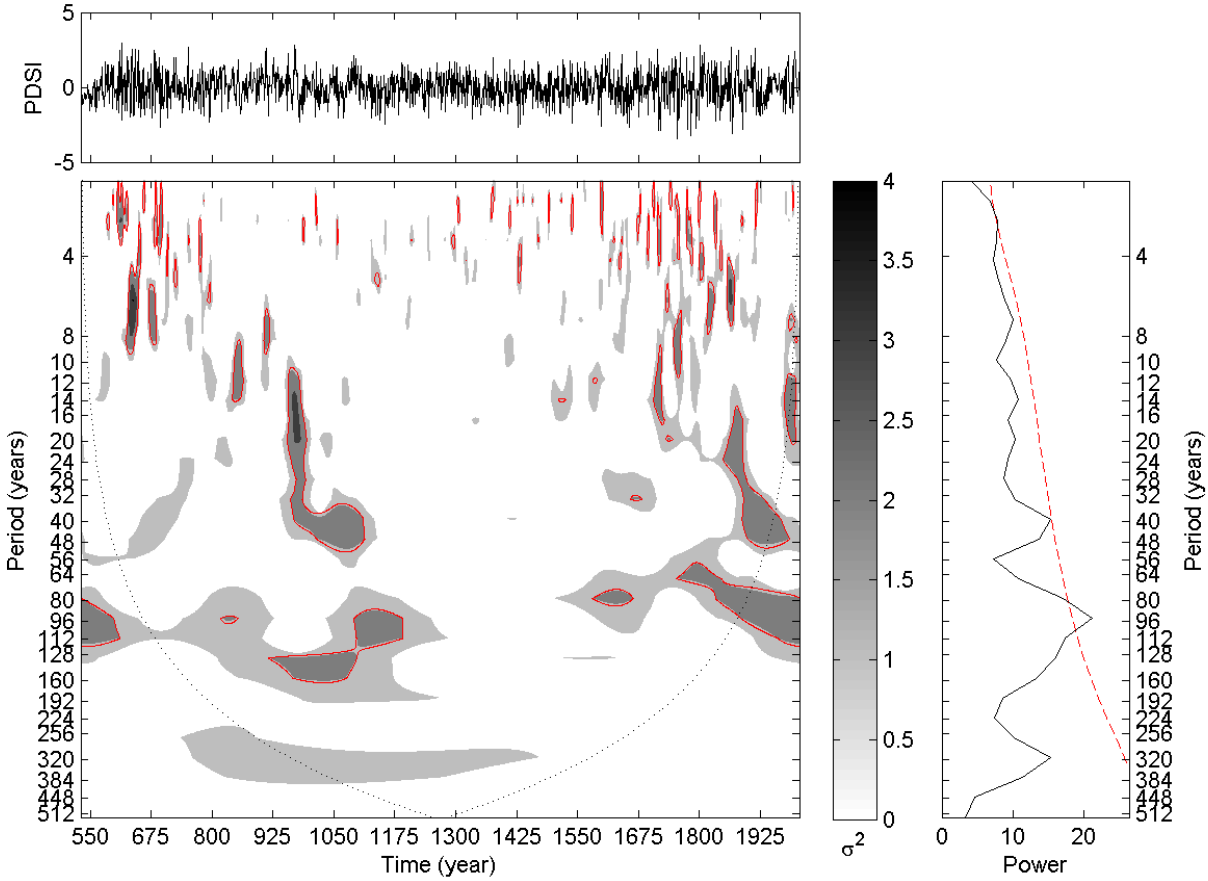

Notes: The black dotted outline on the continuous wavelet spectrum represents the COI. The 5% significance level against red noise is shown as a thin red contour on the continuous wavelet spectrum. The dashed red line on the global wavelet spectrum denotes the 95% confidence level.

Figure B.9 | Detrended reconstructed PDSI time series (top), continuous wavelet spectrum (bottom), and global wavelet spectrum (right) for grid number 55 of the *Cook et al.* [2008] dataset.

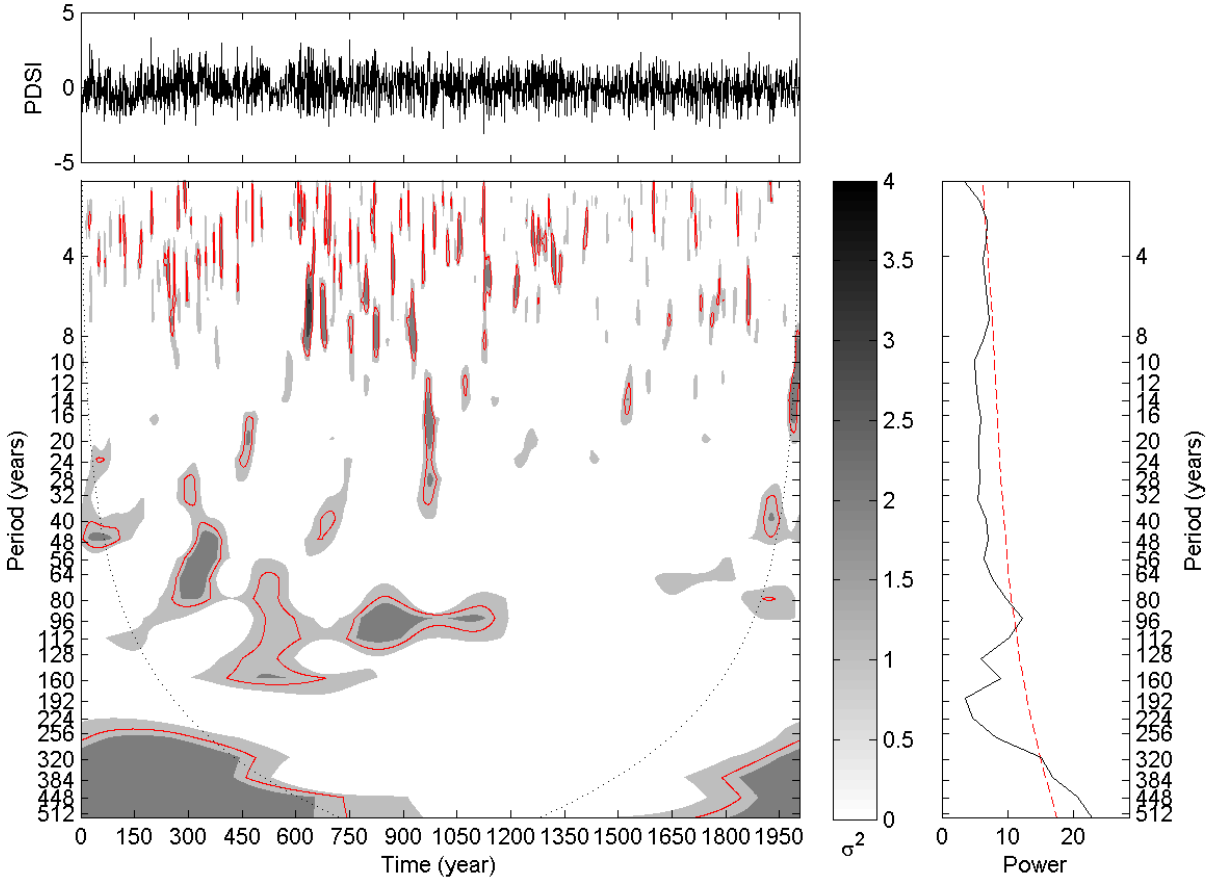

Notes: The black dotted outline on the continuous wavelet spectrum represents the COI. The 5% significance level against red noise is shown as a thin red contour on the continuous wavelet spectrum. The dashed red line on the global wavelet spectrum denotes the 95% confidence level.

Figure B.10 | Detrended reconstructed PDSI time series (top), continuous wavelet spectrum (bottom), and global wavelet spectrum (right) for grid number 56 of the *Cook et al.* [2008] dataset.

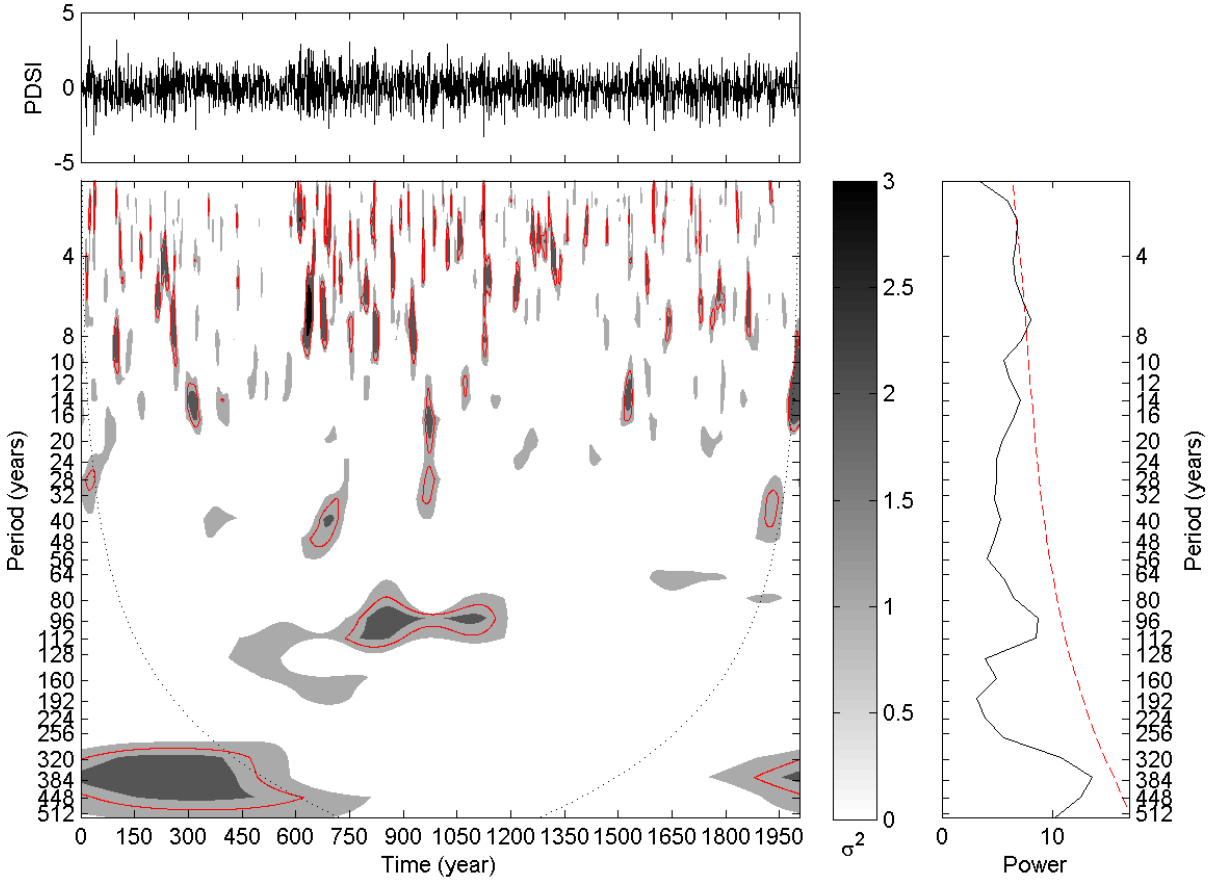

Notes: The black dotted outline on the continuous wavelet spectrum represents the COI. The 5% significance level against red noise is shown as a thin red contour on the continuous wavelet spectrum. The dashed red line on the global wavelet spectrum denotes the 95% confidence level.

Figure B.11 | Detrended reconstructed PDSI time series (top), continuous wavelet spectrum (bottom), and global wavelet spectrum (right) for grid number 57 of the *Cook et al.* [2008] dataset.

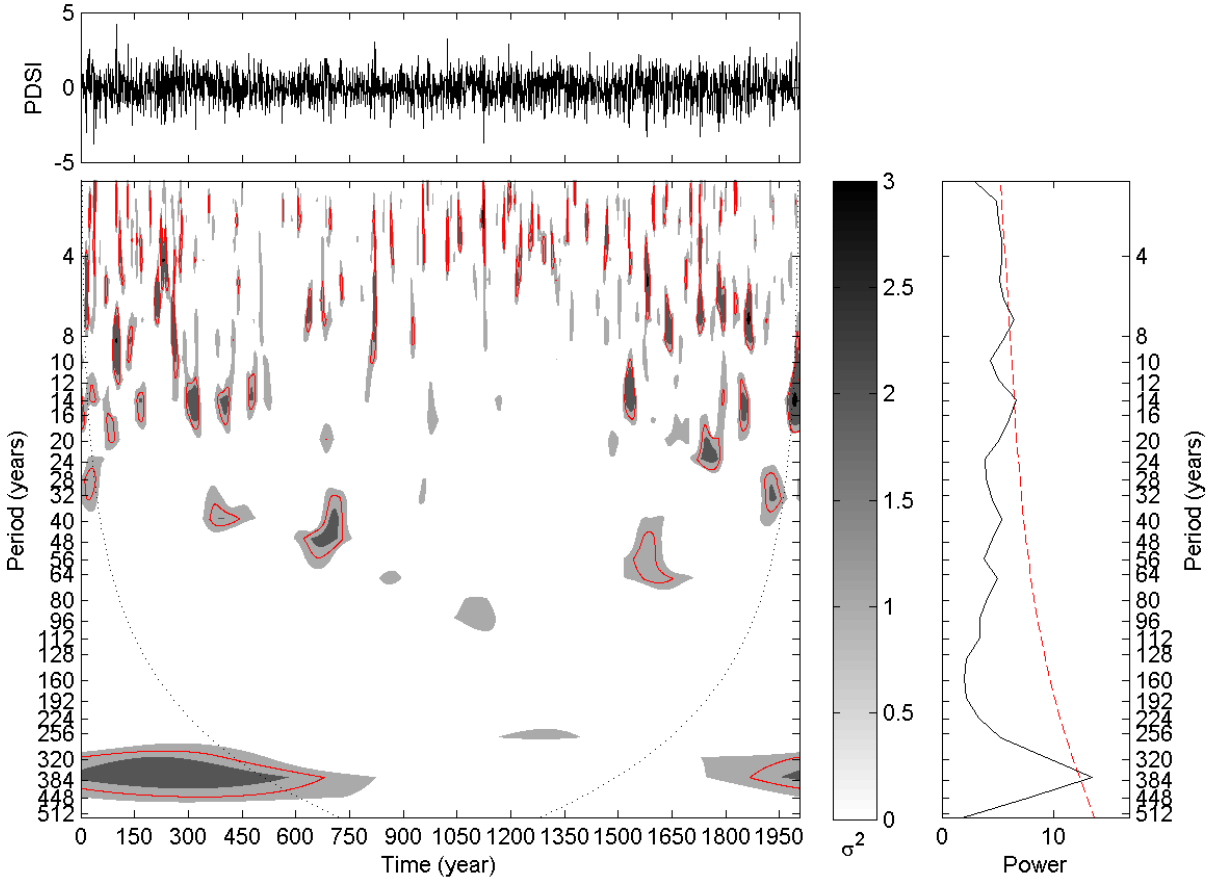

Notes: The black dotted outline on the continuous wavelet spectrum represents the COI. The 5% significance level against red noise is shown as a thin red contour on the continuous wavelet spectrum. The dashed red line on the global wavelet spectrum denotes the 95% confidence level.

Figure B.12 | Detrended reconstructed PDSI time series (top), continuous wavelet spectrum (bottom), and global wavelet spectrum (right) for grid number 58 of the *Cook et al.* [2008] dataset.

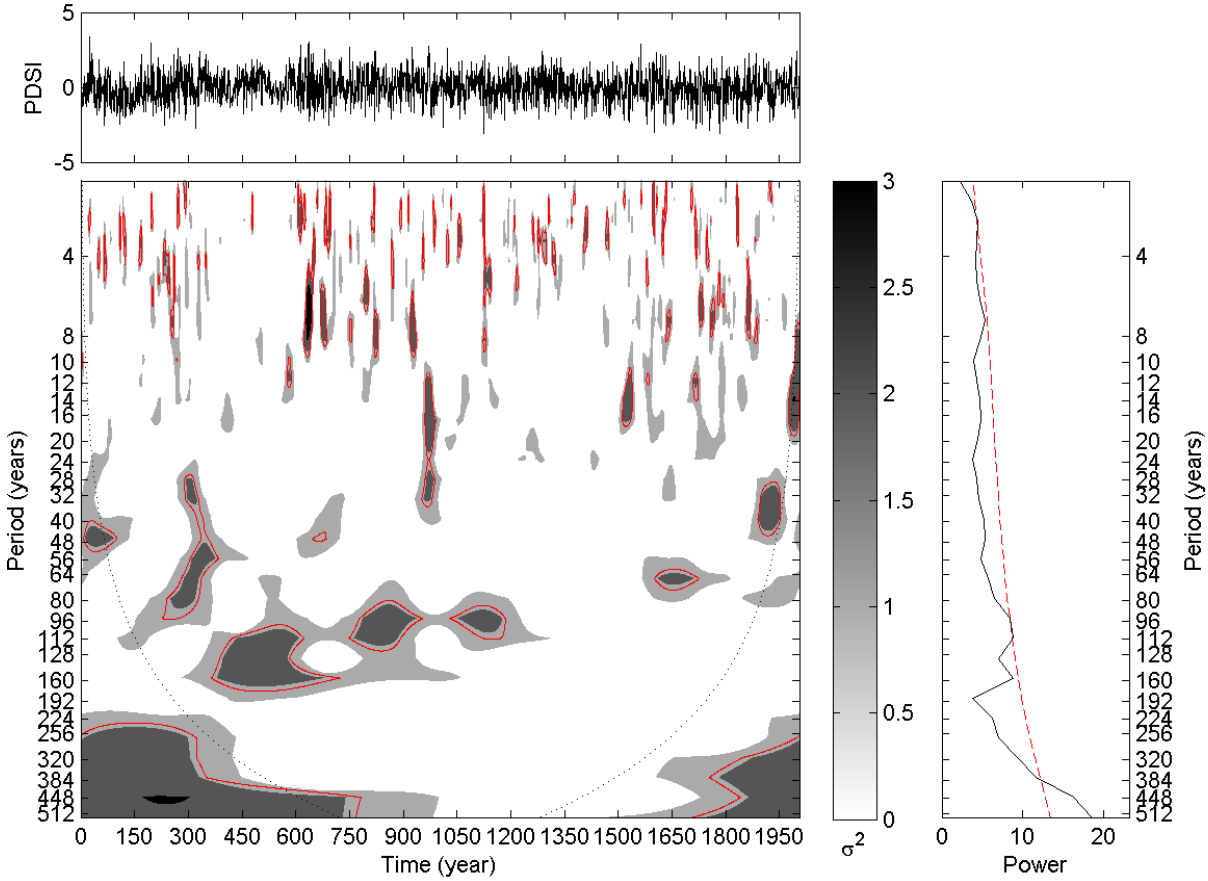

Notes: The black dotted outline on the continuous wavelet spectrum represents the COI. The 5% significance level against red noise is shown as a thin red contour on the continuous wavelet spectrum. The dashed red line on the global wavelet spectrum denotes the 95% confidence level.

Figure B.13 | Detrended reconstructed PDSI time series (top), continuous wavelet spectrum (bottom), and global wavelet spectrum (right) for grid number 69 of the *Cook et al.* [2008] dataset.

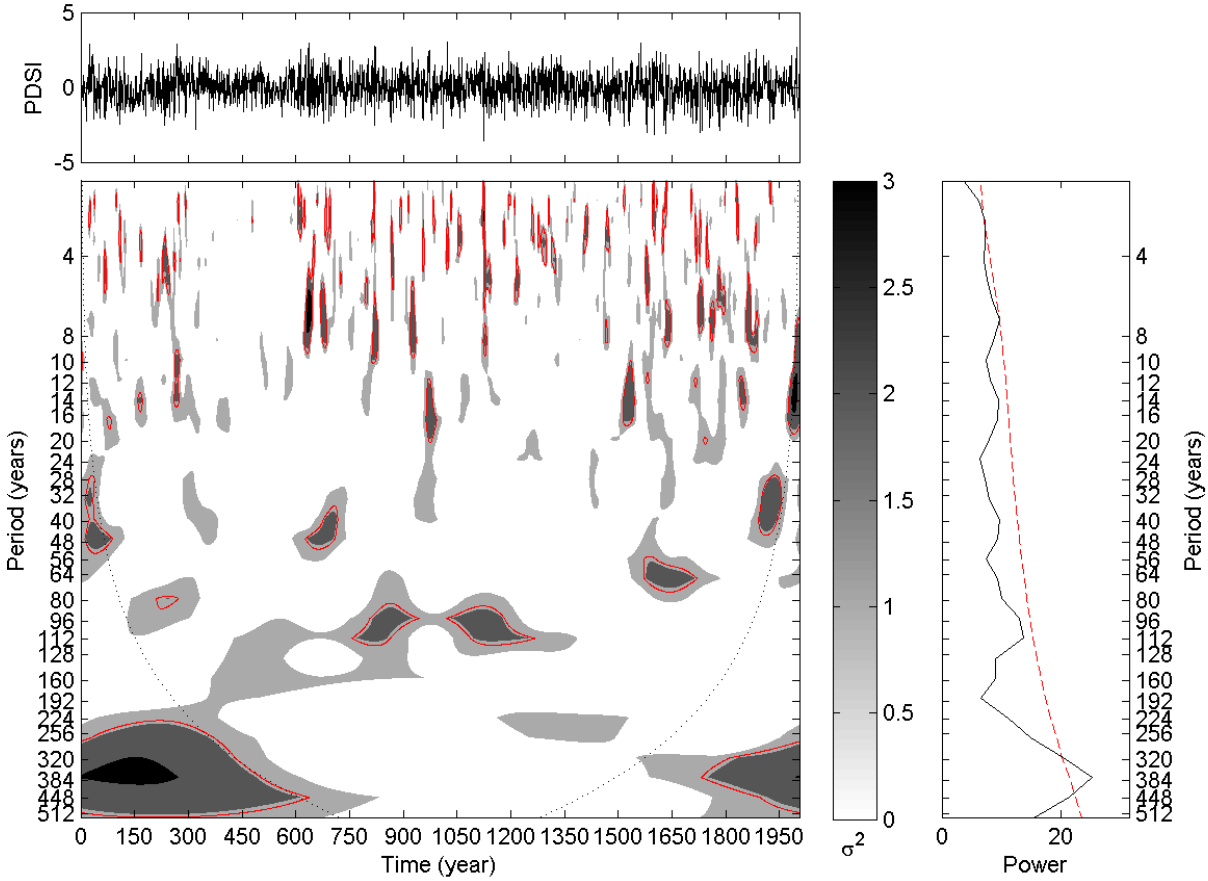

Notes: The black dotted outline on the continuous wavelet spectrum represents the COI. The 5% significance level against red noise is shown as a thin red contour on the continuous wavelet spectrum. The dashed red line on the global wavelet spectrum denotes the 95% confidence level.

Figure B.14 | Detrended reconstructed PDSI time series (top), continuous wavelet spectrum (bottom), and global wavelet spectrum (right) for grid number 70 of the *Cook et al.* [2008] dataset.

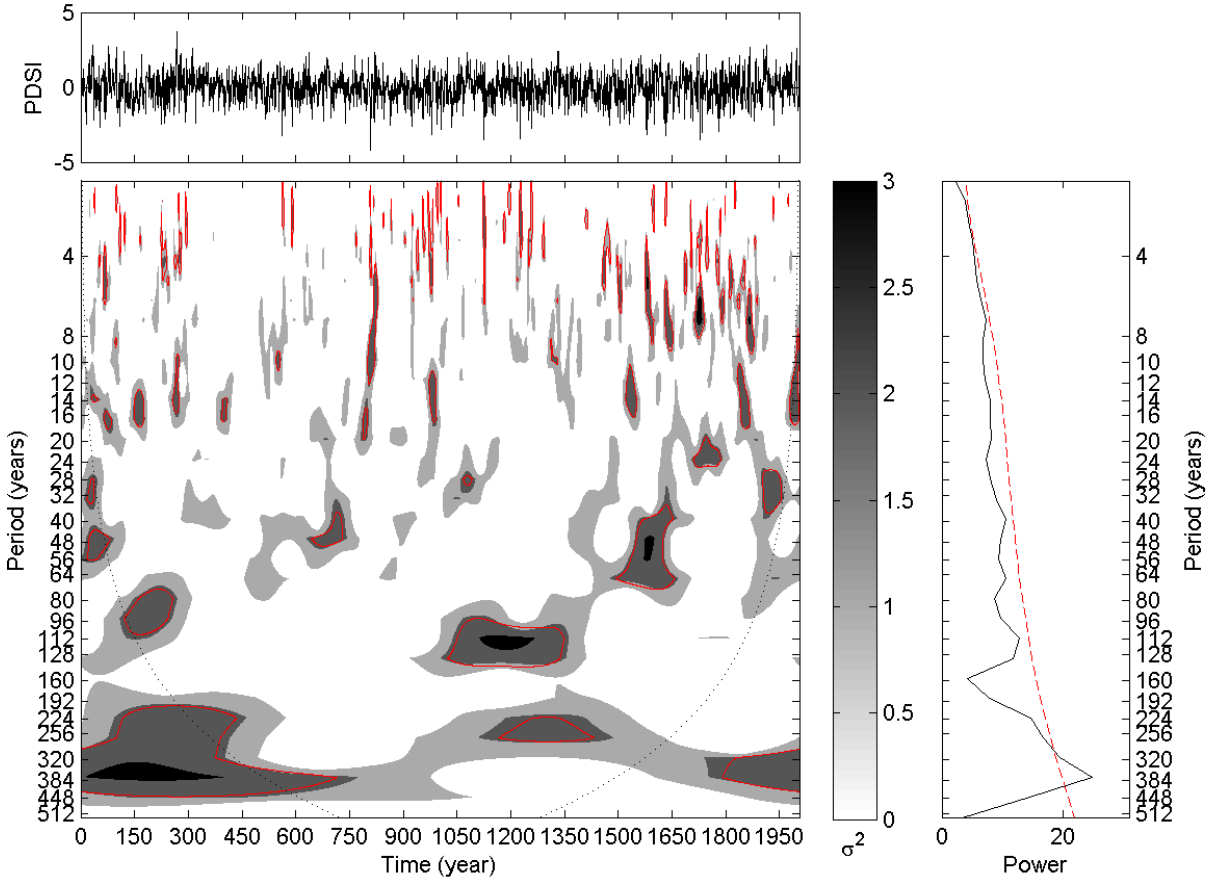

Notes: The black dotted outline on the continuous wavelet spectrum represents the COI. The 5% significance level against red noise is shown as a thin red contour on the continuous wavelet spectrum. The dashed red line on the global wavelet spectrum denotes the 95% confidence level.

Figure B.15 | Detrended reconstructed PDSI time series (top), continuous wavelet spectrum (bottom), and global wavelet spectrum (right) for grid number 71 of the *Cook et al.* [2008] dataset.

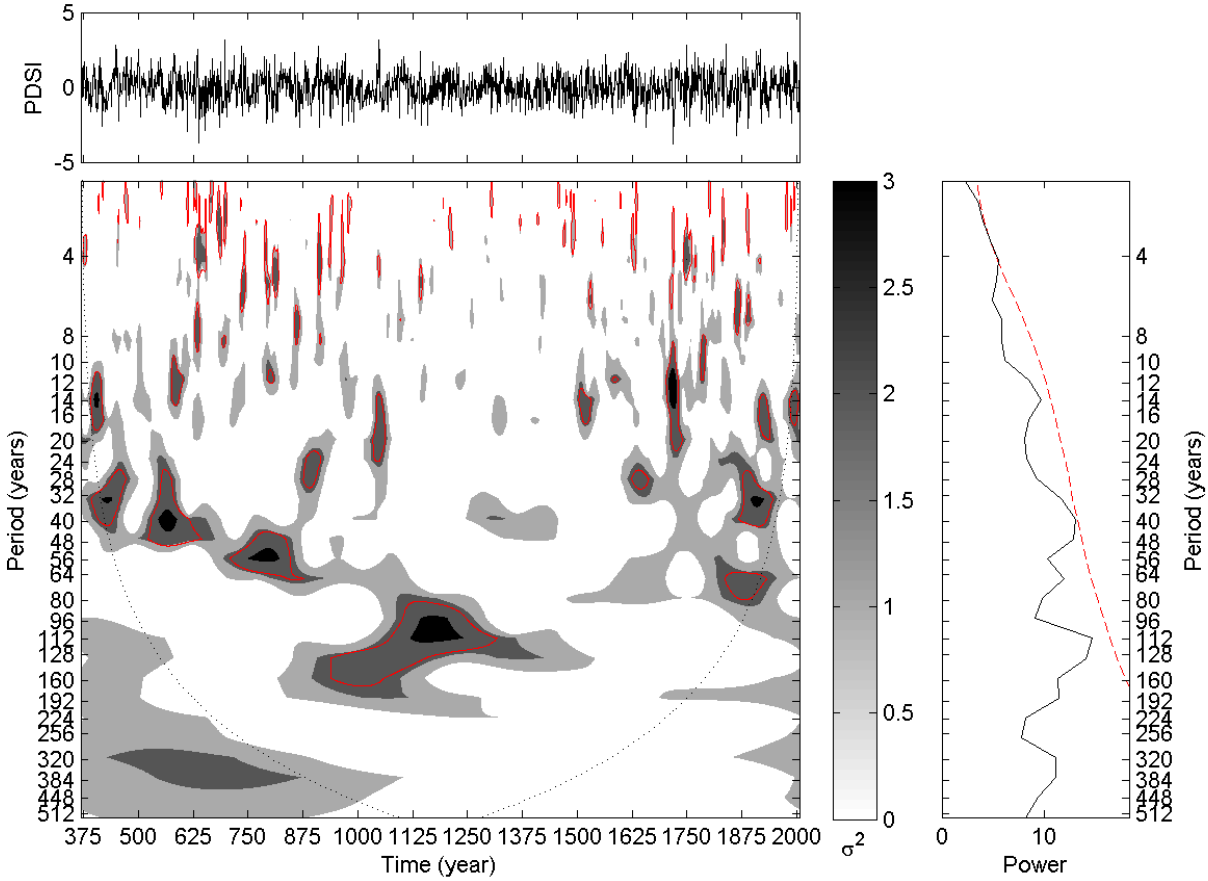

Notes: The black dotted outline on the continuous wavelet spectrum represents the COI. The 5% significance level against red noise is shown as a thin red contour on the continuous wavelet spectrum. The dashed red line on the global wavelet spectrum denotes the 95% confidence level.

Figure B.16 | Detrended reconstructed PDSI time series (top), continuous wavelet spectrum (bottom), and global wavelet spectrum (right) for grid number 83 of the *Cook et al.* [2008] dataset.

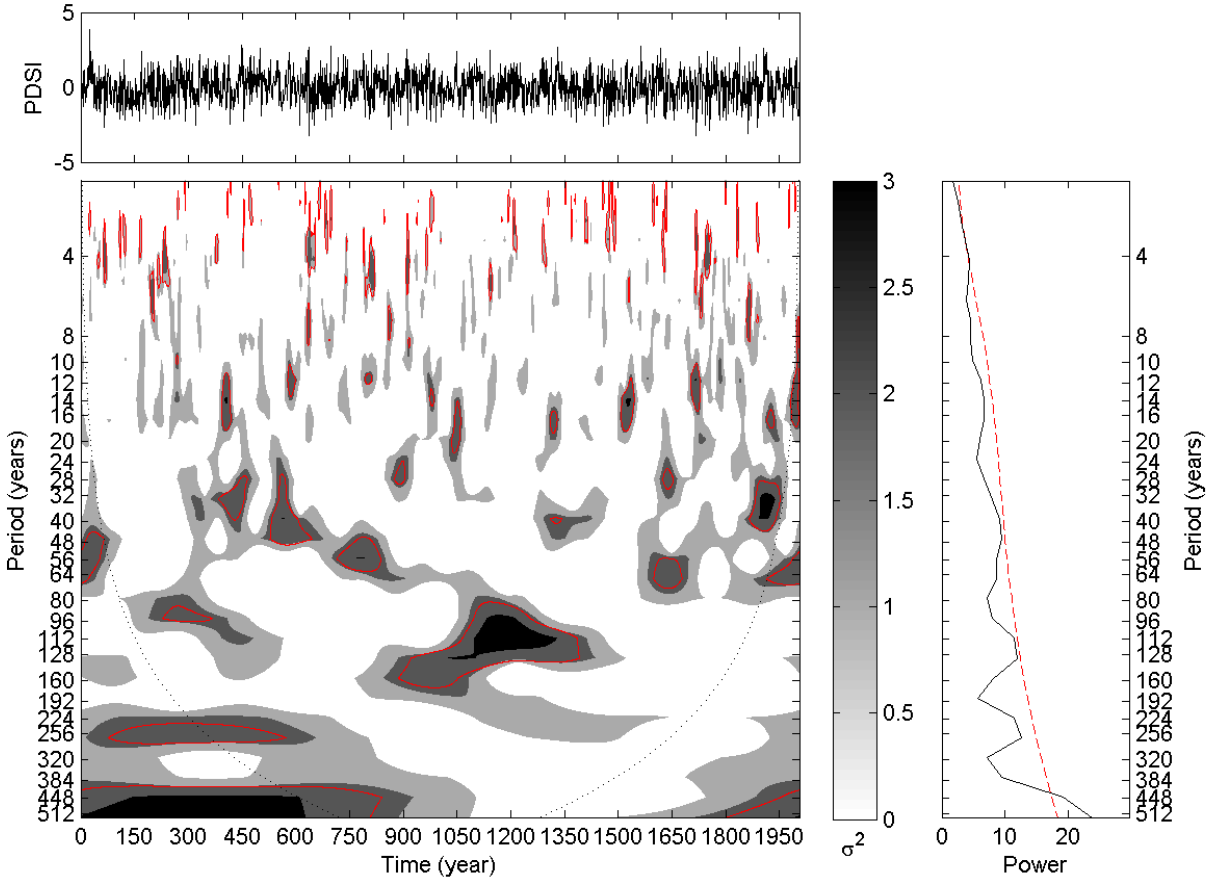

Notes: The black dotted outline on the continuous wavelet spectrum represents the COI. The 5% significance level against red noise is shown as a thin red contour on the continuous wavelet spectrum. The dashed red line on the global wavelet spectrum denotes the 95% confidence level.

Figure B.17 | Detrended reconstructed PDSI time series (top), continuous wavelet spectrum (bottom), and global wavelet spectrum (right) for grid number 84 of the *Cook et al.* [2008] dataset.

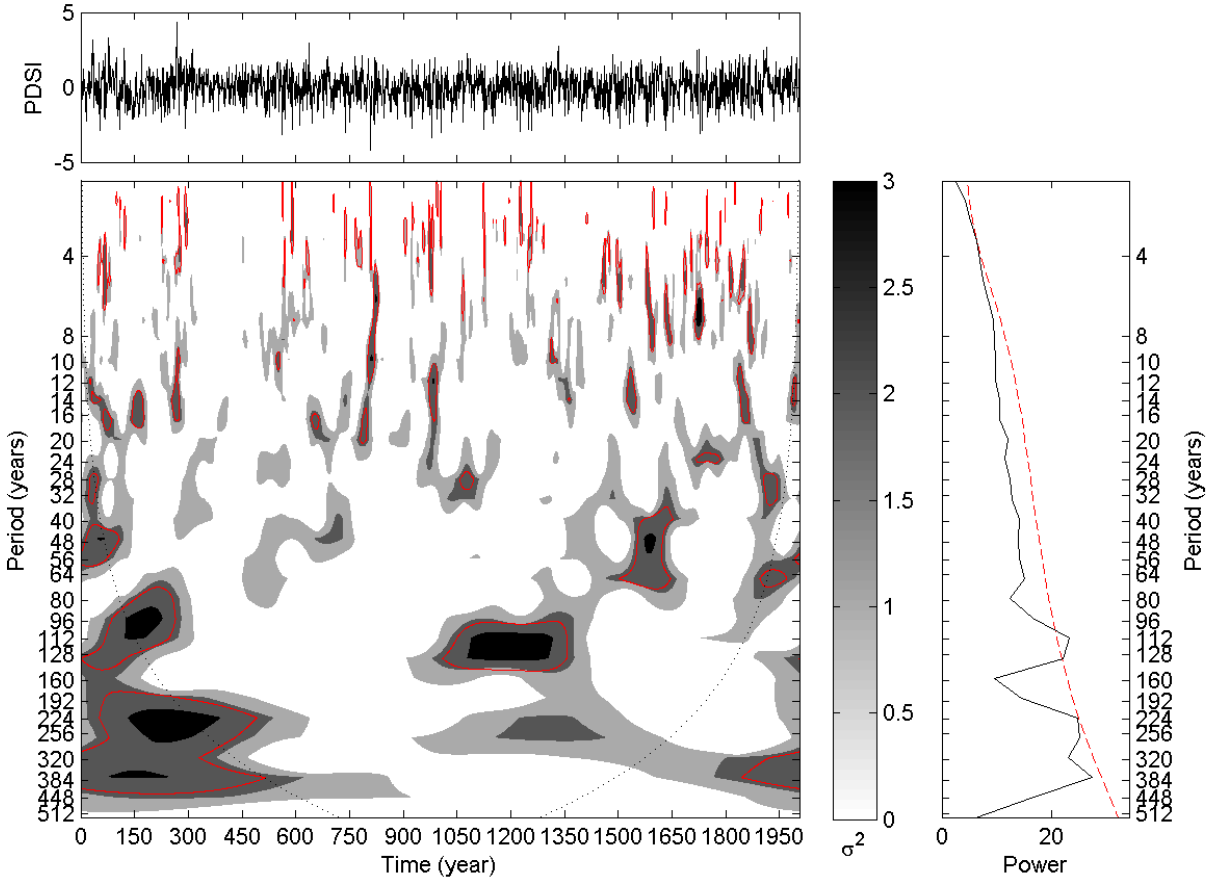

Notes: The black dotted outline on the continuous wavelet spectrum represents the COI. The 5% significance level against red noise is shown as a thin red contour on the continuous wavelet spectrum. The dashed red line on the global wavelet spectrum denotes the 95% confidence level.

Figure B.18 | Detrended reconstructed PDSI time series (top), continuous wavelet spectrum (bottom), and global wavelet spectrum (right) for grid number 86 of the *Cook et al.* [2008] dataset.

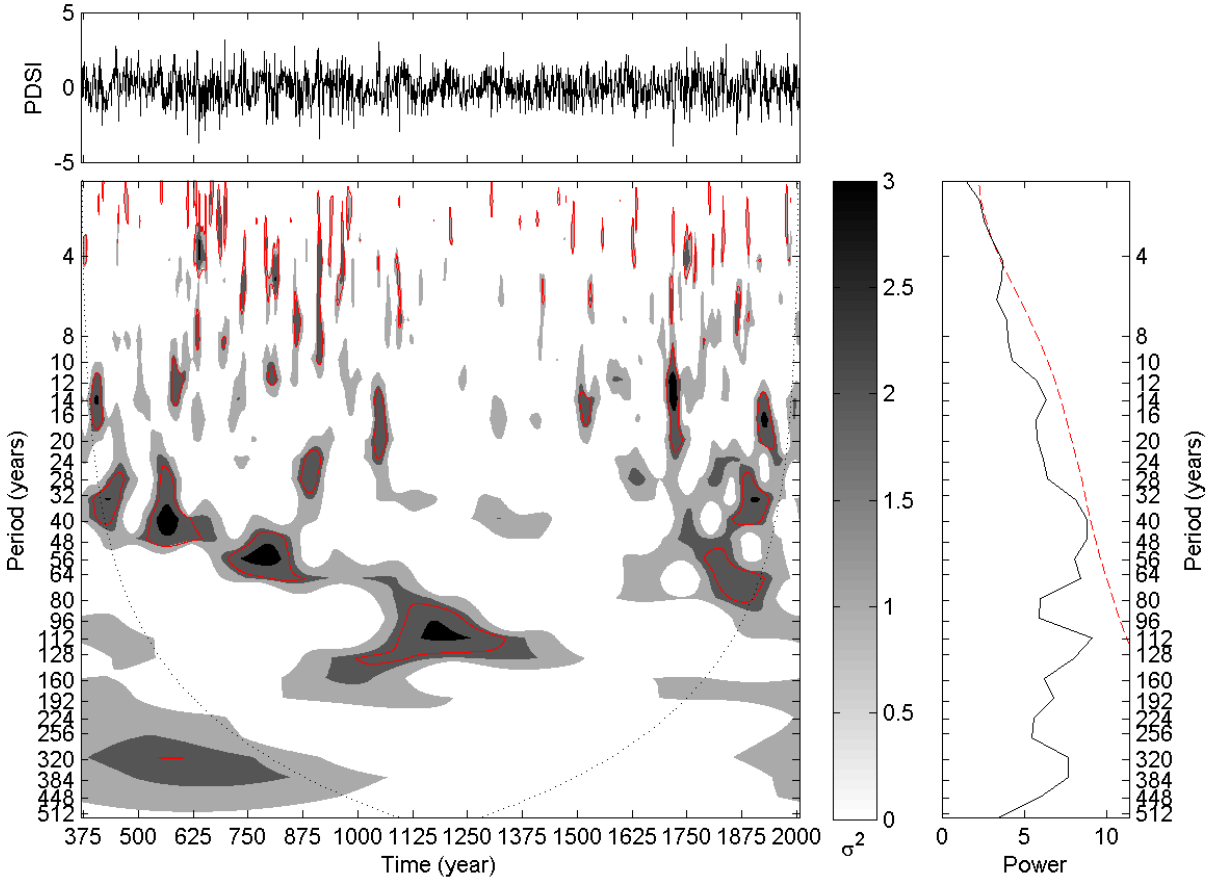

Notes: The black dotted outline on the continuous wavelet spectrum represents the COI. The 5% significance level against red noise is shown as a thin red contour on the continuous wavelet spectrum. The dashed red line on the global wavelet spectrum denotes the 95% confidence level.

Figure B.19 | Detrended reconstructed PDSI time series (top), continuous wavelet spectrum (bottom), and global wavelet spectrum (right) for grid number 99 of the *Cook et al.* [2008] dataset.

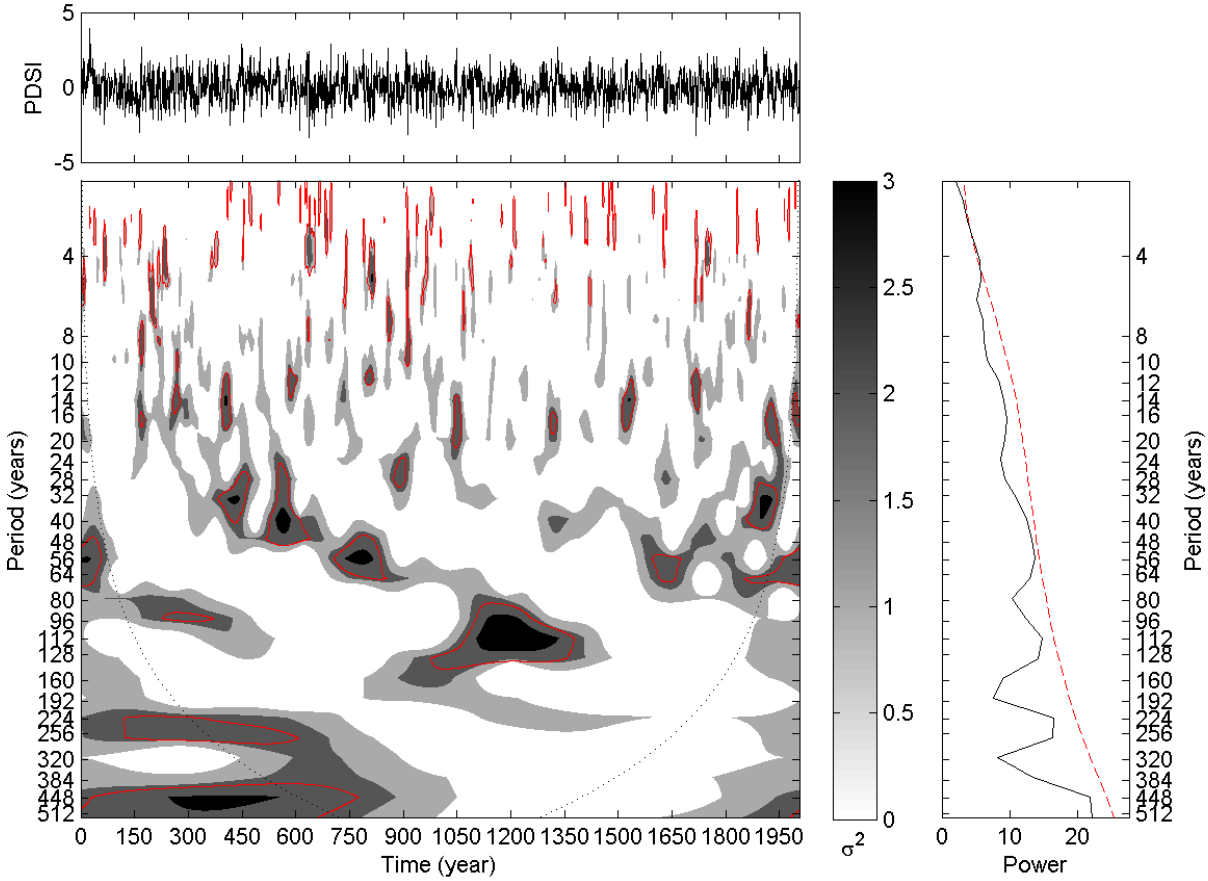

Notes: The black dotted outline on the continuous wavelet spectrum represents the COI. The 5% significance level against red noise is shown as a thin red contour on the continuous wavelet spectrum. The dashed red line on the global wavelet spectrum denotes the 95% confidence level.

Figure B.20 | Detrended reconstructed PDSI time series (top), continuous wavelet spectrum (bottom), and global wavelet spectrum (right) for grid number 100 of the *Cook et al.* [2008] dataset.

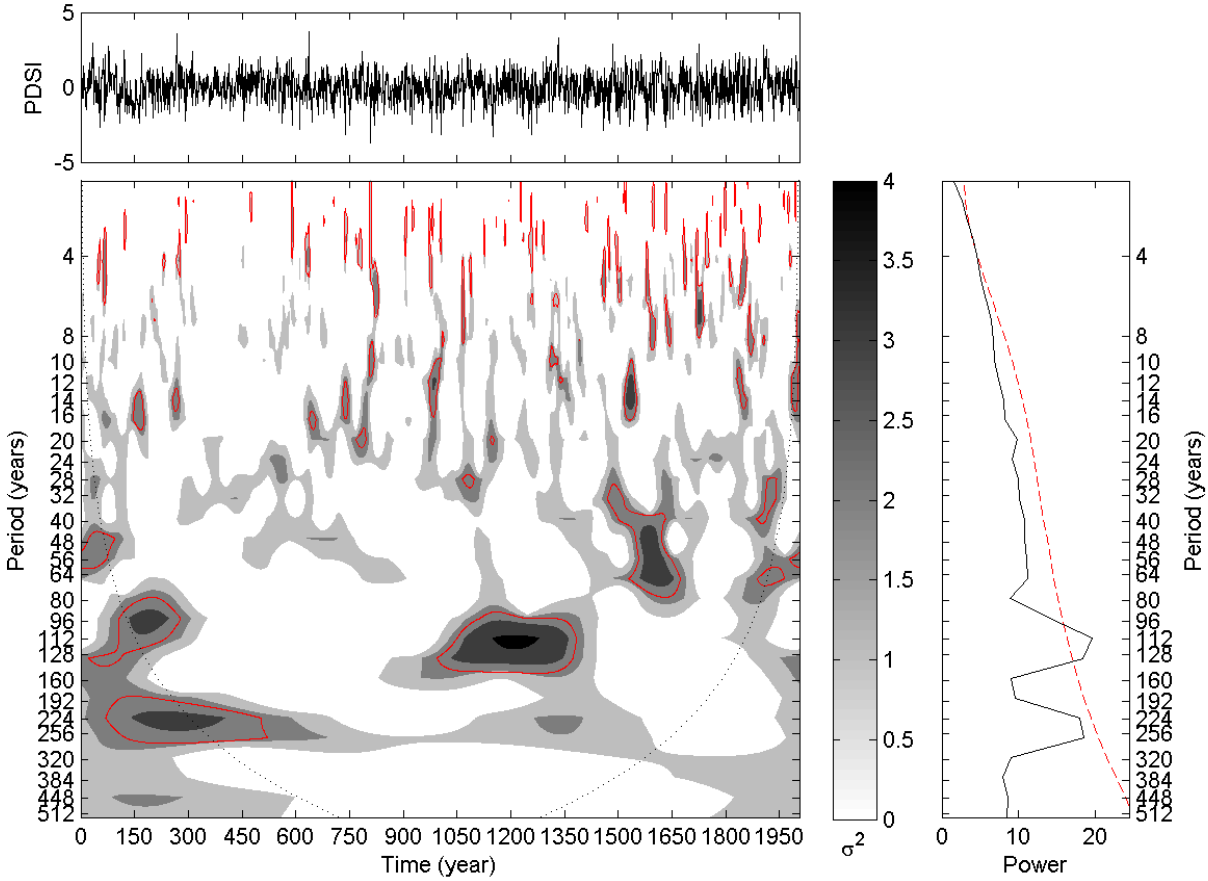

Notes: The black dotted outline on the continuous wavelet spectrum represents the COI. The 5% significance level against red noise is shown as a thin red contour on the continuous wavelet spectrum. The dashed red line on the global wavelet spectrum denotes the 95% confidence level.

Figure B.21 | Detrended reconstructed PDSI time series (top), continuous wavelet spectrum (bottom), and global wavelet spectrum (right) for grid number 101 of the *Cook et al.* [2008] dataset.

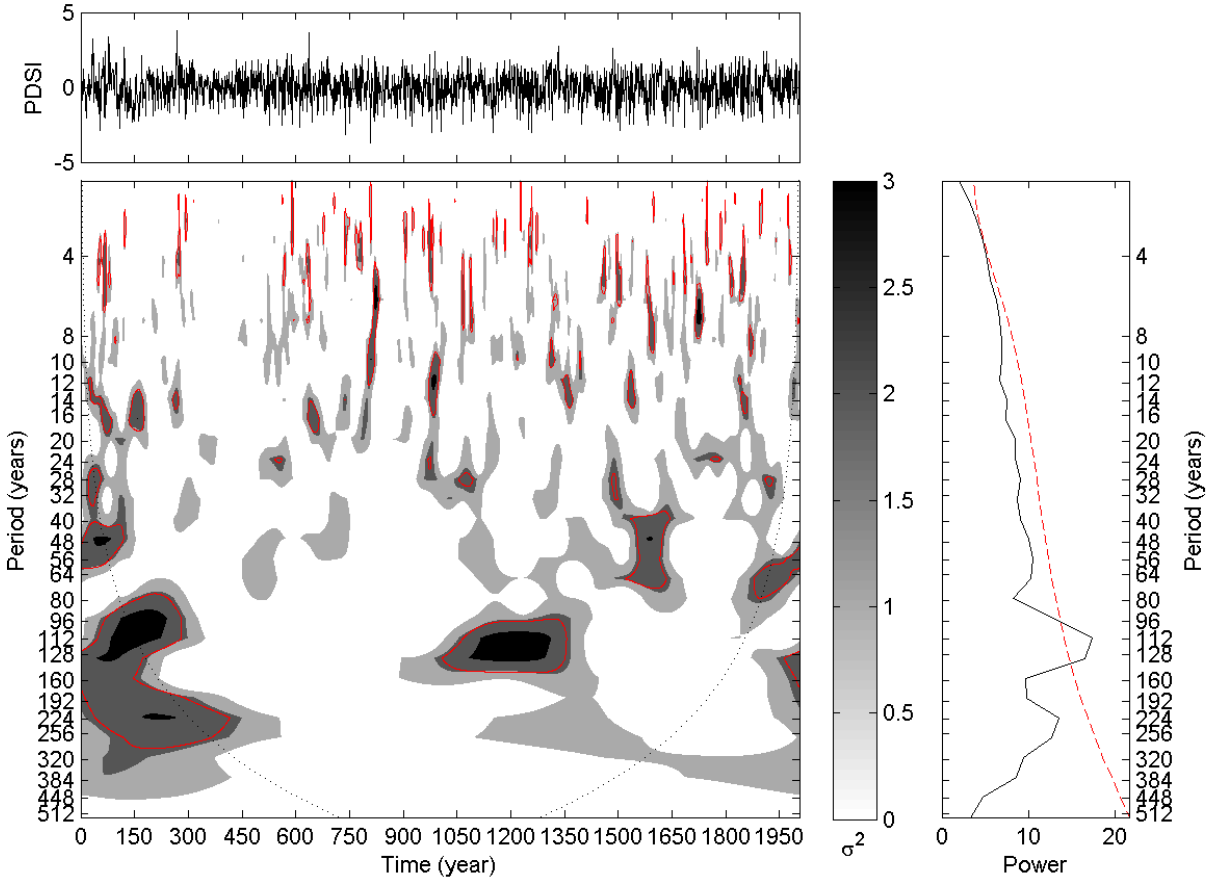

Notes: The black dotted outline on the continuous wavelet spectrum represents the COI. The 5% significance level against red noise is shown as a thin red contour on the continuous wavelet spectrum. The dashed red line on the global wavelet spectrum denotes the 95% confidence level.

Figure B.22 | Detrended reconstructed PDSI time series (top), continuous wavelet spectrum (bottom), and global wavelet spectrum (right) for grid number 102 of the *Cook et al.* [2008] dataset.

B.2. Additional Cross Wavelet Transform Plots

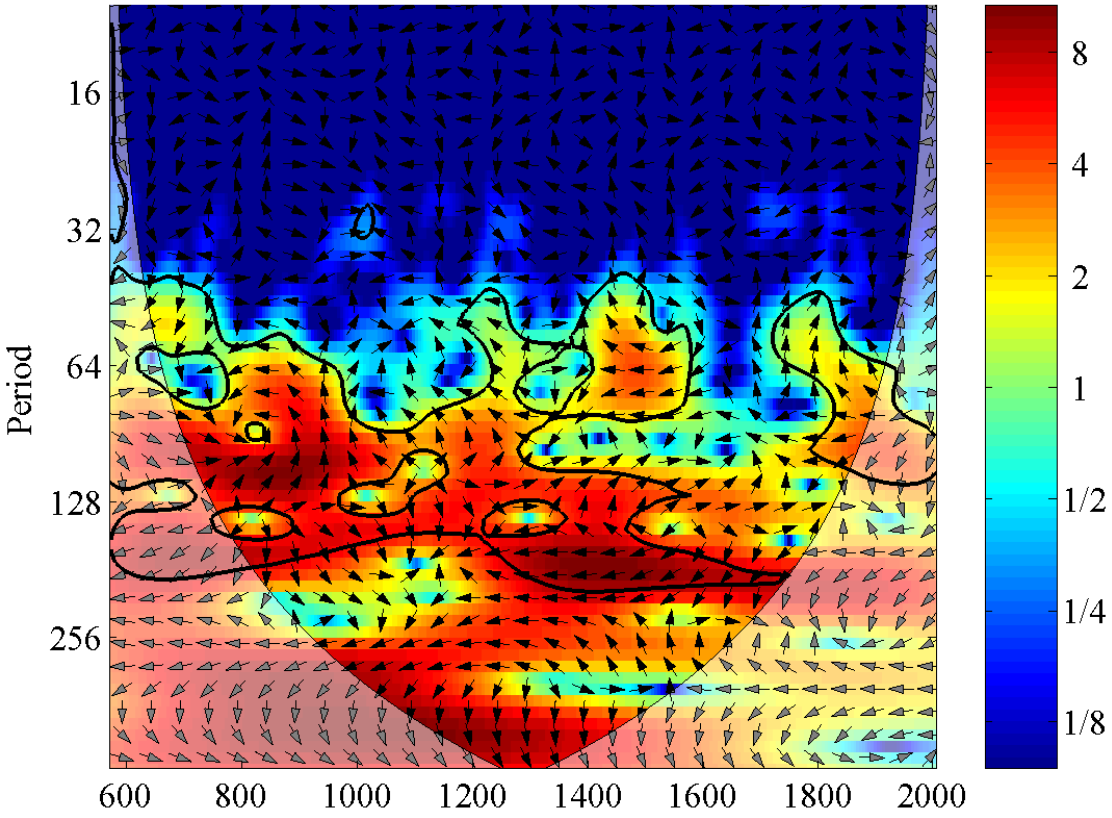

Notes: The thin black represents the COI. The 5% significance level against red noise is shown as a thick contour. The relative phase relationship is shown as arrows (with in-phase pointing right and anti-phase pointing left).

Figure B.23 | Cross wavelet transform of the re-sampled PDSI time series for grid number 25 of the *Cook et al.* [2008] dataset and the reconstructed total solar irradiance record of *Steinhilber et al.* [2009].

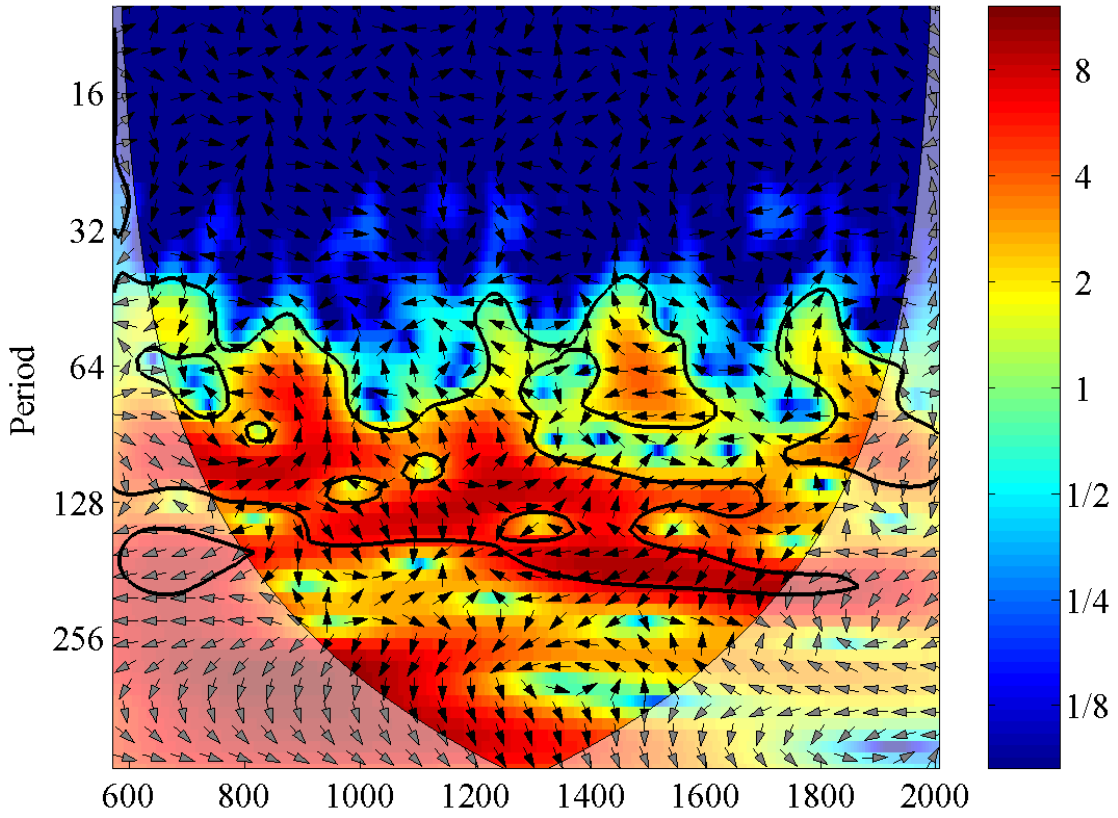

Notes: The thin black represents the COI. The 5% significance level against red noise is shown as a thick contour. The relative phase relationship is shown as arrows (with in-phase pointing right and anti-phase pointing left).

Figure B.24 | Cross wavelet transform of the re-sampled PDSI time series for grid number 32 of the *Cook et al.* [2008] dataset and the reconstructed total solar irradiance record of *Steinhilber et al.* [2009].

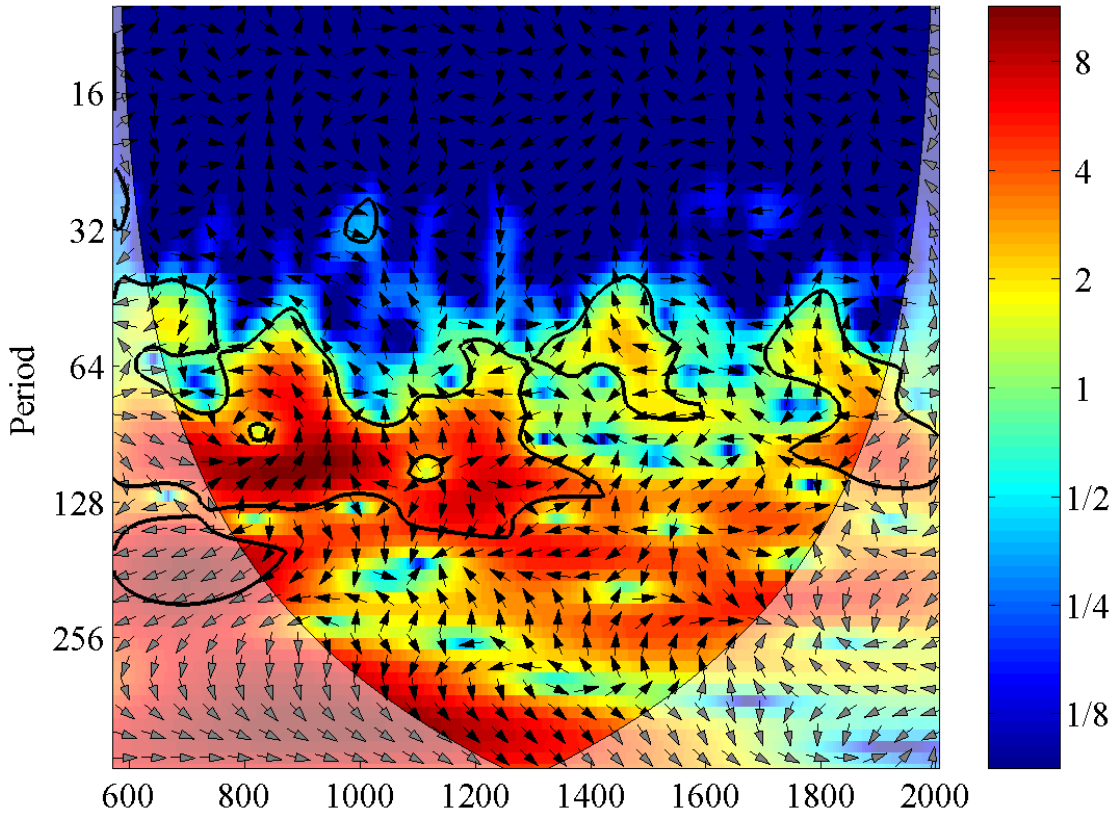

Notes: The thin black represents the COI. The 5% significance level against red noise is shown as a thick contour. The relative phase relationship is shown as arrows (with in-phase pointing right and anti-phase pointing left).

Figure B.25 | Cross wavelet transform of the re-sampled PDSI time series for grid number 33 of the *Cook et al.* [2008] dataset and the reconstructed total solar irradiance record of *Steinhilber et al.* [2009].

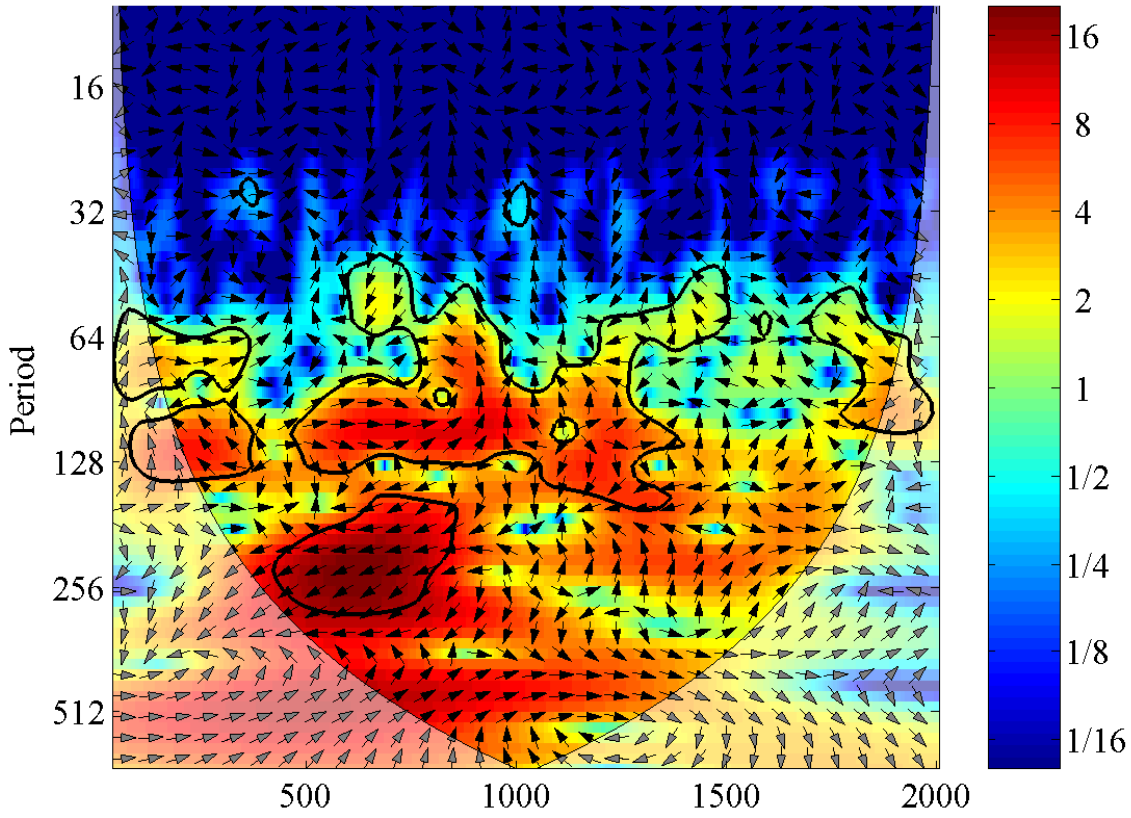

Notes: The thin black represents the COI. The 5% significance level against red noise is shown as a thick contour. The relative phase relationship is shown as arrows (with in-phase pointing right and anti-phase pointing left).

Figure B.26 | Cross wavelet transform of the re-sampled PDSI time series for grid number 34 of the *Cook et al.* [2008] dataset and the reconstructed total solar irradiance record of *Steinhilber et al.* [2009].

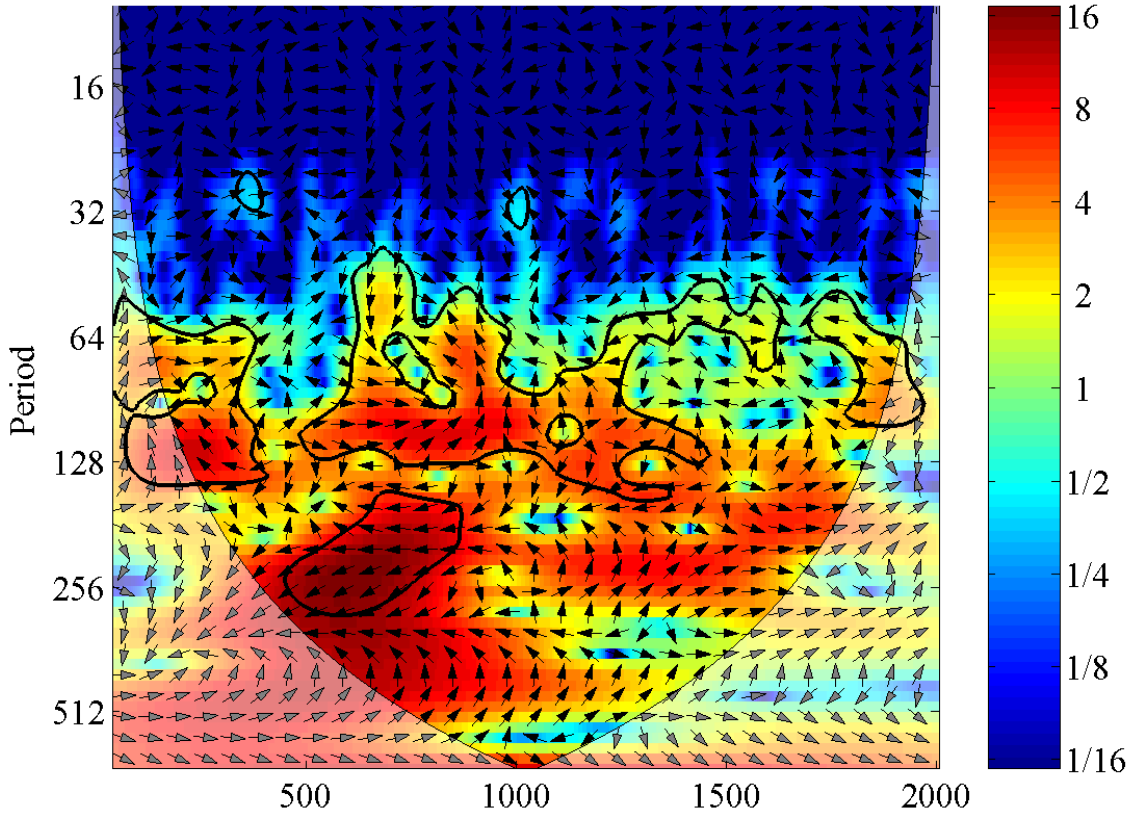

Notes: The thin black represents the COI. The 5% significance level against red noise is shown as a thick contour. The relative phase relationship is shown as arrows (with in-phase pointing right and anti-phase pointing left).

Figure B.27 | Cross wavelet transform of the re-sampled PDSI time series for grid number 35 of the *Cook et al.* [2008] dataset and the reconstructed total solar irradiance record of *Steinhilber et al.* [2009].

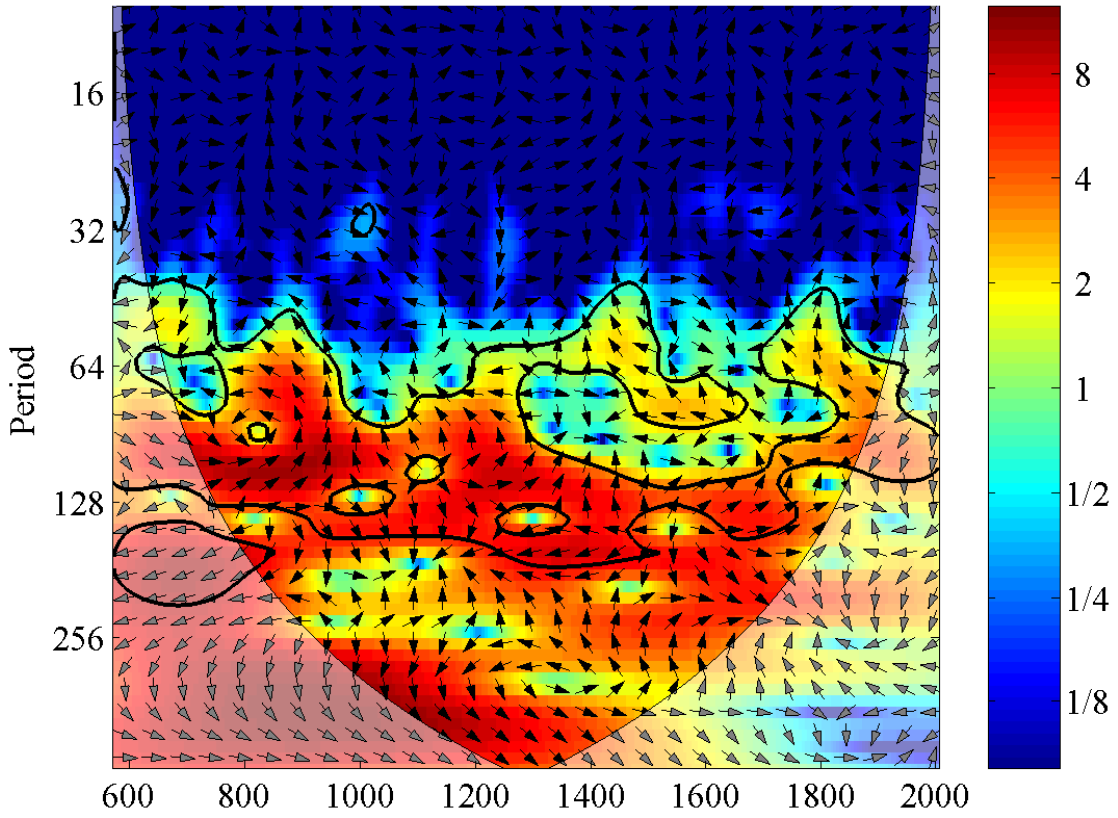

Notes: The thin black represents the COI. The 5% significance level against red noise is shown as a thick contour. The relative phase relationship is shown as arrows (with in-phase pointing right and anti-phase pointing left).

Figure B.28 | Cross wavelet transform of the re-sampled PDSI time series for grid number 43 of the *Cook et al.* [2008] dataset and the reconstructed total solar irradiance record of *Steinhilber et al.* [2009].

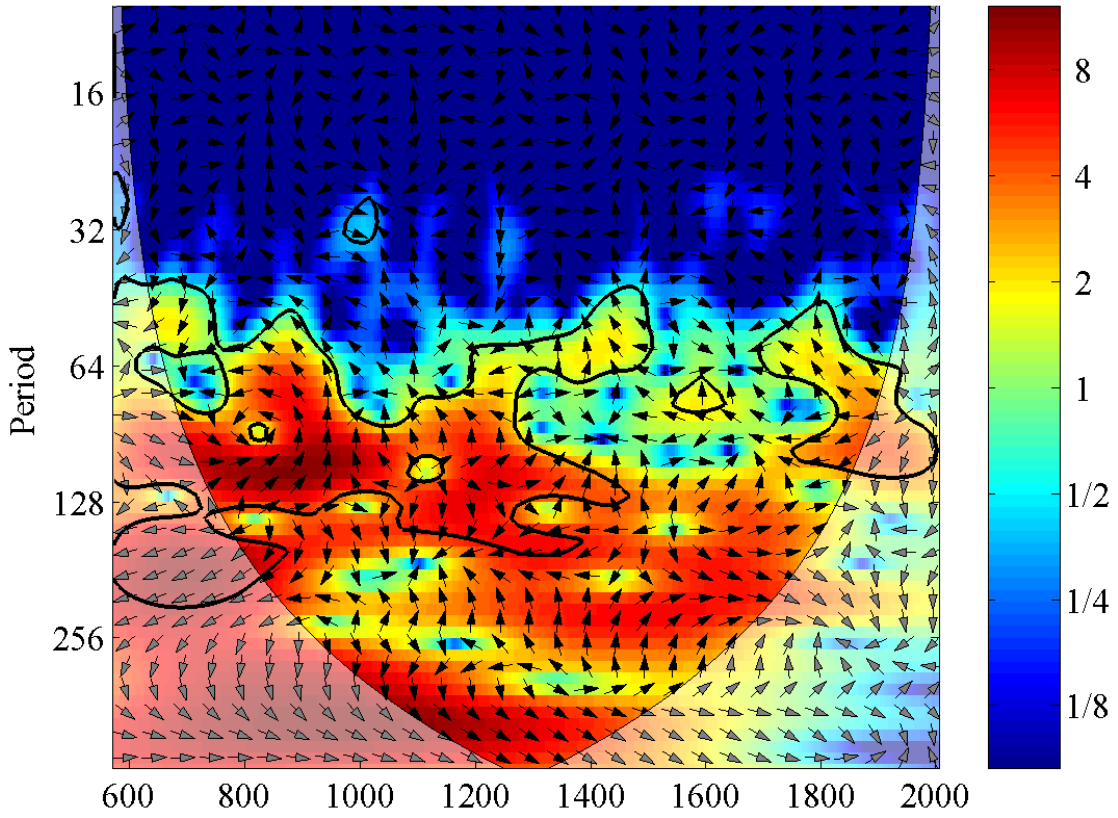

Notes: The thin black represents the COI. The 5% significance level against red noise is shown as a thick contour. The relative phase relationship is shown as arrows (with in-phase pointing right and anti-phase pointing left).

Figure B.29 | Cross wavelet transform of the re-sampled PDSI time series for grid number 44 of the *Cook et al.* [2008] dataset and the reconstructed total solar irradiance record of *Steinhilber et al.* [2009].

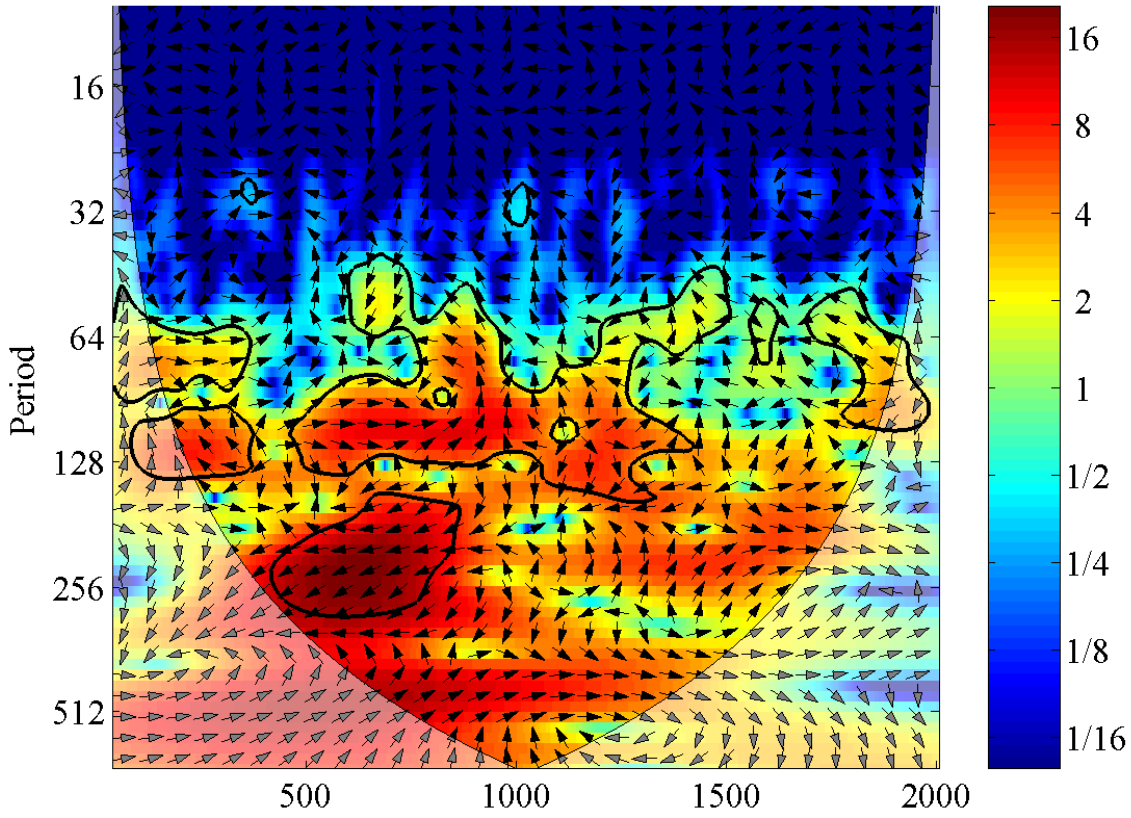

Notes: The thin black represents the COI. The 5% significance level against red noise is shown as a thick contour. The relative phase relationship is shown as arrows (with in-phase pointing right and anti-phase pointing left).

Figure B.30 | Cross wavelet transform of the re-sampled PDSI time series for grid number 45 of the *Cook et al.* [2008] dataset and the reconstructed total solar irradiance record of *Steinhilber et al.* [2009].

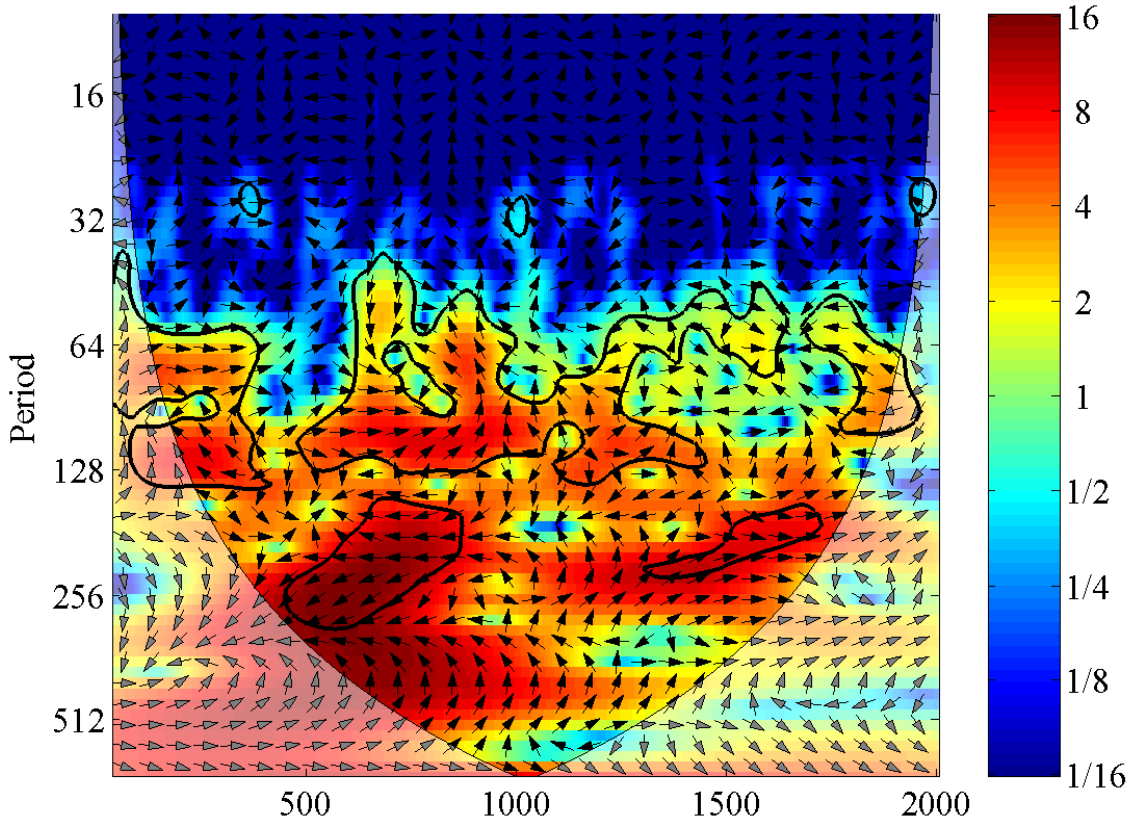

Notes: The thin black represents the COI. The 5% significance level against red noise is shown as a thick contour. The relative phase relationship is shown as arrows (with in-phase pointing right and anti-phase pointing left).

Figure B.31 | Cross wavelet transform of the re-sampled PDSI time series for grid number 46 of the *Cook et al.* [2008] dataset and the reconstructed total solar irradiance record of *Steinhilber et al.* [2009].

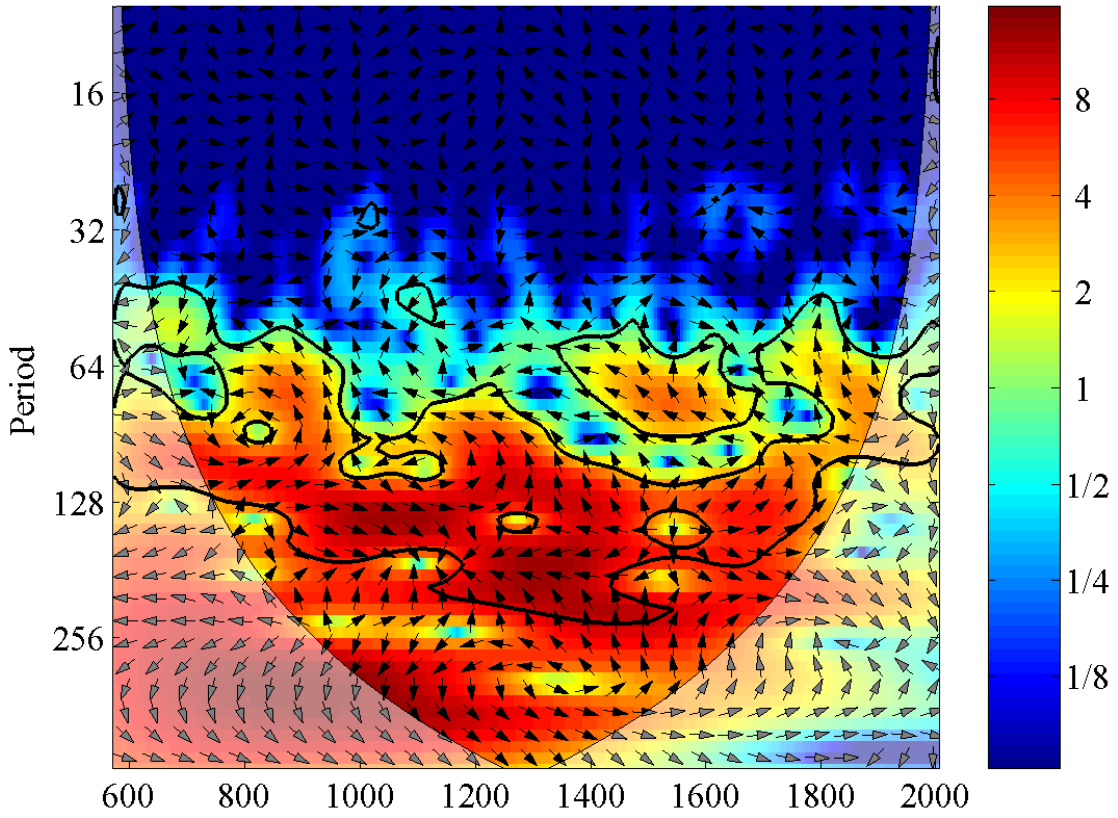

Notes: The thin black represents the COI. The 5% significance level against red noise is shown as a thick contour. The relative phase relationship is shown as arrows (with in-phase pointing right and anti-phase pointing left).

Figure B.32 | Cross wavelet transform of the re-sampled PDSI time series for grid number 55 of the *Cook et al.* [2008] dataset and the reconstructed total solar irradiance record of *Steinhilber et al.* [2009].

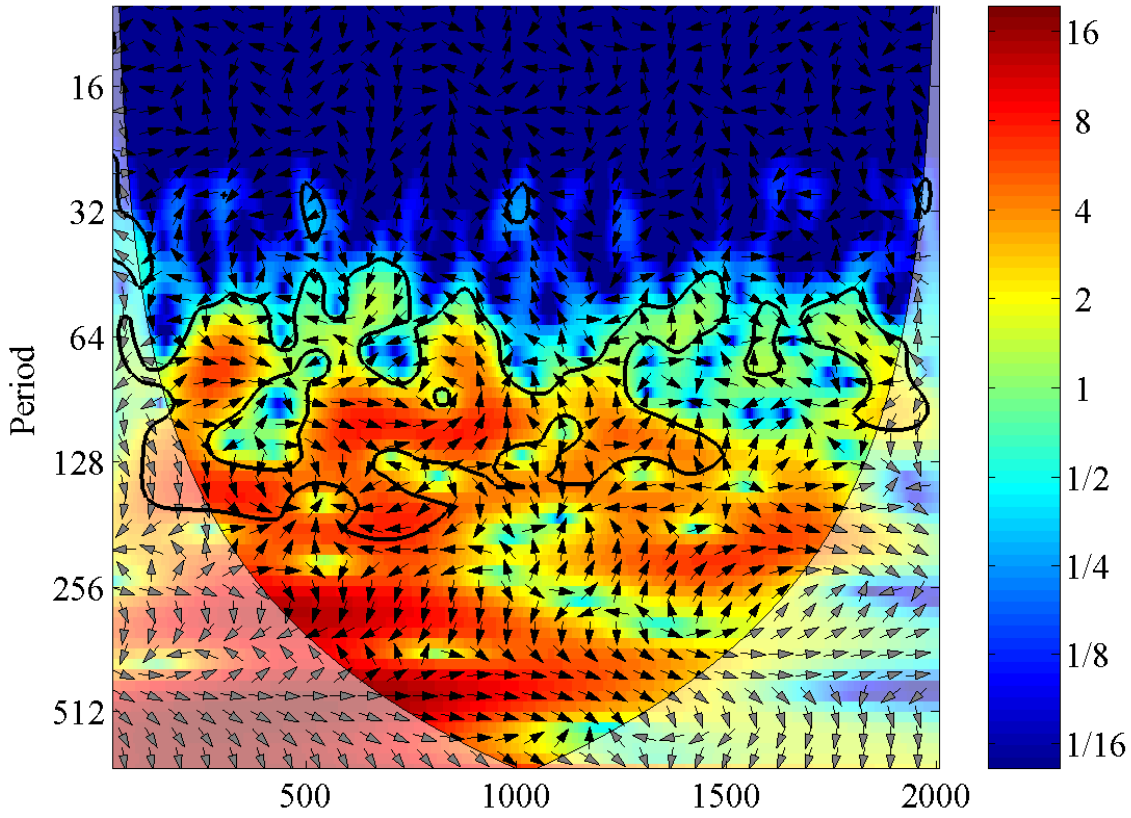

Notes: The thin black represents the COI. The 5% significance level against red noise is shown as a thick contour. The relative phase relationship is shown as arrows (with in-phase pointing right and anti-phase pointing left).

Figure B.33 | Cross wavelet transform of the re-sampled PDSI time series for grid number 56 of the *Cook et al.* [2008] dataset and the reconstructed total solar irradiance record of *Steinhilber et al.* [2009].

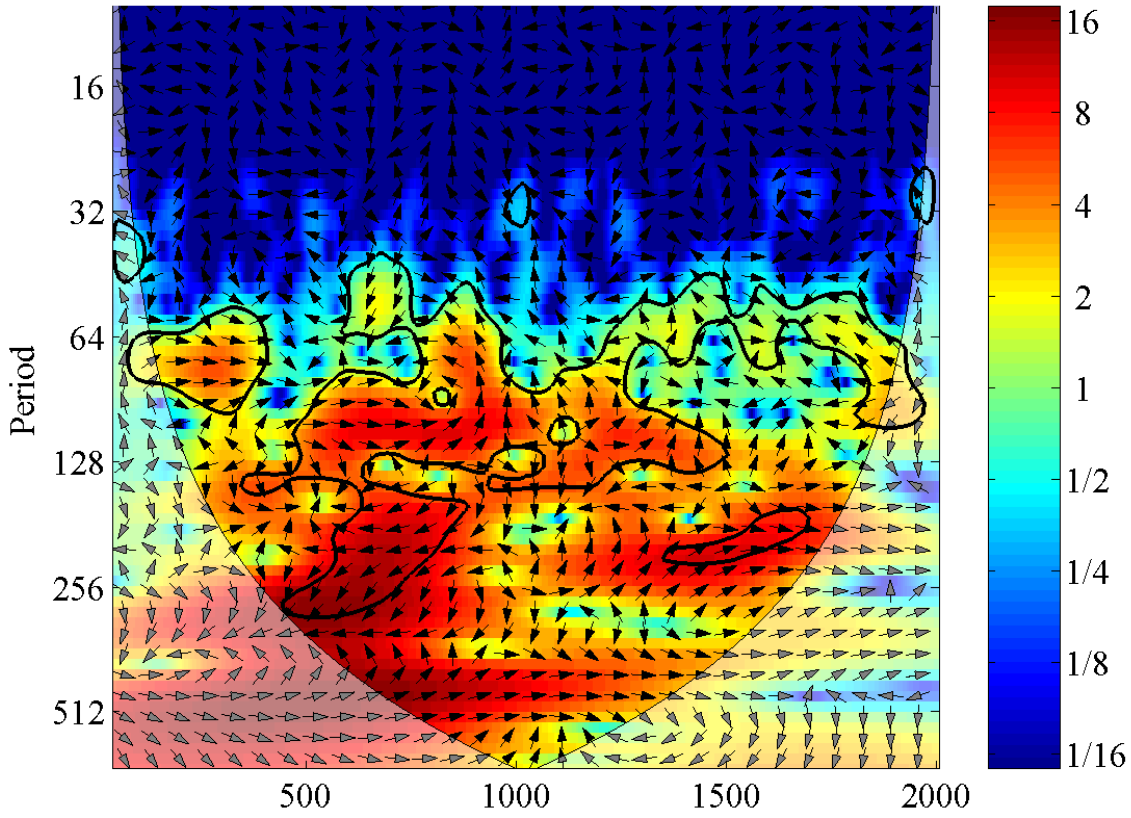

Notes: The thin black represents the COI. The 5% significance level against red noise is shown as a thick contour. The relative phase relationship is shown as arrows (with in-phase pointing right and anti-phase pointing left).

Figure B.34 | Cross wavelet transform of the re-sampled PDSI time series for grid number 57 of the *Cook et al.* [2008] dataset and the reconstructed total solar irradiance record of *Steinhilber et al.* [2009].

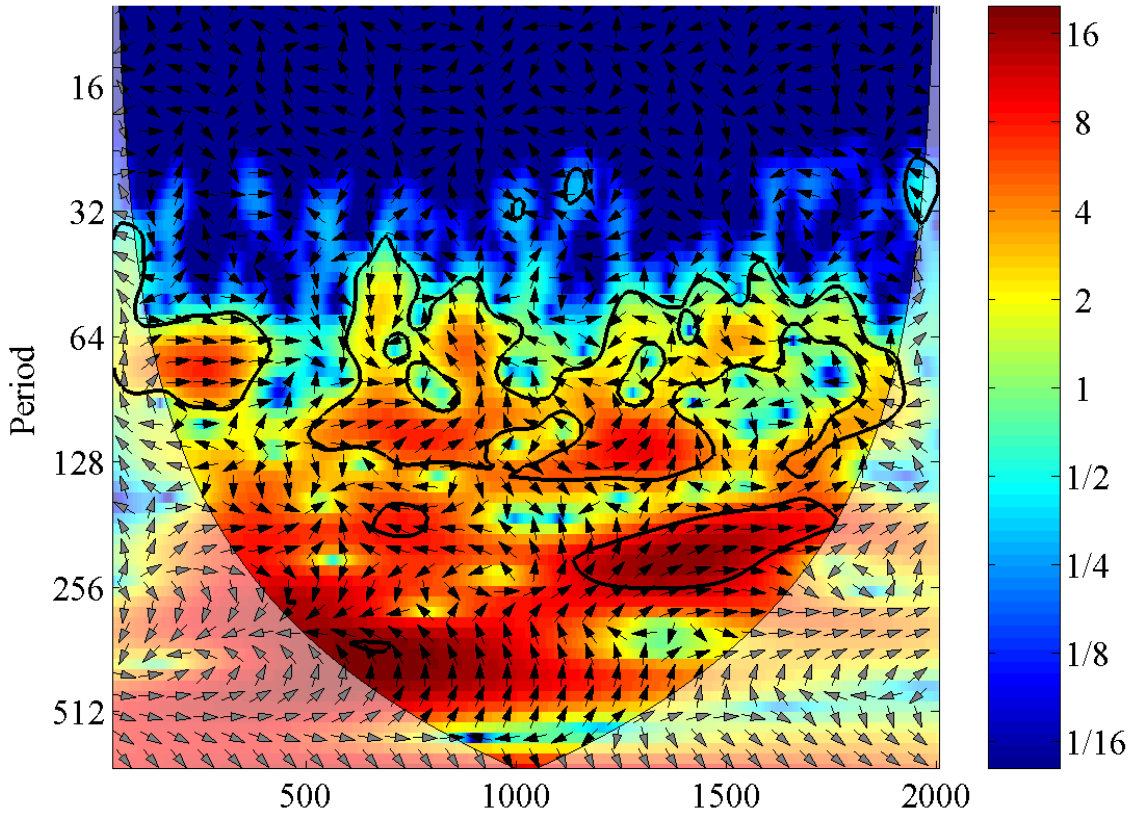

Notes: The thin black represents the COI. The 5% significance level against red noise is shown as a thick contour. The relative phase relationship is shown as arrows (with in-phase pointing right and anti-phase pointing left).

Figure B.35 | Cross wavelet transform of the re-sampled PDSI time series for grid number 58 of the *Cook et al.* [2008] dataset and the reconstructed total solar irradiance record of *Steinhilber et al.* [2009].

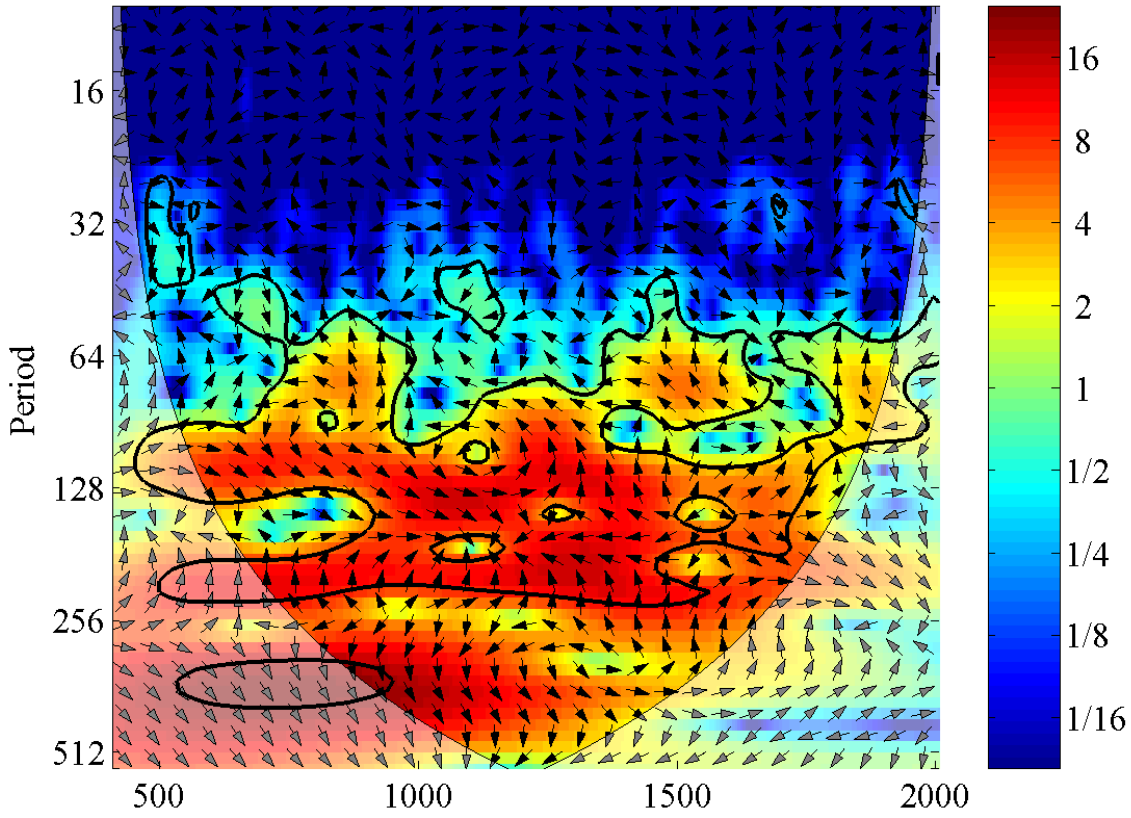

Notes: The thin black represents the COI. The 5% significance level against red noise is shown as a thick contour. The relative phase relationship is shown as arrows (with in-phase pointing right and anti-phase pointing left).

Figure B.36 | Cross wavelet transform of the re-sampled PDSI time series for grid number 68 of the *Cook et al.* [2008] dataset and the reconstructed total solar irradiance record of *Steinhilber et al.* [2009].

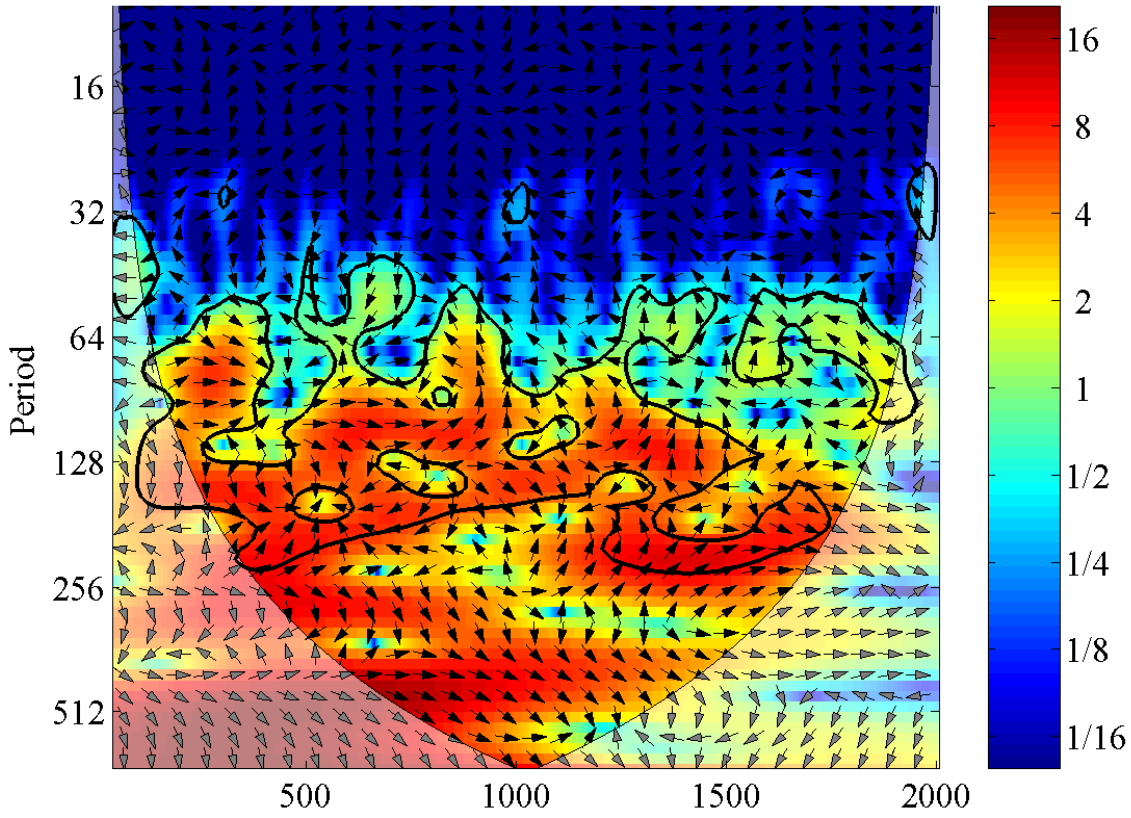

Notes: The thin black represents the COI. The 5% significance level against red noise is shown as a thick contour. The relative phase relationship is shown as arrows (with in-phase pointing right and anti-phase pointing left).

Figure B.37 | Cross wavelet transform of the re-sampled PDSI time series for grid number 69 of the *Cook et al.* [2008] dataset and the reconstructed total solar irradiance record of *Steinhilber et al.* [2009].

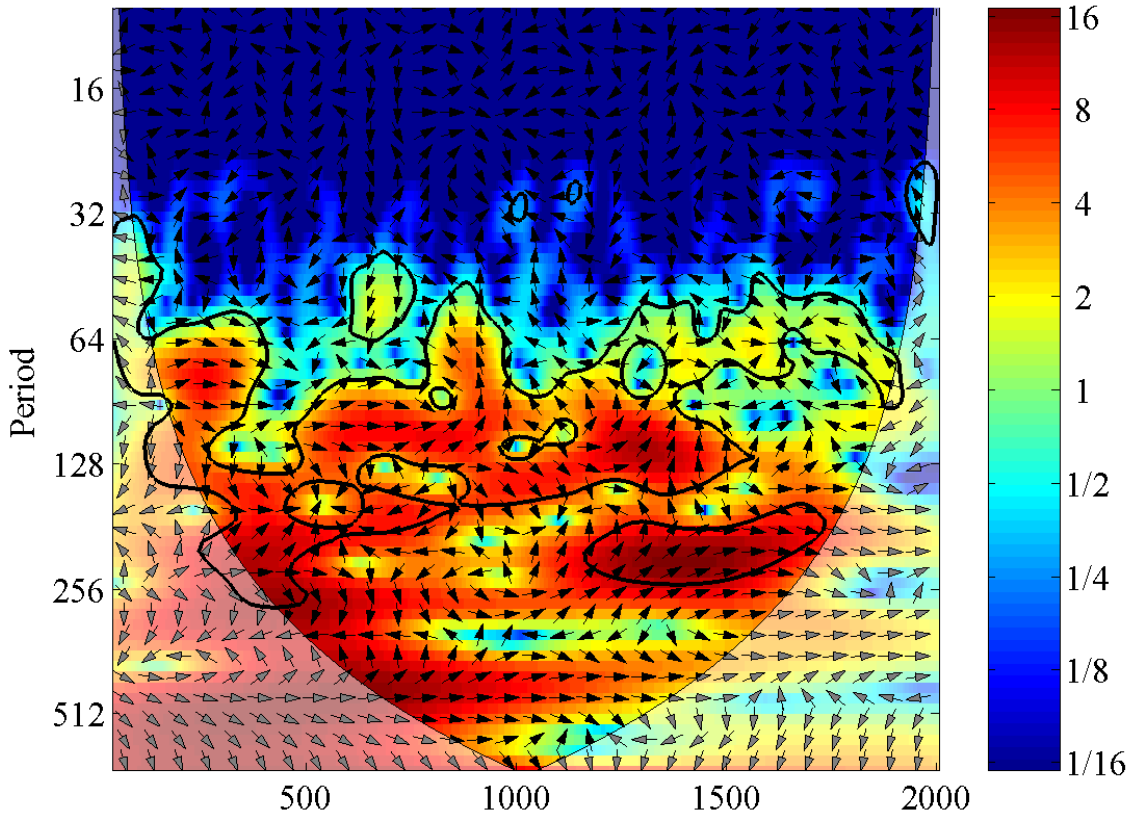

Notes: The thin black represents the COI. The 5% significance level against red noise is shown as a thick contour. The relative phase relationship is shown as arrows (with in-phase pointing right and anti-phase pointing left).

Figure B.38 | Cross wavelet transform of the re-sampled PDSI time series for grid number 70 of the *Cook et al.* [2008] dataset and the reconstructed total solar irradiance record of *Steinhilber et al.* [2009].

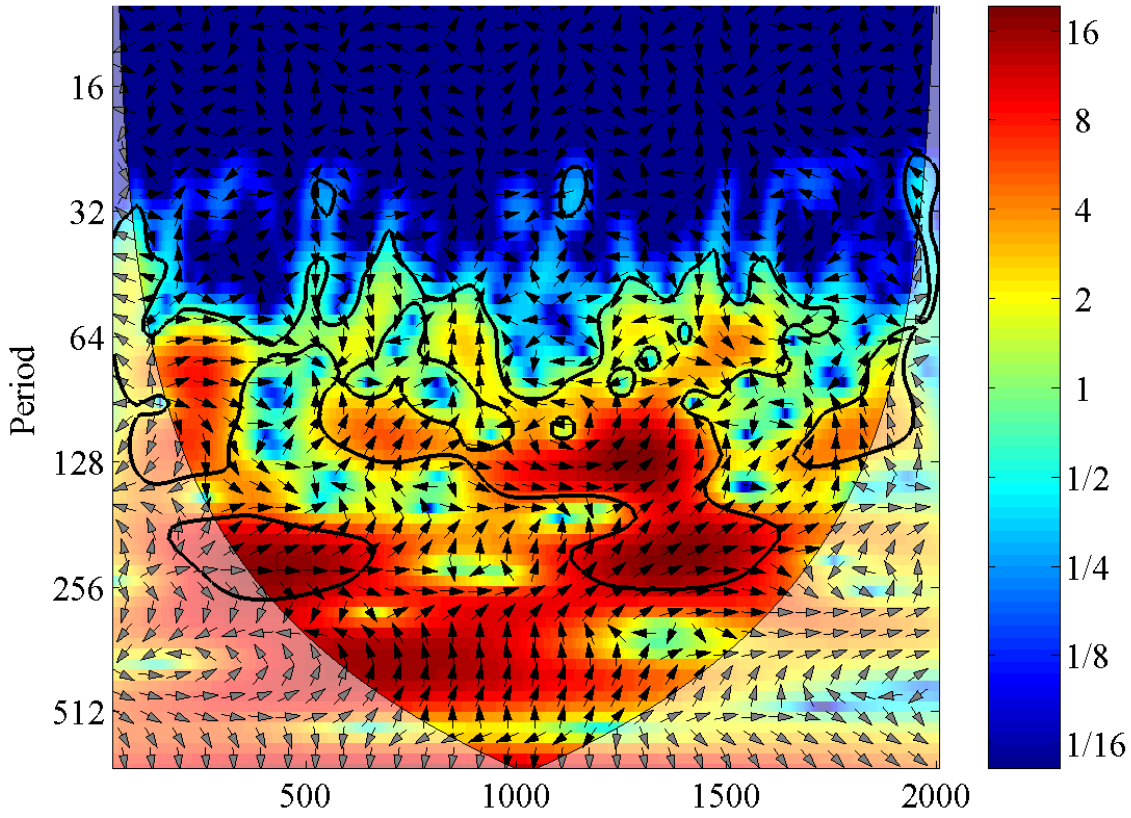

Notes: The thin black represents the COI. The 5% significance level against red noise is shown as a thick contour. The relative phase relationship is shown as arrows (with in-phase pointing right and anti-phase pointing left).

Figure B.39 | Cross wavelet transform of the re-sampled PDSI time series for grid number 71 of the *Cook et al.* [2008] dataset and the reconstructed total solar irradiance record of *Steinhilber et al.* [2009].

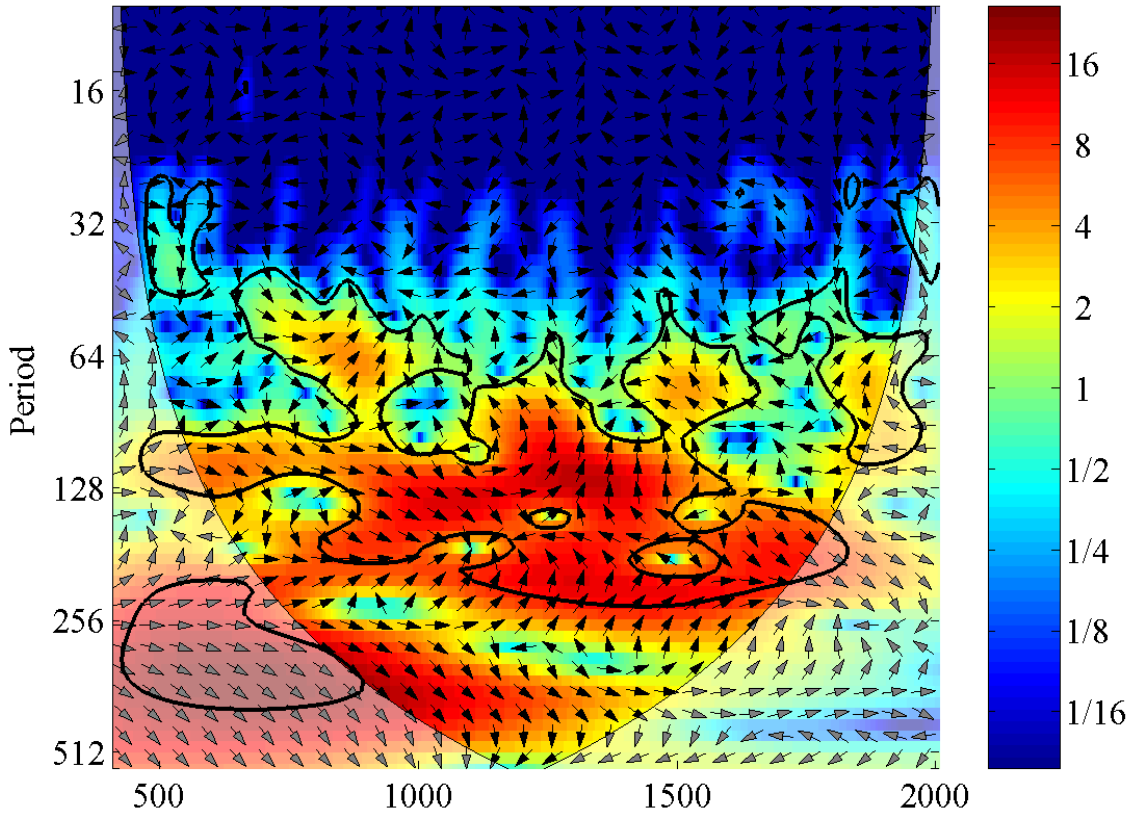

Notes: The thin black represents the COI. The 5% significance level against red noise is shown as a thick contour. The relative phase relationship is shown as arrows (with in-phase pointing right and anti-phase pointing left).

Figure B.40 | Cross wavelet transform of the re-sampled PDSI time series for grid number 83 of the *Cook et al.* [2008] dataset and the reconstructed total solar irradiance record of *Steinhilber et al.* [2009].

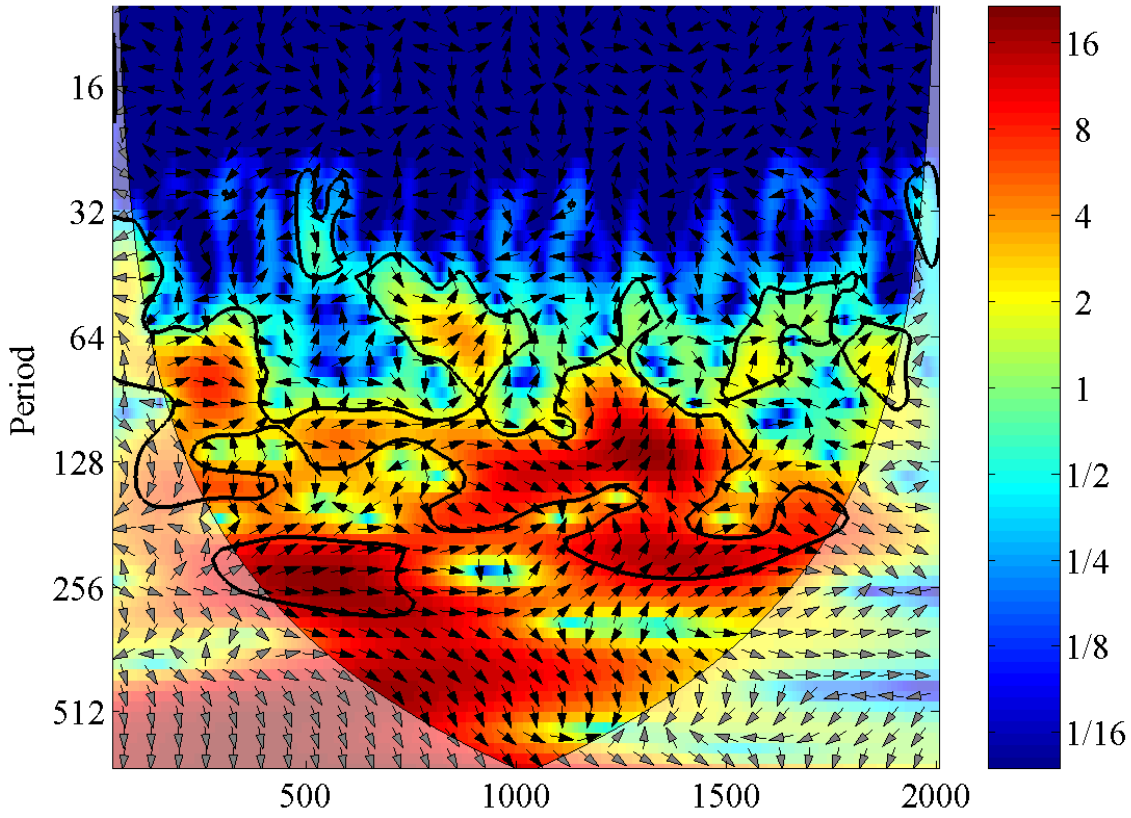

Notes: The thin black represents the COI. The 5% significance level against red noise is shown as a thick contour. The relative phase relationship is shown as arrows (with in-phase pointing right and anti-phase pointing left).

Figure B.41 | Cross wavelet transform of the re-sampled PDSI time series for grid number 84 of the *Cook et al.* [2008] dataset and the reconstructed total solar irradiance record of *Steinhilber et al.* [2009].

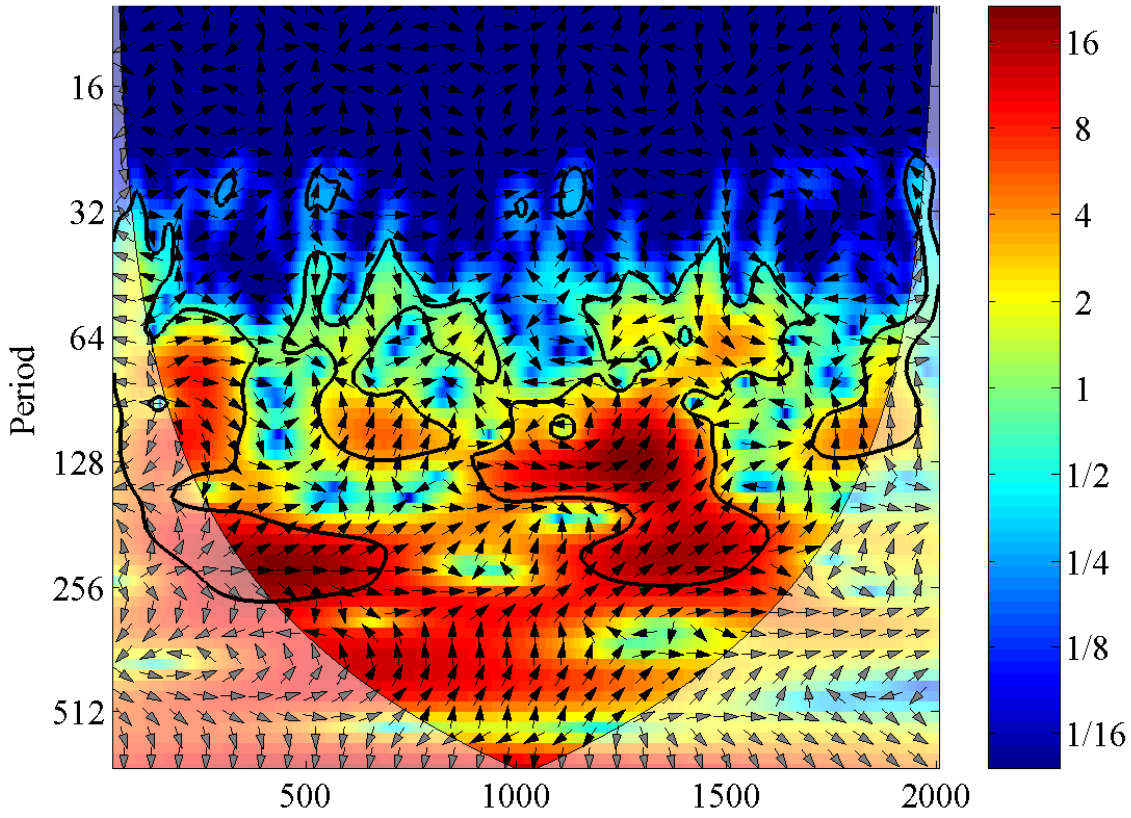

Notes: The thin black represents the COI. The 5% significance level against red noise is shown as a thick contour. The relative phase relationship is shown as arrows (with in-phase pointing right and anti-phase pointing left).

Figure B.42 | Cross wavelet transform of the re-sampled PDSI time series for grid number 86 of the *Cook et al.* [2008] dataset and the reconstructed total solar irradiance record of *Steinhilber et al.* [2009].

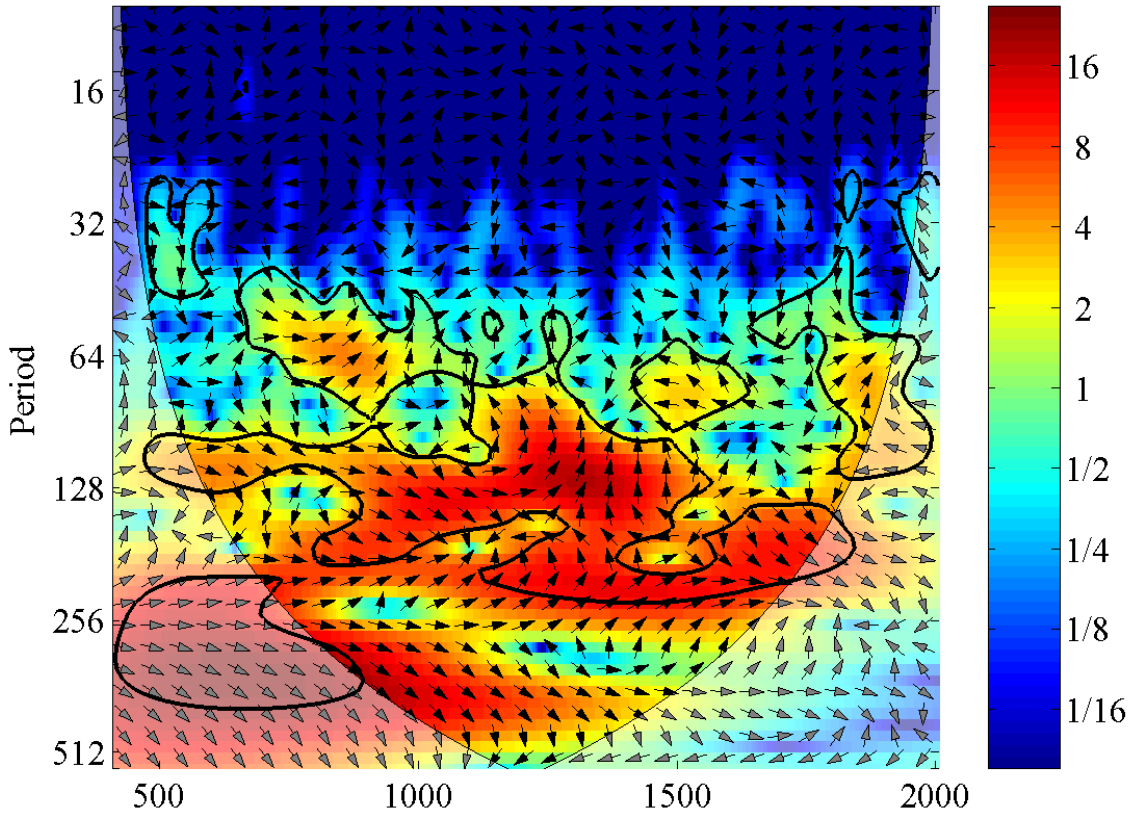

Notes: The thin black represents the COI. The 5% significance level against red noise is shown as a thick contour. The relative phase relationship is shown as arrows (with in-phase pointing right and anti-phase pointing left).

Figure B.43 | Cross wavelet transform of the re-sampled PDSI time series for grid number 99 of the *Cook et al.* [2008] dataset and the reconstructed total solar irradiance record of *Steinhilber et al.* [2009].

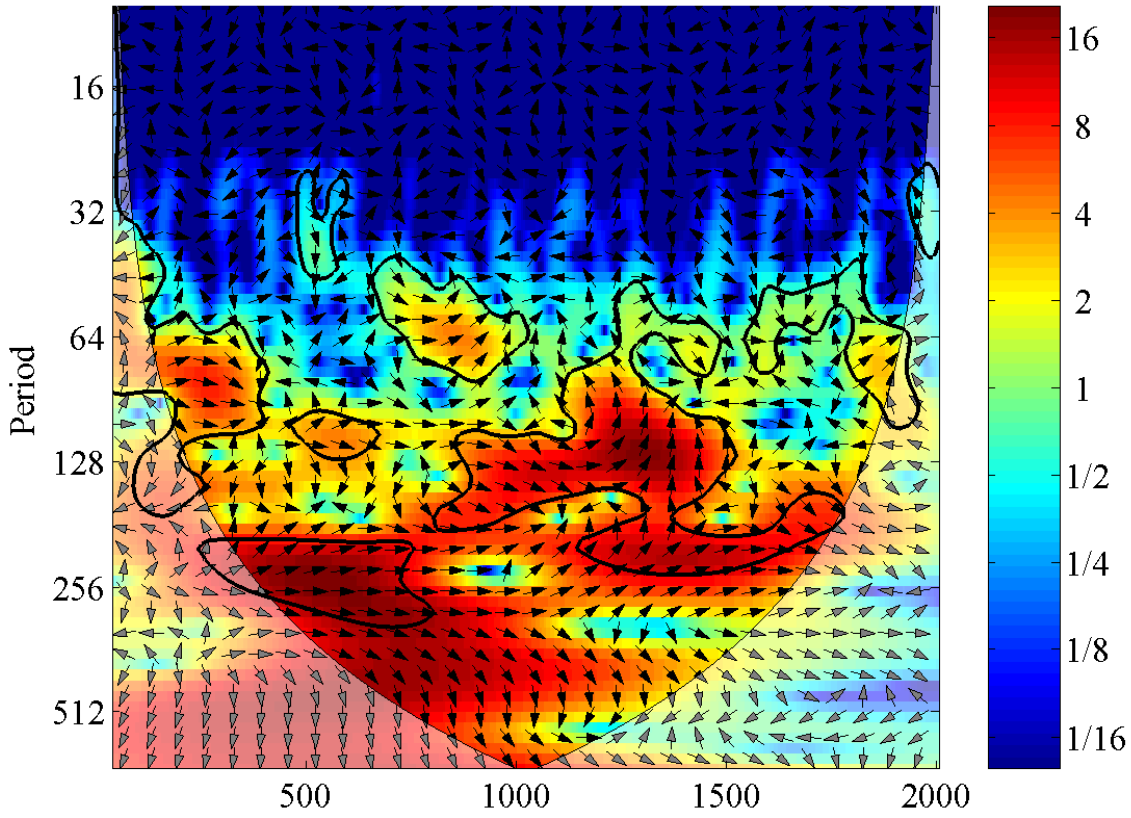

Notes: The thin black represents the COI. The 5% significance level against red noise is shown as a thick contour. The relative phase relationship is shown as arrows (with in-phase pointing right and anti-phase pointing left).

Figure B.44 | Cross wavelet transform of the re-sampled PDSI time series for grid number 100 of the *Cook et al.* [2008] dataset and the reconstructed total solar irradiance record of *Steinhilber et al.* [2009].

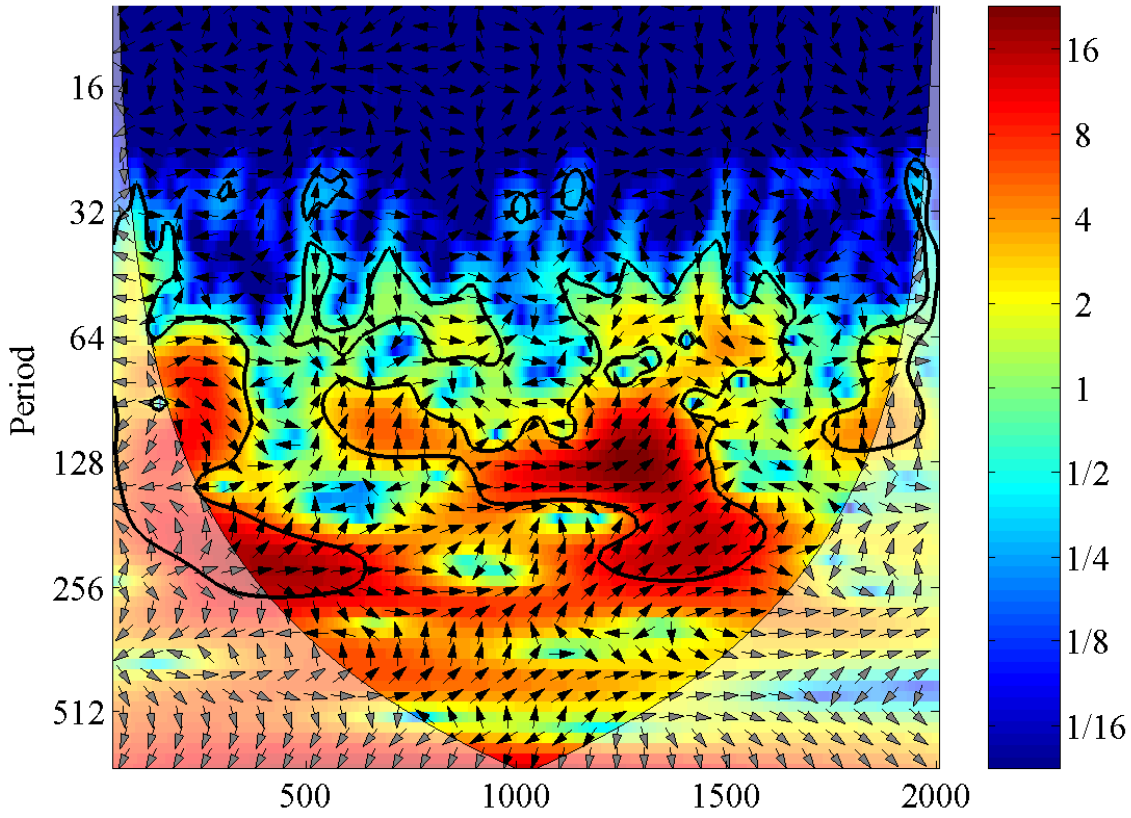

Notes: The thin black represents the COI. The 5% significance level against red noise is shown as a thick contour. The relative phase relationship is shown as arrows (with in-phase pointing right and anti-phase pointing left).

Figure B.45 | Cross wavelet transform of the re-sampled PDSI time series for grid number 102 of the *Cook et al.* [2008] dataset and the reconstructed total solar irradiance record of *Steinhilber et al.* [2009].

B.3. Additional Wavelet Coherence Plots

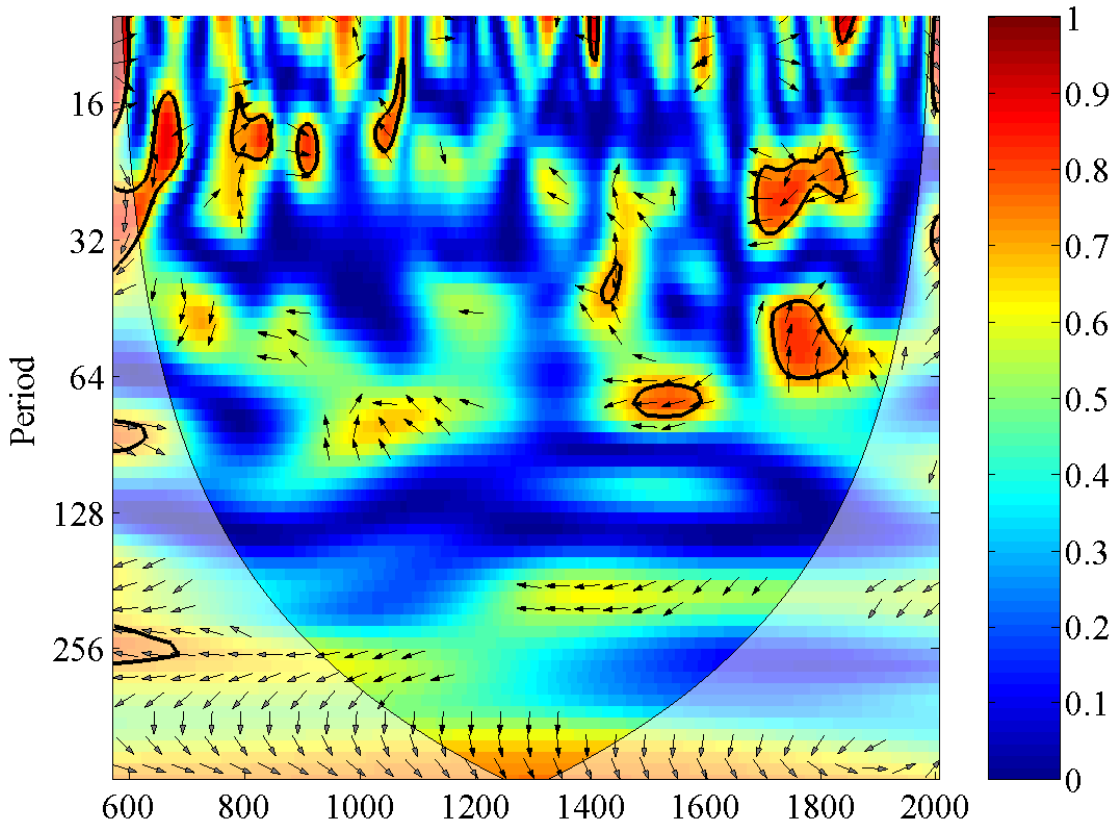

Notes: The thin black represents the COI. The 5% significance level against red noise is shown as a thick contour.

Figure B.46 | Squared wavelet coherence between the re-sampled PDSI time series for grid number 25 of the *Cook et al.* [2008] dataset and the reconstructed total solar irradiance record of *Steinhilber et al.* [2009].

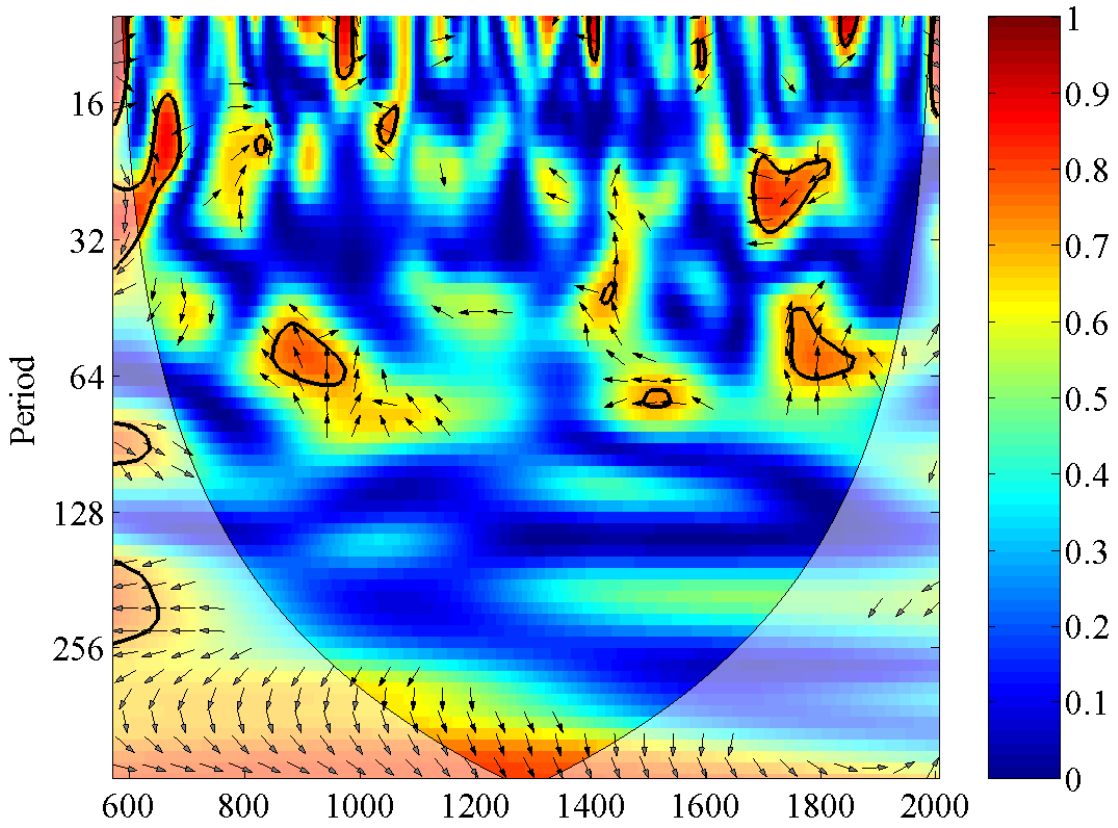

Notes: The thin black represents the COI. The 5% significance level against red noise is shown as a thick contour.

Figure B.47 | Squared wavelet coherence between the re-sampled PDSI time series for grid number 32 of the *Cook et al.* [2008] dataset and the reconstructed total solar irradiance record of *Steinhilber et al.* [2009].

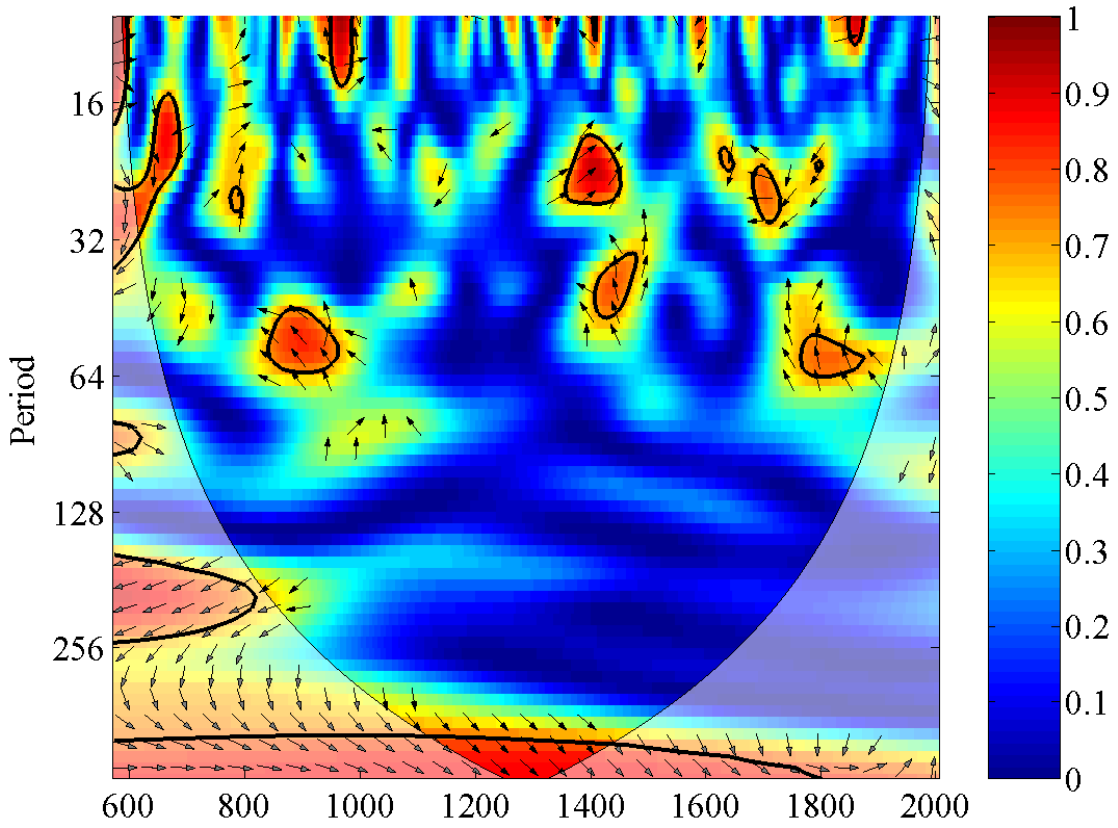

Notes: The thin black represents the COI. The 5% significance level against red noise is shown as a thick contour.

Figure B.48 | Squared wavelet coherence between the re-sampled PDSI time series for grid number 33 of the *Cook et al.* [2008] dataset and the reconstructed total solar irradiance record of *Steinhilber et al.* [2009].

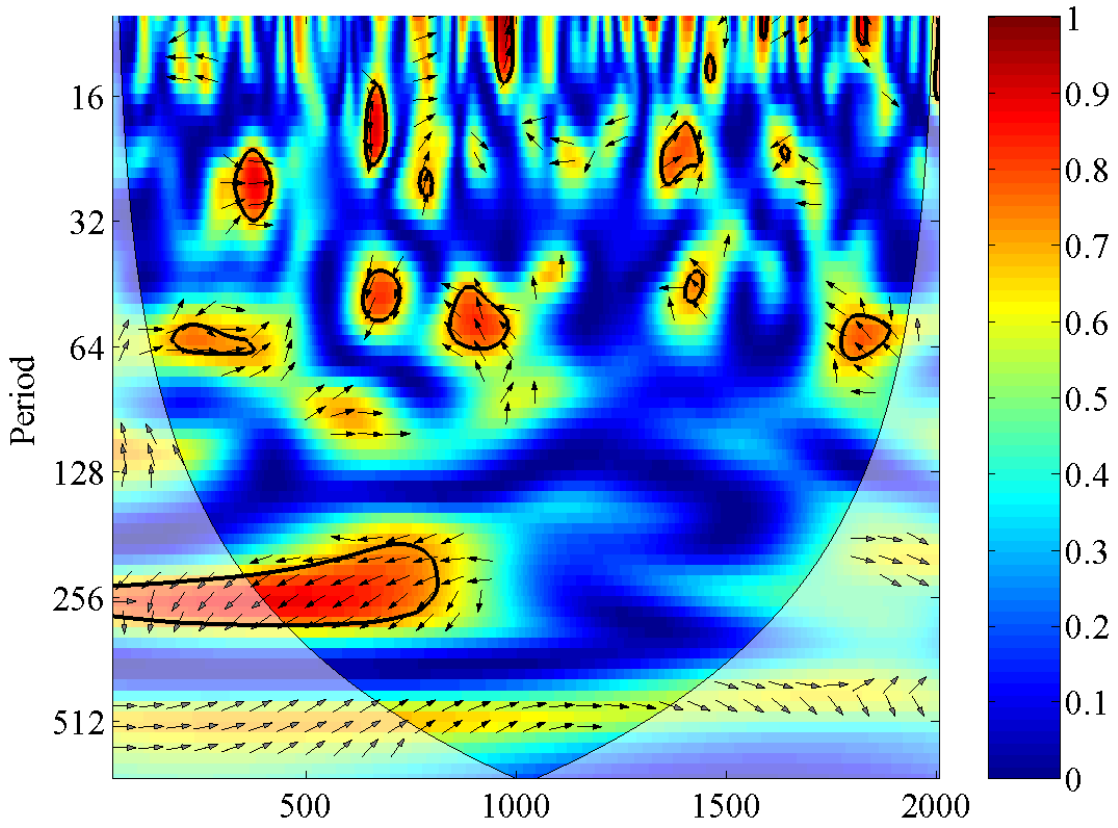

Notes: The thin black represents the COI. The 5% significance level against red noise is shown as a thick contour.

Figure B.49 | Squared wavelet coherence between the re-sampled PDSI time series for grid number 34 of the *Cook et al.* [2008] dataset and the reconstructed total solar irradiance record of *Steinhilber et al.* [2009].

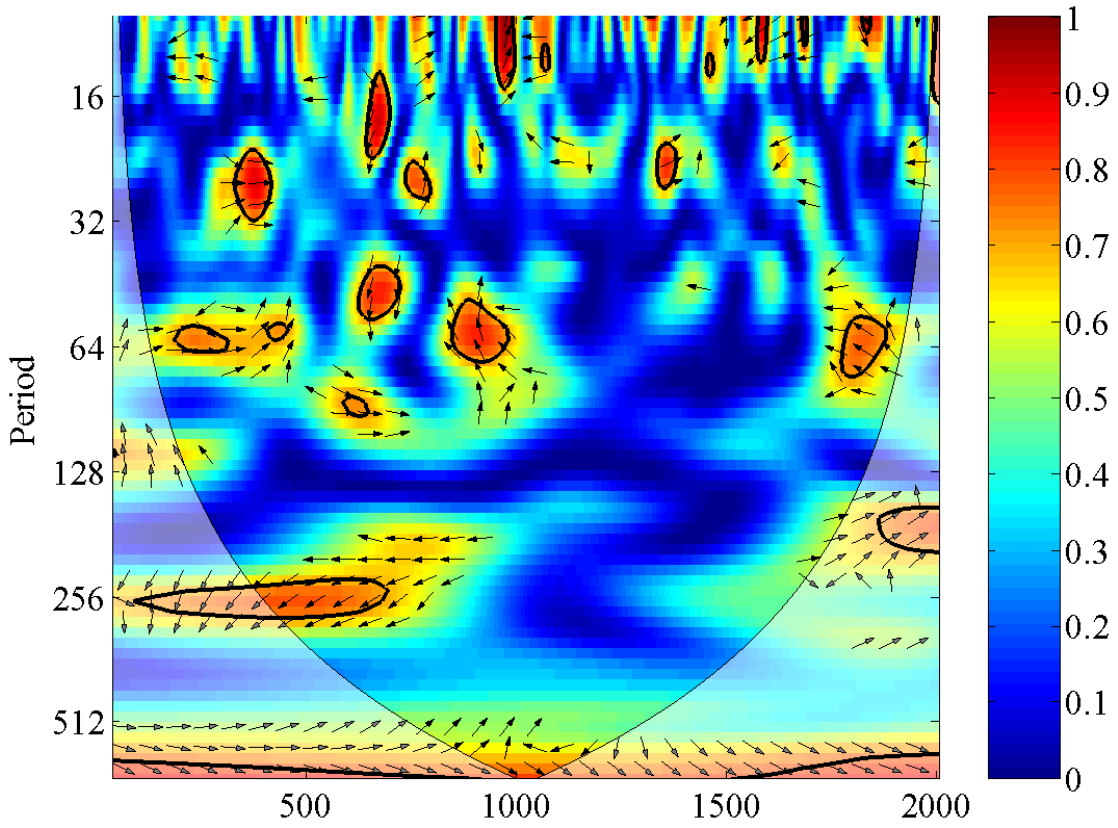

Notes: The thin black represents the COI. The 5% significance level against red noise is shown as a thick contour.

Figure B.50 | Squared wavelet coherence between the re-sampled PDSI time series for grid number 35 of the *Cook et al.* [2008] dataset and the reconstructed total solar irradiance record of *Steinhilber et al.* [2009].

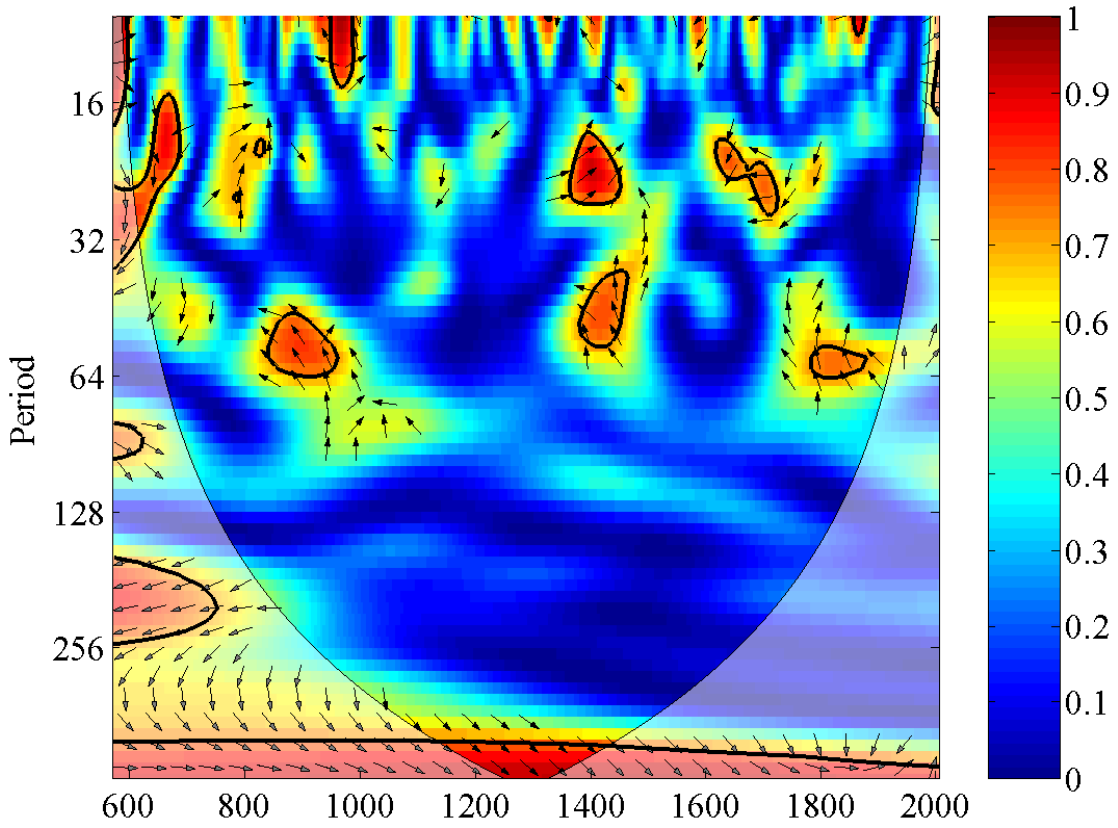

Notes: The thin black represents the COI. The 5% significance level against red noise is shown as a thick contour.

Figure B.51 | Squared wavelet coherence between the re-sampled PDSI time series for grid number 43 of the *Cook et al.* [2008] dataset and the reconstructed total solar irradiance record of *Steinhilber et al.* [2009].

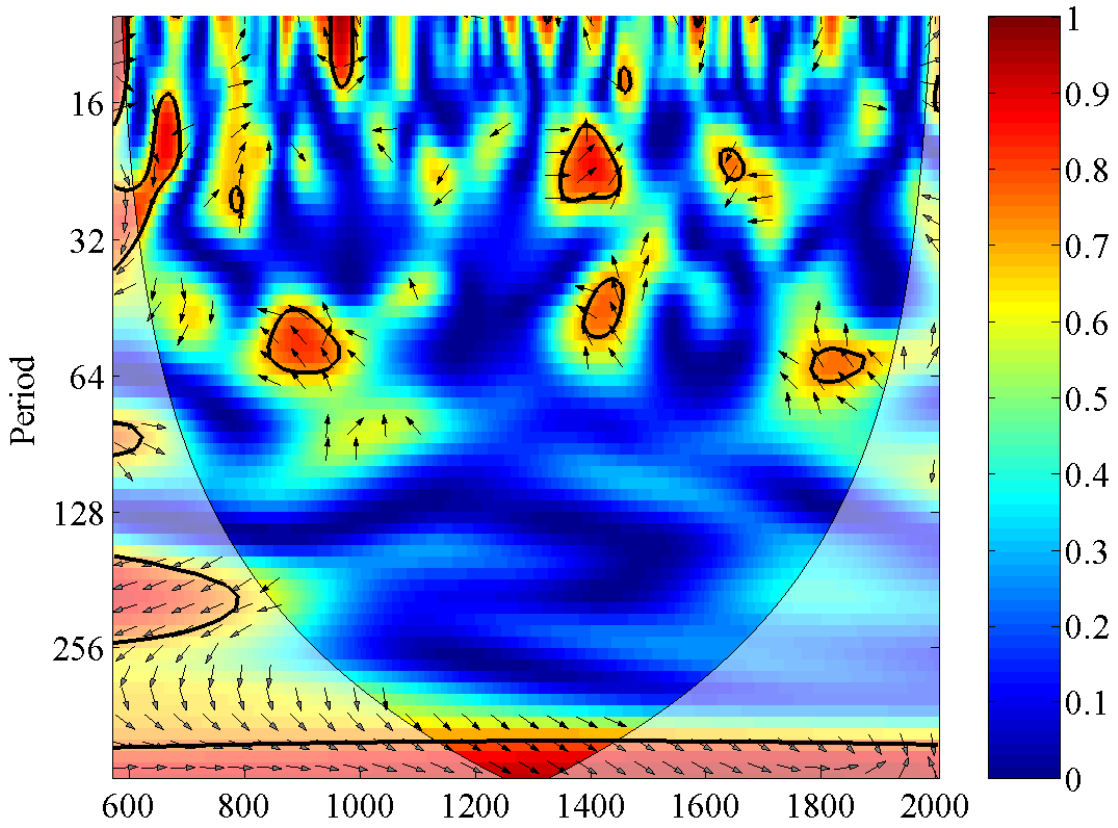

Notes: The thin black represents the COI. The 5% significance level against red noise is shown as a thick contour.

Figure B.52 | Squared wavelet coherence between the re-sampled PDSI time series for grid number 44 of the *Cook et al.* [2008] dataset and the reconstructed total solar irradiance record of *Steinhilber et al.* [2009].

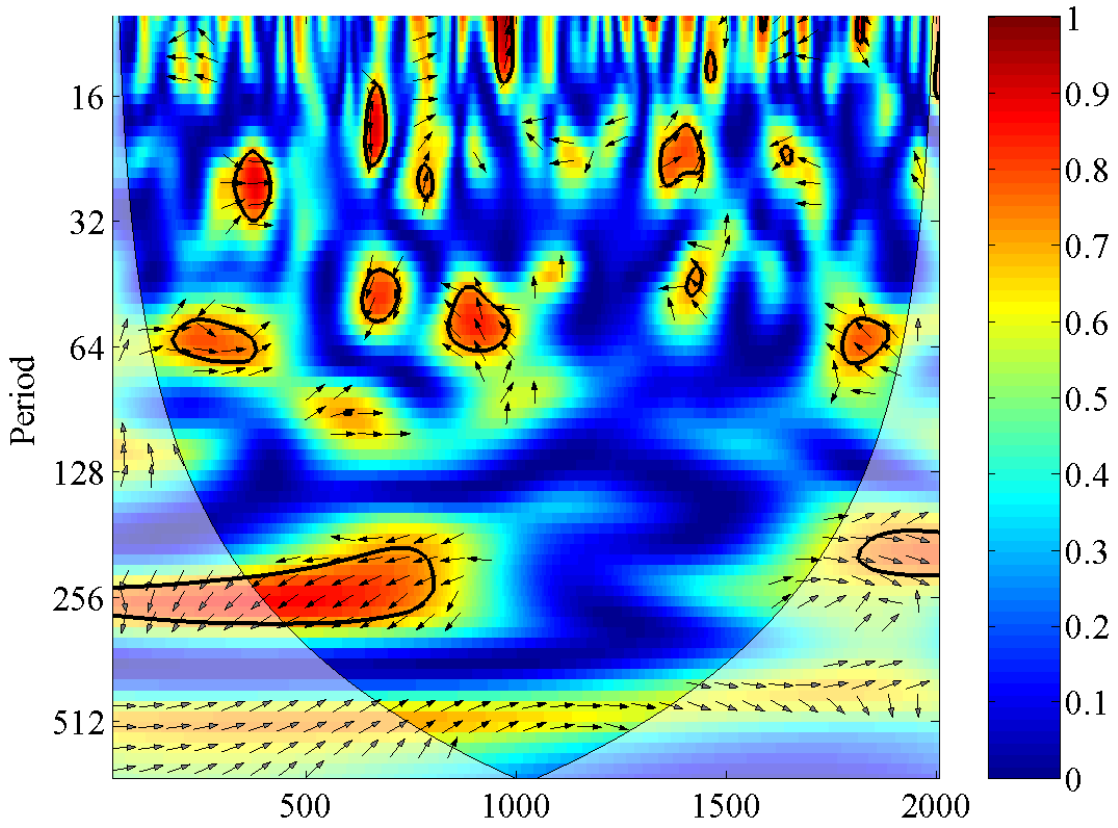

Notes: The thin black represents the COI. The 5% significance level against red noise is shown as a thick contour.

Figure B.53 | Squared wavelet coherence between the re-sampled PDSI time series for grid number 45 of the *Cook et al.* [2008] dataset and the reconstructed total solar irradiance record of *Steinhilber et al.* [2009].

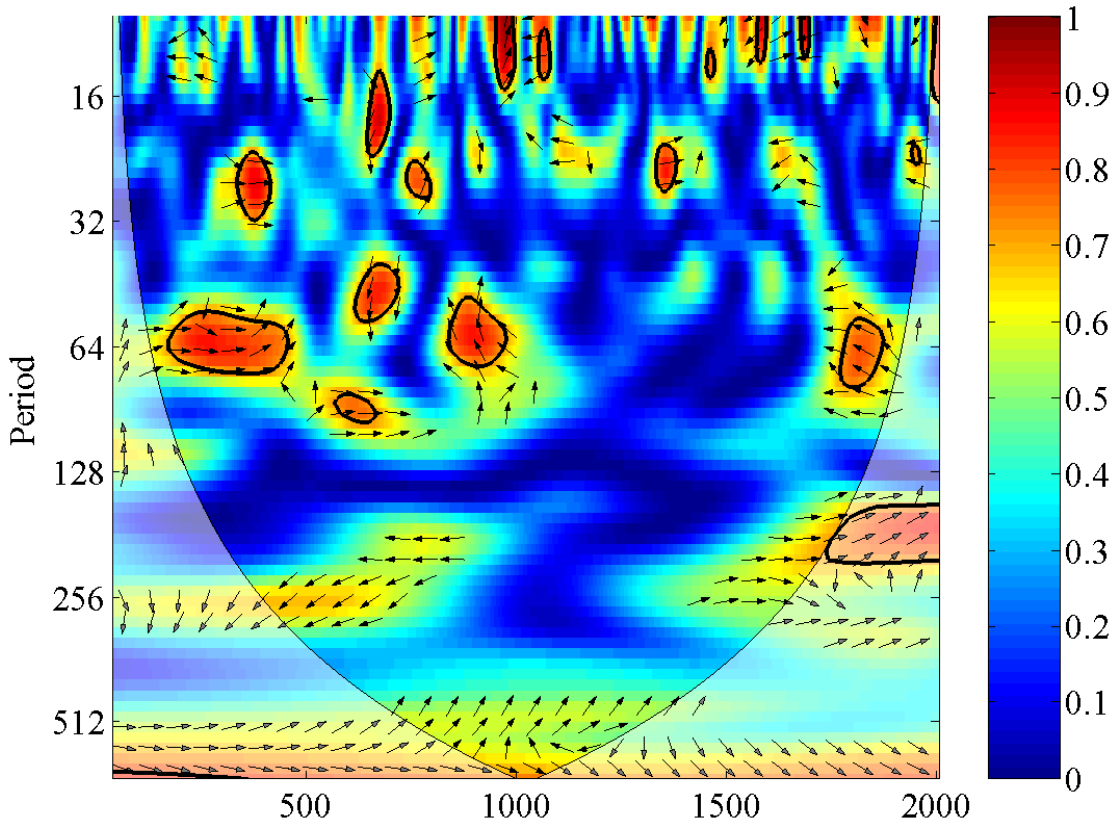

Notes: The thin black represents the COI. The 5% significance level against red noise is shown as a thick contour.

Figure B.54 | Squared wavelet coherence between the re-sampled PDSI time series for grid number 46 of the *Cook et al.* [2008] dataset and the reconstructed total solar irradiance record of *Steinhilber et al.* [2009].

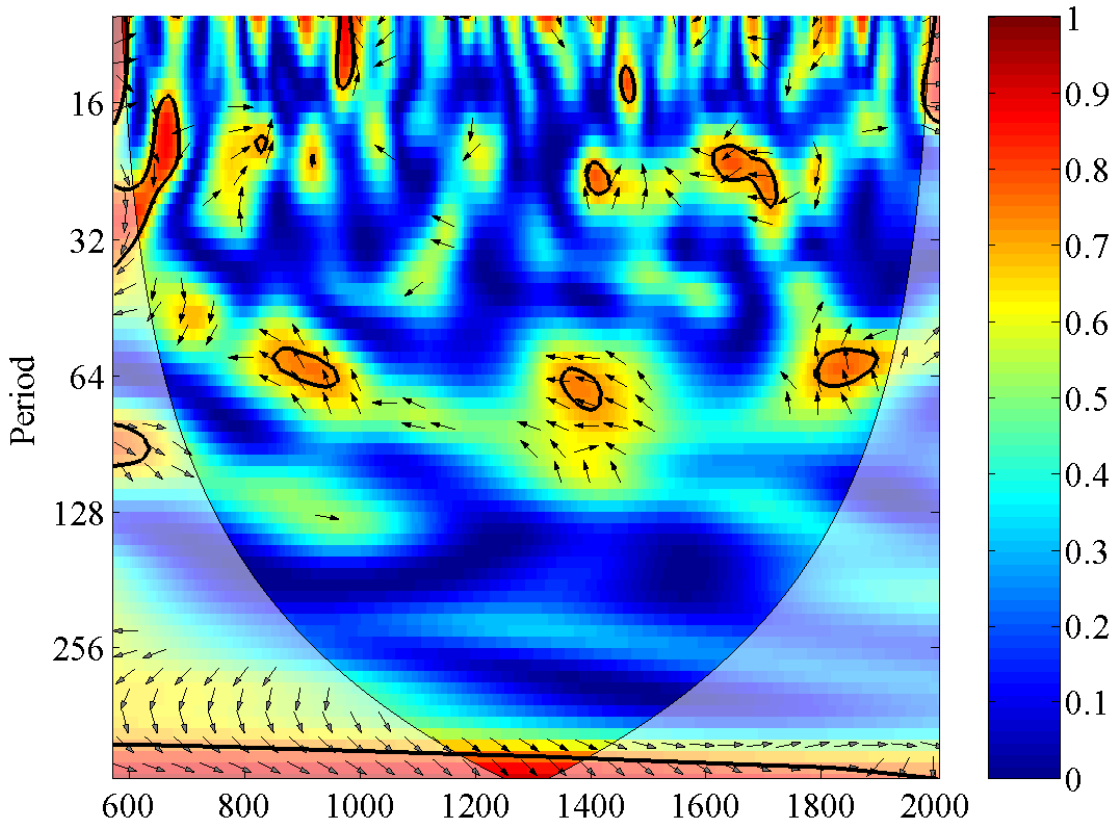

Notes: The thin black represents the COI. The 5% significance level against red noise is shown as a thick contour.

Figure B.55 | Squared wavelet coherence between the re-sampled PDSI time series for grid number 55 of the *Cook et al.* [2008] dataset and the reconstructed total solar irradiance record of *Steinhilber et al.* [2009].

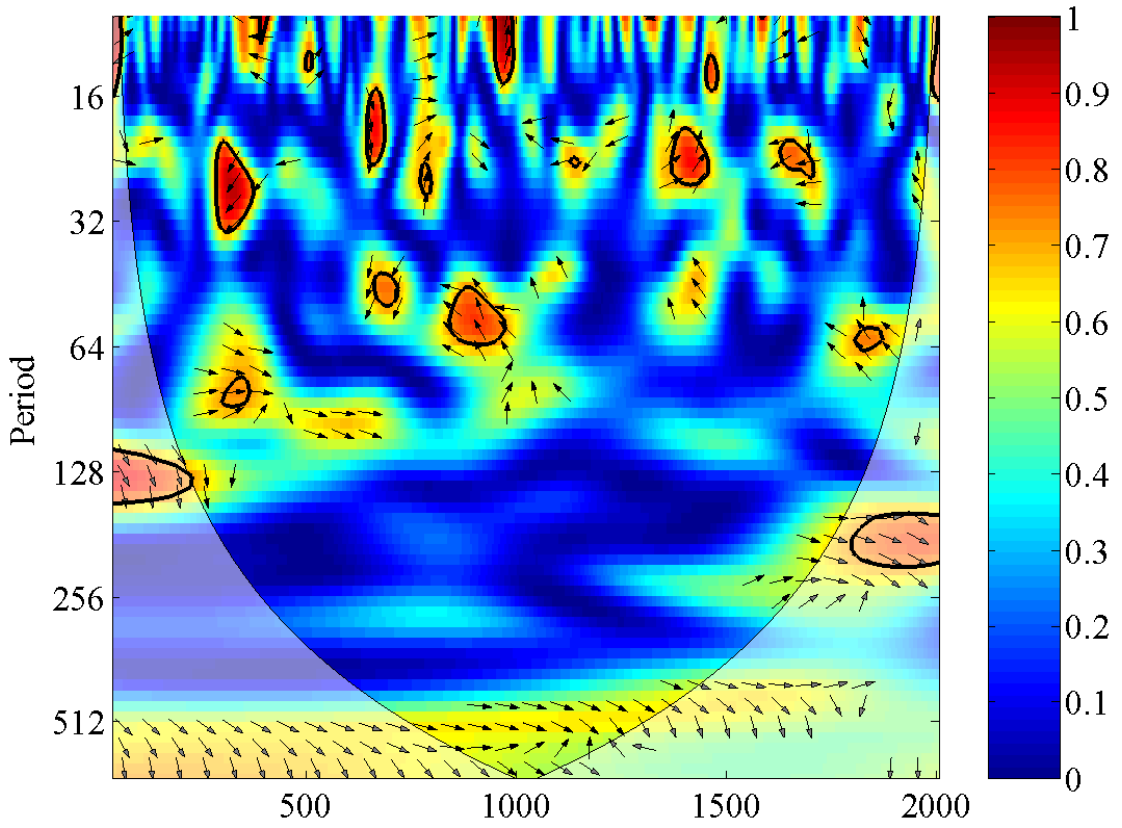

Notes: The thin black represents the COI. The 5% significance level against red noise is shown as a thick contour.

Figure B.56 | Squared wavelet coherence between the re-sampled PDSI time series for grid number 56 of the *Cook et al.* [2008] dataset and the reconstructed total solar irradiance record of *Steinhilber et al.* [2009].

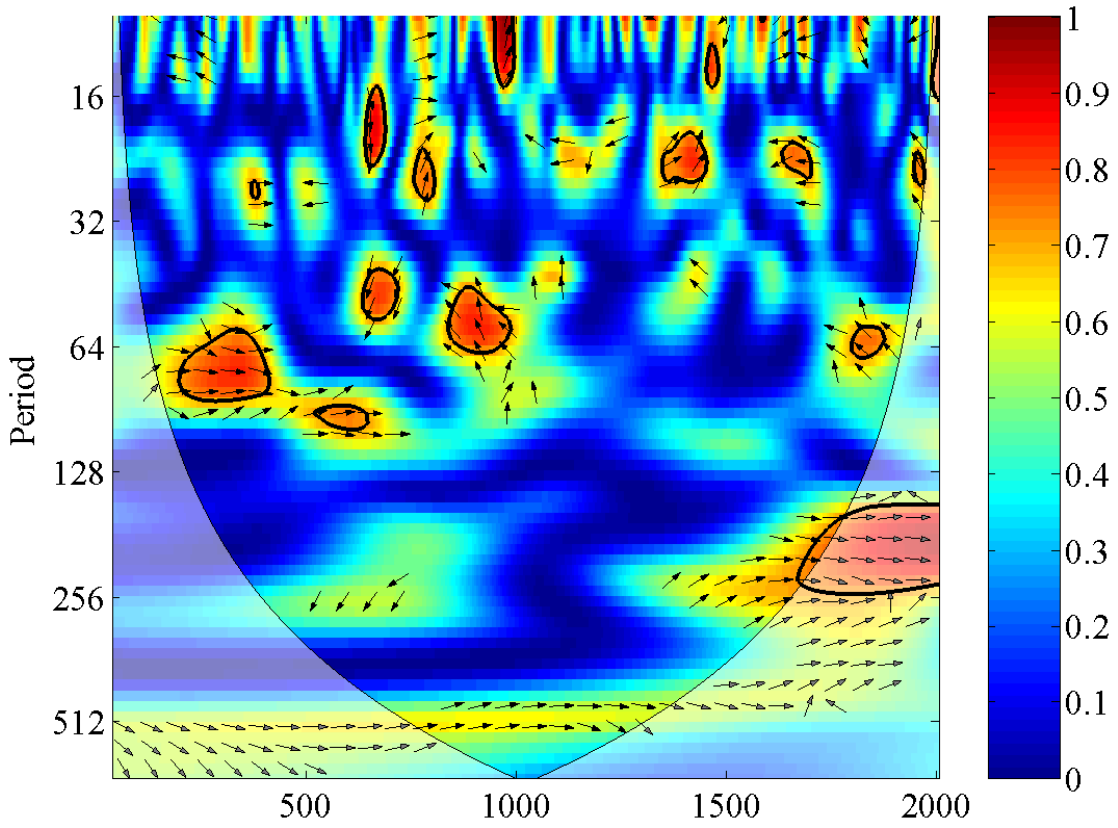

Notes: The thin black represents the COI. The 5% significance level against red noise is shown as a thick contour.

Figure B.57 | Squared wavelet coherence between the re-sampled PDSI time series for grid number 57 of the *Cook et al.* [2008] dataset and the reconstructed total solar irradiance record of *Steinhilber et al.* [2009].

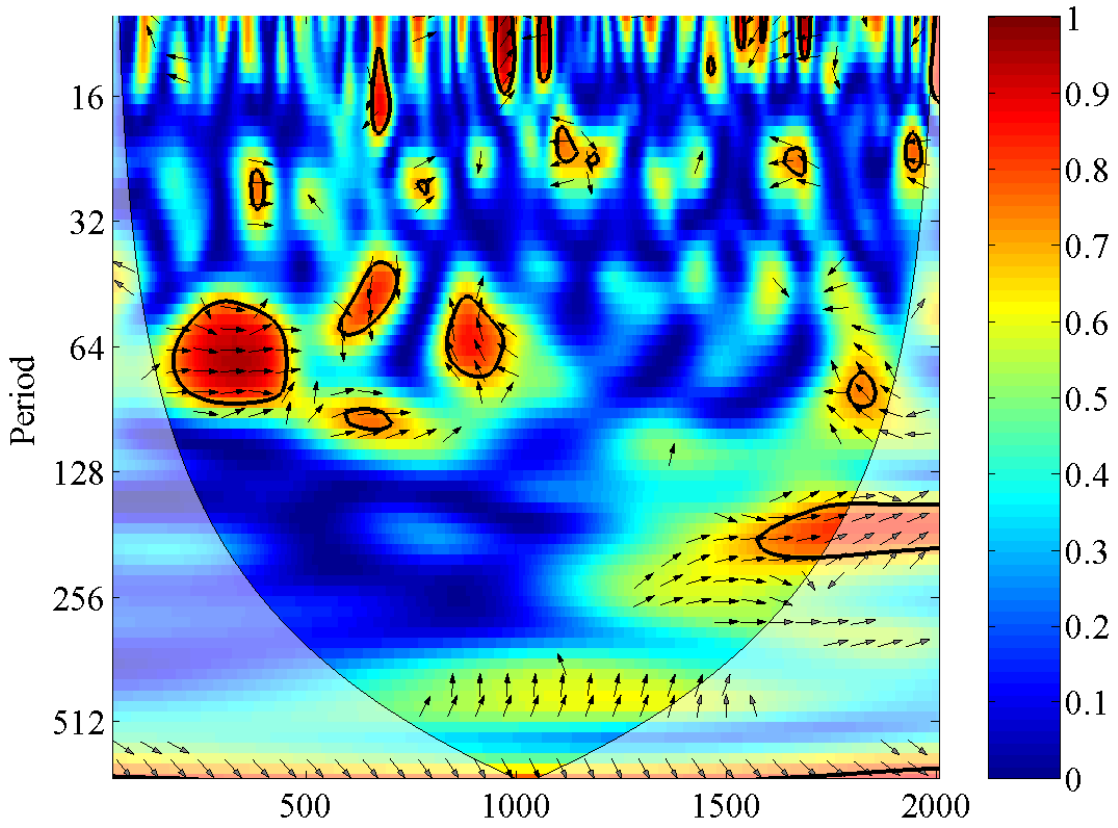

Notes: The thin black represents the COI. The 5% significance level against red noise is shown as a thick contour.

Figure B.58 | Squared wavelet coherence between the re-sampled PDSI time series for grid number 58 of the *Cook et al.* [2008] dataset and the reconstructed total solar irradiance record of *Steinhilber et al.* [2009].

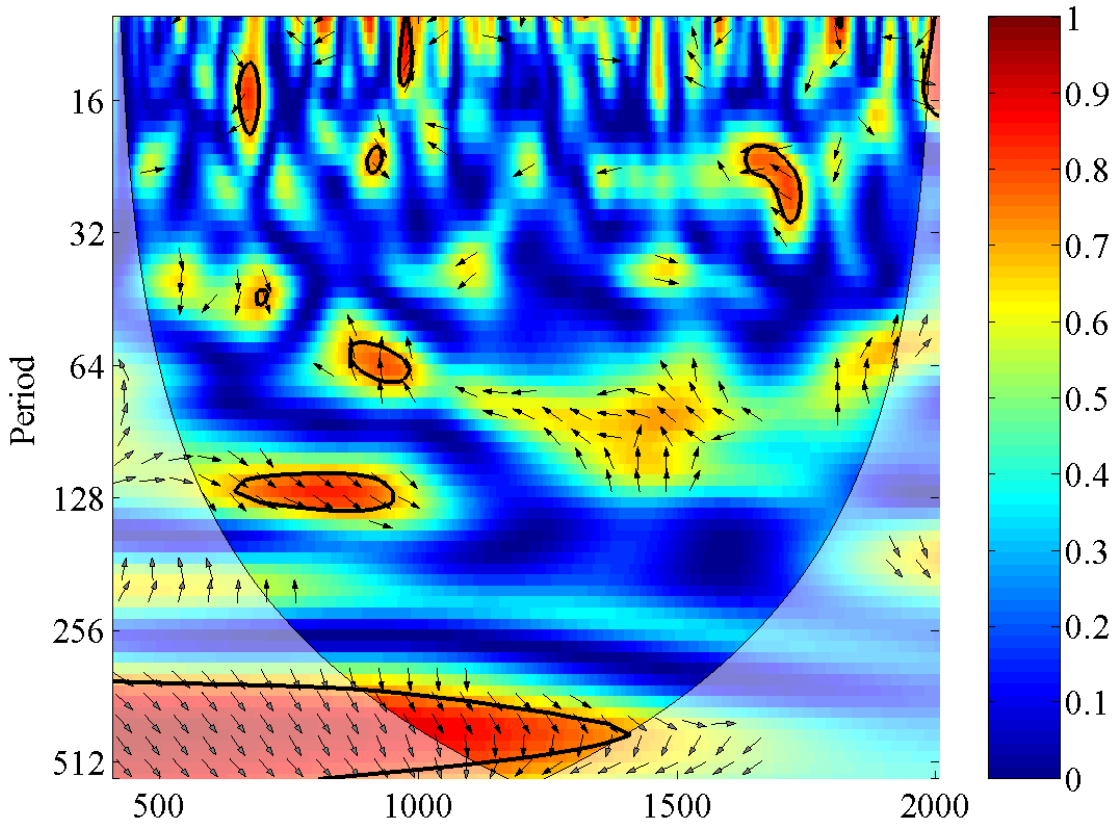

Notes: The thin black represents the COI. The 5% significance level against red noise is shown as a thick contour.

Figure B.59 | Squared wavelet coherence between the re-sampled PDSI time series for grid number 68 of the *Cook et al.* [2008] dataset and the reconstructed total solar irradiance record of *Steinhilber et al.* [2009].

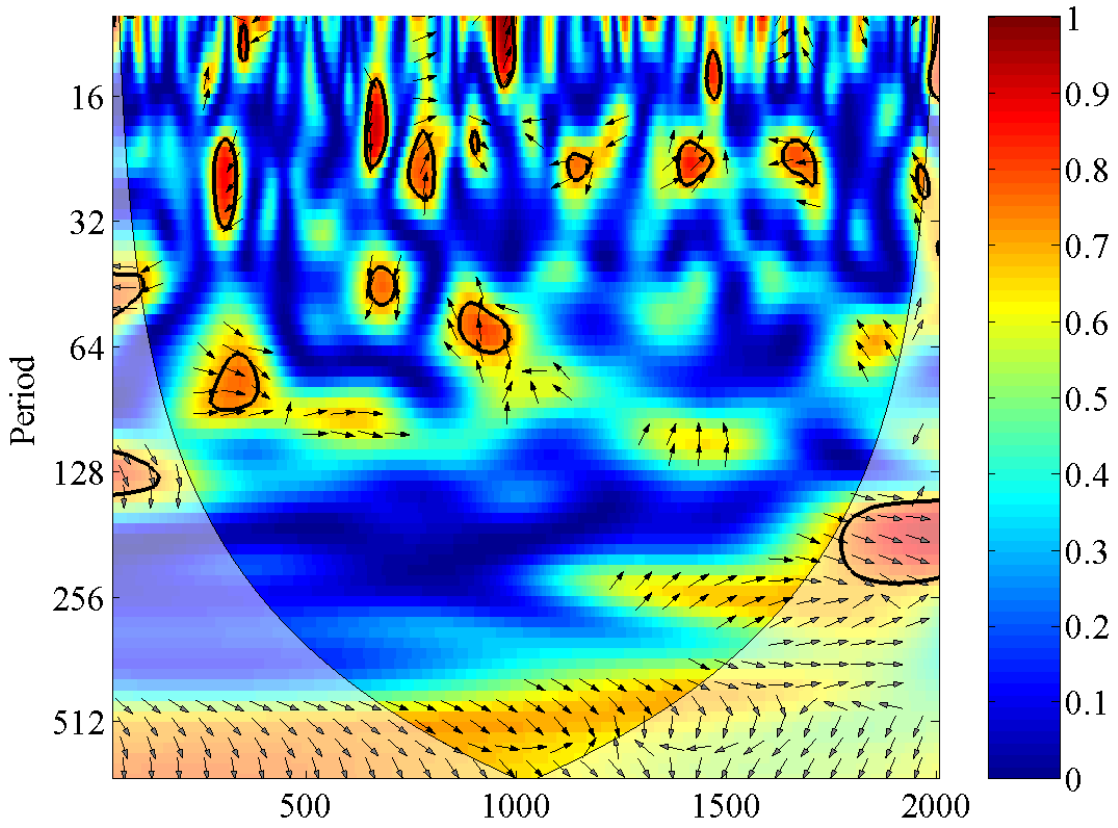

Notes: The thin black represents the COI. The 5% significance level against red noise is shown as a thick contour.

Figure B.60 | Squared wavelet coherence between the re-sampled PDSI time series for grid number 69 of the *Cook et al.* [2008] dataset and the reconstructed total solar irradiance record of *Steinhilber et al.* [2009].

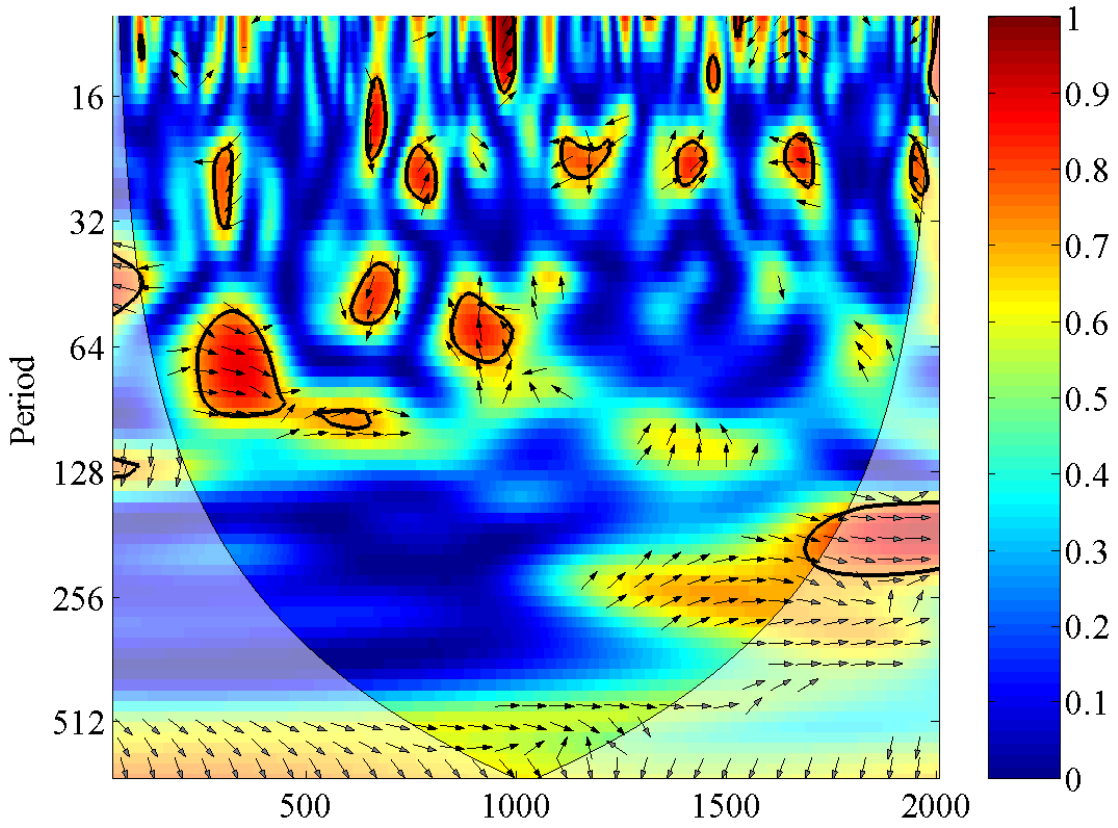

Notes: The thin black represents the COI. The 5% significance level against red noise is shown as a thick contour.

Figure B.61 | Squared wavelet coherence between the re-sampled PDSI time series for grid number 70 of the *Cook et al.* [2008] dataset and the reconstructed total solar irradiance record of *Steinhilber et al.* [2009].

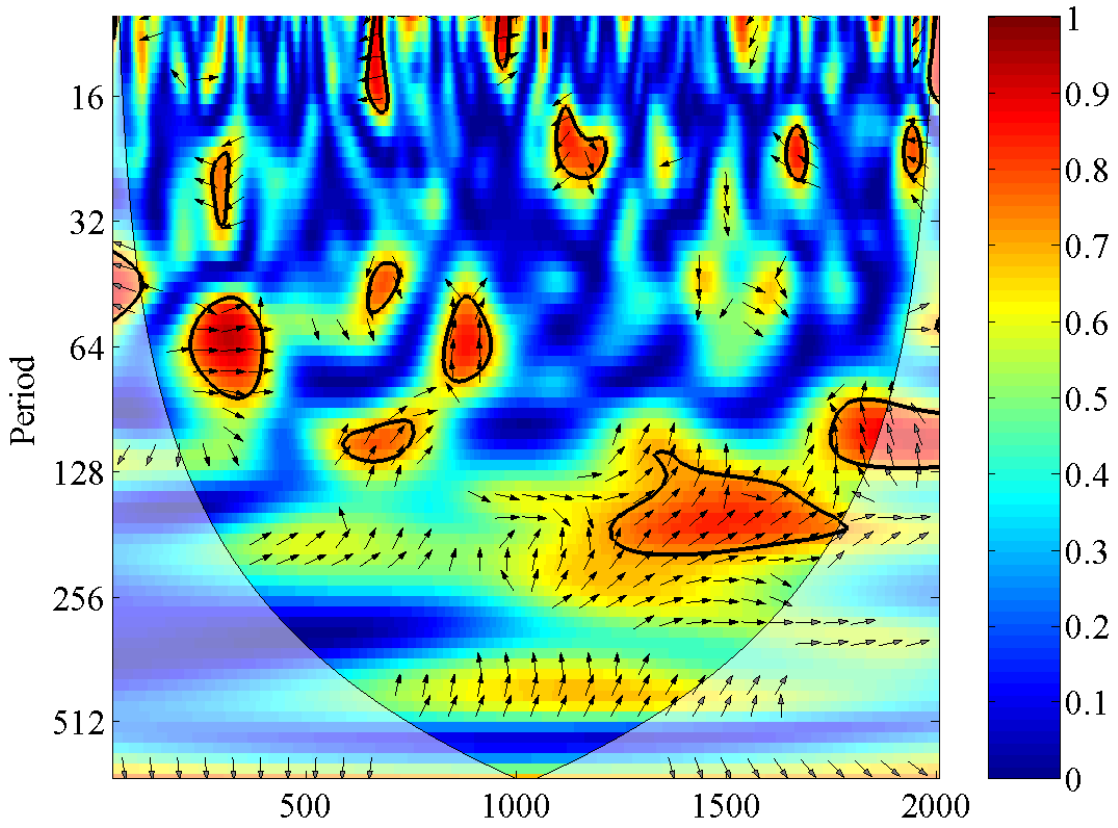

Notes: The thin black represents the COI. The 5% significance level against red noise is shown as a thick contour.

Figure B.62 | Squared wavelet coherence between the re-sampled PDSI time series for grid number 71 of the *Cook et al.* [2008] dataset and the reconstructed total solar irradiance record of *Steinhilber et al.* [2009].

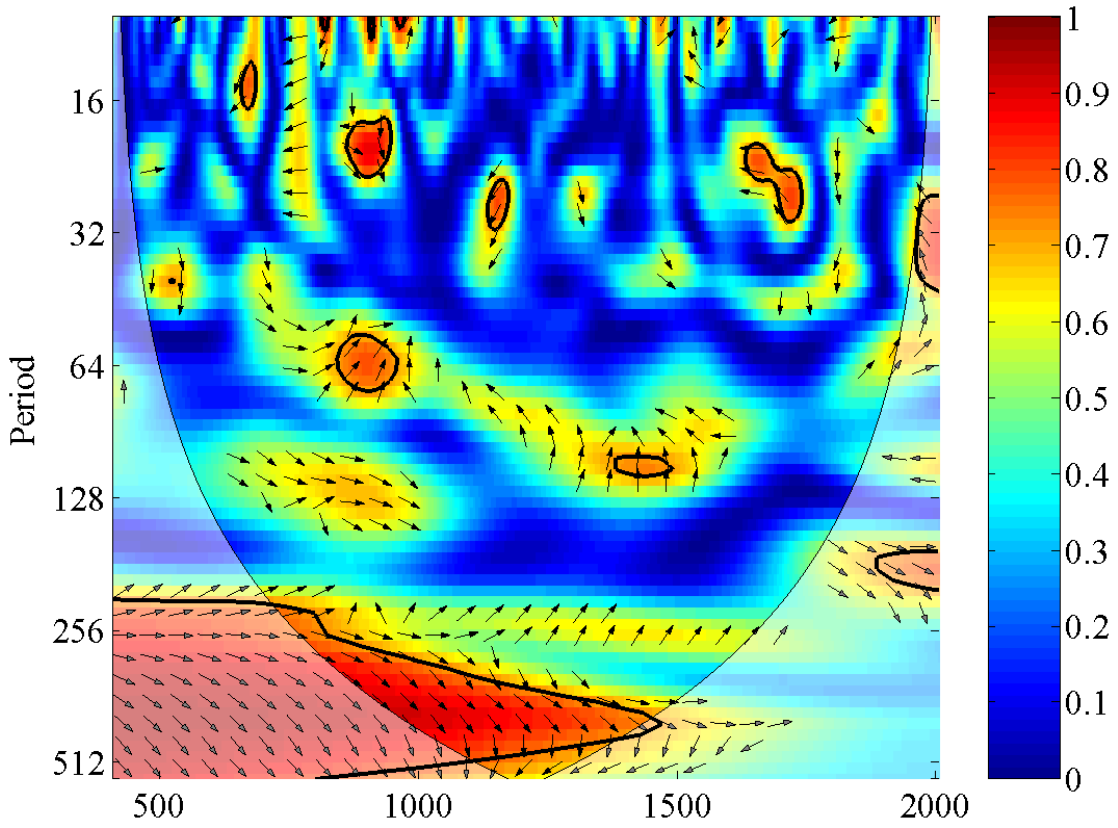

Notes: The thin black represents the COI. The 5% significance level against red noise is shown as a thick contour.

Figure B.63 | Squared wavelet coherence between the re-sampled PDSI time series for grid number 83 of the *Cook et al.* [2008] dataset and the reconstructed total solar irradiance record of *Steinhilber et al.* [2009].

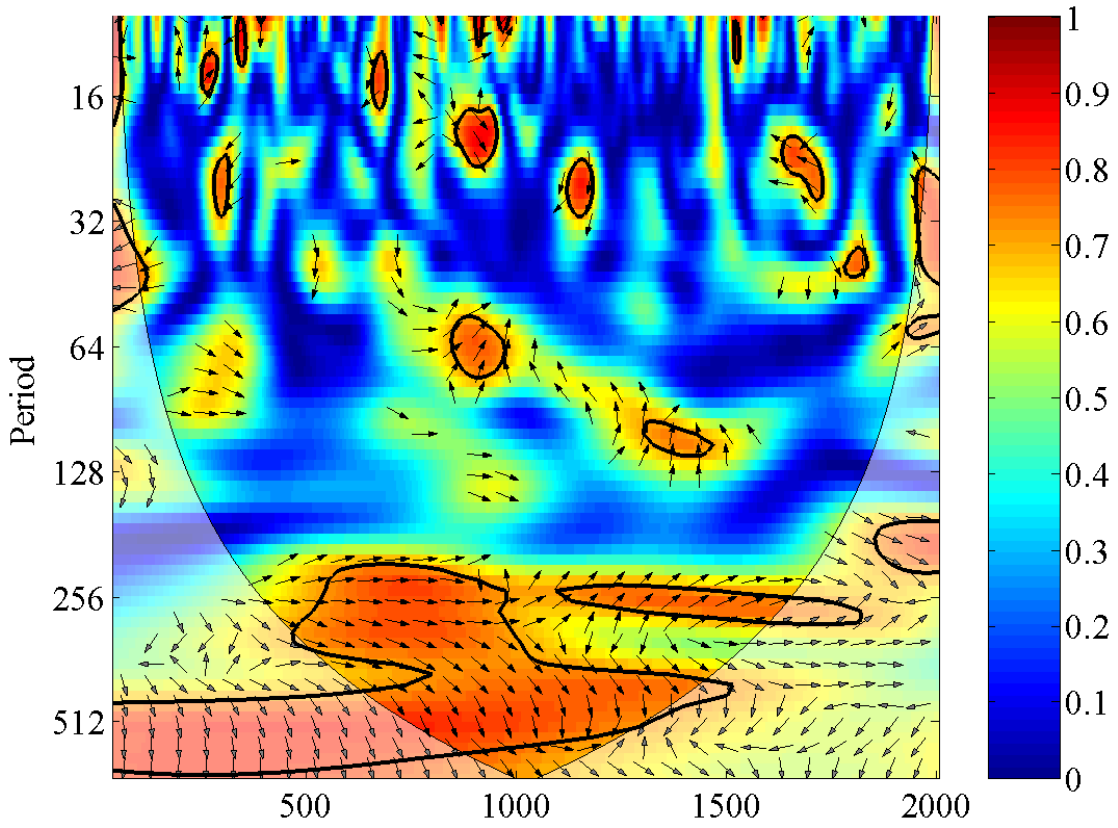

Notes: The thin black represents the COI. The 5% significance level against red noise is shown as a thick contour.

Figure B.64 | Squared wavelet coherence between the re-sampled PDSI time series for grid number 84 of the *Cook et al.* [2008] dataset and the reconstructed total solar irradiance record of *Steinhilber et al.* [2009].

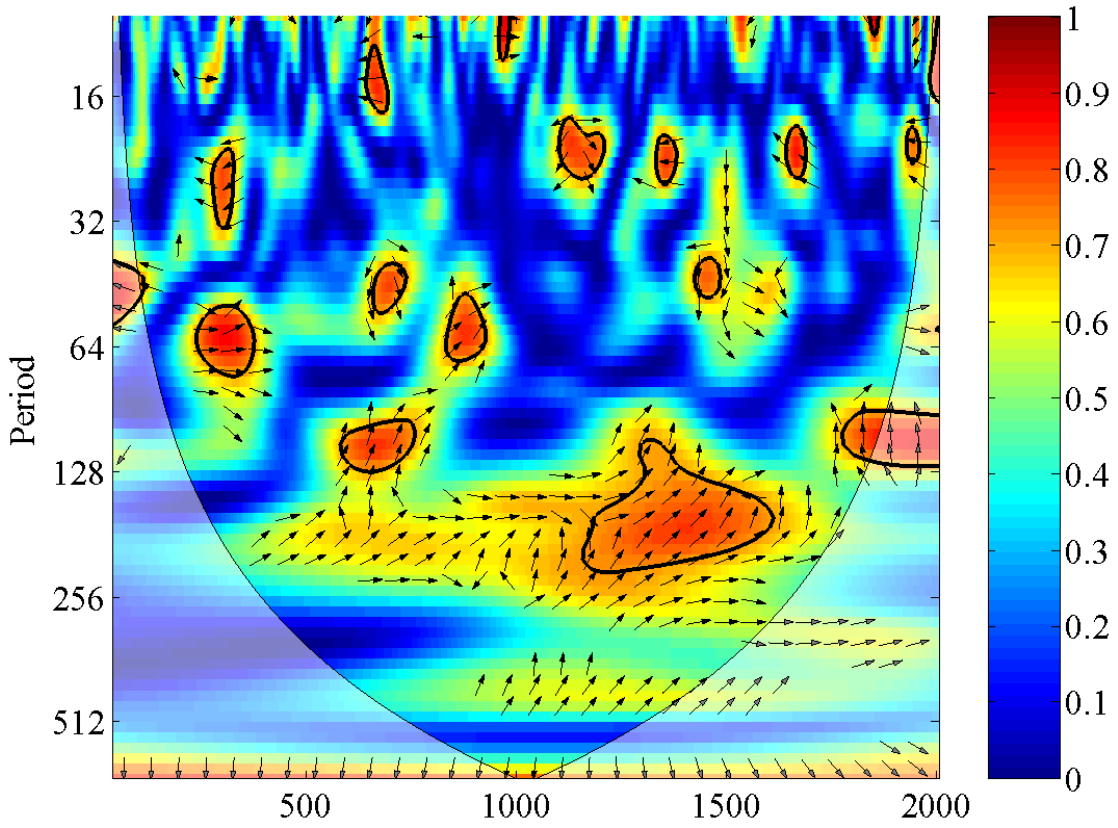

Notes: The thin black represents the COI. The 5% significance level against red noise is shown as a thick contour.

Figure B.65 | Squared wavelet coherence between the re-sampled PDSI time series for grid number 86 of the *Cook et al.* [2008] dataset and the reconstructed total solar irradiance record of *Steinhilber et al.* [2009].

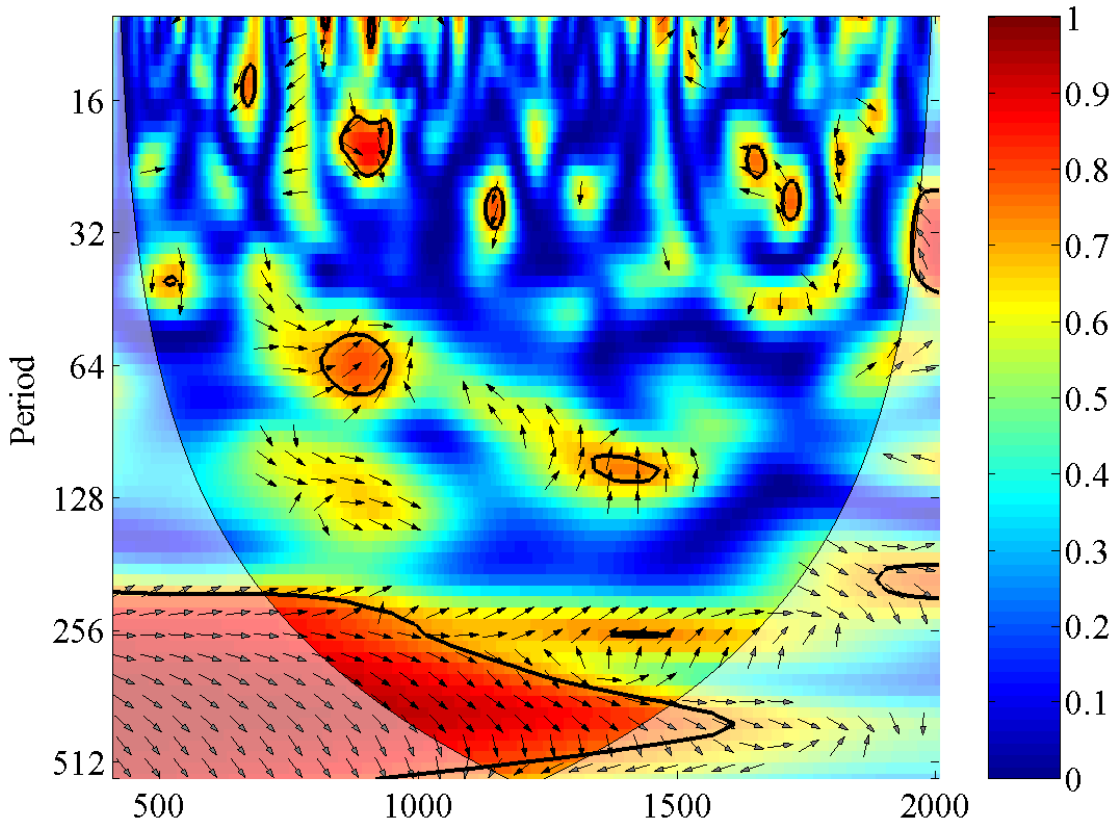

Notes: The thin black represents the COI. The 5% significance level against red noise is shown as a thick contour.

Figure B.66 | Squared wavelet coherence between the re-sampled PDSI time series for grid number 99 of the *Cook et al.* [2008] dataset and the reconstructed total solar irradiance record of *Steinhilber et al.* [2009].

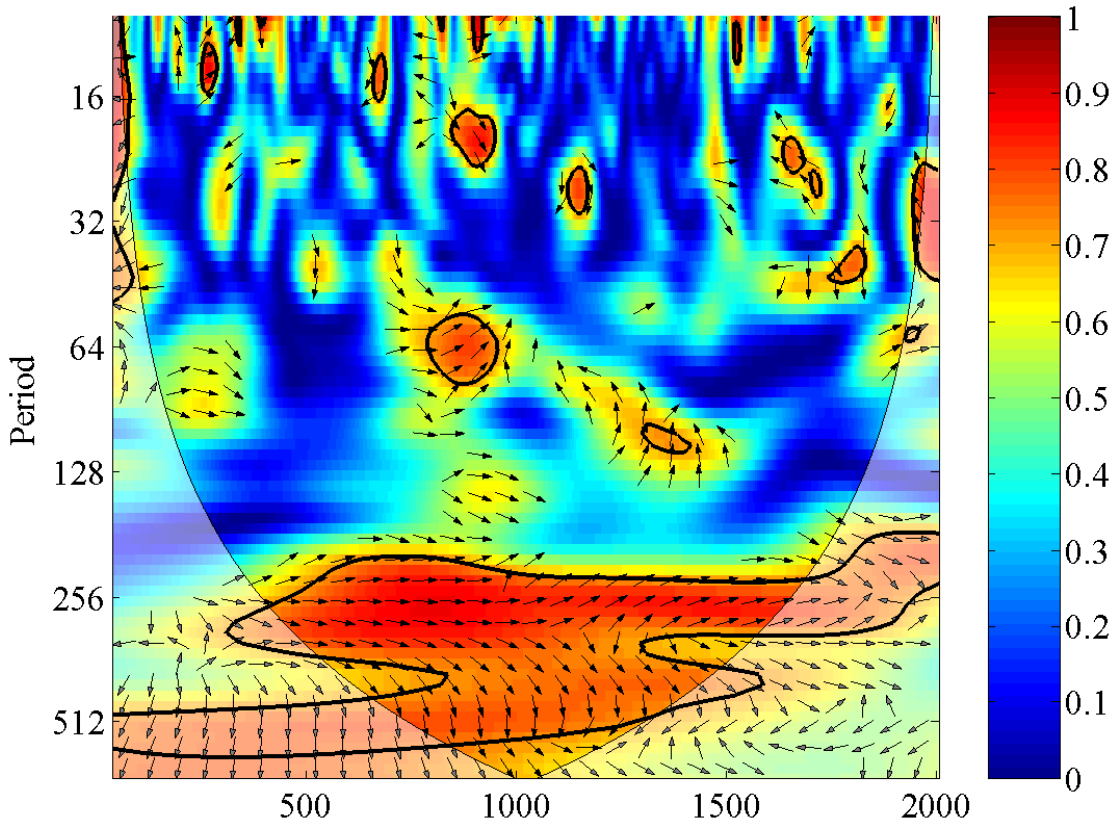

Notes: The thin black represents the COI. The 5% significance level against red noise is shown as a thick contour.

Figure B.67 | Squared wavelet coherence between the re-sampled PDSI time series for grid number 100 of the *Cook et al.* [2008] dataset and the reconstructed total solar irradiance record of *Steinhilber et al.* [2009].

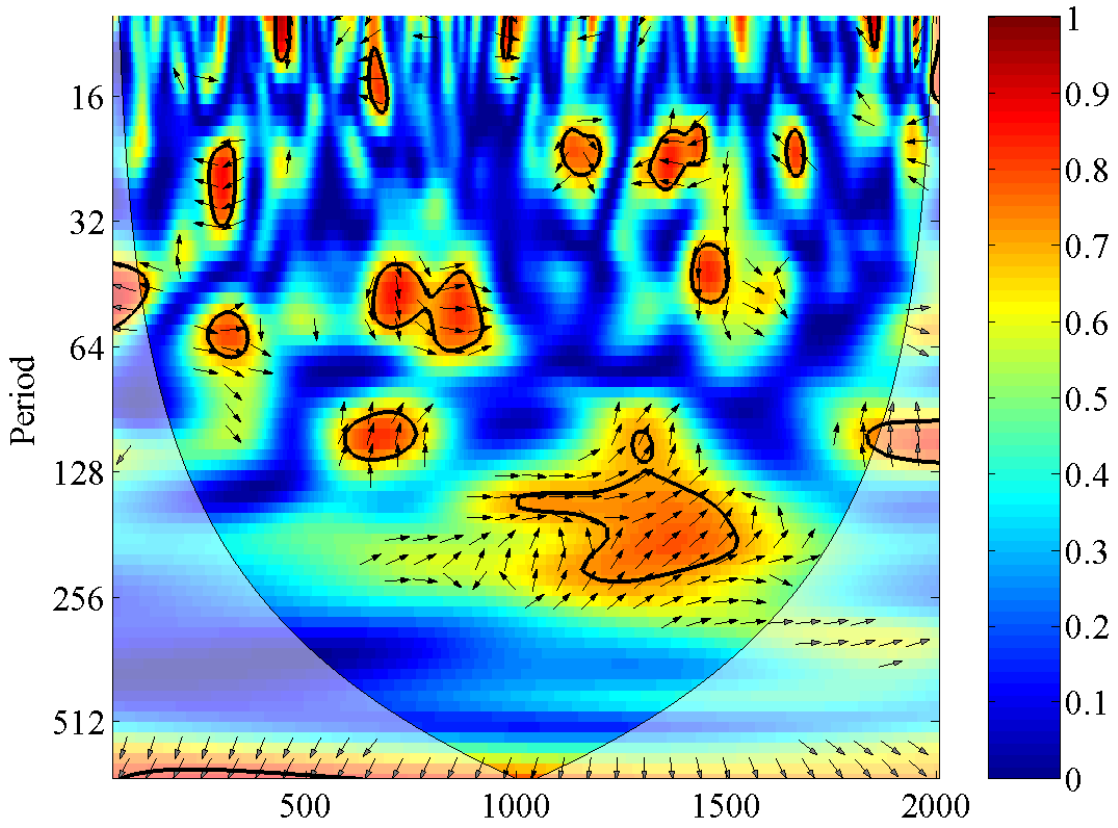

Notes: The thin black represents the COI. The 5% significance level against red noise is shown as a thick contour.

Figure B.68 | Squared wavelet coherence between the re-sampled PDSI time series for grid number 101 of the *Cook et al.* [2008] dataset and the reconstructed total solar irradiance record of *Steinhilber et al.* [2009].

APPENDIX C

FINITE ELEMENT GROUNDWATER MODEL CODE

This Appendix contains the MATLAB code for the finite element groundwater model.

C.1. MATLAB Code for Finite Element Groundwater Model

```
% MATLAB code to solve the transient groundwater flow equation using
% the finite element method. The work was done as part of a Ph.D.
% project at Vanderbilt University from 2009-2017.

% Authors: Leslie Lyons Duncan, George Hornberger
% Corresponding Author: Leslie Lyons Duncan
% (leslie.l.duncan@gmail.com)

%%%%%%%%%%%%%%%%%%%%%%%%%%%%%%%%%%%%%%%%%%%%%%%%%%%%%%%%%%%%%%%%%%%%%%%%%%%%
% DEFINITION OF VARIABLES
% NOTE: UNITS ARE GIVEN IN [BRACKETS] AND MATRIX DIMENSIONS ARE GIVEN
% IN (PARENTHESES) WHERE APPLICABLE.
%%%%%%%%%%%%%%%%%%%%%%%%%%%%%%%%%%%%%%%%%%%%%%%%%%%%%%%%%%%%%%%%%%%%%%%%%%%%

%%%%%%%%%%%%%%%%%%%%%%%%%%%%%%%%%%%%%%%%%%%%%%%%%%%%%%%%%%%%%%%%%%%%%%%%%%%%
% MAIN SCRIPT (fem_main.m) % % % % % % % % % % % % % % % % % % % % % % % % % %
%%%%%%%%%%%%%%%%%%%%%%%%%%%%%%%%%%%%%%%%%%%%%%%%%%%%%%%%%%%%%%%%%%%%%%%%%%%%
%
% NOTES:    The variable params is composed of data contained within
%           the external data file params_ROSETTA.in produced by
%           ROSETTA. ROSETTA is a USDA program that uses properties
%           from surrogate soil data (such as texture data and bulk
%           density) to estimate these hydraulic properties: (1) water
%           retention parameters according to van Genuchten (1980);
%           (2) saturated hydraulic conductivity; and (3) unsaturated
%           hydraulic conductivity parameters according to van
%           Genuchten (1980) and Mualem (1976). The van Genuchten
%           unsaturated soil hydraulic properties estimated from %
           ROSETTA were used to estimate the relatedparameters (i.e.,
%           A anc c) for the Cooley and Westphal (1974) model to
%           define unsaturated soil hydraulic properties.
%           M = NUMBER OF ELEMENTS
```

```
%           N = NUMBER OF NODES
%           U = NUMBER OF DIFFERENT GEOLOGIC UNITS
%
% Av:       Empirical parameter used to interrelate values of pressure
%           head, relative permeability, and water saturation (1xU)
% alpha:    Basis function coefficients for nodes i, j, and k for all
%           elements (Mx3)
% beta:     Basis function coefficients for nodes i, j, and k for all
%           elements (Mx3)
% beti:     Beta value for node i of element number elem (1x1)
% betj:     Beta value for node j of element number elem (1x1)
% betk:     Beta value for node k of element number elem (1x1)
% cv:       Empirical parameter used to interrelate values of pressure
%           head, relative permeability, and water saturation (1xU)
% d:        Empirical parameter used to interrelate values of pressure
%           head, relative permeability, and water saturation (1x1)
% delt:     Element area of element number elem (1x1)
% delta:    Element areas for all elements (Equation (11.3) on pg. 11-
%           3 of Hornberger and Wiberg (2005)) (Mx1)
% delta_t:  Time step [HR]
% dSedp:    The first derivative of effective saturation with respect
%           to pressure head (dSe/dpsi in Equation (5) of Cooley
%           (1983))
% dum:      Dummy variable used to calculate ksat
% elem:     Element number
% F:        Left-hand vector - i.e., the global coefficient matrix
%           plus the time derivative term matrix (NxN)
% FF:       Dummy variable from Equation (6) of Cooley (1983) used to
%           calculate zeta
% G:        Global coefficient matrix (NxN)
% gamma:    Basis function coefficients for nodes i, j, and k for all
%           elements (Mx3)
% h:        Total hydraulic head [FT] (Nx1)
% h_half:   Prediction of total hydraulic head at 1/2 time step
%           (Douglas and Jones (1963)) [FT]
% h_old:    Hydraulic head at each of N nodes at the previous time
%           step [FT] (Nx1)
% i:        Node i value of element number elem (1x1)
% j:        Node j value of element number elem (1x1)
% k:        Node k value of element number elem (1x1)
% kr:       Relative permeability, which is assumed to be a scalar
%           function of water saturation (Sw) (Equation (3) of Cooley
%           (1983)) [FT/HR] (Nx1)
% Kx:       Horizonatal saturated hydraulic conductivity in element
%           number order [FT/HR] (Mx1)
% Kz:       Vertical saturated hydraulic conductivity in element
%           number order [FT/HR] (Mx1)
% ln_pnd:   Distance between pond boundary nodes [FT]
% ln_top:   Distance between top boundary nodes (includes pond nodes)
%           [FT]
% lx_pnd:   Difference between x coordinate values for pond boundary
%           nodes [FT]
```

```
% lx_top:   Difference between x coordinate values for top boundary
%           nodes [FT]
% lz_pnd:   Difference between z coordinate values for pond boundary
%           nodes [FT]
% lz_top:   Difference between z coordinate values for top boundary
%           nodes [FT]
% n:        Porosity in element number order [DIMENSIONLESS] (Mx1)
% P:        Time derivative term matrix (NxN)
% param:    Empirical parameters (i.e., A, c, and d) used to
%           interrelate values of pressure head, relative
%           permeability, and water saturation (Cooley, 1983; Cooley
%           and Westphal, 1974) (Ux3)
% params:   van Genuchten parameter alpha (related to inverse of air
%           entry suction; row 1), van Genuchten parameter n (related
%           to pore size distribution; row 2), van Genuchten parameter
%           theta_s (saturated moisture content; row 3), van Genuchten
%           parameter theta_r (residual moisture content; row 4),
%           horizontal saturated hydraulic conductivity (row 5),
%           vertical saturated hydrualic conductivity (row 6),
%           specific storage (row 7), and porosity (row 8); there are
%           5 columns which correspond to each different geologic unit
%           (10xU)
% ph:       Pressure head at each of N nodes at the previous time step
%           [FT] (Nx1)
% ph_init:  Pressure head at each of N nodes, as determined from
%           steady state model [Nx1]
% pptr:     Hourly precipitation recharge data within simulation time
%           [FT/HR] (tx1)
% RHS:      Right-hand vector (Nx1)
% Se:       Effective saturation
% Sf:       Dummy variable from Equation (7) of Cooley (1983) used to
%           calculate zeta
% seepf:    Seepage face nodes at or below the river stage
% seepface: Seepage face nodes - i.e., all nodes along the river bank
%           that are at or below the water table
% sface:    Seepage face nodes above the river stage
% stage:    Hourly river stage data within simulation time [FT ASL]
%           (tx1)
% Sr:       Residual, or non-moving, water saturation in element
%           number order [DIMENSIONLESS] (Mx1)
% Ss:       Specific storage in element number order [1/FT] (Mx1)
% Sw:       Water saturation (varies between 0 for dry condtions and 1
%           for saturated conditions)
% Sy:       Specific yield [DIMENSIONLESS]
% t:        Number of time steps (and total simulatioin time) [HR]a
% tt:       Elapsed time within simulation [HR]
% zeta:     First term of time derivative in Equation (5) of Cooley
%           (1983)

%%%%%%%%%%%%%%%%%%%%%%%%%%%%%%%%%%%%%%%%%%%%%%%%%%%%%%%%%%%%%%%%%%%%%%%%%%%
% FUNCTIONS % % % % % % % % % % % % % % % % % % % % % % % % % % % % % % % %
```

```
%%%%%%%%%%%%%%%%%%%%%%%%%%%%%%%%%%%%%%%%%%%%%%%%%%%%%%%%%%%%%%%%%%%%%%%%%%%%

% get_mesh.m % % % % % % % % % % % % % % % % % % % % % % % % % % % % % % % % % %
%
% NOTES:     This function reads external data files produced by a mesh
%            generation software. These data files contain information
%            regarding mesh connectivities, soil type identities, and
%            boundary condition assignments.
%            M = Number OF ELEMENTS
%            N = NUMBER OF NODES
%
% coordin:   Node number (column 1), x coordinate (column 2), z
%            coordinate (column 3), and boundary condition assignment
%            (column 4) for each of N nodes (Nx4)
% ele2nd:    Elements attached to each N node (Nx10); see comments in
%            lines 70-73 of getmesh.m
% frst:      Node i (for element) or x coordinate, in feet, (for node)
%            for each data entry ((M+N)x1)
% frth:      Index specifying geologic unit type for each element
%            (index is zero for each node) ((M+N)x1)
% ind:       Index specifying the data entry type - i.e., E3T for
%            element or ND for node - within 2D_Mesh_data.2dm ((M+N)x1)
% ndbnk:     Nodes on seepage face boundary (i.e., nodes between stream
%            and no flux boundary), sorted in ascending x coordinate
%            order
% ndbtm:     Nodes on bottom boundary of mesh (i.e., z coordinate = 0),
%            sorted in ascending x coordinate order
% ndlft:     Nodes on left boundary (i.e., x coordinate = minimum),
%            sorted in descending z coordinate order
% ndpnd:     Nodes on pond boundary of mesh, sorted in ascending x
%            coordinate order
% ndrgt:     Nodes on right boundary of mesh (i.e., x coordinate =
%            maximum), sorted in ascending z coordinate order
% ndstm:     Nodes on stream boundary of mesh (i.e., nodes in stream
%            channel), sorted in ascending x coordinate order
% ndtop:     Nodes on top boundary of mesh, sorted in ascending x
%            coordinate order (includes nodes on pond boundary of mesh)
% nele2nd:   Number of elements attached to each N node (Nx1)
% nelem:     Number of elements (1x1)
% nnodes:    Number of nodes (1x1)
% node:      Nodes numbered in ascending order (Nx1)
% nodes:     i, j, and k nodes for each of M elements (Mx3)
% nodexz:    x (column 1) and z (column 2) coordinates for each of N
%            nodes (Nx2)
% num:       Element or node number for each data entry ((M+N)x1)
% scnd:      Node j (for element) or z coordinate, in feet, (for node)
%            for each data entry ((M+N)x1)
% soilid:    Index specifying geologic unit type for each of M elements
%            (Mx1)
% temp:      Temporary variable used to sort boundary nodes in
%            ascending order, based either on the the x or z
```

```
%           coordinates
% thrd:     Node k (for element) or placeholder - i.e., zero - (for
%           node) for each data entry  ((M+N)x1)

% SeD.m % % % % % % % % % % % % % % % % % % % % % % % % % % % % % % % % % % %
%
% NOTES:    This function calculates the effective saturation from
%           pressure head and the empirical parameters A, c, and d
%           (Cooley, 1983; Cooley and Westphal, 1974).
%           N = NUMBER OF NODES
%           U = NUMBER OF GEOLOGIC UNITS
%
% A:        Empirical parameter, for each of U geologic units, used to
%           interrelate values of pressure head, relative
%           permeability, and water saturation repeated N times in
%           adjoining columns (NxU)
% c:        Empirical parameter, for each of U geologic units, used to
%           interrelate values of pressure head, relative
%           permeability, and water saturation repeated N times in
%           adjoining columns (NxU)
% nr:       Number of rows in the variable param (equal to the number
%           of geologic units)
% ph:       Pressure head at each of N nodes at the previous time step
%           [FT] (Nx1)
% phm:      Matrix of pressure head at each of N nodes at the previous
%           time step repeated in adjoining columns for each of U
%           geologic units [FT] (NxU)
% Se:       Effective saturation at each of N nodes for each of U
%           geologic units (NxU)

% dSedp.m % % % % % % % % % % % % % % % % % % % % % % % % % % % % % % % % % %
%
% NOTES:    This function calculates the first derivative of effective
%           saturation (Se) with respect to pressure head (ph). This
%           function uses pressure head and the empirical parameters %
           A, c, and d (Cooley, 1983; Cooley and Westphal, 1974).
%          N  = NUMBER OF NODES
%          U = NUMBER OF GEOLOGIC UNITS
%
% A:        Empirical parameter, for each of U geologic units, used to
%           interrelate values of pressure head, relative
%           permeability, and water saturation repeated N times in
%           adjoining columns (NxU)
% c:        Empirical parameter, for each of U geologic units, used to
%           interrelate values of pressure head, relative
%           permeability, and water saturation repeated N times in
%           adjoining columns (NxU)
% dSedp:    The first derivative of effective saturation with respect
%           to pressure head (dSe/dpsi in Equation (5) of Cooley
%           (1983)) at each of N nodes for each of U geologic units
%           (NxU)
```

```
% nr:        Number of rows in the variable param (equal to the number
%            geologic units)
% ph:        Pressure head at each of N nodes at the previous time step
%            [FT] (Nx1)
% phm:       Matrix of pressure head at each of N nodes at the previous
%            time step repeated in adjoining columns for each of U
%            geologic units [FT] (NxU)

% krelt.m % % % % % % % % % % % % % % % % % % % % % % % % % % % % % % % %
%
% NOTES:     This function calculates the relative permeability, which
%            is assumed to be a scalar function of water saturation
%            (Sw). This function uses pressure head and the empirical
%            parameters A, c, and d (Cooley, 1983; Cooley and Westphal,
%            1974).
%            N = NUMBER OF NODES
%            U = NUMBER OF GEOLOGIC UNITS
%
% A:         Empirical parameter, for each of U geologic units, used to
%            interrelate values of pressure head, relative
%            permeability, and water saturation repeated N times in
%            adjoining columns (NxU)
% c:         Empirical parameter, for each of U geologic units, used to
%            interrelate values of pressure head, relative permeability
%            permeability, and water saturation repeated N times in
%            adjoining columns (NxU)
% d:         Empirical parameter used to interrelate values of pressure
%            head, relative permeability, and water saturation repeated
%            N times in adjoining U columns (NxU)
% kr:        Relative permeability, which is assumed to be a scalar
%            function of water saturation (Sw), at each of N nodes for
%            each of U geologic units (NxU) (Equation (3) of Cooley
%            (1983)) (NxU)
% ph:        Pressure head at each of N nodes at the previous time step
%            [FT] (Nx1)
% phm:       Matrix of pressure head at each of N nodes at the previous
%            time step repeated in adjoining columns for each of U
%            geologic units [FT] (NxU)

%%%%%%%%%%%%%%%%%%%%%%%%%%%%%%%%%%%%%%%%%%%%%%%%%%%%%%%%%%%%%%%%%%%%%%%%
% REFERENCES % % % % % % % % % % % % % % % % % % % % % % % % % % % % % % %
%%%%%%%%%%%%%%%%%%%%%%%%%%%%%%%%%%%%%%%%%%%%%%%%%%%%%%%%%%%%%%%%%%%%%%%%

% Brooks, R. H., and A. T. Corey (1966). Properties of porous media
% affecting fluid flow. J. Irrig. Drain. Div. Am. Soc. Civ. Eng.
% 92(IR2): 61-68.

% Cooley, R. L. (1983). Some neew procedures for numerical solution of
% variably saturated flow problems. Water Resour. Res. 19(5):1271-
% 1285.
```

```
% Cooley, R. L. and J. A. Westphal (1974). An evaluation of the theory
% of ground-water and river-water interchange, Winnemucca Reach of the
% Humboldt River, Nevada. Hydrol. Water Resour. Publ. 19, 74 pp.,
% Cent. For Water Resour. Res., Univ. of Nev., Reno.

% Douglas, J. J. and B. F. Jones (1963). On predictor-corrector method
% for non-linear paraboloc differential equations. J. SIAM, 11: 195
% 204.

% Hornberger, G. and P. Wiberg (2005). Numerical Methods in the
% Hydrological Sciences. AGU, Washington, DC.

% Mualem, Y. (1976). A new model predicting the hydraulic conductivity
% of unsaturated porous media. Water Resour. Res. 12: 513-522.

% van Genuchten, M. Th. (1980). A closed-form equation for predicting
% the hydraulic conductivity of unsaturated soils. Soil Sci. Am. J.
% 44: 892-898.

%% MATLAB CODE
%%%%%%%%%%%%%%%%%%%%%%%%%%%%%%%%%%%%%%%%%%%%%%%%%%%%%%%%%%%%%%%%%%%%%%%%

%%%%%%%%%%%%%%%%%%%%%%%%%%%%%%%%%%%%%%%%%%%%%%%%%%%%%%%%%%%%%%%%%%%%%%%%
% BEGIN % % % % % % % % % % % % % % % %  % % % % % % % % % % % % % % % %
%%%%%%%%%%%%%%%%%%%%%%%%%%%%%%%%%%%%%%%%%%%%%%%%%%%%%%%%%%%%%%%%%%%%%%%%

tic
clear all;
clc;

%%%%%%%%%%%%%%%%%%%%%%%%%%%%%%%%%%%%%%%%%%%%%%%%%%%%%%%%%%%%%%%%%%%%%%%%
% READ IN EXTERNALLY CREATED MESH % % % % % % % % % % % % % % % % % % % %
%%%%%%%%%%%%%%%%%%%%%%%%%%%%%%%%%%%%%%%%%%%%%%%%%%%%%%%%%%%%%%%%%%%%%%%%

[nodexz nodes nnodes nelem nbnd nbes belnd bnode bdrynode ndbnk ...
 ndbtm ndlft ndrgt ndstm ndtop Neumann channd nchand eletobn ...
 nchanes elechan ele2nd nele2nd soilid tbnode] = getmesh_test;

clearvars coordin ndbtm ndlft ele2nd nele2nd

%%%%%%%%%%%%%%%%%%%%%%%%%%%%%%%%%%%%%%%%%%%%%%%%%%%%%%%%%%%%%%%%%%%%%%%%
% DEFINE UNSATURATED AND SATURATED SOIL HYDRAULIC PROPERTIES
%%%%%%%%%%%%%%%%%%%%%%%%%%%%%%%%%%%%%%%%%%%%%%%%%%%%%%%%%%%%%%%%%%%%%%%%

fid = fopen('params_ROSETTA.in');
CC = textscan(fid,'%s %f %f %f %f %f','headerlines',1);
params(:,1) = CC{1,2};
params(:,2) = CC{1,3};
params(:,3) = CC{1,4};
params(:,4) = CC{1,5};
```

```
params(:,5) = CC{1,6};

clearvars CC

dum = ones(nelem,1);

% Assign residual water saturation based on geologic unit type
Sr(:,1) = dum*params(4,1);
Sr(soilid == 2,1) = dum(soilid == 2)*params(4,2);
Sr(soilid == 3,1) = dum(soilid == 3)*params(4,3);
Sr(soilid == 4,1) = dum(soilid == 4)*params(4,4);
Sr(soilid == 5,1) = dum(soilid == 5)*params(4,5);

% Hydraulic conductivity values are multiplied by 1.4273, since
% initial groundwater model results indicated that original hydraulic
% conductivity values were too small to push desired rate of water
% through the domain.
% Assign horizontal hydraulic conductivity, Kx, based on geologic unit
% type
Kx(:,1) = dum*params(5,1)*1.4273;
Kx(soilid == 2,1) = dum(soilid == 2)*params(5,2)*1.4273;
Kx(soilid == 3,1) = dum(soilid == 3)*params(5,3)*1.4273;
Kx(soilid == 4,1) = dum(soilid == 4)*params(5,4)*1.4273;
Kx(soilid == 5,1) = dum(soilid == 5)*params(5,5)*1.4273;

% Assign vertical hydraulic conductivity, Kz, based on geologic unit
% type
Kz(:,1) = dum*params(6,1)*1.4273;
Kz(soilid == 2,1) = dum(soilid == 2)*params(6,2)*1.4273;
Kz(soilid == 3,1) = dum(soilid == 3)*params(6,3)*1.4273;
Kz(soilid == 4,1) = dum(soilid == 4)*params(6,4)*1.4273;
Kz(soilid == 5,1) = dum(soilid == 5)*params(6,5)*1.4273;

% Assign specific storage, Ss, based on geologic unit type
Ss(:,1) = dum*params(7,1);
Ss(soilid == 2,1) = dum(soilid == 2)*params(7,2);
Ss(soilid == 3,1) = dum(soilid == 3)*params(7,3);
Ss(soilid == 4,1) = dum(soilid == 4)*params(7,4);
Ss(soilid == 5,1) = dum(soilid == 5)*params(7,5);

% Assign porosity, pors, based on geologic unit type
pors(:,1) = dum*params(8,1);
pors(soilid == 2,1) = dum(soilid == 2)*params(8,2);
pors(soilid == 3,1) = dum(soilid == 3)*params(8,3);
pors(soilid == 4,1) = dum(soilid == 4)*params(8,4);
pors(soilid == 5,1) = dum(soilid == 5)*params(8,5);

% Assign Cooley and Westphal empirical parameter A based on geologic
% unit type
A(:,1) = dum*6;
A(soilid == 2,1) = dum(soilid == 2)*3.1;
```

```
A(soilid == 3,1) = dum(soilid == 3)*2;
A(soilid == 4,1) = dum(soilid == 4)*2.2;
A(soilid == 5,1) = dum(soilid == 5)*3.4;

% Assign Cooley and Westphal empirical parameter A based on geologic
% unit type
c(:,1) = dum*1.2;
c(soilid == 2,1) = dum(soilid == 2)*0.7;
c(soilid == 3,1) = dum(soilid == 3)*0.3;
c(soilid == 4,1) = dum(soilid == 4)*0.2;
c(soilid == 5,1) = dum(soilid == 5)*0.8;

% Assign van Genuchten parameter alpha based on geologic unit type
alpha(:,1) = dum*params(1,1);
alpha(soilid == 2,1) = dum(soilid == 2)*params(1,2);
alpha(soilid == 3,1) = dum(soilid == 3)*params(1,3);
alpha(soilid == 4,1) = dum(soilid == 4)*params(1,4);
alpha(soilid == 5,1) = dum(soilid == 5)*params(1,5);

% Assign van Genuchten parameter n based on geologic unit type.
n(:,1) = dum*params(2,1);
n(soilid == 2,1) = dum(soilid == 2)*params(2,2);
n(soilid == 3,1) = dum(soilid == 3)*params(2,3);
n(soilid == 4,1) = dum(soilid == 4)*params(2,4);
n(soilid == 5,1) = dum(soilid == 5)*params(2,5);

alphav = params(1,:);
nv = params(2,:);
% Calculate air entry pressure using van Genuchten parameters alpha
% and n.
hae = ((1-(1./nv)).^(1./nv))./alphav;

Av = [6; 3.1; 2; 2.2; 3.4];
cv = [1.2; 0.7; 0.3; 0.2; 0.8];
d = repmat(2,5,1); % This exponent almost always is between 3 and 4
                   % (Brooks and Corey, 1966). However, Gu (2008) uses
                   % 2.
param = [Av cv d hae'];
FF = Sr./(1-Sr); % Equation (6) of Cooley (1983)
Sf = (1-Sr).*Ss; % Equation (7) of Cooley (1983)
Sy = (1-Sr).*pors; % Equation (8) of Cooley (1983)

%%%%%%%%%%%%%%%%%%%%%%%%%%%%%%%%%%%%%%%%%%%%%%%%%%%%%%%%%%%%%%%%%%%%%%%%%%%%
% LOAD DATA % % % % % % % % % % % % % % % % % % % % % % % % % % % % % % % % %
%%%%%%%%%%%%%%%%%%%%%%%%%%%%%%%%%%%%%%%%%%%%%%%%%%%%%%%%%%%%%%%%%%%%%%%%%%%%

% Set hourly river stage for 10 years
% BASE, CLIMATE, AND POND SIMULATIONS
stage = ones(3652*24,1)*386.3400;

% Set hourly precipitation recharge for 10 years
```

```
% BASE, WEEKLY HYDROGRAPH, AND ANNUAL HYDROGRAPH SIMULATIONS
pptr = ones(3652*24,1)*7.4905*10^(-6); % base precipitation recharge
                                       % rate of 20 mm/yr
% CLIMATE SIMULATION - i.e., INCREASED RECHARGE FROM PRECIPITATION
% pptr = ones(3652*24,1)*(7.4905*(10^(-6))*2); % double the
%                                               % precipitation
%                                               % recharge rate of
%                                               % 20 mm/yr

% POND SIMULATION
% pptr = ones(3652*2*24,1)*7.4905*10^(-6); % base precipitation
%                                          % recharge rate of 20
%                                          % mm/yr (for 20 years)

% % Set hourly pond recharge for 20 years - 10x the "normal"
% % precipitation recharge rate of 20 mm/yr for the first 10 years and
% % zero thereafter
% pondr = [ones(3652*24,1)*7.4905*10^(-5); zeros(3652*24,1)];

% Load steady state head data - this serves as the initial
% condition for the dynamic model
% BASE SIMULATION
ph_init = load('h.nonlinear_LI_newmesh_RGT527-65_Kx1-4');
h_old = ph_init + nodexz(:,2);
% CLIMATE SIMULATION - i.e., INCREASED RECHARGE FROM PRECIPITATION
% ph_init = load('h.nonlinear_LI_newmesh_RGT658-65_Kx1-4');
% h_old = ph_init + nodexz(:,2);
% WEEKLY HYDROGRAPH, ANNUAL HYDROGRAPH, AND POND SIMULATIONS
% h_init = load('h_out_Lesmesh_pptr_anisohetero_9-26-16_RGT527-65_Kx1-
4.txt');
% h_init = reshape(h_init,nnodes,length(h_init)/nnodes);
% h_old = h_init(:,end);

delta_t = 1;
t = length(pptr);

clearvars h_init

%%%%%%%%%%%%%%%%%%%%%%%%%%%%%%%%%%%%%%%%%%%%%%%%%%%%%%%%%%%%%%%%%%%%%%%%%%%
% CALCULATE TOP ELEMENT DIMENSIONS (USED TO CALCULATE NORMAL RECHARGE)
%%%%%%%%%%%%%%%%%%%%%%%%%%%%%%%%%%%%%%%%%%%%%%%%%%%%%%%%%%%%%%%%%%%%%%%%%%%

temp = [ndbnk(end); ndtop];  % Add an extra node for the beginning of
                             % the Neumann (i.e., flux) boundary nodes
                             % vector so that the lengths of the top
                             % boundary elements can be calculated.
                             % NOTE: This may have to be changed
                             % depending on the particular mesh and
                             % boundary conditions,

lx_top = diff(nodexz(temp,1));
```

```
lz_top = diff(nodexz(temp,2));
ln_top = sqrt(lz_top.^2 + lx_top.^2);

clearvars temp

% POND SIMULATION
% ndpnd = ndtop(nodexz(ndtop,1)>8000 & nodexz(ndtop,1)<8800);
% temp = ndtop(nodexz(ndtop,1)>=8000 & nodexz(ndtop,1)<=8800);
%
% lx_pnd = diff(nodexz(temp,1));
% lz_pnd = diff(nodexz(temp,2));
% ln_pnd = sqrt(lz_pnd.^2 + lx_pnd.^2);
%
% clearvars temp

%%%%%%%%%%%%%%%%%%%%%%%%%%%%%%%%%%%%%%%%%%%%%%%%%%%%%%%%%%%%%%%%%%%%%%%%%%%%%%%
% PRE-ASSIGN VARIABLE MATRICES % % % % % % % % % % % % % % % % % % % % % % % % %
%%%%%%%%%%%%%%%%%%%%%%%%%%%%%%%%%%%%%%%%%%%%%%%%%%%%%%%%%%%%%%%%%%%%%%%%%%%%%%%

% This improves computation speed.
G = zeros(nnodes,nnodes);
hs = zeros(1,t);
P = zeros(nnodes,nnodes);
RHS = zeros(nnodes,1);

%%%%%%%%%%%%%%%%%%%%%%%%%%%%%%%%%%%%%%%%%%%%%%%%%%%%%%%%%%%%%%%%%%%%%%%%%%%%%%%
% FLOW SIMULATION % % % % % % % % % % % % % % % % % % % % % % % % % % % % % % % %
%%%%%%%%%%%%%%%%%%%%%%%%%%%%%%%%%%%%%%%%%%%%%%%%%%%%%%%%%%%%%%%%%%%%%%%%%%%%%%%

for ii = 1:(t/2)
    disp(['ii = ',num2str(ii),'/',num2str(t)])

    % Set river stage at time step ii
    hs(ii) = stage(ii);

    % Determine seepage face
    seepface = ndbnk(h_old(ndbnk) >= nodexz(ndbnk,2));
    seepf = ndbnk(nodexz(ndbnk,2) <= hs(ii));

    % Hydraulic Properties and Associated Terms from Cooley and
    % Westphal Model (Cooley, 1983; Cooley and Westphal, 1974)
    ph = h_old - nodexz(:,2);
    Se = SwD_hetero(param,ph);
    dSep = dswdp_hetero(param,ph);
    kr = krelt_hetero(param,ph);

    G = zeros(nnodes,nnodes);
    P = zeros(nnodes,nnodes);
    F = zeros(nnodes,nnodes);
    RHS = zeros(nnodes,1);
```

```
for elem = 1:nelem
    % Retrieve i, j, and k node values for element number elem
    % from the mesh connectivity table.
    i = nodes(elem,1);
    j = nodes(elem,2);
    k = nodes(elem,3);

    % Retrieve i, j, and k beta values for element number elem.
    beti = nodexz(j,2)-nodexz(k,2);
    betj = nodexz(k,2)-nodexz(i,2);
    betk = nodexz(i,2)-nodexz(j,2);

    % Retrieve i, j, and k gamma values for element number elem.
    gami = nodexz(k,1)-nodexz(j,1);
    gamj = nodexz(i,1)-nodexz(k,1);
    gamk = nodexz(j,1)-nodexz(i,1);

    % Retrieve delta value for element number elem.
    delt = (nodexz(i,1)*nodexz(j,2)-nodexz(j,1)*nodexz(i,2)) + ...
           (nodexz(k,1)*nodexz(i,2)-nodexz(i,1)*nodexz(k,2)) + ...
           (nodexz(j,1)*nodexz(k,2)-nodexz(k,1)*nodexz(j,2));

    % Calculate average relative permeability (KR) from i, j, and
    % k nodal values of relative permeability (kr) for element
    % number elem. Assign horizontal hydraulic conductivity (KX)
    % and vertical hydraulic conductivity (KZ) from ROSETTA
    % parameter estimates for element number elem.
    KR = (kr(i)+kr(j)+kr(k))/3;
    KX = Kx(elem);
    KZ = Kz(elem);
    zeta = (Se(:,soilid(elem)) + FF(elem))*Sf(elem);

    % Add the element values to the global coefficient matrix
    % (Equation (11.8) of Hornberger and Wiberg (2005)).
    G(i,i) = G(i,i) + KR*KX*beti*beti/(4*delt) + ...
             KR*KZ*gami*gami/(4*delt);
    G(i,j) = G(i,j) + KR*KX*beti*betj/(4*delt) + ...
             KR*KZ*gami*gamj/(4*delt);
    G(i,k) = G(i,k) + KR*KX*beti*betk/(4*delt) + ...
             KR*KZ*gami*gamk/(4*delt);
    G(j,i) = G(j,i) + KR*KX*betj*beti/(4*delt) + ...
             KR*KZ*gamj*gami/(4*delt);
    G(j,j) = G(j,j) + KR*KX*betj*betj/(4*delt) + ...
             KR*KZ*gamj*gamj/(4*delt);
    G(j,k) = G(j,k) + KR*KX*betj*betk/(4*delt) + ...
             KR*KZ*gamj*gamk/(4*delt);
    G(k,i) = G(k,i) + KR*KX*betk*beti/(4*delt) + ...
             KR*KZ*gamk*gami/(4*delt);
    G(k,j) = G(k,j) + KR*KX*betk*betj/(4*delt) + ...
             KR*KZ*gamk*gamj/(4*delt);
    G(k,k) = G(k,k) + KR*KX*betk*betk/(4*delt) + ...
```

```
                KR*KZ*gamk*gamk/(4*delt);

    % Add the element values to the time derivative term matrix
    % (Box 11.1 of Hornberger and Wiberg (2005)).
    P(i,i) = 1*delt/12*((2*zeta(i)+zeta(j)+zeta(k)) + ...
             Sy(elem)*(2*dSep(i,soilid(elem))+ ...
             dSep(j,soilid(elem))+ dSep(k,soilid(elem))));
    P(j,j) = 1*delt/12*((zeta(i)+2*zeta(j)+zeta(k)) + ...
             Sy(elem)*(dSep(i,soilid(elem))+ ...
             2*dSep(j,soilid(elem))+ dSep(k,soilid(elem))));
    P(k,k) = 1*delt/12*((zeta(i)+zeta(j)+2*zeta(k)) + ...
             Sy(elem)*(dSep(i,soilid(elem))+ ...
             dSep(j,soilid(elem))+ 2*dSep(k,soilid(elem))));
    P(i,j) = 0;
    P(i,k) = 0;
    P(j,i) = 0;
    P(j,k) = 0;
    P(k,i) = 0;
    P(k,j) = 0;
end

% Set right-hand side of groundwater flow equation and solve.
% NOTE: All zero-flux (no-flow) boundaries are "natural" - i.e.,
% there is no extra work necessary in setting the right hand side
% vector.
F = G + 2*P/delta_t;
RHS = 2*P*h_old/delta_t;

% Set fixed head boundary condition for right-hand, upslope nodes.
% Boundary Conditions with matrix notation
[nRows,~] = size(F);
ndrgt_fh = ndrgt(nodexz(ndrgt,2) <= 527.65);
RHS(ndrgt_fh) = 527.65;
diagIdx = (ndrgt_fh - 1).*(nRows + 1) + 1;
F(ndrgt_fh,:) = 0;
F(diagIdx) = 1;

% Set fixed head boundary condition for river channel nodes.
% Boundary Conditions with matrix notation
RHS(ndstm) = hs(ii);
diagIdx = (ndstm - 1).*(nRows + 1) + 1;
F(ndstm,:) = 0;
F(diagIdx) = 1;

% Set fixed head boundary condition for seepage face nodes that
% are below the river stage.
% Boundary Conditions with matrix notation
RHS(seepf) = hs(ii);
diagIdx = (seepf - 1).*(nRows + 1) + 1;
F(seepf,:) = 0;
F(diagIdx) = 1;
```

```
    % Set fixed head boundary condition for seepage face nodes (if any
    % exist) that are above the river stage. Note that the pressure
    % head at seepage face nodes is 0.
    if length(seepface) > length(seepf)
        sface = seepface(nodexz(seepface,2) - hs(ii) > 0);
        % Boundary Conditions with matrix notation
        RHS(sface) = nodexz(sface,2);
        diagIdx = (sface - 1).*(nRows + 1) + 1;
        F(sface,:) = 0;
        F(diagIdx) = 1;
    end

    % Set Neumann boundary (i.e., flux boundary) condition for nodes
    % on top of hillslope.
    % Boundary Conditions with matrix notation
    pptrn = pptr(ii).*(lx_top./ln_top);
    RHS(ndtop(1)) = RHS(ndtop(1)) + pptrn(1) + pptrn(2)/2;
    RHS(ndtop(2:length(ndtop)-2)) = RHS(ndtop(2:length(ndtop)-2)) ...
                                    + pptrn(2:(end-2))./2 + ...
                                    pptrn(3:(end-1))./2;
    RHS(ndtop(end-1)) =  RHS(ndtop(end-1)) + pptrn(end-1)/2 + ...
                         pptrn(end)/2;
    RHS(ndtop(end)) = RHS(ndtop(end)) + pptrn(end)/2;

%     % Set Neumann boundary (i.e., flux boundary) condition for pond
%     % nodes on top of hillslope.
%     temp = pondr(ii) - pptr(ii);
%     pondrn = temp.*(lx_pnd./ln_pnd);
%     clearvars temp
%     RHS(ndpnd(1)) = RHS(ndpnd(1)) + pondrn(1) + pondrn(2)/2;
%     RHS(ndpnd(2:length(ndpnd)-1)) = RHS(ndpnd(2:length(ndpnd)-1))...
%                                     + pondrn(2:(end-2))./2 + ...
%                                     pondrn(3:(end-1))./2;
%     RHS(ndpnd(end)) =  RHS(ndpnd(end)) + pondrn(end) + ...
%                        pondrn(end-1)/2;

    % Solve the groundwater flow equation.
    h_half = sparse(F)\RHS;


%%%%%%%%%%%%%%%%%%%%%%%%%%%%%%%%%%%%%%%%%%%%%%%%%%%%%%%%%%%%%%%%%%%%%%%%%%%%%%%
% Corrector to advance to the next time step (Douglas and Jones
% (1963))
%%%%%%%%%%%%%%%%%%%%%%%%%%%%%%%%%%%%%%%%%%%%%%%%%%%%%%%%%%%%%%%%%%%%%%%%%%%%%%%

    % Pre-assign matrices to improve computation speed.
    G = zeros(nnodes,nnodes);
    F = zeros(nnodes,nnodes);
    P = zeros(nnodes,nnodes);
    RHS = zeros(nnodes,1);
```

```
% Hydraulic Properties and Associated Terms from Cooley and
% Westphal Model (Cooley, 1983; Cooley and Westphal, 1974)
ph = h_half - nodexz(:,2);
Se = SwD_hetero(param,ph);
dSep = dswdp_hetero(param,ph);
kr = krelt_hetero(param,ph);

% Determine seepage face.
seepface = ndbnk(h_half(ndbnk) >= nodexz(ndbnk,2));
seepf = ndbnk(nodexz(ndbnk,2) <= hs(ii));

for elem = 1:nelem
    % Retrieve i, j, and k node values for element number elem
    % from the mesh connectivity table.
    i = nodes(elem,1);
    j = nodes(elem,2);
    k = nodes(elem,3);

    % Retrieve i, j, and k beta values for element number elem.
    beti = nodexz(j,2)-nodexz(k,2);
    betj = nodexz(k,2)-nodexz(i,2);
    betk = nodexz(i,2)-nodexz(j,2);

    % Retrieve i, j, and k gamma values for element number elem.
    gami = nodexz(k,1)-nodexz(j,1);
    gamj = nodexz(i,1)-nodexz(k,1);
    gamk = nodexz(j,1)-nodexz(i,1);

    % Retrieve delta value for element number elem.
    delt = (nodexz(i,1)*nodexz(j,2)-nodexz(j,1)*nodexz(i,2)) + ...
           (nodexz(k,1)*nodexz(i,2)-nodexz(i,1)*nodexz(k,2)) + ...
           (nodexz(j,1)*nodexz(k,2)-nodexz(k,1)*nodexz(j,2));

    % Calculate average relative permeability (KR) from i, j, and
    % k nodal values of relative permeability (kr) for element
    % number elem. Assign horizontal hydraulic conductivity (KX)
    % and vertical hydraulic conductivity (KZ) from ROSETTA
    % parameter estimates for element number elem.
    KR = (kr(i)+kr(j)+kr(k))/3;
    KX = Kx(elem);
    KZ = Kz(elem);

    zeta = (Se(:,soilid(elem)) + FF(elem))*Sf(elem);

    % Add the element values to the global coefficient matrix
    % (Equation (11.8) of Hornberger and Wiberg (2005)).
    G(i,i) = G(i,i) + KR*KX*beti*beti/(4*delt) + ...
             KR*KZ*gami*gami/(4*delt);
    G(i,j) = G(i,j) + KR*KX*beti*betj/(4*delt) + ...
             KR*KZ*gami*gamj/(4*delt);
```

```
    G(i,k) = G(i,k) + KR*KX*beti*betk/(4*delt) + ...
             KR*KZ*gami*gamk/(4*delt);
    G(j,i) = G(j,i) + KR*KX*betj*beti/(4*delt) + ...
             KR*KZ*gamj*gami/(4*delt);
    G(j,j) = G(j,j) + KR*KX*betj*betj/(4*delt) + ...
             KR*KZ*gamj*gamj/(4*delt);
    G(j,k) = G(j,k) + KR*KX*betj*betk/(4*delt) + ...
             KR*KZ*gamj*gamk/(4*delt);
    G(k,i) = G(k,i) + KR*KX*betk*beti/(4*delt) + ...
             KR*KZ*gamk*gami/(4*delt);
    G(k,j) = G(k,j) + KR*KX*betk*betj/(4*delt) + ...
             KR*KZ*gamk*gamj/(4*delt);
    G(k,k) = G(k,k) + KR*KX*betk*betk/(4*delt) + ...
             KR*KZ*gamk*gamk/(4*delt);

    % Add the element values to the time derivative term matrix
    % (Box 11.1 of Hornberger and Wiberg (2005)).
    P(i,i) = 1*delt/12*((2*zeta(i)+zeta(j)+zeta(k)) + ...
             Sy(elem)*(2*dSep(i,soilid(elem))+ ...
             dSep(j,soilid(elem))+ dSep(k,soilid(elem))));
    P(j,j) = 1*delt/12*((zeta(i)+2*zeta(j)+zeta(k)) + ...
             Sy(elem)*(dSep(i,soilid(elem))+ ...
             2*dSep(j,soilid(elem)) + dSep(k,soilid(elem))));
    P(k,k) = 1*delt/12*((zeta(i)+zeta(j)+2*zeta(k)) + ...
             Sy(elem)*(dSep(i,soilid(elem))+ ...
             dSep(j,soilid(elem))+ 2*dSep(k,soilid(elem))));
    P(i,j) = 0;
    P(i,k) = 0;
    P(j,i) = 0;
    P(j,k) = 0;
    P(k,i) = 0;
    P(k,j) = 0;
end

% Set right-hand side of groundwater flow equation.
% NOTE: All zero-flux (no-flow) boundaries are "natural" - i.e.,
% there is no extra work necessary in setting the right hand side
% vector.
F = G + P/delta_t;
RHS = P*h_half/delta_t;

% Set fixed head boundary condition for right-hand, upslope nodes.
% Boundary Conditions with matrix notation
[nRows,~] = size(F);
ndrgt_fh = ndrgt(nodexz(ndrgt,2) <= 527.65);
RHS(ndrgt_fh) = 527.65;
diagIdx = (ndrgt_fh - 1).*(nRows + 1) + 1;
F(ndrgt_fh,:) = 0;
F(diagIdx) = 1;

% Set fixed head boundary condition for river channel nodes.
```

```
    % Boundary Conditions with matrix notation
    RHS(ndstm) = hs(ii);
    diagIdx = (ndstm - 1).*(nRows + 1) + 1;
    F(ndstm,:) = 0;
    F(diagIdx) = 1;

    % Set fixed head boundary condtion for seepage face nodes that are
    % below the river stage.
    % Boundary Conditions with matrix notation
    RHS(seepf) = hs(ii);
    diagIdx = (seepf - 1).*(nRows + 1) + 1;
    F(seepf,:) = 0;
    F(diagIdx) = 1;

    % Set fixed head boundary condition for seepage face nodes (if any
    % exist) that are above the river stage. Note that the pressure
    % head at seepage face nodes is 0.
    if length(seepface) > length(seepf)
        sface = seepface(nodexz(seepface,2) - hs(ii) > 0);
        % Boundary Conditions with matrix notation
        RHS(sface) = nodexz(sface,2);
        diagIdx = (sface - 1).*(nRows + 1) + 1;
        F(sface,:) = 0;
        F(diagIdx) = 1;
    end

    % Set Neumann boundary (i.e., flux boundary) condition for nodes
    % on top of hillslope.
    % Boundary Conditions with matrix notation
    pptrn = pptr(ii).*(lx_top./ln_top);
    RHS(ndtop(1)) = RHS(ndtop(1)) + pptrn(1) + pptrn(2)/2;
    RHS(ndtop(2:length(ndtop)-2)) = RHS(ndtop(2:length(ndtop)-2)) ...
                                    + pptrn(2:(end-2))./2 + ...
                                    pptrn(3:(end-1))./2;
    RHS(ndtop(end-1)) =  RHS(ndtop(end-1)) + pptrn(end-1)/2 + ...
                         pptrn(end)/2;
    RHS(ndtop(end)) = RHS(ndtop(end)) + pptrn(end)/2;

%     % Set Neumann boundary (i.e., flux boundary) condition for pond
%     % nodes on top of hillslope.
%     temp = pondr(ii) - pptr(ii);
%     pondrn = temp.*(lx_pnd./ln_pnd);
%     clearvars temp
%     RHS(ndpnd(1)) = RHS(ndpnd(1)) + pondrn(1) + pondrn(2)/2;
%     RHS(ndpnd(2:length(ndpnd)-1)) = RHS(ndpnd(2:length(ndpnd)-1))...
%                                     + pondrn(2:(end-2))./2 + ...
%                                     pondrn(3:(end-1))./2;
%     RHS(ndpnd(end)) =  RHS(ndpnd(end)) + pondrn(end) + ...
%                        pondrn(end-1)/2;

    % Solve groundwater flow equation.
```

```
    h = sparse(F)\RHS;

    % Assign the total head values at time step t as the previous
    % total head values at time step t+1.
    h_old = h;

    % Output the total head values at each time step t to the same
    % text file.
    % NOTE: THIS CONCATENATES THE VALUES AT 12:00 AM EACH DAY
    % VERTICALLY - i.e., THE VALUES AT TIME STEP t OCCUPY ROWS 1
    % THROUGH N, THE VALUES AT TIME STEP t+1 OCCUPY ROWS N+1 THROUGH
    % 2N, etc.
    if ii == 1
        FIDh = fopen('h_out.txt','w');
        fprintf(FIDh,'%6.12f\n',h_old);
        fclose(FIDh);
    elseif rem((ii-1),24) == 0
        FIDh = fopen('h_out.txt','a');
        fprintf(FIDh,'%6.12f\n',h_old);
        fclose(FIDh);
    else
        continue
    end

end
toc
```